

University of St Andrews

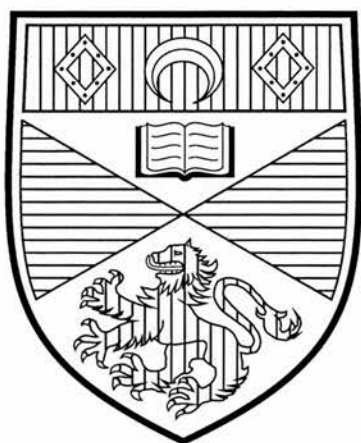


Full metadata for this thesis is available in
St Andrews Research Repository
at:

<http://research-repository.st-andrews.ac.uk/>

This thesis is protected by original copyright

First Principles Calculations of Non – Defective and Defective Oxides



University
of
St Andrews

Derek Stewart Middlemiss

Submitted to the University of St. Andrews as
part of the requirement for the degree of
Doctor of Philosophy in the Faculty of Science

September 2004



(i) I, Derek Stewart Middlemiss, hereby certify that this thesis, which is approximately sixty-seven thousand words in length, has been written by me, that it is the record of work carried out by me and that it has not been submitted in any previous application for a higher degree.

Date: 12th January
2005 Signature of Candidate:

(ii) I was admitted as a research student in September 2000 and as a candidate for the degree of Doctor of Philosophy in August 2001; the higher study for which this is a record was carried out at the University of St. Andrews between 2000 and 2003.

Date: 12th January
2005 Signature of Candidate:

(iii) I hereby certify that the candidate has fulfilled the conditions of the Resolutions and Regulations appropriate for the degree of Doctor of Philosophy in the University of St. Andrews and that the candidate is qualified to submit this thesis in application for that degree.

Date: Signature of Supervisor:
12th Jan 2005

(iv) In submitting this thesis to the University of St. Andrews I understand that I am giving my permission for it to be made available for use in accordance with the regulations of the University Library for the time being in force, subject to any copyright vested in the work not being affected thereby. I also understand that the title and abstract will be published, and that a copy of the work may be made available to any bona fide library or research worker.

Date: 12th January
2005 Signature of Candidate:

Dedication

To my family, for their courage.

Abstract of Thesis

The hybrid Hartree-Fock – density functional method is investigated for suitability in application to calculations of the electronic structure and related properties of transition metal oxides. The proportion of exact exchange in the hybrid functional is the key variable in the study. Calculated values for the properties of NiO and MnO are compared with experiment in order to permit the performance of the hybrid functionals to be assessed. Amongst the properties considered are the equation of state parameters, detail of electronic structure, magnetic coupling constants, crystal field excitation energies, spin-lattice interaction strength, the character of hole states and high pressure phase diagrams. The final conclusion of the work is that no one hybrid functional can give a quantitatively correct description of all properties, either within a single material or across the range of transition metal monoxides. One novel and highly successful feature of the work is the mapping of $d \rightarrow d$ transition energies onto crystal field Hamiltonians, with the aim of obtaining a more fundamental understanding of the nature of such excitations, and their modification by the crystalline environment.

In addition, the hybrid functional method was used in a separate study which sought to address experimental uncertainties surrounding the electronic structure of and conducting state within non-defective vanadium monoxide. The perfect material was found to be an insulator, in keeping with the other first row oxides, and so a further examination of the effect of defects was initiated. Complex defective forms of the material were treated via structural optimisation in the plane-wave pseudopotential method. The final section of the thesis deals with the crystal field excitations in $\text{Sr}_2\text{CuO}_2\text{Cl}_2$, their modification by hole doping and any potential rôle they may play in the high temperature superconductivity common to the cuprates.

Contents

Chapter 1: Background, Theory and Aims

A Brief Introduction to the Transition Metal Oxides	1
The Simulation of Condensed Matter	13
The Hartree-Fock Theory for Solids: The CRYSTAL Code	15
The Plane-Wave Pseudopotential Method: The CASTEP Code	20
Hybrid Hartree-Fock – Density Functional Hamiltonians	24
Aims of the Current Work	27

Chapter 2: A Hybrid Hamiltonian Study of the Structural and Electronic Properties of bulk NiO and MnO

Introduction and Methods	31
Electronic Structure of NiO	34
Electronic Structure of MnO	39
The Equation of State for NiO	44
The Equation of State for MnO	47
The Magnetic Properties of NiO	49
The Magnetic Properties of MnO	52
The Spin-Lattice Distortion in MnO	56
The Crystal Field Excitations in MnO and the Effect of Correlation	61
The Pressure Induced B1 to B8 Transition in MnO	65
Conclusions	82

Chapter 3: A Hybrid Hamiltonian Study of the Crystal Field Excitations in Bulk NiO

Introduction	89
Theoretical and Computational Methods	91
Results	94
Discussion	106
Conclusions	118

Chapter 4: A Hybrid Hamiltonian Study of Hole States in Pure and Li-Doped NiO

Introduction	121
Defect States of $\text{Li}_x\text{Ni}_{1-x}\text{O}$	122
Hybrid Scheme and Computational Conditions	123
Results	124
Discussion	134

Chapter 5: A Hybrid Hamiltonian Study of Vanadium Monoxide

Introduction	138
Theoretical Methods	142
Results and Discussion	145
Summary and Conclusions	169

Chapter 6: A Plane Wave Pseudopotential Study of Defective Structures in Vanadium Monoxide

Introduction	175
The Plane Wave Pseudopotential Method	176
The 1 in 4 (NbO-Type) Defect Structure	178
The 1 in 8 Ordered Defect Structure	188
The 1 in 6 (TiO-Type) Defect Structure	193
Conclusions	202

Chapter 7: A UHF Study of Crystal Field Excitations in Pure and Hole-Doped $\text{Sr}_2\text{CuO}_2\text{Cl}_2$

Introduction	205
Theoretical Method	206
Results	206
Conclusions	216

Chapter 8: Conclusions, Publications and Acknowledgements

A Universal Functional for the Transition Metal Oxides?	219
Publications Arising from this Work	223
Acknowledgements	223

Chapter 1

Background, Theory and Aims

1. A Brief Introduction to the Transition Metal Oxides

The progressive filling of the 3d shell with increasing atomic number is the most important unifying feature and cause of most of the complexity in compounds of the transition metals. In this thesis, attention is focussed upon the compounds formed by combination with oxygen (TMOs). The binary oxides already offer up a vast range of compounds, such as the monoxides MO (M representing a transition metal) in which the rocksalt structure predominates, the corundum-type structure of the sesquioxides M_3O_4 , and the rutile-type structure of the dioxides MO_2 . The inclusion of ternary compounds vastly increases the complexity; the added atoms often originate outside the transition group. A wide range of electrical conductivity is found, from good insulators like TiO_2 at one extreme to metals like ReO_3 at the other. Semi-conducting behaviour such as that observed in $Fe_{0.9}O$ is infrequently observed, and some of the most complex oxides, like $YBa_2Cu_3O_7$ are high temperature superconductors. Many oxides, particularly those containing early transition metal atoms, show complex non-stoichiometric phases, the structures of many of which are still unclear.

How do chemists and solid state physicists think about the TMOs? A common starting point is a notional oxidation state for each element present. In almost all cases, each oxygen ion is assigned a charge of -2 units of the proton charge, i.e. two excess electrons. Metal atoms are then assigned counterbalancing charges, leading to Mn^{2+} in MnO and Ti^{4+} in TiO_2 . In some cases, the oxidation state of the cation in the oxide environment is clear, e.g. Li^+ , but some transition metals manifest with variable oxidation states, and an appeal is usually then made to the energies of the various oxidation states in other environments. Mixed valency compounds do occur, of which Fe_3O_4 [1] is perhaps the best known example. Is it appropriate to think of two Fe^{3+} ions to every Fe^{2+} ion in this material, or is some 'delocalised' $Fe^{2\frac{2}{3}+}$ state closer to the truth? In fact, the cation oxidation states in Fe_3O_4 change abruptly at 120K, a point which is termed the Verwey transition. Below this temperature, integral Fe^{2+} and Fe^{3+} cation states dominate, while above it, a description involving one Fe^{3+} to two $Fe^{2\frac{1}{2}+}$

cations is appropriate, with a corresponding increase in conductivity. Turning to a discussion of the anion, the O^{2-} state is most frequently found, although O^- often occurs as a paramagnetic defect.

In thinking about the electron configurations of the 3d transition metal ions in oxides, it should be borne in mind that it is always the 4s electrons that are first removed by ionisation. Attention then focuses upon the remaining d^n electrons, as the determinant of most of the interesting physics and chemistry of the compounds. To appreciate the influence of the d-electrons, consider that all the d^0 oxides are found to be diamagnetic insulators. Allied to the concept of electron configuration is the spin moment of the metal ion. Hund's first rule is generally observed in the 3d oxides, and so unpaired electrons arrange themselves to maximise the spin multiplicity. In the 4d and 5d series, arrangements of the electrons with low total spin are more common, due to the increased interaction of the ion with its surroundings.

The ionic radius of the M^{2+} 3d ions in their high spin configurations generally falls with increasing atomic number, save between V^{2+} and Mn^{2+} , where there is an abrupt rise from ~ 68 to ~ 83 pm respectively [2]. The rise is linked to the fact that metal-metal bonding is generally found in oxides of Ti^{2+} and V^{2+} , but is absent in oxides of the later metals. In general, though, the trend is a decreasing one, and this can be linked to the increase in nuclear charge, the effect of which is only partially shielded by the electrons added to the 3d shell. In terms of crystal geometry, low values of coordination of metal ions are preferred for small radii, and vice-versa. Thus, tetrahedral structures are found for radii less than ~ 50 pm and octahedral structures for radii in the range ~ 50 to ~ 80 pm. It should be noted that the ionic radii on which this rule is based are now thought to be rather low, and revised radii were later published [3]. The radii quoted in this revised article for all the ions occurring in the present work are shown in Table 1 below.

In the binary, rocksalt structured monoxides, non-defective phases (to a good approximation) are generally found for compounds which contain metals occurring late in the series, and complex defective phases for early members. NbO, in the 4d series deserves particular mention for its high concentration of 25% vacancies on both anion and cation sublattices.

Cation	Radius (pm)
Ni ²⁺ HS	83
Mn ²⁺ HS	97
Mn ²⁺ LS	81
V ²⁺	93
Sr ²⁺	132
Li ⁺	90

Anion	Radius (pm)
O ²⁻	126
Cl ⁻	167

Table 1. The effective ionic radii for all ions occurring in the present work, as presented in the data of Shannon [3]. HS and LS indicate high- and low-spin states respectively.

It is arguable that the presence of defects at such concentration should really be considered as a separate structural phase. Wüstite, or Fe_{1-x}O always presents as slightly metal deficient, and a range of defect cluster models have been advanced to account for this [4]. In contrast to the picture for wüstite, where defect clusters are separated from each other, in TiO_{1.0}, an ordered phase of defects is formed extending throughout the whole lattice, in which 1 in 6 sites on both sublattices are vacant [5].

In thinking about the electronic structure of the TMOs, it must be conceded that no one model can reproduce all the observed behaviour, at even a qualitative level. At one extreme, there is the ionic model, in which all the bonding interactions are neglected and only the electrostatic perturbation caused by the extended lattice at each site is considered. The crystal field theory is a part of this wider approach. At the other extreme is band theory, which implicitly takes each electron as part of an infinite lattice. It should be stressed that many authors refer to the electrons in band theory as ‘delocalised’. This is loose language, for the single particle states in band theory may be concentrated closely around one site in a cell, and it is this picture of the charge distribution that is periodically replicated throughout space.

(i) The Ionic Model

The crystal field (CF) theory is a highly simplified model, in which the orbital overlap between cation and neighbouring anion states is neglected. Experience has shown that the electrostatic considerations of the CF model alone cannot reproduce experimental values for the crystal field splitting energy, and so the ligand field theory incorporating bonding interactions was developed [6]. The energy difference in the simple theory between the high lying e_g and low lying t_{2g} symmetry orbitals is useful, in a qualitative sense for the explanation of transitions to low spin states, and the Jahn-Teller distortion of the local environment of ions with particular d-electron configurations. Quantitative applications come from the analysis of the characteristic $d \rightarrow d$ excitations in TMOs. Such transitions are forbidden by the Laporte selection rule, and typically appear with weak intensity in optical absorption. The Kanamori CF Hamiltonian [7] is an effective tool in the analysis of such transitions, and takes the following form, for an isolated metal site

$$\hat{H}_{CF} = \hat{H}_{CF}^0 + \frac{1}{2} \sum_{\bar{\gamma}} \sum_{\bar{\sigma}} C(1,2) a_{\gamma_1 \sigma_1}^\dagger a_{\gamma_2 \sigma_2}^\dagger a_{\gamma_2 \sigma_2} a_{\gamma_1 \sigma_1} ,$$

in which $\bar{\gamma} = \gamma_1 \gamma_2 \gamma_1' \gamma_2'$ and $\bar{\sigma} = \sigma_1 \sigma_2 \sigma_1' \sigma_2'$. The integrals of the two-electron interactions are

$$C(1,2) = \left\langle \gamma_1 \sigma_1, \gamma_2 \sigma_2 \left| \frac{e^2}{|\mathbf{r}_1 - \mathbf{r}_2|} \right| \gamma_1' \sigma_1', \gamma_2' \sigma_2' \right\rangle ,$$

where γ and γ' label the orbitals of the d-manifold, and σ and σ' the electron spin. The single-particle creation and annihilation operators follow the usual notation. Three distinct types of d-d interaction can be identified,

- (i) intraband Coulomb terms $U = \langle \gamma \sigma, \gamma \sigma' \| \gamma \sigma, \gamma \sigma' \rangle$ with $\sigma \neq \sigma'$
- (ii) interband Coulomb terms $U' = \langle \gamma \sigma, \gamma' \sigma' \| \gamma \sigma, \gamma' \sigma' \rangle$ with $\gamma \neq \gamma'$
- (iii) interband exchange terms $J = \langle \gamma \sigma, \gamma' \sigma' \| \gamma' \sigma, \gamma \sigma' \rangle$ with $\gamma \neq \gamma'$

These can be written in terms of the Racah A, B and C parameters of atomic spectroscopy [8], with an orbital independent value for U of $A+4B+3C$. U' and J on

the other hand are orbital dependent, as shown in Table 2, but may be conveniently averaged over the d-manifold for the purposes of simplification, leading to the orbital (γ) and spin (σ) independent expressions

$$U' = A - B + C$$

$$J = \frac{5}{2}B + C$$

The ground and spin-allowed d→d excited state electron configurations may now be mapped onto H_{CF} , respecting the orbital dependence of the interactions presented in Table 2. The theory as developed so far does not account for the perturbing presence of the crystalline environment, and the crystal field splitting, Δ_{CF} , must be added depending upon whether the initial and final orbitals are at different relative energies. More specifically, the energy of an $e_g \rightarrow t_{2g}$ transition would be lowered by Δ_{CF} , while the opposite is true for a $t_{2g} \rightarrow e_g$ transition. It is obvious that neither the $t_{2g} \rightarrow t_{2g}$ nor $e_g \rightarrow e_g$ transitions involve a change in crystal field energy.

γ	γ'	U'	J
xy, yz, xz	xy, yz, xz	$A-2B+C$	$3B+C$
x^2-y^2, z^2	x^2-y^2, z^2	$A-4B+C$	$4B+C$
xy	x^2-y^2	$A+4B+C$	C
xy	z^2	$A-4B+C$	$4B+C$
yz, xz	x^2-y^2	$A-2B+C$	$3B+C$
yz, xz	z^2	$A+2B+C$	$B+C$

Table 2. Interband Coulomb and exchange integrals, U' and J as a function of d-orbitals, γ and γ' expressed in terms of the Racah A, B and C parameters.

Now, the excitation energies can be calculated as differences between the individual energies of crystal field states. It is important to note that the three radial Slater integrals F_0 , F_2 and F_4 could be used instead of the Racah A, B and C parameters, for each set of parameters can be expressed in terms of the other. The Racah A parameter is not involved in the energies of d→d excitations (it appears only in transitions for which the number of electrons in the d-manifold changes), and B, C and Δ_{CF} are often

treated as adjustable parameters in the fitting of experimental spectra. The energies of the crystal field states are usually interpreted with the aid of a Tanabe-Sugano diagram [9], which, for each d^n configuration, present the energy of the various states plotted against the ratio D / B , for a fixed ratio $C / B \approx 4.5$, where conventionally, $\Delta_{CF} = 10Dq$. The crystal field splitting is generally larger for smaller metal oxygen distances, and shows a rough falling trend with progression from early to late transition metals. The 4d and 5d series have larger Δ_{CF} than those in 3d compounds, due to the increased radius of the d-shell, and this fact taken in combination with lowered B and C parameters (i.e. lowered Hund's rule exchange) leads to the predominance of low spin states in compounds of the 4d and 5d transition metals.

(ii) The Cluster Model

The ionic model can be applied to the study of the band gaps in the oxides, although approximations of the effect of the Madelung potential, polarisation and band broadening due to overlap are necessary. For such purposes, the cluster model may be the next most appropriate method. Here the electronic structure of a small cluster of metal and oxygen atoms is calculated, in a geometry representative of the true bulk material. Band structure effects are still absent, but the full complement of molecular methods may be employed, including schemes such as configuration interaction (CI), which seek to treat the electron correlation. Here, the band gap may be estimated as the difference in energy between the cluster with one electron either removed or added. Such a CI calculation for an $(NiO_6)^{n-}$ cluster leads to an estimated band gap of ~ 10 eV, which is lowered to ~ 4.5 eV through estimation of the polarisation effect [10]. The $d \rightarrow d$ excitation spectra of TMOs are also well reproduced by the correlated method. One of the most important applications of CI cluster calculations has been to show that the $d^8 \underline{L}$ (ionised O^{2-}) state is a lower energy than d^7 (ionised Ni^{2+}) in NiO. Single particle theory estimates of the band gap are considered in the next chapter.

(iii) Spin Polarised Band Theory

In a simple band picture of the electronic structure of the TMOs, the most pressing difficulty lies with the fact that the 3d-manifold in these compounds is generally

partially occupied, and this necessarily leads to a metallic ground state within the Bloch-Wilson picture. De Boer and Verwey showed, in 1937, that a number of TMOs, NiO and MnO included, were excellent insulators [11]. It was not until twelve years later in 1949 that Mott [12-15] advanced one potential explanation for the discrepancy. His picture of the anomalous insulating state was of electrons localised by strong mutual interactions, where conductivity is strongly suppressed by the high energy cost of double occupation of d-orbital. It is important to note the difference between a Mott insulator and a conventional band insulator. In the former, the electrons are physically localised at atomic sites, while in the latter, the insulating behaviour arises from a full band in which there are no free Bloch states at thermally accessible energies to carry current. The one-particle states in the latter may very well be delocalised over the whole of the crystal. Slater [16] proposed in 1951 that the insulating state could be reproduced by band theory if the correct magnetic ground state were imposed. The cell length of the antiferromagnetic structure is twice that in the non-magnetic cell, and as a result, Bragg reflection at the edge of the halved Brillouin zone can open a small gap. However, Slater's proposal cannot be the whole truth, for the insulating behaviour in TMOs is generally found to be independent of the state magnetic order or disorder, and the size of the Slater energy gap is still much smaller than experiment. It is important to note that the purported 'failure of band theory' to produce an insulating state is a loose term, for periodic UHF calculations conducted for the TMOs within the framework of band theory show great improvement over LDA results. It is clear, therefore, that it is the choice of Hamiltonian *within* band theory that determines the agreement of calculated properties with experiment.

To see why the LDA Hamiltonian should fare so badly in the TMOs, consider that the self-interaction present in the LDA Hartree potential is not fully corrected by a corresponding term in the exchange-correlation potential. The net effect of this is to push occupied levels upward in energy relative to the virtual orbitals, where the shift is larger (of the order 10 eV in NiO) for the highly localised metal d-states than for oxygen states. This, in combination with wide bands, leads to the metallic state common in pure DFT approaches. Self-interaction correction can yield an insulating state in the TMOs [19]. The counter question is of interest too, namely, why does the LDA do so well in other materials, if the electron correlations of the type described here are absent within it? A large part of its success is summed up by the Landau

quasiparticle picture, in which the results obtained for a non-interacting electron gas can be transferred to an interacting one, provided that the electron mass is renormalised.

(iv) The Mott-Hubbard Model

In the TMOs, the strong electron correlation leads to an insulating state of the type discussed by Mott. To see why this should be so, take as an example the Ni^{2+} ion and consider the energy required to transfer an electron from one Ni^{2+} ion to another, creating a $\text{Ni}^+, \text{Ni}^{3+}$ pair. This is given, for gas phase ions by

$$U = \left\{ I : \text{ionisation potential of } \text{Ni}^{2+} \right\} - \left\{ A : \text{electron affinity of } \text{Ni}^{2+} \right\} \\ = 36 \text{ eV} - 18 \text{ eV} = 18 \text{ eV}$$

This is a very large energy, and while screening mechanisms in the solid state will reduce it, the conducting state still seems to be ruled out. Hubbard, from 1963 onward took the concepts developed by Mott and extended them to include itinerant electron behaviour [20-22]. The resulting Mott-Hubbard (MH) Hamiltonian is of the form

$$\hat{H} = \sum_{\substack{i \neq j \\ \sigma = \uparrow \text{ or } \downarrow}} T_{ij} a_{i\sigma}^\dagger a_{j\sigma} + U \sum_i a_{i\uparrow}^\dagger a_{i\uparrow} a_{i\downarrow}^\dagger a_{i\downarrow},$$

where the creation and annihilation operators act at lattice sites \mathbf{R}_i and σ labels electron spin. The U parameter is as given above, and T is the transfer matrix, the off-diagonal elements of which relate to the transfer of an electron (without change in spin) from site i to site j . As the distance between the atomic sites decreases (equivalent to increasing pressure), the elements of the transfer matrix increase. The result is the formation of the electron and hole Hubbard sub-bands, of width W_e and W_h respectively. The energy gap is given by $E_g = U - \frac{1}{2}(W_e + W_h)$ and disappears at a critical lattice constant, at which point an insulator to metal transition occurs.

The Hubbard model lacks interatomic correlation and is analytically soluble only when the T -matrix couples nearest neighbour sites. Nevertheless, the qualitative picture of a gap bordered by metal derived states is very useful in interpreting the electronic structure of the TMOs.

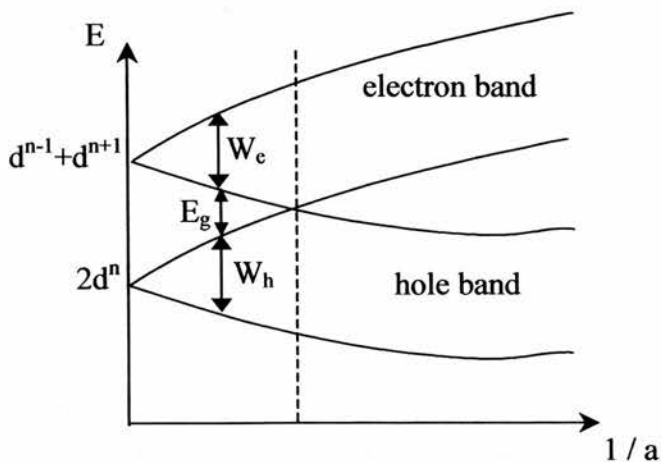


Figure 1. The electron and hole sub-bands in the Hubbard model, as a function of the inverse of the lattice constant. Dotted line marks insulator to metal transition.

(v) The ZSA Scheme

While the MH scheme as described above is qualitatively correct for some TMOs, problems were encountered in trying to apply it more widely to the chalcogenides. While the gaps in compounds containing V and Ti seem to be well described by the Mott-Hubbard model, the gap widths in the Co, Ni and Cu compounds seem to be related to the electronegativity of the anion [23]. Such a dependence cannot be easily accounted for in the MH scheme. Moreover, the compounds NiS, CuS and CoS are all metals, which in the MH picture would require a reduction in the value of U from the 7 – 10 eV typical in the oxides to 1 – 2 eV in the sulfides. While the Hubbard U parameter is reduced from its free ion value by screening in oxides, it is hard to conceive of such a strong dependence on the nature of the coordinating anion.

Zaanen, Sawatzky and Allen (ZSA) in 1985 [24] postulated that the process required to explain the two observations above is the metal to anion charge transfer $d^n \rightarrow d^{n+1} + \underline{L}$, occurring with energy Δ , where \underline{L} indicates a hole in the anion valence band. If $\Delta > U$ then the lower Hubbard sub-band lies above the anion p band, and the system is characterised a MH insulator, whereas, if $\Delta < U$ then the opposite order of bands prevails, and the system is a charge transfer (CT) insulator. The energy Δ is also found to be directly related to the electronegativity of the anion, which would place the late TM compounds as CT insulators. The phase diagram of the ZSA model is shown in Figure 2 below.

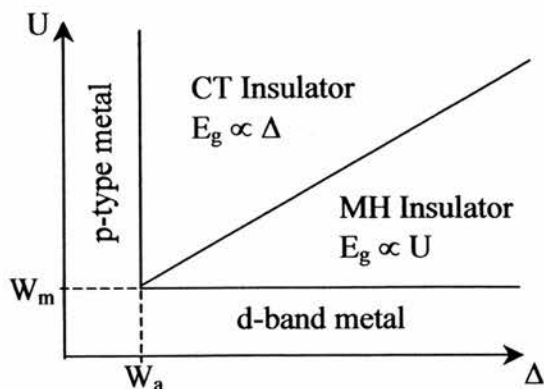


Figure 2. A simplified version of the full ZSA phase diagram, omitting intermediate regions. W_m and W_a are the widths of the metal and anion bands respectively.

The ZSA model now provides an adequate description of a wide variety of transition metal compounds. Of course, the nature of the states at the valence band edge has new implications for hole doping of TMOs, for it can no longer be assumed that the lowest ionised state has d^{n-1} character. The CT insulating state predicted for NiO within the ZSA model is consistent with the results of correlated cluster calculations described earlier in Section (ii) of this chapter.

(vi) The Origin of Magnetic Interactions

The terms “magnetic insulator” and “Mott-Hubbard insulator” are generally taken to be synonymous. The former invokes explicitly the concept of the coexistence of unpaired spins and an energy gap, while the latter establishes that the gap is bordered by metal derived states. Of course, the discussion of the ZSA scheme in the last section has shown that CT insulating states are likely in the late transition metal oxides, and unpaired spins are found there too. How do such spin moments order themselves, and what interactions drive the ordering?

The direct magnetic dipole interaction of the moments is too small to account for the observed ordering temperatures in the TMOs, and instead some interaction through orbital overlap must be considered. Taking as a model two unpaired single electrons distributed one electron apiece to two atoms, the energy difference between the singlet and triplet states is

$$\Delta E_{S-T} = 2K - 4St,$$

where the first term, $2K$ is the potential exchange interaction which favours the triplet configuration, and the second term is the kinetic exchange interaction, which depends upon the overlap integral, S , of the orbitals and the hopping integral, t , between them. The kinetic exchange favours the singlet configuration, and is usually the dominant term for all but the smallest atomic separations.

Considering only the metal sublattice of the face centred cubic structure, any given metal atom has twelve nearest neighbour metal atoms at a distance of $\sqrt{2} d_{M-O}$, where d_{M-O} is the metal to oxygen distance. At first sight, the observed magnetic ordering could be due to a direct overlap interaction between nearest neighbour metal atoms, but there are two facts that rule this explanation out. The first is that approximated values for this interaction render it too small to satisfactorily account for the critical temperatures of most TMOs. The second, and more convincing reason is that, in the observed type-2 antiferromagnetic (AF_2) alignment in MnO and NiO, the spins of the nearest neighbour metal atoms align themselves in a six-parallel and six-antiparallel pattern, which means that the direct overlap cannot contribute to the ordering energy. Instead, some other interaction must be sought, and it is the indirect interaction of metal sites at a separation of $2d_{M-O}$ through overlap with the intervening oxygen atom that dominates. Such an indirect overlap is termed ‘superexchange’ in the TMO related literature. A perturbation approximation of the Mott-Hubbard Hamiltonian leads to an superexchange integral of the following form

$$J = 2t^2 \left(\frac{1}{U} + \frac{1}{\Delta} \right).$$

To appreciate the physical basis for the superexchange interaction, consider the following lowest energy arrangement of spins on a linear $M - O - M$ path: $M(\uparrow) - O(\uparrow\downarrow) - M(\downarrow)$. Now, it is only for antiparallel metal spins that the excited $M(\uparrow\downarrow) - O(\uparrow\downarrow) - M(0)$ and $M(\uparrow\downarrow) - O(0) - M(\uparrow\downarrow)$ charge transfer configurations can occur, with the effect that the energy is lowered. Thus, superexchange always favours

antiferromagnetism. The strength of the superexchange interaction decreases rapidly as the M – O – M path moves away from linearity, until, at 90°, a ferromagnetic coupling arises from the potential exchange term.

The magnetic alignments considered in the following work are the ferromagnetic (FM) and the antiferromagnetic type-I (AF₁), type-II (AF₂) and type-III (AF₃) states, the magnetic environments of which are as defined in Table 3 below.

	FM	AF ₁	AF ₂	AF ₃
nn parallel	12	4	6	4
nn antiparallel	0	8	6	8
nnn parallel	6	6	0	4
nnn antiparallel	0	0	6	2

Table 3. The magnetic environment of a metal atom in four alignments, where nn and nnn indicates nearest neighbour and next-nearest neighbour atoms respectively.

Most first principles codes can calculate total energies for user-defined spin alignments, in which the moments are limited to two degrees of freedom, namely a direction, either up or down, and a magnitude. The Ising Hamiltonian can be used in interpreting the results of such calculations, for it has the same constraint on spin orientation. Now, the direct, J_d , and superexchange, J_{se} , integrals can be extracted by mapping any three independent total energies (normally, the FM, AF₁ and AF₂ alignments are used) onto a Hamiltonian of the form,

$$\hat{H}_{\text{Ising}} = \hat{H}_{\text{Ising}}^0 - \frac{J_d}{2} \sum_{ij}^{\text{nn}} \sigma_i \sigma_j + \frac{J_{se}}{2} \sum_{ij}^{\text{nnn}} \sigma_i \sigma_j$$

where the summations run over the nearest neighbours (nn) and next-nearest neighbours (nnn) of any given metal site, and the spin variable, σ , takes values of ± 1 . In this form, the magnitudes squared of the local spin density differences, S_z^2 , are subsumed into J_d and J_{se} , which are then more correctly termed coupling energies. The corresponding mapping equations are of the form,

$$E(M) = E_{\text{ising}}^0 - \frac{J_d}{2} [N_{nn}(\uparrow\uparrow) - N_{nn}(\uparrow\downarrow)] + \frac{J_{se}}{2} [N_{nnn}(\uparrow\uparrow) - N_{nnn}(\uparrow\downarrow)]$$

where N_{nn} and N_{nnn} are the numbers of nn and nnn parallel ($\uparrow\uparrow$) and anti-parallel ($\uparrow\downarrow$) spins in the M alignment. The coupling constants are then given by

$$J_d = \frac{1}{8} [E(\text{AF}_1) - E(\text{FM})]$$

$$J_{se} = J_d - \frac{1}{6} [E(\text{AF}_2) - E(\text{FM})]$$

in which the energies of the magnetic states are per formula unit.

This completes the very brief overview of the properties of the TMOs that will be given here. The focus has been upon concepts and theory of direct relevance to the following work. For further reading, a fuller and non-mathematical background can be found in the monograph by Cox [25], while more technical treatments are provided by Brandow [26] and Hüfner [27].

2. The Simulation of Condensed Matter

Much of the modern interest in the theory of condensed matter arises from early *ad hoc* theories of cohesion in solids and liquids. Qualitative concepts such as molecular, ionic, metallic and covalent bonding were developed to describe extremal cases, and had only a limited predictive power when applied to intermediate systems. By way of example, take zinc oxide, α -quartz and corundum; materials in which the bonding is known to exhibit a mixed covalent – ionic character. Such concepts remain useful, however, in the interpretation of experimental and theoretical results. Applying a simple model to the end result of a sophisticated calculation may seem perverse, but in many cases, the phenomena under investigation are complex and it is necessary to find some way of focussing upon only the crucial details. Consider the energy difference between two different magnetic states of a crystal. The value itself can communicate little, but taken together with a simple spin Hamiltonian, concepts of

magnetic interaction begin to emerge, and the tools provided by statistical mechanics can be brought to bear, yielding *ab initio* predictions of macroscopic behaviour. As a further example, consider that the application of a tight binding Hamiltonian to the interpretation of an *ab initio* band structure provides a rational way of thinking about interactions between the constituent atoms of a material, and their dependence on interatomic distance etc.

It is worth drawing a distinction between two broad classes of computational scheme. The set of *ab initio* or first principles methods require as initial information only a specification of the atoms present, the crystallographic structure, and other details such as the charge and spin of the simulated cell. Empirical methods, on the other hand, usually require, in addition to the above information, a parameterised form for the force-field between the atoms. Such force fields are fitted to data derived either from experiment or from limited sets of first principles calculations. *Ab initio* methods are capable of dealing with changes in the bonding character of solids, for they implicitly contain some notion of electronic structure, whereas empirical methods generally do not. The force-field methods do have the advantage that their reduced computational demands lead naturally to applications in simulating extremely large ensembles of atoms, such as extended crystal defects, zeolite cages and polymer crystals. So-called hybrid or QM/MM (Quantum Mechanics / Molecular Mechanics) schemes are of particular interest, for they offer up the possibility of simulating small, active areas of a material with an expensive, first principles approach, while modelling the response of the rest of the ensemble with an inexpensive force-field approach.

However, the rising ratio of computational power to price, efficient numerical algorithms and massively parallel machines has meant that first principles methods can now model systems containing up to $10^3 - 10^4$ atoms. This limit seems set to quickly rise with the continuing development of so-called “linear scaling” methods, implemented in codes such as SIESTA. *Ab initio* calculations have proved to be of great use in simulating materials under conditions that are either prohibitively adverse or are impractical to bring into the laboratory. Examples of this are the simulation of materials under high pressure, high temperature, and in strong electric, magnetic and radiation fields.

3. The Hartree-Fock Method for Solids: The CRYSTAL Code.

The Hartree-Fock (HF) method has proved an incredibly popular choice for the simulation of the electronic structure of atoms, molecules, clusters and solids over the past three decades. The history of the theory properly begins with Hartree, Fock and Slater's [28-29] derivation of the HF equations, but the modern implementation is made possible by the pioneering vision of Boys [30] in suggesting the use of Gaussian-type functions (GTFs) as a basis set. This overcame the problems caused by a lack of an analytic method for the calculation of three- and four-centre two-electron integrals when using a basis of Slater-type orbitals (STOs). STOs are rarely used now, save where high accuracy is needed, or in semi-empirical methods where three- and four-centre integrals are neglected. Indeed, it was the HF method which gave rise to a whole series of semi-empirical methods which neglect varying numbers of the bielectronic integrals, or attempt to include some component of electron correlation in an approximate way [31]. The HF method has an undeservedly bad reputation amongst the solid state theory community, due to its poor performance in the jellium model and the difficulties in treating the non-local exchange operator correctly. In recent years it has become clear that the performance of HF theory in the jellium model is not a reasonable basis for a judgement as to its usefulness in real materials.

(i) Molecular Theory

The molecular HF theory will be developed here first, and then specialised to account for periodic solids. As a starting point, consider the non-relativistic Born-Oppenheimer Hamiltonian below, expressed in atomic units for a system of m electrons and N nuclei, each of separate charge Z_A

$$\hat{H} = -\sum_{i=1}^m \frac{\nabla_i^2}{2} - \sum_{i=1}^m \sum_{A=1}^N \frac{Z_A}{|\mathbf{r}_i - \mathbf{R}_A|} + \sum_{i=1}^m \sum_{j>i}^m \frac{1}{|\mathbf{r}_i - \mathbf{r}_j|} + \sum_{A=1}^N \sum_{B>A}^N \frac{Z_A Z_B}{|\mathbf{R}_A - \mathbf{R}_B|}. \quad (1)$$

The form of the HF wavefunction is that of a single determinant, expressed as an antisymmetrised product thus

$$\Psi = \hat{A} \left(\prod_{i=1}^m \psi_i(\mathbf{r}_i) \chi_i \right). \quad (2)$$

The Hartree-Fock theory offers the assurance that the single determinant arrived at by variation has the lowest energy of any trial determinant.

Now, for closed shell systems, a restricted form of the theory may be applied, in which both the α - and β -spin orbitals have the same spatial part. The determinant is then composed of a product of $m/2$ doubly occupied orbitals, thus

$$\Psi_{CS} = \hat{A} \left(\prod_{i=1}^{m/2} \psi_i(\mathbf{r}_{2i-1}) \chi(\alpha) \psi_i(\mathbf{r}_{2i}) \chi(\beta) \right). \quad (2)$$

Forming the expectation value of Ψ_{CS} with the Born-Oppenheimer Hamiltonian (1) leads to

$$\begin{aligned} E_{CS} &= \langle \Psi_{CS} | H | \Psi_{CS} \rangle \\ &= 2 \sum_{i=1}^{m/2} \int d\mathbf{r} \left[\psi_i^*(\mathbf{r}) \left(-\frac{\nabla^2}{2} + v(\mathbf{r}) \right) \psi_i(\mathbf{r}) \right] \\ &\quad + \sum_{ij}^{m/2} \int d\mathbf{r} d\mathbf{r}' \left(\psi_i^*(\mathbf{r}) \psi_i(\mathbf{r}) \right) \left(\psi_j^*(\mathbf{r}') \psi_j(\mathbf{r}') \right) \frac{1}{|\mathbf{r} - \mathbf{r}'|} \\ &\quad - \sum_{ij}^{m/2} \int d\mathbf{r} d\mathbf{r}' \left(\psi_i^*(\mathbf{r}) \psi_j(\mathbf{r}) \right) \left(\psi_j^*(\mathbf{r}') \psi_i(\mathbf{r}') \right) \frac{1}{|\mathbf{r} - \mathbf{r}'|}. \end{aligned} \quad (3)$$

Minimising this energy with respect to variations in the orbitals, while respecting their orthonormality leads to the HF equations

$$\begin{aligned} \hat{F}\psi_i(\mathbf{r}) &= \left[-\frac{\nabla^2}{2} + v(\mathbf{r}) + \int d\mathbf{r}' \left(\frac{\rho(\mathbf{r}')}{|\mathbf{r} - \mathbf{r}'|} \right) \right] \psi_i(\mathbf{r}) - \sum_{j=1}^{m/2} \int d\mathbf{r}' \left(\frac{\psi_j^*(\mathbf{r}') \psi_i(\mathbf{r}')}{|\mathbf{r} - \mathbf{r}'|} \right) \psi_j(\mathbf{r}) \\ &= \varepsilon_i \psi_i(\mathbf{r}). \end{aligned} \quad (4)$$

The electron density is defined as the sum of the squares of the spatial part of each orbital in the normal way. Now, the molecular orbitals are expressed as linear combinations of the n local, real functions ϕ_μ of the basis set

$$\psi_i(\mathbf{r}) = \sum_{\mu=1}^n c_{\mu i} \phi_\mu(\mathbf{r}). \quad (5)$$

In preparation for their efficient solution, the set of HF equations, which number one for each doubly occupied molecular orbital may now be expressed in matrix notation

$$FC = SCE, \quad (6)$$

where F is the Fock matrix, S the overlap, C the matrix of coefficients and E the eigenvalues. The various contributions to the F matrix

$$F_{\mu\nu} = T_{\mu\nu} + Z_{\mu\nu} + B_{\mu\nu} + X_{\mu\nu}, \quad (7)$$

are of kinetic, electron-nuclear, bielectronic and exchange origin respectively, and have the explicit forms

$$\begin{aligned} T_{\mu\nu} &= -\frac{1}{2} \int \varphi_{\mu}(\mathbf{r}) \nabla_{\mathbf{r}}^2 \varphi_{\nu}(\mathbf{r}) d\mathbf{r}, \\ Z_{\mu\nu} &= \sum_{\Lambda=1}^N \int \varphi_{\mu}(\mathbf{r}) \frac{Z_{\Lambda}}{|\mathbf{r} - \mathbf{R}_{\Lambda}|} \varphi_{\nu}(\mathbf{r}) d\mathbf{r}, \\ B_{\mu\nu} &= \sum_{\lambda\rho}^n P_{\lambda\rho}(\mu\nu|\lambda\rho), \\ X_{\mu\nu} &= -\frac{1}{2} \sum_{\lambda\rho}^n P_{\lambda\rho}(\mu\lambda|\nu\rho), \end{aligned} \quad (8)$$

where

$$\begin{aligned} (\mu\nu|\lambda\rho) &= \iint \varphi_{\mu}(\mathbf{r}) \varphi_{\nu}(\mathbf{r}) \frac{1}{|\mathbf{r} - \mathbf{r}'|} \varphi_{\lambda}(\mathbf{r}') \varphi_{\rho}(\mathbf{r}') d\mathbf{r} d\mathbf{r}', \\ P_{\mu\nu} &= 2 \sum_{i=1}^{m/2} c_{\mu i}^* c_{\nu i}, \\ E_{CS} &= \frac{1}{2} \sum_{\mu\nu}^n P_{\mu\nu} (F_{\mu\nu} + T_{\mu\nu} + Z_{\mu\nu}) \end{aligned} \quad (9)$$

The formalism of the closed-shell method is complete at this point: the calculation of E_{CS} and all derived values and function proceeds by self-consistent diagonalisation of the Fock matrix. However, the transition metal bearing compounds that form the basis for this study possess unpaired spins, and a method is required that can account for this. Two choices exist in the literature: the unrestricted (UHF) and restricted half-closed shell (RHF) theories. In the RHF method, the wavefunction is composed of a single determinant in which m_d orbitals are doubly occupied and m_s singly occupied. All singly occupied orbitals have parallel spin, so antiferromagnetic solutions cannot exist within the RHF method. In the UHF method, no constraint is placed upon the spin orbitals, the spatial and spin parts are formally separate so that singly-occupied orbitals of the form $\psi^{\alpha}(\mathbf{r})\chi(\alpha)$ or $\psi^{\beta}(\mathbf{r})\chi(\beta)$ result, and the method can produce antiferromagnetic solutions. It is important to note that the RHF method produces wavefunctions that are eigenfunctions of both the S^2 and S_z operators, whereas the UHF solutions are eigenfunctions of S_z alone, and that in the latter case, this can lead to problems with spin contamination. The derivation of equations analogous to

equations (6) to (9) above for both these cases is not presented here, a full account may be found in reference [31].

(ii) Extension to Periodic Boundary Conditions

The further specialisation of the closed-shell HF method for application to infinite periodic systems proceeds as follows. One cell from amidst the crystal is chosen and termed the 'reference cell', namely, the cell from which all other distances are measured. It is clear that the basis from which the wavefunction is constructed must respect the translational symmetry of the crystal. This can be achieved by the use of Bloch functions (BFs). Starting with a set of localised functions in the reference cell, $\phi_\mu(\mathbf{r})$ ($\mu = 1, 2, \dots, p$) a BF corresponding to each localised function may be derived

$$\phi_\mu(\mathbf{k}, \mathbf{r}) = \sum_{\mathbf{G}} \exp(i\mathbf{k} \cdot \mathbf{G}) \phi_\mu(\mathbf{r} - \mathbf{G}), \quad (10)$$

where \mathbf{G} is a translation vector of the direct lattice and \mathbf{k} is a vector in the first Brillouin zone (BZ). Expressed in the basis of Bloch functions (in \mathbf{k} -space), the elements of the Fock matrix become

$$F_{\mu\nu}(\mathbf{k}) = \sum_{\mathbf{G}} \exp(i\mathbf{k} \cdot \mathbf{G}) F_{\mu\nu}(\mathbf{G}), \quad (11)$$

where $F_{\mu\nu}(\mathbf{G})$ should be regarded as the matrix element of the operator between the μ -th localised function in the reference cell and the ν -th function in the cell located at vector \mathbf{G} relative to the reference cell. The equation in the periodic system analogous to (6) above is

$$F(\mathbf{k}) C(\mathbf{k}) = S(\mathbf{k}) C(\mathbf{k}) E(\mathbf{k}). \quad (12)$$

In principle, this should be diagonalised for each \mathbf{k} -point in the first BZ. Since \mathbf{k} is a continuous variable, the number of such points is infinite, but the problem is made tractable by recognising that each \mathbf{k} -point can be taken to be representative of a small volume element of reciprocal space surrounding it. Thus, diagonalisation can proceed upon a finite mesh of \mathbf{k} -points, and the total energy can be converged with respect to the density of this mesh. Expressions analogous to equations (8) and (9) may now be derived, but little is gained by presenting them here. Suffice it to say that, while the formal derivation may be complete, the equations are useless as they stand, for all summations occurring in the Coulomb and exchange series are over the infinite set of direct lattice vectors. It is clear that some sort of truncation of the series must be

implemented, on the basis of the assessed contribution of each individual term to the sum.

The truncation depends upon the following facts (i) that the overlap between two GTFs decays exponentially with distance: this is used to select integrals for evaluation in most of the infinite series, and (ii) that the density matrix elements $P_{\mu\nu}(\mathbf{G})$ decay with distance; at an exponential rate for an insulating system, and much more slowly for a conductor, and this permits truncation of the exchange series in the Fock matrix and total energy expressions. Multipolar expansions of the charge in the cell in combination with the Ewald technique are also reduced to reduce the size of the Coulomb series, and the point symmetry of the system can be used to limit the number of Fock matrix elements considered, the number of k-points at which diagonalisation occurs and the number of bielectronic integrals stored.

It is appropriate to present an account of the treatment of open-shell, periodic systems. The UHF method in periodic boundary conditions is a generalisation of the theory presented above. Rather than dealing with only one Fock matrix for doubly occupied states, two must now be considered and solved self-consistently, corresponding to the two sets of α and β electrons. Predictably, a density matrix and a Fock matrix for each spin also arise. A much fuller treatment of the application of the Hartree-Fock method to crystalline systems than that presented here may be found in reference [32]

The CRYSTAL98 version of the code has been used for most of the calculations presented in this thesis [33]. For most of the author's time spent working in this area, the CRYSTAL95 and 98 codes were unique in their provision of so-called hybrid Hamiltonians that mix varying amounts of Fock and density functional exchange and correlation into one method. More recently, a new version of the Gaussian suite of programs was released that also permits hybrid calculations. It may be useful to the reader to describe the operation of the CRYSTAL code. In general, the code attempts to keep all relevant quantities in a real-space representation for as much of the SCF cycle as possible. The algorithm for the UHF case proceeds as follows, where the superscript σ refers to spin. Geometry and basis set input data are read and the symmetry analysed. The integrals are classified for retention and those selected are

computed and stored to disk. The initial Fock matrices are constructed in real space, $F^\sigma(\mathbf{G})$ and the SCF process begins. Firstly $F^\sigma(\mathbf{G})$ is Fourier transformed into the Bloch basis, $F^\sigma(\mathbf{k})$, and then diagonalised, yielding the eigenvector, $C^\sigma(\mathbf{k})$, and eigenvalue, $\epsilon^\sigma(\mathbf{k})$, matrices. The Fermi energy and real space density matrices, $P^\sigma(\mathbf{G})$ are then constructed, and from them the real space Fock matrix, $P^\sigma(\mathbf{G})$, to start the next cycle. At each iteration, the changes in total energy and eigenvalues are computed and compared to the last iteration, as criteria for halting the SCF loop. Mulliken population analysis is typically employed in gauging whether the solution obtained is the one sought.

4. The Plane Wave Pseudopotential Method: The CASTEP Code

(i) Density Functional Theory

Only the most basic principles of the density functional theory will be presented here, a much fuller treatment is available in references [31] and [34]. In 1965, Hohenberg and Kohn [35] laid the foundation of the method with their proof that the total energy of a gas of electrons, including exchange and correlation is a unique functional of the charge density. A variational principle was also established, namely that the minimal energy of the total energy functional is achieved only for the ground state charge density. Kohn and Sham, in 1965 [36] provided the next step by showing that the many-body problem may be replaced by a coupled set of single-particle equations. As a first step, consider the total energy functional written as

$$E[n(\mathbf{r})] = \int d\mathbf{r} \{V_{en}(\mathbf{r})n(\mathbf{r})\} + \frac{1}{2} \iint d\mathbf{r} d\mathbf{r}' \left\{ \frac{n(\mathbf{r})n(\mathbf{r}')}{|\mathbf{r} - \mathbf{r}'|} \right\} + G[n(\mathbf{r})], \quad (13)$$

for a fixed set of nuclei. The first two terms in $E[n(\mathbf{r})]$ are the electron-nuclear and electron-electron Coulomb terms respectively, where the latter is equivalent to the classical Hartree energy. $G[n(\mathbf{r})]$ can be viewed as the ‘troublesome’ term in the equation, for it contains the kinetic, exchange and correlation contributions, the exact functional form of each of which is currently unknown

$$G[n(\mathbf{r})] = T[n(\mathbf{r})] + E_{xc}[n(\mathbf{r})]. \quad (14)$$

$T[n(\mathbf{r})]$ is the kinetic energy of a system of electrons at density $n(\mathbf{r})$. Imposing a stationary condition on $E[n(\mathbf{r})]$ with respect to variations in the charge density leads to

$$\int \delta n(\mathbf{r}) \left\{ \frac{\delta T[n(\mathbf{r})]}{\delta n(\mathbf{r})} + V_{\text{en}}(\mathbf{r}) + \int d\mathbf{r}' \left\{ \frac{n(\mathbf{r}')}{|\mathbf{r}-\mathbf{r}'|} \right\} + \mu_{\text{xc}}(\mathbf{r}) \right\} = 0, \quad (15)$$

where $\mu_{\text{xc}}(\mathbf{r})$ is the functional derivative

$$\mu_{\text{xc}}(\mathbf{r}) = \frac{\delta E_{\text{xc}}[n(\mathbf{r})]}{\delta n(\mathbf{r})}. \quad (16)$$

The density variations in equation (15) must conserve total particle number, and this constraint leads to an expression of the form

$$\frac{\delta E[n(\mathbf{r})]}{\delta n(\mathbf{r})} = \frac{\delta T[n(\mathbf{r})]}{\delta n(\mathbf{r})} + V_{\text{en}}(\mathbf{r}) + \int d\mathbf{r}' \left\{ \frac{n(\mathbf{r}')}{|\mathbf{r}-\mathbf{r}'|} \right\} + \mu_{\text{xc}}(\mathbf{r}) = \lambda, \quad (17)$$

where λ is the appropriate Lagrange multiplier. Adding an effective potential $V_{\text{eff}}(\mathbf{r})$ and neglecting the nucleus-electron and electron-electron interaction yields

$$\frac{\delta E[n(\mathbf{r})]}{\delta n(\mathbf{r})} = \frac{\delta T[n(\mathbf{r})]}{\delta n(\mathbf{r})} + V_{\text{eff}}(\mathbf{r}) = \lambda. \quad (18)$$

The two theories can be made equivalent, providing that the effective potential of equation (17) is given by

$$V_{\text{eff}}(\mathbf{r}) = V_{\text{en}}(\mathbf{r}) + \int d\mathbf{r}' \left\{ \frac{n(\mathbf{r}')}{|\mathbf{r}-\mathbf{r}'|} \right\} + \mu_{\text{xc}}(\mathbf{r}). \quad (19)$$

So far, no concept of how to deal with the kinetic functional has been advanced. In fact, the solution lies in avoiding the functional route for this quantity, and instead finding the total kinetic energy as the sum of the kinetic energies of each one-electron Kohn-Sham state, thus

$$T = \sum_{i=1}^N \left\langle \psi_i \left| -\frac{\nabla^2}{2} \right| \psi_i \right\rangle, \quad (20)$$

where N is the number of electrons. The Kohn-Sham equations may now be written as

$$\left\{ -\frac{\nabla^2}{2} + V_{\text{eff}}(\mathbf{r}) \right\} \psi_i(\mathbf{r}) = \epsilon_i \psi_i(\mathbf{r}), \quad (21)$$

and can be conceptualised as describing the motion of non-interacting electrons under the influence of the potential $V_{\text{eff}}(\mathbf{r})$. The variation in density mentioned earlier is now accomplished by variation in the set of Kohn-Sham states, $\{\psi_i(\mathbf{r})\}$. The exchange-correlation component is dealt with by the specification of a parameterised form for the exchange correlation energy per electron at a point in the electron gas, ϵ_{xc} , that

depends only upon the electron density at that point, $\epsilon_{xc}[n(\mathbf{r})]$ (the local density approximation), or upon the density and the gradient at a point $\epsilon_{xc}[n(\mathbf{r}), \nabla_{\mathbf{r}}]$ (the generalised gradient approximation).

One important problem in DFT is the presence of the electron self-interaction. As it stands, the Hartree potential contains the spurious interaction of an electron with its own density distribution. This overestimation of the electron-electron interaction should be removed by an equivalent but opposite contribution in the exchange-correlation energy, but most functionals succeed only partially in this regard. In the hydrogen atom, for example, the LDA removes 95% of the self-interaction, but the amount removed in other systems is liable to be smaller and difficult to estimate. Schemes exist for removing the self-interaction exactly, but at the price of introducing a Kohn-Sham potential which is orbital dependent. In the Hartree-Fock method, the self-interaction terms in the Coulomb and exchange series cancel exactly.

(ii) Plane Wave Basis

Bloch's Theorem dictates that the Kohn-Sham states, $\psi_i(\mathbf{r})$ must have the form of the product of a wave-like part with wave vector \mathbf{k} and a cell periodic part as shown below

$$\psi_i(\mathbf{r}) = \exp(i\mathbf{k} \cdot \mathbf{r}) u_i(\mathbf{r}). \quad (22)$$

The cell periodic component, $u_i(\mathbf{r})$ may be expanded in a finite number of plane waves with wave vectors which are all members of the set of reciprocal lattice vectors $\{\mathbf{T}\}$ of the crystal

$$u_i(\mathbf{r}) = \sum_{\mathbf{T}} c_{i\mathbf{T}} \exp(i\mathbf{T} \cdot \mathbf{r}). \quad (23)$$

where all \mathbf{T} must obey the relationship $\mathbf{T} \cdot \mathbf{G} = 2\pi n$ for all \mathbf{G} , \mathbf{G} being a direct lattice vector and n an integer. Combining equations (22) and (23) leads to the following form for the Kohn-Sham states

$$\psi_i(\mathbf{r}) = \sum_{\mathbf{T}} c_{i, \mathbf{k} + \mathbf{T}} \exp(i(\mathbf{k} + \mathbf{T}) \cdot \mathbf{r}). \quad (24)$$

The problem of an infinite set of \mathbf{k} -vectors is solved, as in the CRYSTAL code, by calculation only at the points of a sufficiently dense mesh in reciprocal space.

Substituting the above form for the Kohn-Sham state into equation (21) leads to a new form for the KS equations

$$\sum_{\mathbf{T}'} \{ \mathbf{k} + \mathbf{T} | \delta_{\mathbf{T}\mathbf{T}'} + V_{\text{en}}(\mathbf{T} - \mathbf{T}') + V_{\text{H}}(\mathbf{T} - \mathbf{T}') + V_{\text{xc}}(\mathbf{T} - \mathbf{T}') \} c_{i,\mathbf{k}+\mathbf{T}'} = \epsilon_i c_{i,\mathbf{k}+\mathbf{T}'}, \quad (24)$$

where V_{H} is the Hartree potential. The usual technique of diagonalisation of the Hamiltonian matrix could now be used to arrive at the ground state, as in the CRYSTAL code. However, the use of a plane wave basis makes this problematic, as the large number of individual functions (plane waves) makes the diagonalisation routine particularly inefficient. Instead, the Car-Parrinello method is used, which deals with both nuclear and electronic degrees of freedom on the same footing, employing a molecular dynamics approach in a fictitious time for electronic structure. Orthonormality in the electronic dynamics is enforced by the use of Lagrangian constraints. The dynamics of the nuclei may be evolved from a knowledge of the Hellmann-Feynman forces acting upon them, as long as the effective electronic timestep is kept much shorter than the nuclear timestep.

Now, calculations employing a plane wave basis usually encounter difficulties in accurately representing the form of the valence states that penetrate the core of the atom. The reason for this is that, within this region, orthogonality to core states requires the valence states to have many nodes, and the description of these requires a prohibitively large basis set extending to high Fourier components. The solution normally adopted is to remove the bare Coulomb potential of the nucleus, and the associated core states, and replace them with a *pseudopotential*. Simply put, this is the potential that a valence state outside the core region would feel if the core were still present. Much smaller plane wave bases result, although the presence of the pseudopotential does involve additional computational complexity. As an example of this, consider that an accurate potential must scatter valence electrons of varying angular momenta by varying amounts, a property which is termed ‘non-locality’ of the pseudopotential. The selection of core states for the pseudising procedure also involves difficulties, for normally only those states which are unaffected by bonding may be safely included in the core. Some low lying atomic states are termed ‘semi-core’ and generally mean trouble for the user, for semi-core states are high enough in energy to play some part in bonding, while being low enough in energy that their exclusion from the core leads to ‘hard’ pseudopotentials with high kinetic energy

cutoffs for plane wave sets. The 3s and 3p states in the transition metals are good examples of semi-core states.

The CASTEP code [38] employs all of the formalism presented above, and has coded within it the LDA and various GGA functionals. The ability of the code to perform full structural optimisation was put to use in the work of this thesis. The advantages of the plane wave method for such optimisations are described further in Chapter 6.

5. Hybrid Hartree-Fock – Density Functional Hamiltonians

It is clear from previous sections that a qualitatively correct electronic structure for transition metal compounds relies upon the use of an orbital dependent potential. This can be achieved within DFT by way of the self-interaction corrected and exact exchange schemes. The LDA+U method [39] adds a user-defined, on-site Coulomb interaction U to the normal LDA description of the valence bands, providing another route to orbital dependence. Yet another alternative is to mix pure HF and DFT exchange, yielding a hybrid Hamiltonian which may or may not include the DF correlation functional, and it is this method which forms the focus of this thesis.

The original hybrid method is due to Becke [40,41] and was developed to improve the theoretical thermochemistry and geometry of small molecules. Hybrid Hamiltonians in general contain one or more adjustable parameters, of which the most crucial is their fractional content of HF exchange. The adjustable parameters are usually either postulated or fitted to experimental data, where the B3PW functional [41] is one example of the fitted type. The method became very popular in the molecular theoretical chemistry community after it was included in the popular GAUSSIAN suite of programs in 1994 [42], although the LYP correlation functional was used, rather than the original PW functional employed by Becke. The B3LYP method, as it became known, yielded optimised geometries and formation energies in good agreement with experiment. The solid state community first started to use hybrid methods following their inclusion in the CRYSTAL98 [33] code. While many methods and concepts of worth can be gleaned from the molecular theory, the transferability of functionals of proven value from molecular to solid state

calculations is not guaranteed, for solids often have long range electrostatic interactions which can act to localise electrons to a greater extent than in molecules.

Since their introduction in the solid state, hybrid functionals have already found a wide variety of applications. In the oxides, hydroxides and halides of main group elements [43–45], for example, ionic charges are found to lie upon a clear trend, with HF charges being the highest, LDA the lowest, and B3LYP and GGA lying at intermediate values. For all fifteen halides considered in Ref. [45], the B3LYP ionic charges yield the closest agreement with experiment. Taking the alkaline earth compounds [43,44] and the halides [45] together, the optimised lattice constants follow the trend

$$(\text{LDA}) < \text{Experiment} < (\text{PW} \approx \text{B3LYP}) < \text{BLYP},$$

while the bulk moduli at the equilibrium structures follow the trend

$$(\text{Experiment} \approx \text{BLYP}) < (\text{PW} \approx \text{B3LYP}) < (\text{LDA} \approx \text{HF}).$$

The calculated band gaps [46] are very interesting, for the available evidence suggests that the under- and overestimation typical of LDA (or GGA) and HF methods respectively can be ‘averaged’ by the B3LYP scheme, yielding gaps in good agreement with experiment. The calculated vibrational energies show a similar trend, and are again in good agreement with experiment within B3LYP. The cohesive energies of the alkali earth oxides and hydroxides [43,44], and the TMOs [48] are underestimated by up to 1 eV per molecule at the B3LYP and BLYP levels, and are heavily underestimated within HF theory and overestimated within the LDA.

All the published literature suggests that the transition metal compounds cause particular difficulty, and that this is due to the myriad of electronic states the unpaired spins can adopt. For example, in FeS₂ [47], the difference between lattice parameters predicted at LDA and UHF levels is as large as 15% of the experimental value. In MgO, the equivalent range is ~ 5 %, in NiO ~ 2% and in CoO ~ 3 % [48]. The bulk modulus in NiO across the range from B3LYP to UHF varies by 28 % of experiment, and the lowest value, that for UHF is ~ 60 GPa higher than experiment [49]. The

magnetic coupling between the spins is greatly affected changing content of exact exchange. In NiO [48,49], CoO [48], La₂CuO₄ [50] and KMnF₃, the UHF method underestimates and the LDA overestimates the experimental values by factors of ~ 3 and $\sim 4-5$ respectively. All of the studies for the TMOs above use quite coarse increments of weights of exact exchange, and it is clear that trends in properties will become clearer for a range of calculations at, say, 10% increments of exact exchange.

The exact formulation of a hybrid functional will now be discussed in greater detail. The B3LYP functional will be used as an example. The essence of this method is that the exchange-correlation contribution to the Kohn-Sham Hamiltonian, $f_{\text{B3LYP}}^{\text{xc}}$, is given by

$$f_{\text{B3LYP}}^{\text{xc}} = f_{\text{B3}}^{\text{x}} + 0.81f_{\text{LYP}}^{\text{c}} + 0.19f_{\text{VWN}}^{\text{c}},$$

where $f_{\text{LYP}}^{\text{c}}$ and $f_{\text{VWN}}^{\text{c}}$ are the correlation functionals of Lee, Yang and Parr [51] and Vosko, Wilk and Nusair [52] respectively. The exchange functional, f_{B3}^{x} , is a weighted sum of exact UHF ($f_{\text{UHF}}^{\text{x}}$) and gradient-corrected LSDA ($f_{\text{LSDA}}^{\text{x}} + 0.9\Delta f_{\text{B88}}^{\text{x}}$) [41] contributions

$$f_{\text{B3}}^{\text{x}} = (1 - F_0)(f_{\text{LSDA}}^{\text{x}} + 0.9\Delta f_{\text{B88}}^{\text{x}}) + F_0 f_{\text{UHF}}^{\text{x}}$$

and F_0 an arbitrary weighting parameter. F_0 values of 1 and 0 correspond to exact exchange (UHF) and pure DFT descriptions respectively, while a value of 0.2 corresponds exactly to Becke's original three parameter exchange functional (B3) [41]. The presence of only 20% of the exact exchange is not sufficient to cancel the DFT Coulomb self-interaction, but, as discussed earlier, the method has been shown to yield values for the energy gap in close agreement with experimental band gaps of varying provenance. For some studies, the results from the Becke-LYP hybrid were compared with those from a different scheme that used the Perdew-Wang (PW) 1991 exchange and correlation functionals [53].

The approach followed in all the subsequent work of this thesis was to vary F_0 in the range $0 \leq F_0 \leq 1$, yielding a series of hybrid Hamiltonians. It was arranged that, where appropriate, the B3LYP ($F_0 = 0.2$) potential was included in the range. The pure UHF method was normally used as well, for the purposes of comparison.

6. Aims of the Current Work

The experimental and theoretical background presented in Sections 1 and 5 makes it clear that either a pure density functional or Hartree-Fock Hamiltonian cannot hope to give an adequate description of all the computed properties of transition metal oxides. This is not a surprising conclusion; the TMOs do represent something of a ‘worst case’ scenario for current first principles methods, due to the presence of many near degenerate d-electron configurations and the strong intra-atomic correlation. There is limited evidence within the literature that systematic improvement of calculated properties is possible where the DFT and HF approaches yield values that bracket experiment. What is lacking, though, is a thorough investigation of this effect for a series of Hamiltonians with close-spaced contents of exact exchange. The current work hopes to address the question of whether there is a ‘universal’ hybrid functional for the TMOs that gives an adequate description of most calculated properties, in the same way that the B3LYP functional is regarded in computational chemistry. In answering this, a range of late and early transition metal oxides will be used, concentrating upon the binary monoxides in the rocksalt structure. The literature survey has thrown up some initial prospects as follows:

- (i) The most fundamental calculated properties of the TMOs are likely to be the dependence of equation of state parameters and electronic structure upon F_0 , both with and without DFT correlation. In this regard, it is hoped to expand upon the studies already entered into the literature.
- (ii) The dependence of phase transition pressures upon exact exchange content has not been investigated in the TMOs, and so a study of the high pressure phases in MnO in different Hamiltonians is planned. Structural optimisation of low symmetry cells will be computationally demanding, and so it is envisaged that a coarse set of F_0 values will be necessary here.
- (iii) Recent GGA DFT calculations have predicted a high-spin to low-spin transition in MnO, FeO, CoO and NiO at pressures attained in the Earth’s lower mantle and core. The results of the calculations may have important consequences for geophysical modelling, and it is desirable to check whether the magnetic collapse at reasonably low pressure is a general feature of all Hamiltonians.

- (iv) Also planned is a study of the magnitude of the magnetostrictive distortion in MnO as a function of F_0 . The literature values are for the pure DFT and UHF limits only. The magnetostriction effect may seem an odd choice of subject, but its importance lies in the fact that it gives a clear structural indication of the strength of magnetic coupling without recourse to a phenomenological Hamiltonian.
- (v) To date, most of the studies of electronic defects in the TMOs have used the UHF method alone. It is hoped to explore the nature of hole and electron addition states with varying F_0 .

7. References

- [1] D. B. Brown (ed.), *Mixed Valence Compounds*, D. Reidel, Dordrecht
- [2] R. D. Shannon and C. T. Prewitt, *Acta Cryst. B* **25**, 925 (1970)
- [3] R. D. Shannon, *Acta Cryst. A* **32**, 751 (1976)
- [4] C. R. A. Catlow and B. E. F. Fender, *J. Phys. C: Solid State Phys.* **8**, 3267 (1975)
- [5] A. F. Wells, *Structural Inorganic Chemistry 5th Edn*, Oxford University Press, Oxford 1984
- [6] M. Gerloch and R. C. Slade, *Ligand Field Parameters*, Cambridge University Press, Cambridge 1973
- [7] J. Kanamori, *J. Phys. Chem. Solids* **10**, 87 (1959)
- [8] J. S. Griffith, *The Theory of Transition Metal Ions*, Cambridge University Press, Cambridge, 1964
- [9] S. Sugano, Y. Tanabe and H. Kamimura, *Multiplets of Transition-Metal Ions in Crystals*, Academic Press, New York 1970
- [10] G. J. M. Janssen and W. C. Nieuwpoort, *Phys. Rev. B* **38**, 137 (1987)
- [11] J. H. de Boer and E. J. W. Verwey, *Proc. Phys. Soc.* **49**, 59 (1937)
- [12] N. F. Mott, *Proc. Phys. Soc. A* **62**, 416 (1949)
- [13] N. F. Mott, *Prog. Metal Phys.* **3**, 76 (1952)
- [14] N. F. Mott, *Can. J. Phys.* **34**, 1356 (1956)
- [15] N. F. Mott, *Phil. Mag.* **6**, 281 (1961)
- [16] J. C. Slater, *Phys. Rev.* **82**, 538 (1951)

- [17] W. C. Mackrodt, N. M. Harrison, V. R. Saunders, N. L. Allan, M. D. Towler, E. Apra and R. Dovesi, *Phil. Mag A* **68**, 653 (1993)
- [18] M. D. Towler, N. L. Allan, N. M. Harrison, V. R. Saunders, W. C. Mackrodt and E. Apra, *Phys. Rev. B* **50**, 5041 (1994)
- [19] A. Svane and O. Gunnarson, *Phys. Rev. Lett.* **65**, 1148 (1990)
- [20] J. Hubbard, *Proc. R. Soc. A* **276**, 238 (1963)
- [21] J. Hubbard, *Proc. R. Soc. A* **277**, 237 (1964)
- [22] J. Hubbard, *Proc. R. Soc. A* **281**, 401 (1964)
- [23] S. Huefner, *Solid State Commun.* **49**, 1177 (1984)
- [24] J. Zaanen, G. A. Sawatzky and J. W. Allen, *Phys. Rev. Lett.* **55**, 418 (1985)
- [25] P. A. Cox, *Transition Metal Oxides: An Introduction to their Electronic Structure and Properties*, Oxford University Press, Oxford (1992)
- [26] B. H. Brandow, *Adv. Phys.* **26**, 651 (1977)
- [27] S. Hüfner, *Adv. Phys.* **43**, 183 (1994)
- [28] V. Fock, *Z. Phys.* **61**, 126 (1930)
- [29] J. C. Slater, *Phys. Rev.* **35**, 210 (1930)
- [30] S. F. Boys, *Proc. Roy. Soc. A* **201**, 125 (1950)
- [31] F. Jensen, *Introduction to Computational Chemistry*, Wiley (New York) 1999
- [32] C. Pisani, R. Dovesi and C. Roetti, *Hartree-Fock Ab Initio Treatment of Crystalline Systems*, Lecture Notes Chem., Vol. 48, Springer-Verlag, Berlin 1988
- [33] V. R. Saunders, R. Dovesi, C. Roetti, M. Causà, N. M. Harrison, R. Orlando and C. M. Zicovich-Wilson, *CRYSTAL98 User's Manual*, Università di Torino, Torino, 1998
- [34] J. M. Thijssen, *Computational Physics*, Cambridge (Cambridge) 1999
- [35] P. Hohenberg and W. Kohn, *Phys. Rev.* **136**, B864 (1965)
- [36] W. Kohn and L. J. Sham, *Phys. Rev.* **140**, A1133 (1965)
- [37] R. Car and M. Parrinello, *Phys. Rev. Lett.* **55**, 2471 (1985)
- [38] M. C. Payne, M. P. Teter and J. D. Joannopoulos, *Rev. Mod. Phys.* **64**, 1045 (1992)
- [39] V. I. Anisimov, J. Zaanen and O. K. Andersen, *Phys. Rev. B* **44**, 942 (1991)
- [40] A. D. Becke, *J. Chem. Phys.* **98**, 1372 (1993)
- [41] A. D. Becke, *J. Chem. Phys.* **98**, 5648 (1993)
- [42] GAUSSIAN94 (Revision A.I), Gaussian Inc, Pittsburgh, PA, USA

- [43] P. Baranek, A Lichanot, R. Orlando and R. Dovesi, Chem. Phys. Lett. **240**, 362 (2001)
- [44] M. Mérawa, B. Civalleri, P. Ugliengo, Y. Noël and A. Lichanot, J. Chem Phys. **119**, 1045 (2003)
- [45] N. Wilson and J. Muscat, Molec. Simul. **28**, 903 (2002)
- [46] J. Muscat, A. Wander and N. M. Harrison, Chem. Phys. Lett. **342**, 397 (2001)
- [47] J. Muscat, A. Hung, S. Russo and I. Yarovsky, Phys. Rev B **65**, 054107 (2002)
- [48] T. Bredow and A. R. Gerson, Phys. Rev. B **61**, 5194 (2000)
- [49] I. de P. R. Moreira, F. Illas and R. L. Martin, Phys. Rev. B **65**, 155102 (2002)
- [50] J. K. Perry, J. Tahir-Kheli, W. A. Goddard, Phys. Rev. B **63**, 144510 (2001)
- [51] C. Lee, W. Yang and R. G. Parr, Phys Rev. B **37**, 785 (1988)
- [52] S. H. Vosko, L. Wilk and M. Nusair, Can. J. Phys. **58**, 1200 (1980)
- [53] J. P. Perdew and Y. Wang, Phys. Rev B **45**, 13244 (1992)

Chapter 2

A Hybrid Hamiltonian Study of the Structural and Electronic Properties of Bulk NiO and MnO

1. Introduction and Methods

As discussed in Chapter 1, nickel oxide continues to attract interest as the paradigmatic magnetic insulator [1]. To recap the history, NiO was, for many years, thought to be a Mott-Hubbard system [2], in that metal derived states compose the valence and conduction band edges, separated by a gap ~ 4 eV in width [3]. In this picture, the first ionised state of the lattice would be approximately d^7 , or Ni^{3+} . Local density approximation calculations by Terakura *et al* [4] in the experimentally observed AF_2 magnetic alignment support this view of the insulating character of NiO, albeit with a significantly underestimated energy gap of width ~ 0.4 eV. More recently, the application of generalised gradient approximation functionals [5] to NiO has served to improve the agreement between experimental and calculated gap widths, while leaving the MH character of the insulating state unchanged. The agreement between the picture of NiO arising within the MH scheme and the results of the density functional calculations lead to the sense that a consistent picture had been formed. However, as discussed in Chapter 1, the ZSA [6] scheme classifies the later TM oxides, including NiO, as charge-transfer systems with first ionised states of largely O(2p) character, in contrast to the earlier oxides, notably TiO and VO, which, it was argued, possessed gap states of essentially d character, leading to $\sim d^{n-1}$ holes. Direct UHF calculations of the first ionised state in Li-doped NiO [7] and the self-trapped hole in NiO [8] show the O(p) character of the hole. Experimental support for $d^8\bar{L}$ holes in NiO was found in the O k-edge spectra of Li-doped NiO ($Li_xNi_{1-x}O$) in the range $0 \leq x \leq 0.5$, which showed the presence of empty O(p) states ~ 4 eV below the conduction band edge [9]. Importantly, these data also confirmed the insulating nature of the first ionised state within the specified range of stoichiometry.

Subsequent spectroscopic studies have confirmed these observations, notably in respect of the lower energy of the $d^8\bar{L}$ state in $\text{Li}_x\text{Ni}_{1-x}\text{O}$ relative to d^7 [10-12].

By and large, more recent first principles calculations of NiO have concluded that the ground electronic state is essentially CT insulating. Spin unrestricted, periodic Hartree-Fock (UHF) calculations [13] based on localised orbitals found NiO to be a largely ionic, charge-transfer magnetic insulator in the FM (ferromagnetic), AF_1 and AF_2 spin alignments with local moments close to the measured values, but, as expected, with an energy gap greatly in excess of the observed absorption edge. DFT calculations within the SIC (self interaction correction) [14] and LDA+U (local density approximation plus additional local potential, U) [15] schemes have also attested to the charge transfer character of NiO, as have recent self-consistent GW calculations, which arrive at essentially the same description as the UHF approach [16]. The work discussed here is by no means the first to apply hybrid functionals to NiO, for Bredow and Gerson [17] and Moreira *et al* [18] have employed a variety of schemes in seeking to systematically improve agreement with experimental data. Some of the results from these studies were discussed earlier in Section 5 of Chapter 1.

The situation is less clear for MnO, since it occupies an intermediate position in the ZSA phase diagram. An analysis of the x-ray photoelectron and bremsstrahlung-isochromat spectroscopies of MnO by van Elp *et al* [19] supports this view, as do self-interaction corrected LDA calculations by Svane and Gunnarsson [20]. As in NiO, LDA calculations [4] have found a MH energy gap $\sim 1.0\text{eV}$ in width (experimental range 3.6 – 3.8 eV), increasing to $\sim 1.4\text{eV}$ with application of GGA functionals [21,22]. The recent GGA study by Pask *et al* also includes an examination of magnetic coupling constants and the rhombohedral spin-lattice distortion [22]. Hartree-Fock calculations, meanwhile, result in a charge-transfer insulating ground state [13], with localised $d^5\bar{L}$ and delocalised d^6 first ionised and electron addition states respectively [23].

The foregoing discussion addresses the current understanding of the electronic structure of MnO and NiO, but no mention has yet been made of their crystal structures. In Sections 2 (vii) and (ix) of this chapter, the distortion of the low pressure structure away from cubic symmetry and the pressure induced structural transitions will be analysed.

Computational Method and Conditions

The hybrid calculations conducted in this study are performed using the CRYSTAL98 code, as described previously in Chapter 1. The localised basis set adopted is maintained unchanged over all magnetic states and crystal structures, and thus it is essential to ensure that the basis is well converged initially. As an example, the basis sets for Mn and O are presented in the table below. The basis set for Ni and O is very similar in terms of provision of numbers of shells and atomic functions, but, of course, the optimised contraction exponents and coefficients differ. The study of high pressure phase transitions in MnO presented in Section 2(ix) of this chapter discusses the effect of adding an extra O(d) polarisation shell to the basis.

A Monkhorst-Pack shrinking factor of 8 was used for cells of all sizes, and truncation thresholds of 10^{-7} , 10^{-7} , 10^{-7} , 10^{-7} and 10^{-14} for the Coulomb and exchange series ensured convergence of the total UHF energies of the B1 AF₂, AF₁ and FM magnetic states to ≤ 0.1 meV in both materials, while SCF convergence thresholds were set to 10^{-7} Ha for both eigenvalues and total energies. These tolerances are similar to those used for a wide range of previous calculations. Mulliken population analyses of the crystalline orbitals were used to extract the net atomic charges, magnetic moments and individual orbital occupations as in previous studies.

No.	Type	Exponent	1 st Coeff.	2 nd Coeff.	No.	Type	Exponent	1 st Coeff.	2 nd Coeff.
<i>Mn Core Basis</i>					<i>O Core Basis</i>				
1	s	292601.0	0.000227		1	s	8020.0	0.00108	
		42265.0	0.0019				1338.0	0.00804	
		8947.29	0.0111				255.4	0.05324	
		2330.32	0.0501				69.22	0.1681	
		702.047	0.1705				23.90	0.3581	
		242.907	0.3691				9.264	0.3855	
		94.955	0.4035				3.851	0.1468	
		39.5777	0.1437				1.212	0.0728	
2	sp	732.14	-0.0052	0.0086	2	sp	49.43	-0.00883	0.00958
		175.551	-0.0673	0.0612			10.47	-0.0915	0.0696
		58.5093	-0.1293	0.2135			3.235	-0.0402	0.2065
		23.129	0.2535	0.4018			1.217	0.3790	0.3470
		9.7536	0.6345	0.4012	<i>O Valence Basis</i>				
		3.4545	0.2714	0.2222	3	sp	0.4763	1.0	1.0
3	sp	38.389	0.0157	-0.0311	4	sp	0.1760	1.0	1.0
		15.4367	-0.2535	-0.0969					
		6.1781	-0.8648	0.2563					
		2.8235	0.9337	1.6552					
<i>Mn Valence Basis</i>									
4	sp	1.2086	1.0	1.0					
5	sp	0.4986	1.0	1.0					
6	d	22.5929	0.0708						
		6.1674	0.3044						
		2.0638	0.5469						
		0.7401	0.5102						
7	d	0.2490	1.0						

2. Results

(i) Electronic Structure of NiO

The electronic structure of the ferromagnetic (FM) and antiferromagnetic (AF₂) spin alignments in NiO have been calculated based upon a hybrid scheme using the Perdew-Wang 1991 exchange and correlation functionals (hereafter denoted PW91-PW91 in an *exchange-correlation* notation) at a fixed lattice constant of 4.2 Å, which is close to the measured low temperature value, 4.1705 Å [24]. The results are presented in Table 1 below and will now be discussed. Within the PW91-PW91 scheme, the lower energy AF₂ spin alignment is predicted to be a largely ionic, d⁸ CT insulator from the correlated UHF (F₀ = 1.0) limit down to 30% exact exchange. Within this range, in Table 1, the Fermi energy, E_F, varies from -9.52 eV to

-5.02 eV, the local spin moment from 1.92 μ_B to 1.76 μ_B , the eigenvalue energy gap from 14.2 eV to 6.4 eV and the weight of O(p) states at E_F from 92% to 71%. Between 30% and 20% exact exchange there is a change in the nature of the gap states, for at 20% exact exchange the weight of O(p) states at E_F is 41% , indicating an essentially MH system, but the change in the ionic charge across this transition is $< 0.5\%$ and that of the local moment $< 4\%$. For comparison, the $F_0 = 0.2$ Becke-LYP (B3LYP) Hamiltonian with 20% exact exchange leads to ionic charges and local moments which are within 0.5% of the PW91 values, but the O(p) weight at E_F is higher at 51%, which is just at the transition from CT to MH behaviour, and the energy gap 0.1 eV less. As the amount of exact exchange is reduced further, the ionicity and local moment are decreased, though the system remains insulating at the DFT limit, where the weight of O(p) states at E_F is less than 10% , the local moment 1.36 μ_B and the energy gap 0.8 eV. There is essentially no change in the electronic structure of the higher energy FM spin alignment, which also undergoes a CT to MH transition between 30% and 20% exact exchange. The principal difference is that for the FM alignment there is a displacement of the majority and minority spin bands of 0.5 eV – 1.0 eV, which at the DFT limit leads to a filled to unfilled gap of ~ 0.3 eV for both the majority and minority spin bands, but a *net* gap which is close to zero. In the 3d transition metal oxides, the orbital contribution to the magnetic moment is quenched by the strong crystal field, and thus a direct comparison of the Mulliken-derived cation spin polarisation to experimental values is meaningful. Following this prescription, the calculated moments for the AF₂ alignment as presented in Table 1 compare with experimental values of 1.90 μ_B to 1.64 μ_B [25-27], which supports weights of exact exchange in a broad range $F_0 = 0.1 - 0.9$, whereas the measured strong adsorption edge at ~ 4 eV [3], if it can be equated with the energy gap, would seem to favour a lower weight in the range $F_0 = 0.1 - 0.2$. The Fermi energy supports F_0 in the range 0.2 – 0.3, where the former value already leads to E_F in excellent agreement with experiment.

F_0	FM						AF ₂				
	E_F	q_M	n_{Ni}	$W_{O\alpha}$	$W_{O\beta}$	ΔE_g	E_F	q_M	n_{Ni}	W_O	ΔE_g
1.0	-9.26	1.881	1.923	87	91	14.0	-9.52	1.878	1.915	92	14.2
0.9	-8.56	1.871	1.915	85	82	12.7	-8.84	1.868	1.906	92	13.1
0.8	-7.87	1.860	1.905	85	77	11.5	-8.18	1.855	1.895	89	12.1
0.7	-7.19	1.846	1.892	82	91	10.3	-7.53	1.840	1.880	87	10.9
0.6	-6.51	1.829	1.876	80	77	9.0	-6.89	1.821	1.861	83	9.8
0.5	-5.84	1.808	1.855	77	83	8.0	-6.27	1.798	1.836	76	8.7
0.4	-5.16	1.782	1.827	74	70	6.8	-5.64	1.769	1.803	71	7.4
0.3	-4.47	1.749	1.792	70	57	5.5	-5.02	1.731	1.757	71	6.4
0.2	-3.76	1.707	1.745	64	43	4.4	-4.37	1.683	1.693	41	4.5
0.1	-3.00	1.654	1.685	57	18	3.2	-3.62	1.621	1.592	11	2.6
0.0	-13.02	1.590	1.606	44	31	–	-2.53	1.541	1.361	9	0.8
Expt	-4.4 ⁽³⁾		1.64 – 1.90 ⁽¹⁾			~ 4 (2)					

(1) Refs. [25-27] (2) Ref. [3] (3) Ref. [30]

Table 1. The Fermi energy, E_F (eV), ionic charge, q_M (e), unpaired Ni spin, n_{Ni} (μ_B), weight of oxygen states at valence band edge, W_O (%) and energy gap, ΔE_g (eV) for the FM and AF₂ alignments in NiO at a fixed lattice constant of 4.2Å with variable amounts of exact exchange, F_0 , in the PW91 hybrid scheme.

The properties emerging from calculations within the Becke-LYP scheme are presented in Table 2 below and are now discussed. In order to assess the influence of using optimised geometries, the lattice constant which minimises the energy was found in the AF₁, AF₂ and FM states at each value of F_0 , and properties were then calculated for these lattices. The net charges in Table 2 indicate that, as F_0 decreases, the covalent character of Ni-O bonding increases, where some 0.35 electrons are transferred back to each metal atom at the DFT limit, relative to the more ionic UHF solution. Metal spin moments in close agreement with the PW91 values were found, decreasing from 1.92 μ_B at UHF to 1.34 μ_B at the DFT limit. The metal spin moment in the AF₂ alignment falls more rapidly with decreasing F_0 than that in FM. A number of competing interactions, each dependent upon lattice constant are expected to play a part in this, but in broad outline, a later study of VO, as presented in Chapter 5 suggests that the intra-atomic exchange interaction weakens as exact exchange decreases, which may provide one possible mechanism for the observed reduction in moment in VO, and by extension, in NiO, although the reason why this effect should be more pronounced in the

AF₂ state is unclear. In Table 2, at low weights of exact exchange, the spin polarisation borne by the oxygen sublattice in the FM alignment becomes appreciable. It should be noted that the presence of a moment on oxygen is forbidden in AF₂ symmetry. As an alternative to the analysis of PW91 states through the weights of oxygen derived states at the Fermi energy used in Table 1 above, Table 2 assesses the character of the insulating state by gauging the difference in energy, Δ_{MO} between the upper oxygen valence band edge and the lower lying point at which the oxygen contribution falls below the metal. The positive values of Δ_{MO} from UHF down to $F_0 = 0.2$ indicate that, within this range, the VBE is dominated by oxygen derived states, with a transition to MH behaviour in the region of $F_0 = 0.1 - 0.2$, as compared to $0.2 - 0.3$ for PW91 above. A least squares fit to the data yields a linear dependence $\Delta_{MO} \approx 4.92 F_0 - 0.57$, although it should be stated that this linear behaviour is clearer at large F_0 .

The band gaps in the Becke-LYP scheme for the AF₁ (not quoted in Table 2), AF₂ and FM states are shown in Figure 1 below, where it is clear that they fall in the order $\Delta E_g(AF_2) > \Delta E_g(AF_1) > \Delta E_g(FM)$ for all values of F_0 . Quadratic fits to the data indicate that all three curves deviate significantly from linearity, with a range in gradients, $\partial(\Delta E_g) / \partial F_0$ from 17.6 to 9.9 eV at $F_0 = 0.0$ and 1.0 respectively in the AF₂ state, from 19.4 to 10.0 eV at $F_0 = 0.1$ and 1.0 respectively in the FM state and from 19.7 to 10.1 eV at $F_0 = 0.1$ and 1.0 respectively in the AF₁ state. The gap widths found in the AF₁ state are very close to the FM values across the range of exact exchange. This is an unexpected finding, since the reduction in the width of the gap in going from the AF₂ to FM states would be ascribed to the exchange splitting of conduction band states caused by the net spin polarisation borne by the lattice in the latter state, and it would be anticipated that the same reasoning would apply to the AF₁ and FM gaps. Within the B3LYP Hamiltonian ($F_0 = 0.2$), it is the AF₂ gap at 4.255 eV which is closest to the ~ 4 eV value taken from the optical absorption experiment by Powell and Spicer [3]. At the DFT extreme, both the AF₁ and FM states become metallic, whereas the AF₂ state remains insulating with $\Delta E_g = 0.709$ eV. Here, for the Becke-LYP scheme, the experimental cation spin moment supports a choice of F_0 in the broad range $0.1 - 1.0$, the experimental Fermi energy supports F_0 in the range $0.2 - 0.3$ and the experimental strong absorption supports $F_0 = 0.1 - 0.2$, thus, it may be concluded that all the ranges of F_0 providing best fits

to experiment are close to those found earlier for the PW91 scheme. Figure 2 below shows atom projected densities of states for the ground AF₂ state at the optimised lattice constants for the UHF, B3LYP (F₀ = 0.2) and pure DFT (F₀ = 0.0) Hamiltonians.

F ₀	AF ₂						FM				
	a ₀	E _F	q	n _{Ni}	ΔE _g	Δ _{MO}	a ₀	E _F	q	n _{Ni} , n _O	ΔE _g
UHF	4.2589	-8.24	1.878	1.924	14.2	4.48	4.2629	-7.99	1.880	1.930, 0.070	13.7
1.0	4.1658	-9.12	1.860	1.907	14.8	4.40	4.1710	-8.79	1.864	1.915, 0.085	14.1
0.9	4.1732	-8.48	1.850	1.897	13.5	3.90	4.1787	-7.97	1.854	1.907, 0.093	12.7
0.8	4.1804	-7.84	1.837	1.886	12.3	2.53	4.1865	-7.38	1.843	1.897, 0.103	11.5
0.7	4.1871	-7.21	1.822	1.871	11.1	2.68	4.1935	-6.75	1.829	1.884, 0.116	10.3
0.6	4.1942	-6.59	1.804	1.852	9.9	2.21	4.2009	-6.11	1.813	1.869, 0.131	9.1
0.5	4.2015	-5.98	1.780	1.827	8.7	1.81	4.2103	-5.49	1.791	1.847, 0.153	7.8
0.4	4.2072	-5.37	1.750	1.793	7.5	1.44	4.2192	-4.73	1.764	1.819, 0.181	6.0
0.3	4.2120	-4.75	1.711	1.747	6.0	1.08	4.2274	-4.17	1.730	1.783, 0.217	4.3
0.2	4.2158	-4.11	1.662	1.681	4.3	0.39	4.2350	-3.36	1.687	1.735, 0.265	2.4
0.1	4.2234	-3.39	1.600	1.581	2.5	—	4.2458	-2.68	1.635	1.677, 0.323	0.7
0.0	4.2238	-2.47	1.519	1.344	0.7	—	4.2563	—	1.510	1.185, 0.236	—
Expt	4.1705 (1)	-4.4 (2)		1.64 – 1.90 ⁽³⁾	~ 4 ⁽⁴⁾						

(1) Ref. [24] (2) Ref. [30] (3) Refs. [25-27] (4) Ref [3]

Table 2. The variation of optimised lattice constant, a₀ (Å), Fermi energy, E_F (eV), ionic charge, q (e), metal, n_{Ni} (μ_B), and oxygen, n_O (μ_B) spin moments, energy gap, ΔE_g (eV) and difference in energy, Δ_{MO} (eV), between upper oxygen and nickel valence band edges in NiO with both composition of the hybrid functional and magnetic state in the Becke-LYP scheme.

The transition from CT to MH behaviour with decreasing amount of exact exchange noted earlier is clear in Figure 2. It is also apparent that the states immediately above the CBE in the UHF AF₂ solution are of mixed character, with oxygen states dominating. The main weight of metal states lies ~ 5 eV higher in energy, which leads to the conclusion that, if the single-particle densities of states are any guide, the band gap excitation in the UHF scheme is not of CT type. At F₀ = 0.2, the CBE is certainly composed of nickel states, but the upper reaches of the valence band are of sufficiently mixed character that a definite classification is not worthwhile. At the pure DFT limit, both the CBE and VBE are clearly composed of metal derived states.

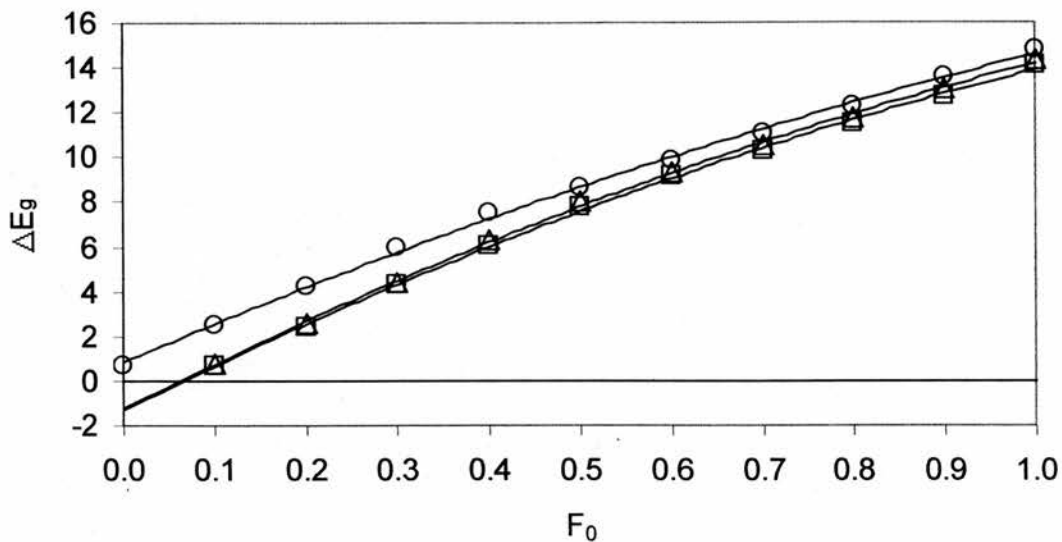


Figure 1. The AF₂ (O), AF₁ (Δ) and FM (□) band gaps, ΔE_g , (eV) for NiO as a function of the proportion of exact exchange, F_0 , in the Becke-LYP Hamiltonian.

(ii) Electronic Structure of MnO

For comparison, the electronic structure of MnO within the Becke-LYP scheme has been calculated at the optimised lattice constant appropriate to each weight of exact exchange, with results presented in Table 3 below and discussed as follows. Overall, the evolution of the electronic structure with the degree of hybridisation is similar to that described above for NiO. For the AF₂ alignment the ionic charge decreases by 15% as the weight of exact exchange decreases from the UHF to DFT limit and the local spin moment by $\sim 8\%$. Figure 3 below shows the variation in band gap with F_0 for the three magnetic states considered. As expected, there is a monotonic decrease in the energy gap as the weight of exact exchange is decreased; only the AF₂ alignment remains insulating at the DFT limit with a gap of 1.4eV. The variation in gap width with F_0 is more linear here than in NiO, with a smaller range in gradients, $\partial(\Delta E_g) / \partial F_0$, from 11.8 to 11.7 eV at $F_0 = 0.0$ and 1.0 respectively in the AF₂ state, from 13.2 to 12.1 eV at $F_0 = 0.1$ and 1.0 respectively in the FM state and from 12.6 to 11.3 eV at $F_0 = 0.1$ and 1.0 respectively in the AF₁ state. Turning again to Table 3, the B3LYP band gaps for the AF₂, AF₁ and FM magnetic alignments are 3.953, 2.855 and

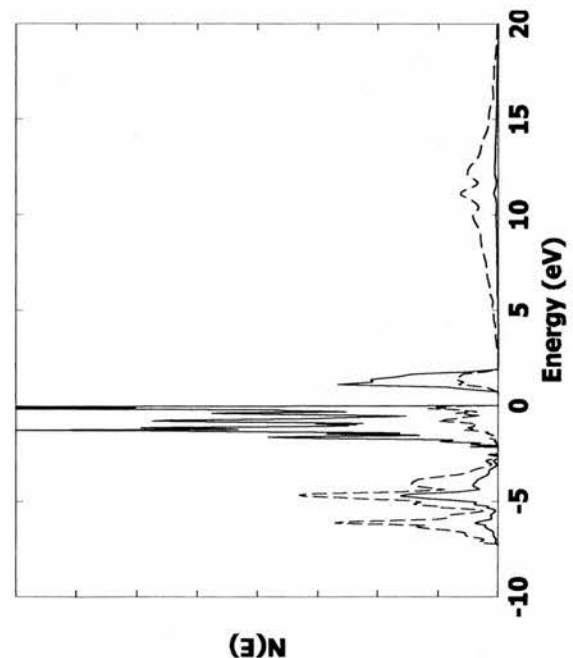
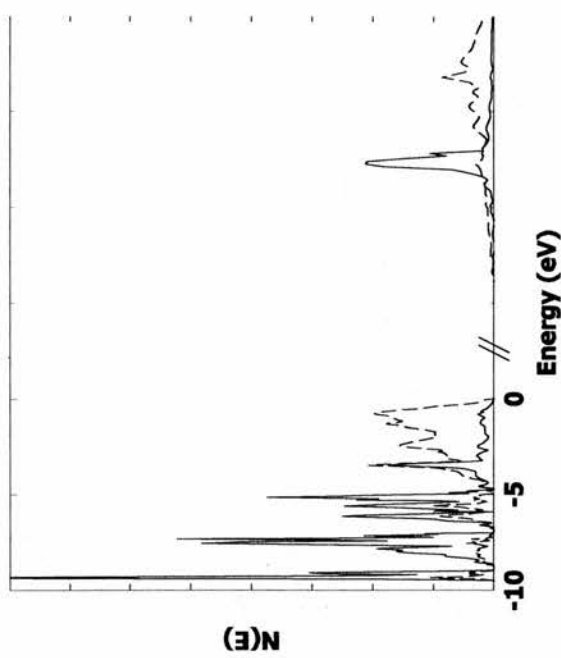
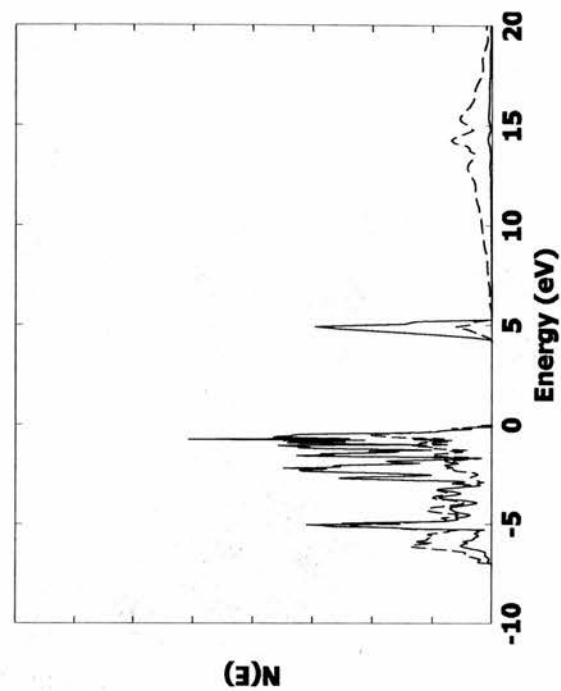


Figure 2. Clockwise from top left: the UHF (note discontinuity on energy axis), $F_0 = 0.2$ (B3LYP) and $F_0 = 0.0$ densities of states for $AF_2 NiO$, calculated at the relevant optimised lattice constant in the Becke-LYP scheme. Solid line shows metal and dashed line, oxygen contributions.

2.052eV respectively, from which it can be seen that, once again, it is the B3LYP AF₂ band gap that lies closest to the experimental value of ~ 3.6 eV [32]. Both sets of energy gap results for MnO and NiO, as presented in Tables 3 and 2 respectively, confirm one of the main results of a previous study by Muscat *et al* [33], namely that the B3LYP potential can yield accurate predictions for the band gaps of transition metal compounds. The experimental cation spin moment supports a value of F_0 in a range 0.0 – 0.4, which is smaller than that found in NiO, and the experimental band gap supports a choice of F_0 in the range 0.1 – 0.2.

F_0	AF ₂					FM				
	a_0	q	n_{Mn}	E_F	ΔE_g	a_0	q	n_{Mn}, n_O	E_F	ΔE_g
1.0	4.4190	1.837	4.878	-8.15	13.29	4.4252	1.835	4.888, 0.112	-7.56	12.27
0.9	4.4273	1.827	4.871	-7.50	12.07	4.4342	1.825	4.882, 0.118	-6.74	10.84
0.8	4.4355	1.815	4.863	-6.87	10.88	4.4435	1.814	4.875, 0.125	-6.11	9.63
0.7	4.4430	1.802	4.853	-6.24	9.69	4.4522	1.801	4.866, 0.134	-5.48	8.39
0.6	4.4509	1.787	4.840	-5.61	8.52	4.4612	1.787	4.856, 0.144	-4.75	7.12
0.5	4.4575	1.770	4.824	-4.99	7.35	4.4696	1.771	4.843, 0.157	-4.17	5.95
0.4	4.4635	1.749	4.802	-4.37	6.21	4.4779	1.752	4.826, 0.174	-3.53	4.73
0.3	4.4693	1.724	4.774	-3.74	8.08	4.4872	1.730	4.806, 0.194	-2.81	3.48
0.2	4.4738	1.694	4.734	-3.12	3.95	4.4952	1.704	4.780, 0.220	-2.19	2.05
0.1	4.4771	1.656	4.674	-2.48	2.83	4.5081	1.672	4.747, 0.253	-1.52	0.64
0.0	4.4742	1.604	4.567	-1.80	1.36	4.4890	1.602	4.547, 0.250	—	—
Expt	4.445 (1)		4.58 – 4.79 (2)		~ 3.6 (3)					

(1) Ref. [31] (2) Refs. [25,27] (3) Ref. [32]

Table 3. The variation of optimised lattice constant, a_0 (Å), Fermi energy, E_F (eV), ionic charge, q (e), metal, n_{Mn} (μ_B), and oxygen, n_O (μ_B) spin moments and energy gap, ΔE_g (eV) in MnO with both composition of the hybrid functional and magnetic state in the Becke-LYP scheme.

Figure 4 below presents the atom projected densities of states for AF₂ MnO at various proportions of exact exchange in the Becke-LYP scheme. As in NiO, the states at the VBE indicate a clear CT insulating character at the UHF limit, an insulator of intermediate character at $F_0 = 0.2$ and MH behaviour at the DFT limit. Again, the states

immediately above the CBE in the UHF calculation are derived from oxygen, with the main weight of metal states lying ~ 3 eV above the edge. Against this, it should be noted that an earlier UHF supercell calculation by Mackrodt and Williamson [23] of the first electron addition state in MnO concluded that it was of delocalised d^6 character. This result shows that the UHF densities of states for unoccupied orbitals is not a reliable guide to the nature of the added electron. States immediately above the CBE in the B3LYP and pure DFT Hamiltonians are definitely of metal character.

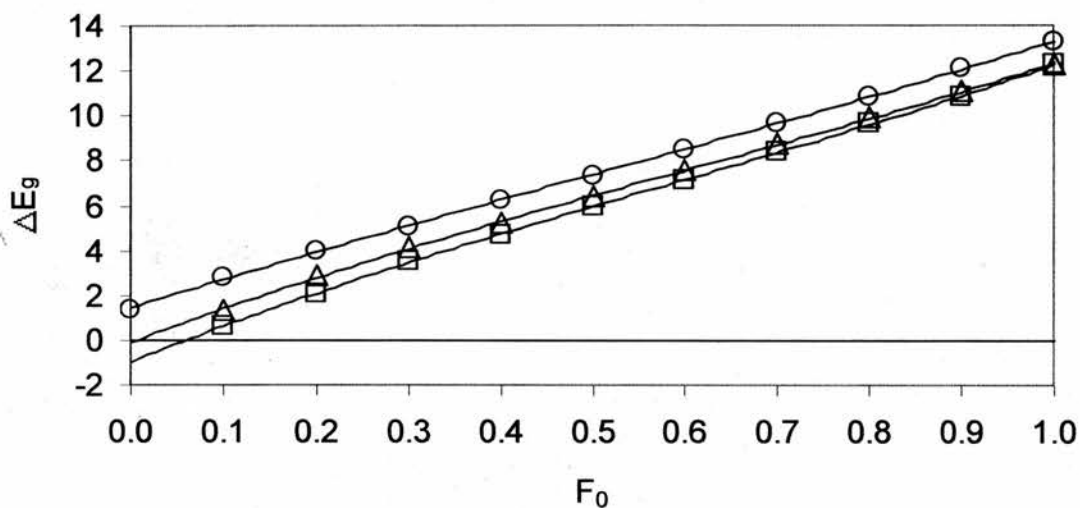


Figure 3. The AF₂ (O), AF₁ (Δ) and FM (\square) band gaps, ΔE_g , (eV) for MnO as a function of the proportion of exact exchange, F_0 , in the Becke-LYP Hamiltonian.

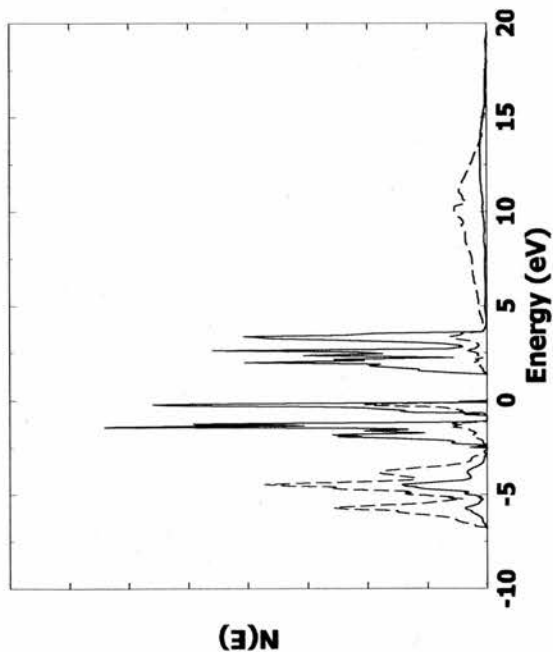
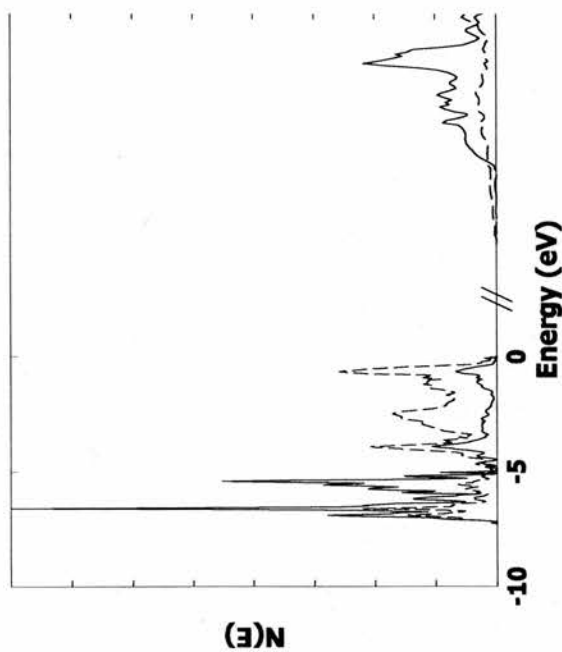
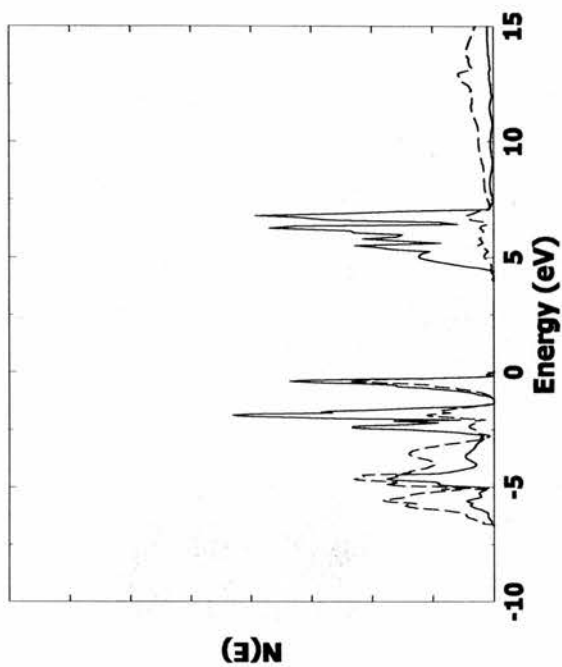


Figure 4. Clockwise from top left: the UHF (note discontinuity on energy axis), $F_0 = 0.2$ (B3LYP) and $F_0 = 0.0$ densities of states for AF_2 MnO, calculated at the relevant optimised lattice constant in the Becke-LYP scheme. Solid line shows metal and dashed line, oxygen contributions.

(iii) The Equation of State for NiO

The optimisation of structures with more than one degree of freedom in the CRYSTAL98 code is made demanding by the lack of atomic forces and cell stresses. The need to consider a sufficient number of separate Hamiltonians to resolve any trend adds to the labour. Fortunately, perfect rocksalt structures are completely specified by a single lattice constant, a_0 , and are thus the ideal choice for examining the effect upon structure of varying the amount of exact exchange in the hybrid Hamiltonian. The structural optimisation was performed by calculating the total energy at thirteen lattice constants within a range of $\sim 10\%$ around the experimental value, and fitting the resulting energy-volume data to the Murnaghan equation of state [34],

$$E(V) = E_0 - \frac{K_0 V_0}{K'_0 - 1} + \frac{K_0 V}{K'_0} \left(\frac{1}{K'_0 - 1} \left(\frac{V_0}{V} \right)^{K'_0} + 1 \right),$$

from which the equilibrium volume, V_0 , the bulk modulus at equilibrium, K_0 , the minimal energy, E_0 , and the pressure derivative of the bulk modulus at equilibrium, K'_0 , are all obtained. A simple least-squares method was employed for the fits, and the numerical stability tested by using different initial values. Table 4 below lists the optimised lattice constants and the equilibrium bulk moduli for the AF₂ and FM states in NiO in the Becke-LYP scheme.

The data in Table 4, in combination with the corresponding graph in Figure 5 shows that the isotropic spin-lattice interaction in NiO increases as the weight of exact exchange falls, for the FM and AF₂ curves grow increasingly separate. The difference between the AF₂ and FM values is 0.12% of the AF₂ value at $F_0 = 1.0$ and 0.53% of the AF₂ value at $F_0 = 0.1$. The most dramatic change in lattice constant results from the introduction of LYP correlation into the UHF Hamiltonian, resulting in a contraction in the AF₂ lattice by $\sim 2.2\%$ of the UHF value. The experimental lattice constant is reproduced by a value of F_0 in the range 0.9 – 1.0. The bulk moduli of the AF₂ and FM states are essentially equal

F_0	AF ₂		FM	
	a_0	K_0	a_0	K_0
UHF	4.2589	209.3	4.2629	210.0
1.0	4.1658	249.2	4.1710	250.1
0.9	4.1732	245.2	4.1787	246.1
0.8	4.1804	241.2	4.1865	241.7
0.7	4.1871	237.5	4.1935	238.1
0.6	4.1942	231.8	4.2009	234.2
0.5	4.2015	225.2	4.2103	229.1
0.4	4.2072	220.3	4.2192	223.5
0.3	4.2120	218.1	4.2274	218.5
0.2	4.2158	212.5	4.2350	212.8
0.1	4.2234	201.4	4.2458	204.2
0.0	4.2238	197.4	4.2563	157.3
Expt	4.1705 (1)	145 – 190 (2)		

(1) Ref. [24], (2) Refs. [35-36]

Table 4. Optimised lattice constants and equilibrium bulk moduli as a function of F_0 for AF₂ and FM NiO in the Becke-LYP scheme.

across the range of exact exchange, although there is, perhaps, a tendency for the FM values to lie a few GPa higher. Again, the most dramatic change arises from the introduction of LYP correlation into the UHF scheme, resulting in an increase in the AF₂ bulk modulus of $\sim 19.1\%$ of the UHF value. The variation in Table 4 and Figure 5 of bulk modulus with F_0 is in qualitative agreement with the notional pattern expected from a knowledge of the variation in lattice constant, for it is known from pseudopotential theory that the bulk modulus of ionic compounds varies approximately as d^{-3} , where d is the interatomic distance [37]. Thus, K_0 increases with falling a_0 as the weight of exact exchange increases, and the UHF bulk moduli are much lower than the $F_0 = 1.0$ values, for the UHF lattice constants are higher. However, a plot of K_0 against d^{-3} for AF₂ NiO (not shown here) reveals a curve that deviates from linearity, the reason being that the bulk modulus in covalent and metallic compounds is known to vary more as d^{-5} , and it has been established that NiO becomes increasingly covalent as F_0 is reduced.

The FM lattice becomes conducting in the pure DFT limit, and while there is no evident discontinuity in the lattice constant, the bulk modulus drops dramatically by ~ 40 GPa. It is surprising that the lattice does not contract in the metallic state, for generally the total energy associated with a partially filled band can be lowered by an increase in width, which in turn requires a reduction in interatomic distance. In summary, no computed value for the bulk modulus of the observed low temperature AF₂ alignment falls within the range of experimental results, although both the pure DFT and UHF values are close to the upper extreme of that range.

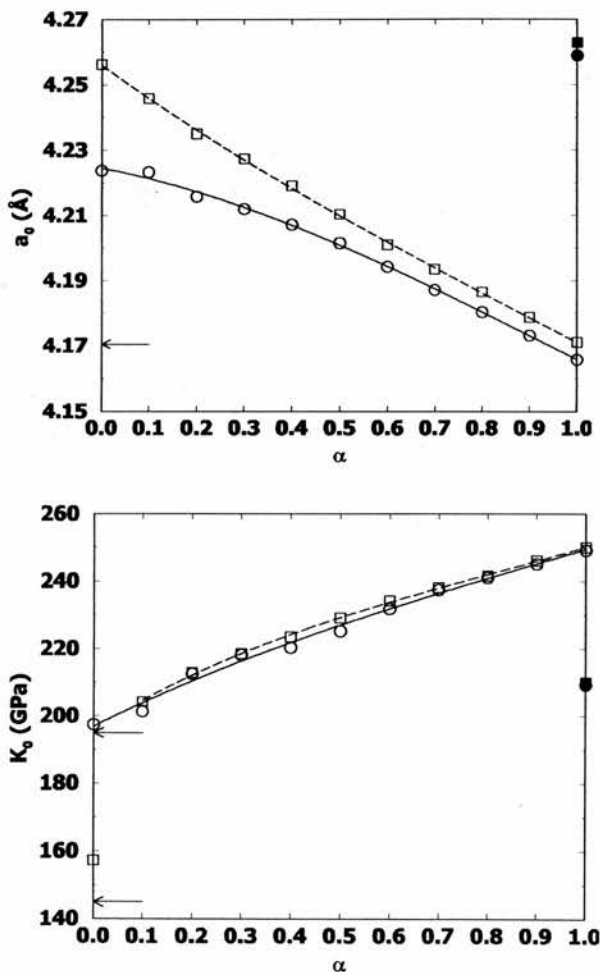


Figure 5. The optimised AF₂ (O) and FM (□) lattice constants, a_0 (Å) and bulk moduli, K_0 (GPa), for NiO in the Becke-LYP scheme as a function of the weight of exact exchange, α . Filled symbols are UHF values, arrows mark experimental value or range.

(iv) The Equation of State of MnO

A similar method to that described above for NiO was applied to MnO, but with the extension that hybrid functionals omitting LYP correlation were also considered, denoted as Becke-no-LYP in the following discussion. Table 5 below presents these results, while Figure 6 plots them. Dealing first with the lattice constants, a very similar pattern emerges in the Becke-LYP results to that established for NiO, where a_0 increases with decreasing weight of exact exchange. The isotropic spin-lattice interaction seems to be comparable in strength to that observed in NiO, and increases with decreasing F_0 . The difference between the AF₂ and FM values is 0.14% of the AF₂ value at $F_0 = 1.0$ and 0.69% of the AF₂ value at $F_0 = 0.1$, both of which compare well with 0.12% and 0.53% in NiO. The AF₂ lattice constants emerging from the Becke-no-LYP scheme are all higher than the corresponding correlated functional values, by $\sim 0.10 \text{ \AA}$ at $F_0 = 1.0$ and $\sim 0.14 \text{ \AA}$ at $F_0 = 0.0$. Thus, the isolated UHF point in the NiO data is shown in MnO to be a part of a smooth curve. The experimental low temperature lattice constant is best matched by a choice of F_0 in the range 0.6 – 0.7 in the Becke-LYP scheme, while those contributed by the Becke-no-LYP scheme are all higher than the experimental value.

The metallic state in the results of Table 5 for FM MnO at $F_0 = 0.0$ in the correlated scheme is accompanied by a discontinuous drop in the lattice constant and bulk modulus, as might be expected. The reduction in bulk modulus is estimated to be approximately 35 GPa, which is close to the estimate of 40 GPa for the same drop in NiO, although there it should be recalled that the lattice constant showed no discontinuity with progress to the metallic state. The AF₂ bulk moduli in the Becke-LYP scheme follow a very similar pattern to those in NiO, namely that K_0 increases with F_0 , again, as would be predicted from the variation in the lattice constant with F_0 . One notable difference in MnO is that the FM bulk moduli deviate significantly away from the AF₂ curve to higher values at low weights of exact exchange. The reason for this difference is unknown currently, and requires further work.

F_0	Becke-LYP				Becke-no-LYP	
	AF ₂		FM		AF ₂	
	a_0	K_0	a_0	K_0	a_0	K_0
1.0	4.4190	193.97	4.4252	195.38	4.5217	163.71
0.9	4.4273	190.65	4.4342	192.19	4.5319	160.42
0.8	4.4355	188.58	4.4435	190.59	4.5419	157.90
0.7	4.4430	183.58	4.4522	185.05	4.5519	155.51
0.6	4.4509	183.18	4.4612	185.20	4.5615	152.49
0.5	4.4575	180.48	4.4696	183.27	4.5714	150.39
0.4	4.4635	178.17	4.4779	182.97	4.5803	147.25
0.3	4.4693	175.27	4.4872	180.34	4.5888	144.07
0.2	4.4738	172.16	4.4952	179.93	4.5965	143.09
0.1	4.4771	167.65	4.5081	176.39	4.6044	138.19
0.0	4.4742	160.57	4.4890	140.38	4.6110	131.22
Expt	4.445 ⁽¹⁾	144 – 162 ⁽²⁾				

(1) Ref. [31] (2) Refs. [31,38 - 41]

Table 5. The variation in optimised lattice constants, a_0 (Å) and equilibrium bulk moduli, K_0 (GPa) for AF₂ and FM MnO in the Becke-LYP scheme, and AF₂ MnO in the Becke-no-LYP scheme with F_0 .

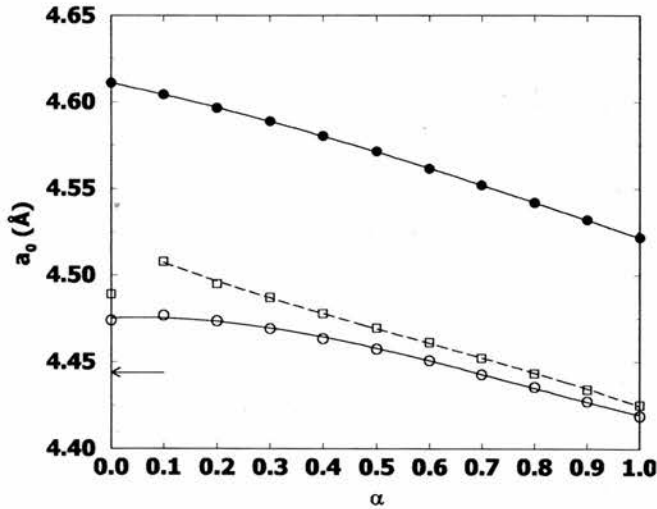


Figure 6. The optimised AF₂ (○) and FM (□) lattice constants, a_0 (Å) and bulk moduli, K_0 (GPa), for MnO as a function of the weight of exact exchange, α . Unfilled symbols are for the Becke-LYP scheme, filled symbols are for the Becke-no-LYP scheme and arrows mark experimental value or range.

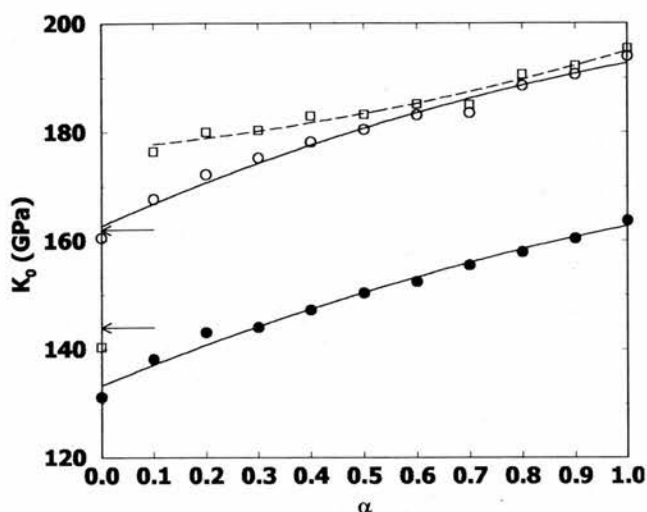


Figure 6. continued

The uncorrelated Becke-no-LYP functional values for K_0 are all lower than correlated values, by ~ 30 GPa at $F_0 = 1.0$ to ~ 29 GPa at $F_0 = 0.0$. At the exact exchange limit, this amounts to some 18.5% of the uncorrelated UHF value, close to the 19.1% found in NiO. In terms of agreement with experiment, only the $F_0 = 0.0$ value for K_0 in the Becke-LYP scheme falls within the combined range of values from X-ray diffraction and ultrasonic measurements, and is close to the uppermost extreme. The values arising from the uncorrelated functional are a much better match for experiment in the rather broad range $0.1 \leq F_0 \leq 0.9$. So, a difficult situation arises in which all the details of the equation of state in MnO cannot be described within the same method, the lattice constant and bulk modulus being better described by correlated and uncorrelated functionals respectively. All indications are that the same problem arises in NiO.

(v) The Magnetic Properties of NiO

As discussed earlier in Chapter 1, the majority of magnetic insulators are characterised by moments which derive from net electron spin density localised largely at cation sites. Recall that the ability to account theoretically for a number of experimental observations, including the magnon spectra, disorder transition temperature and anisotropic spin-lattice interaction (also known as magnetostriction) requires the concept of magnetic exchange.

Chapter 1 introduced an Ising Hamiltonian which incorporated nearest neighbour and next nearest neighbour interactions and onto which the energies of calculations reported here are mapped. Note that a full mapping of the magnon spectra requires a spin Hamiltonian incorporating non-collinear arrangements (the Heisenberg Hamiltonian), but for certain magnon wavevectors, the spin excitation energies can be related to the Ising J_d and J_{se} .

F_0	J_d	J_{se}	T_N^{mf}
uhf	8.601	39.556	89.00
1.0	9.366	56.918	128.07
0.9	9.912	63.298	142.42
0.8	10.736	70.674	159.02
0.7	11.691	80.339	180.76
0.6	13.881	95.065	213.90
0.5	15.879	114.719	258.12
0.4	18.804	141.972	319.44
0.3	22.668	186.187	418.92
0.2	28.542	248.948	560.13
0.1	36.392	353.586	795.57
0.0	85.175	670.744	1509.17
Expt (1)	< +16.2	+229.8 +197.28	525

(1) Refs. [42-43]

Table 6. The variation of direct, $J_d(K)$ and super-exchange, $J_{se}(K)$ coupling constants and fluctuation-corrected mean field Néel temperature, $T_N^{mf}(K)$ with weight of exact exchange, F_0 , for NiO in the Becke-LYP scheme.

Table 6 above presents the values of J_d and J_{se} obtained by performing such a mapping for the total energies of the AF_2 , AF_1 and FM states, all in bi-molecular cells. Although not of import in NiO, note that all coupling constants in this thesis have been divided by an amount of the formal spin of the metal ion squared ($S^2 = 1$ for NiO). The mean-field theory [44] can be used to relate the calculated superexchange coupling constants to the critical disorder, or Néel, temperature, T_N , but it neglects the fluctuations that a full Monte Carlo simulation would incorporate and which act to suppress T_N . Fortunately, a geometry dependent factor is known which relates the calculated mean field critical

temperature to the values of T_N obtained from Ising Model Monte Carlo calculations [44]. In the rocksalt structured oxides, only the superexchange coupling contributes to the energy of the AF_2 ground state, and the required Ni–O–Ni linkages describe a simple cubic lattice, for which the fluctuation correction factor is 0.75172, and T_N^{mf} is then $3S_z^2(0.75172)J_{se}$. The fluctuation corrected values for T_N are also presented in Table 6. In comparing the results it should be borne in mind that only the critical temperature is directly observed in experiments, the values of J_d and J_{se} are obtained by a mapping of the magnon spectra from inelastic neutron scattering studies onto the Heisenberg Hamiltonian.

The most important point to note in Table 6 is the extreme sensitivity of the coupling energy to the weight of exact exchange. In going from pure HF exchange to pure DFT, the direct exchange and superexchange interactions both increase in strength by factors of ~ 10 and ~ 17 respectively; a huge increase in comparison with the effect that change in F_0 has upon the electronic structure and equation of state. The critical temperature displays the same large sensitivity to F_0 , for it is, of course, directly proportional to J_{se} . For an Ising Hamiltonian of the form presented in Chapter 1, values of $J_d > 0$ imply a ferromagnetic coupling, while values of $J_{se} > 0$ imply antiferromagnetic coupling. Thus, in NiO, the direct exchange is ferromagnetic and the superexchange is antiferromagnetic at all weights of exact exchange. An average of the two experimental values for J_{se} yields ~ 214 K, which in the mean field of the Ising Hamiltonian leads to a critical temperature of ~ 482 K after correction for fluctuations, which is in acceptable agreement with the directly observed value of 525 K. The conclusion to be drawn from this observation is that the Ising Hamiltonian, even in the simple mean field, can provide a consistent interpretation of the experimental data, and so the use of it here in interpreting purely theoretical results is justified. Now, turning to a comparison with experiment, it can be seen that values of $F_0 \geq 0.5$ lead to direct coupling constants in the experimental range, while a much narrower range of $0.2 \leq F_0 \leq 0.3$ leads to J_{se} and T_N in agreement with experiment. It is troubling that the two ranges in weight of exact exchange do not overlap, and so no common value of F_0 accurate for both types of coupling can be defined.

(vi) The Magnetic Properties of MnO

Table 7 below presents the results obtained from a similar procedure applied to MnO. Extensions to the analysis conducted for NiO are the consideration of the uncorrelated Becke-no-LYP scheme and the calculation of the Bloch constant, ϵ , which relates the superexchange coupling constant to the cell volume through a dependence of the form $J_{se} \propto V^{-\epsilon}$. In many magnetic transition metal compounds in the rocksalt structure, ϵ has been found to take a value close to $3/3$ [48].

F_0	Becke – LYP				Becke – no – LYP			
	J_d	J_{se}	T_N^{mf}	ϵ	J_d	J_{se}	T_N^{mf}	ϵ
1.0	1.639	6.327	88.97	3.846	-0.032	2.062	29.00	5.317
0.9	0.968	6.852	96.36	3.735	-0.463	2.185	30.72	5.376
0.8	0.204	7.338	103.19	3.735	-0.867	2.379	33.45	5.420
0.7	-0.624	8.155	114.67	3.722	-1.324	2.750	38.67	5.544
0.6	-1.570	9.093	127.87	3.678	-1.877	2.910	40.92	5.395
0.5	-2.656	10.512	147.82	3.674	-2.386	3.458	48.63	5.331
0.4	-4.286	12.108	170.26	3.706	-2.707	4.541	63.86	5.236
0.3	-5.890	15.176	213.41	3.490	-4.036	5.271	74.12	5.008
0.2	-8.966	19.558	275.03	3.403	-5.005	7.316	102.87	4.634
0.1	-13.085	25.913	364.40	3.286	-6.538	10.887	153.09	4.219
0.0	-15.917	37.903	533.00	1.341	-9.700	17.338	243.82	3.419
Expt	-10, ⁽¹⁾ -8.9, -8.5	+11, ⁽¹⁾ +10.3, +9.6	118 ⁽²⁾	$3/3$ ⁽³⁾				

(1) Refs. [45-47] (2) Ref. [32] (3) Ref. [48]

Table 7. The variation of direct, J_d (K) and super-exchange, J_{se} (K) coupling constants, fluctuation-corrected mean field Néel temperature, T_N^{mf} (K) and Bloch constant, ϵ , with weight of exact exchange, F_0 , for MnO in both the Becke-LYP and Becke-no-LYP schemes.

The coupling constants in MnO are much smaller than those in NiO. For example, at $F_0 = 1.0$ in the Becke-LYP scheme, J_d and J_{se} are 9.4 and 56.9 K respectively, as compared to 1.6 and 6.3 K in MnO. It is, of course, expected that the smaller lattice constant in NiO

should lead to stronger magnetic interactions, and this is borne out by a comparison of the average experimental superexchange constant, which is a factor of ~ 21 times larger in NiO than MnO. A similar comparison of average experimental direct coupling constants finds a factor of ~ 2 increase in NiO over MnO. In the current work, it is only at the pure DFT limit that the ratio of J_{se} in NiO and MnO at ~ 18 approaches the averaged experimental value.

Note also in Table 7 the change in the sign of J_d in the Becke-LYP method, from ferromagnetic at $F_0 \geq 0.8$ to antiferromagnetic at lower values. In the Becke-no-LYP scheme, the direct coupling is found to be antiferromagnetic at all weights of exact exchange. The Bethe-Slater theory for the direct exchange in the transition metals indicates that both the magnitude and sign of the direct coupling are determined by the quotient $\frac{D}{d}$, where D is the atomic separation and d is the diameter of the 3d orbital. In particular, there is a crossover from antiferromagnetic to ferromagnetic coupling as this quotient increases. This might provide an explanation for the change in sign of J_d in MnO in the Becke-LYP results presented above. Of course, the optimised lattice constant (and hence, D) increases as F_0 decreases, and it would be expected that this would lead to a change in sign of J_d which is opposite to that found above, but the effect of varying F_0 upon the average d-orbital diameter has not been determined. As found earlier in NiO, J_d and J_{se} show large increases with decreasing F_0 from 1.0 to 0.0 are found here, with the absolute values of Becke-LYP J_d increasing by a factor ~ 10 and J_{se} by a factor ~ 6 , and Becke-no-LYP J_d increasing by a huge factor ~ 300 and J_{se} by ~ 8 . In terms of agreement with experiment, for the Becke-LYP method, choices of F_0 in the range 0.1 – 0.2 and 0.5 – 0.6 reproduce the average experimental J_d and J_{se} respectively, while agreement with the experimental critical temperature requires F_0 in the range 0.6 – 0.7. For the Becke-no-LYP method, the same agreements with experiment are provided by F_0 in the ranges 0.0 – 0.1, 0.1 – 0.2 and 0.1 – 0.2 respectively.

Now, the ability of hybrid Hamiltonians to reproduce the dependence of T_N on pressure can, in theory, be tested by the closeness of their calculated Bloch constants to the value

$\sim 3\frac{1}{3}$, which is an average taken from studies of a number of transition metal compounds. For the Becke-LYP method data in Table 7, F_0 in the range 0.1 – 0.2 provides Bloch constants which bracket the observed value, while in the uncorrelated Becke-no-LYP scheme, the pure DFT limit provides a value close to that observed. It is possible, though, to test the consistency of the $J_{se} \propto V^{-\epsilon}$ trend by directly calculating the fluctuation corrected mean field T_N at each pressure. Now, X-ray diffraction experiments on MnO at room temperature have shown a B1 to rhombohedrally distorted B1 transition at an applied pressure of ~ 30 GPa [31]. The cubic to rhombohedral distortion is a consequence of the anisotropic spin-lattice effect that accompanies AF_2 magnetic ordering, and indicates that the critical temperature has risen from 118 K at ambient pressure, to ~ 300 K (room temperature) in the compressed structure at 30 GPa. From these two points, a pressure gradient for T_N of ~ 6.1 K Pa^{-1} can be calculated.

Plots of T_N against pressure for Becke-LYP and Becke-no-LYP Hamiltonians spanning the full range of F_0 , and using the equation of state results presented earlier are shown in Figure 7 below. For Becke-LYP, the gradients of the fitted lines for $F_0 = 0.2$ and 0.1, at 5.2 and 7.0 K Pa^{-1} respectively enclose the X-ray value, and, moreover, match the range of exact exchange found to fit the Bloch constant above. In the uncorrelated method, F_0 values of 0.1 and 0.0 produce gradients of the fitted lines of 4.7 and 7.0 K Pa^{-1} respectively, bracketing the experimental value. Both of these weights of exact exchange produce Bloch constants that are slightly higher than $3\frac{1}{3}$, but which are still the closest of any of the uncorrelated values. It is of interest to note that the pressure gradients emerging from the correlated Hamiltonians are generally a factor of 1.40 – 1.58 times larger than those in the uncorrelated scheme. This fits with the qualitative picture of correlation producing more diffuse states, and hence greater overlap.

In summary, the description of the pressure dependence of the superexchange interaction, either in terms of the Bloch constant or the directly calculated critical temperature results in a consistent picture. Additionally, in the correlated scheme, the weight of exact exchange required to produce a match in T_N with experiment is appreciably higher than

that needed to reproduce the pressure gradient, whereas in the uncorrelated method, the ranges in F_0 are comparable.

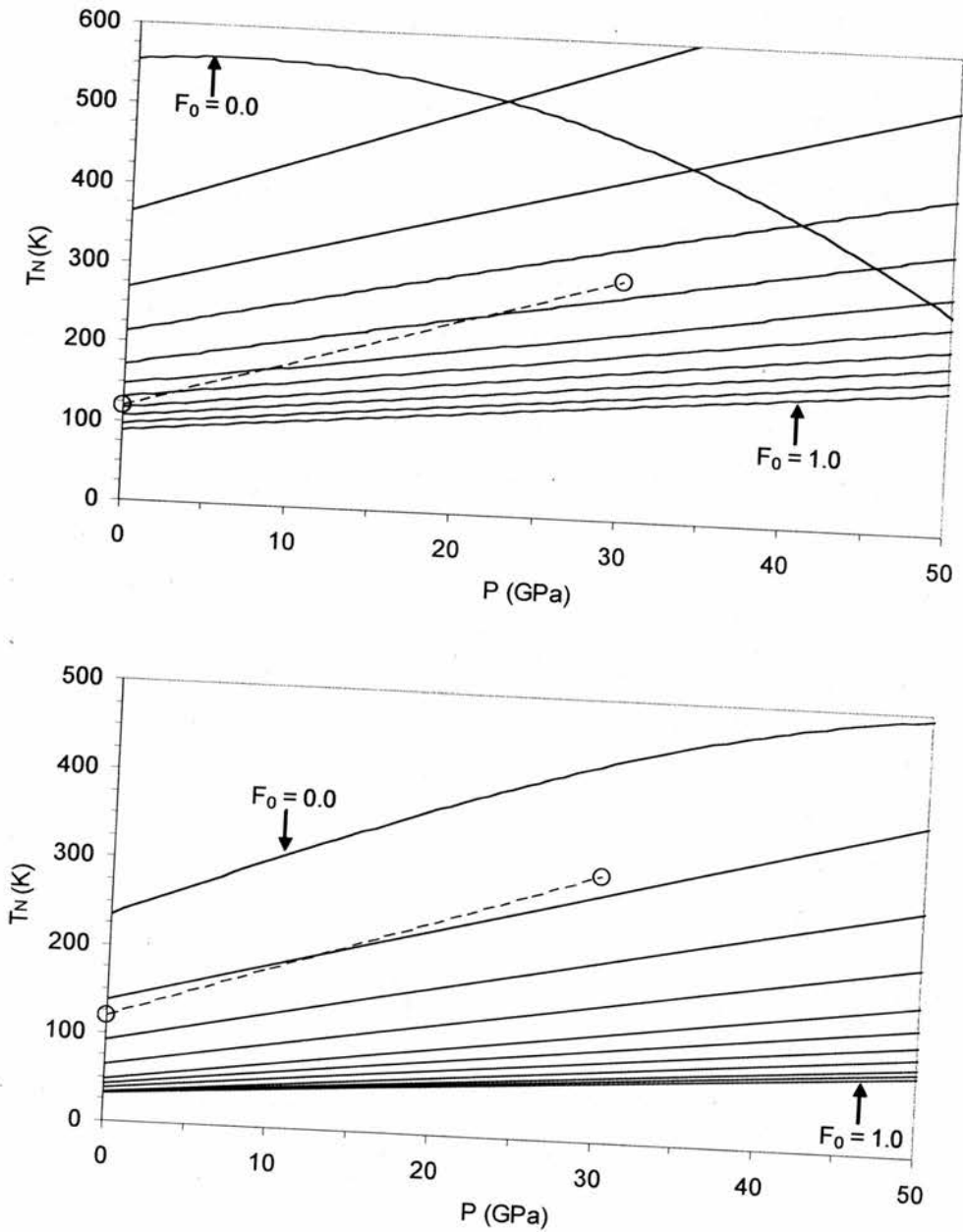


Figure 7. The variation in the critical temperature, T_N (K), with pressure, P (GPa), in MnO for (top panel) the Becke-LYP and (bottom panel) the Becke-no-LYP schemes. F_0 varies from 1.0 (bottom line on each plot) to 0.0 (top line). The experimental values, denoted by circles, are included for comparison.

(vii) The Spin-Lattice Distortion in MnO

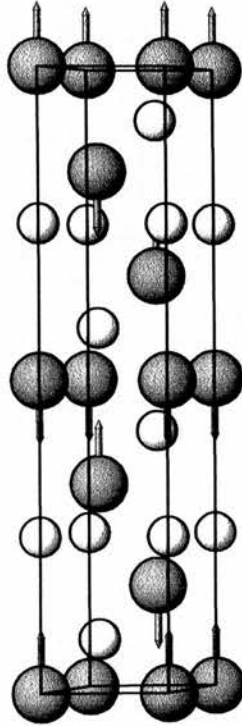


Figure 8. The hexagonal representation of the rhombohedral cell used in the simulation of the spin-lattice distortion. Large grey circles are Mn²⁺ ions, for which the spin orientation is indicated. Small white circles are the O²⁻ ions.

Below the Néel temperature, both AF₂ MnO and NiO undergo a rhombohedral contraction as a result of the interaction between the adjacent antiferromagnetically-aligned hexagonal {111} cation planes of spins. Pask *et al* [22] have argued that while the direct nearest neighbour interaction cannot contribute to the magnetic energy in the AF₂ alignment of the strictly cubic lattice, it is the magnetic component which drives the rhombohedral distortion. To see how this can arise, consider the rhombohedral compression along the [111] axis observed in MnO. In this distorted structure, metal ions within the same (111) hexagonal plane move further apart, while the distance between the

planes decreases. It is also necessary to visualise that, in the AF₂ alignment, ions in the same (111) plane are arranged ferromagnetically with respect to each other, and that the (111) planes follow a pattern of alternating spin orientation in the normal direction. The resulting structure is shown in a hexagonal representation in Figure 8 above, where the (111) planes of the cubic structure are parallel to the *ab*-plane, and the [111] body diagonal of the cube lies along the long *c*-axis of the hexagonal cell. Now, a compression of the cubic cell along [111], as observed in MnO, is equivalent to a decrease in the *c/a* ratio of the hexagonal cell, with the effect that in-plane direct coupling constants are reduced in magnitude, thus $J_d \rightarrow J_{d'}$, where $|J_{d'}| < |J_d|$, and out-of-plane couplings are increased in strength $J_d \rightarrow J_{d''}$, where $|J_{d''}| > |J_d|$. Experimentally, J_d is known to be antiferromagnetic in MnO, which is represented by $J_d < 0$ in the Ising Hamiltonian of Chapter 1, and so $J_{d'} = J_d + \delta$, and $J_{d''} = J_d - \delta$, where δ is a small constant which varies linearly with the absolute value of the change in interatomic distance. Plainly put, the assumption here is that, for small distortions, a reduction in interatomic distance increases the strength of the direct coupling by the same amount that an increase in distance lowers it. Now, in the rhombohedral lattice, the energies of the AF₂, AF₁ and FM states for this Ising Hamiltonian are expressed as

$$E[\text{Rhomb. AF}_2] = E_0 - 3J_{d'} + 3J_{d''} - 3J_{se},$$

$$E[\text{Rhomb. AF}_1] = E_0 + J_{d'} + J_{d''} + 3J_{se},$$

$$E[\text{Rhomb. FM}] = E_0 - 3J_{d'} - 3J_{d''} + 3J_{se}.$$

The next step is to consider the energy differences between rhombohedral and cubic energies, thus

$$E[\text{Cubic AF}_2] - E[\text{Rhomb. AF}_2] = 3J_{d'} - 3J_{d''} = 6\delta,$$

$$E[\text{Cubic AF}_1] - E[\text{Rhomb. AF}_1] = 2J_d - J_{d'} - J_{d''} = 0,$$

$$E[\text{Cubic FM}] - E[\text{Rhomb. FM}] = 3J_{d'} + 3J_{d''} - 6J_d = 0.$$

Of course, the exchange driven distortion will be opposed by the normal elastic response of the crystal, represented in this case by the c_{44} elastic constant. It is clear that, within this simple model, only the AF_2 state is stabilised by a rhombohedral distortion, which for antiferromagnetic direct coupling is predicted to take the form of a compression along the cubic [111] direction. This matches the UHF results of Towler *et al* [13], which reported no deviation from cubic symmetry in MnO in the FM alignment. In contrast, in the case of ferromagnetic direct coupling, represented here by $J_d > 0$, an expansion along [111] is favoured. It must be said that in NiO, just such a situation of ferromagnetic coupling is realised, but compression along the body diagonal is still found in experiment and in UHF calculations [13]. However, the increase in the cubic angle, at $\sim 0.1^\circ$ is approximately one-sixth of that found in MnO.

A study was made of the size of the distortion starting from the optimised cubic structures for each hybrid Hamiltonian. To this end, a hexagonal cell of crystallographic group $R\bar{3}c$ and with the magnetic alignment shown in Figure 8 was set up, where

$$a_{\text{hex}} = \frac{1}{2} \sqrt{2} a_{\text{cub}} ,$$

$$c_{\text{hex}} = 2\sqrt{3} a_{\text{cub}} ,$$

both for the optimised cubic lattice constants, a_{cub} , presented for the Becke-LYP scheme in Section 2(iv) earlier. Approximately ten points of varying ratio $c_{\text{hex}} / a_{\text{hex}}$, all within a range of $\sim 2\%$ of the cubic value were chosen, from which the CRYSTAL code then generates an equivalent but smaller rhombohedral cell. The total energies for each Hamiltonian were calculated¹ and the optimal ratio $c_{\text{hex}} / a_{\text{hex}}$ was determined by least-squares fitting with cubic polynomials. It should be stressed that the differences in energy resulting from the distortion are very small indeed, and so an extremely accurate numerical integration scheme is required if smooth energy versus distortion data are to be obtained. To this end, the normal CRYSTAL98 numerical quadrature scheme based upon atom-centred auxiliary basis functions was replaced by the CRYSTAL2003 scheme of integration upon a mesh of user-defined density, the convergence of which is more easily checked. The optimised rhombohedral cell was then transformed back into a structure

¹ In collaboration with Dr. Furio Corà, Davy Faraday Laboratory, Royal Institution of Great Britain.

close to cubic and the deviation in angle from the cube, $\Delta\gamma$, determined. The results of this process are presented in Table 8 below, and graphically in Figure 9.

F_0	a_0	Init. a_{hex}	Init. c_{hex}	Opt. a_{hex}	Opt. c_{hex}	$\Delta\gamma$
1.0	4.4190	3.1247	15.3079	3.1298	15.2579	+0.1870 ⁽¹⁾
0.9	4.4273	3.1306	15.3368	3.1363	15.2806	+0.2098
0.8	4.4355	3.1364	15.3652	3.1429	15.3018	+0.2361
0.7	4.4430	3.1416	15.3908	3.1490	15.3190	+0.2675
0.6	4.4509	3.1473	15.4184	3.1545	15.3479	+0.2619
0.5	4.4575	3.1519	15.4411	3.1604	15.3579	+0.3088
0.4	4.4635	3.1562	15.4621	3.1663	15.3635	+0.3652
0.3	4.4693	3.1603	15.4822	3.1738	15.3507	+0.4864
0.2	4.4738	3.1634	15.4975	3.1801	15.3351	+0.6006
0.1	4.4771	3.1658	15.5090	3.1874	15.2992	+0.7752
0.0	4.4742	3.1637	15.4990	3.1947	15.2003	+1.1040
Expt	4.445 ⁽²⁾					+0.62 ⁽³⁾

(1) Pure UHF value is +0.1477, (2) Ref. [31], (3) Ref. [49]

Table 8. The optimised cubic lattice constant, a_0 (Å), and the initial hexagonal constants a_{hex} and c_{hex} (Å) which are generated from it, optimised a_{hex} and c_{hex} (Å) and the deviation from the cubic angle, $\Delta\gamma$ (°) for the magnetostrictive distortion in MnO as a function of the weight of exact exchange, F_0 in the Becke-LYP Hamiltonian.

As Table 8 and Figure 9 make clear, the rhombohedral distortion increases in size as the weight of exact exchange decreases. This trend could be due to the already established increase in J_d with falling F_0 , or to a reduction in the c_{44} elastic constant with falling F_0 or to a combination of both factors. Although no data is available in the literature on the effect of exact exchange upon the elastic constants of MnO, Moreira *et al* [18] find a decrease in c_{44} of approximately 30% of the experimental value of 109 GPa in going from a pure UHF to pure DFT Hamiltonian in NiO. While this change would be significant in a discussion of the elastic constants alone, it is a much smaller percentage change than that found in the magnetic coupling constants over the same range. A speculated, similar fall in c_{44} with decreasing F_0 in MnO, and the known increase in J_d would both support the observed trend in $\Delta\gamma$. A weight of exact exchange in the range $0.1 \leq F_0 \leq 0.2$ yields a

value for $\Delta\gamma$ in agreement with that taken from neutron scattering experiments at a temperature of 8K by Shaked *et al* [49]. It should be further noted that this range in F_0 matches that which is required to reproduce the average experimental direct coupling constant, as discussed previously in Section 2(vi). This supports the earlier conclusion that, were the relative insensitivity of c_{44} to weight of exact exchange as found in NiO to be replicated in MnO, the variation in $\Delta\gamma$ with F_0 would be determined primarily by the variation in J_d across the range of Hamiltonians.

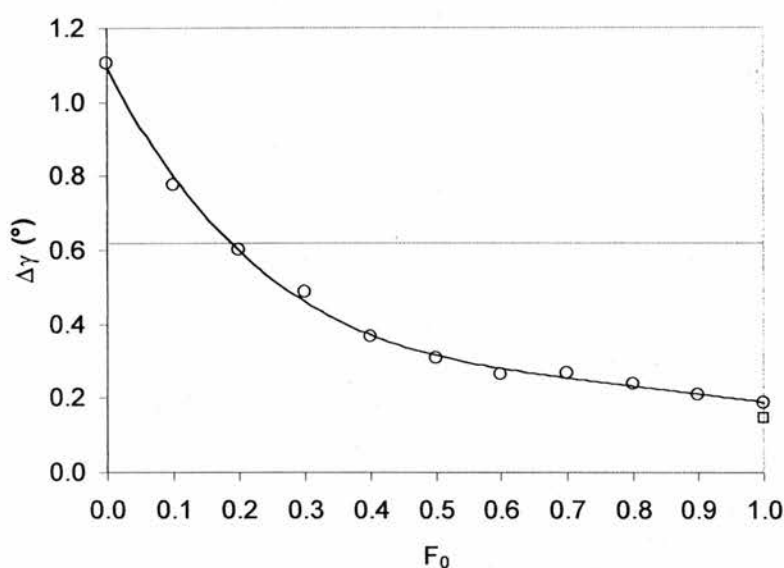


Figure 9. The variation in the deviation from the cubic angle, $\Delta\gamma$ (°) with weight of exact exchange, α in MnO in the Becke-LYP scheme. A square and horizontal grey line mark the UHF and experimental values respectively.

Finally, there remains the question of whether the transition from a cubic to a rhombohedral cell conserves the volume. To address this, the UHF method was used in an optimisation of rhombohedral cells at volumes close to the 23.1124\AA^3 per molecule found in the cubic structure. Five volumes within a range of 2% of the previous value were chosen, and for each volume, six hexagonal cells with varying c/a ratio were set up. The resulting energy versus c/a data were least-squares fitted with cubic polynomials, yielding an energy-volume set. The overall energy volume set was then, in

turn, fitted with a cubic function and the equilibrium volume found. The end result was an equilibrium volume of 23.1401\AA^3 per molecule for rhombohedral cells, which is within $\sim 0.12\%$ of the optimised cubic volume. It can therefore be concluded that rhombohedral distortion does not lead to any significant change in equilibrium volume of MnO, at least at the UHF level. The volume change may well be larger for lower weights of exact exchange, but the time to conduct such a study was not available.

(viii) The Crystal Field Excitations in MnO and the Effect of Electron Correlation

The crystal field or $d \rightarrow d$ transition energies are generally well characterised in the transition metal oxides, as discussed previously in Chapter 1. In optical spectroscopy, the excitations typically occur with weak intensity, for they violate the Laporte selection rule for dipole transitions, and manifest below the strong absorption edge. In the case of MnO, the absorptions are predicted to be particularly weak, for here all $d \rightarrow d$ transitions from the multiplicity-six ground state of the Mn^{2+} ion must involve a reduction in the spin moment from $S = \frac{5}{2}$ to $S = \frac{3}{2}$, and a violation of the spin selection rule. Nevertheless, the low energy excitations have been detected optically in both the equilibrium structure and at high pressure [50-51]. Electron energy loss spectroscopy (EELS) does not suffer under the same selection rules as optical spectroscopy, due to the fermion character and finite momentum of the incoming electrons. It is thus a convenient method for the study of crystal field excitations. Such an EELS experiment in MnO detected a peak at 2.8eV, which was assigned to the ^4G atomic state, with a shoulder at 2.2eV assigned to the crystal field split state [53]. The analysis further suggested that a shoulder at 3.4 eV corresponded to the ^4D state, while another at 4.6 eV was assigned to the ^4P state.

X-ray fluorescence spectroscopy, meanwhile, places the ^4G derived states at $\sim 3\text{eV}$, with a broad quadruplet peak (comprising the ^4G , ^4P and ^4D states) spanning energies between 2 – 5 eV below the recombination peak [52], showing a maximum at an energy of $\sim 3.5\text{ eV}$. The crystal field splitting is not explicitly considered in this work, for the reason that it broadens the observed peaks but is small compared to the exchange splitting between the

6S ground and lowest lying 4G excited states. A shoulder in the peak at $\sim 5\text{eV}$ is assigned to states of 2D , 2F and 4F symmetry. The X-ray fluorescence technique is very useful for it can, like EELS, avoid the effect of the dipole selection rules, although by a very different strategy to that employed in EELS. XFS splits the dipole forbidden transition into two allowed transitions, namely the excitation of an electron from a core state, and subsequently, either a recombination decay, or a decay to a state lacking a core hole.

Optical absorption studies in the equilibrium structure detects peaks at 2.01, 2.5 and 2.94 eV assigned as ${}^4T_{1g}$, ${}^4T_{2g}$ and ${}^4A_{1g}$ (in the cubic field nomenclature), all of which involve a transition of the type $e_g(\uparrow) \rightarrow t_{2g}(\downarrow)$ [50,51]. The lowest energy excitation corresponds to the lower of the crystal field split transitions from the 6S ground states to an atomic state of type 4G , i.e. $x^2-y^2(\uparrow) \rightarrow xy(\downarrow)$, and is close in energy to the 2.2eV found in the EELS study. The optical absorption study was extended to high pressures, and all the assigned excitations are found to decrease in energy with increasing pressure due to the concomitant increase in the crystal field splitting. The ${}^4T_{1g}$ energy was found to vary as a^{-5} , as predicted by crystal field theory up to pressures of ~ 25 GPa, beyond which the effect of the increasing Mn(3d) band widths become important. At equilibrium, a value of 0.090 eV for the Racah B parameter and 1.17 eV for the crystal field splitting is obtained through comparison with the Sugano-Tanabe diagram. The ratio C / B has been found to be roughly constant in the range 4.2 – 4.5 for transition metal ions in the gas phase, as substitutional impurities and in compound [54]. So, taking C / B = 4.35, a value for the Racah C parameter of ~ 0.39 eV can be estimated for Mn^{2+} from the optical data. The correspondence between the parameters derived from optical absorption and the X-ray fluorescence data may now be checked. Firstly, all of the microstates that fall within the 4G , 4P and 4D multiplets were assigned an energy by use of the Kanamori crystal field Hamiltonian discussed in Chapter 1. The average was calculated, emerging as $14.75B+6C$, which, inserting the optical parameters, amounts to 3.67 eV, in good agreement with the maximum of ~ 3.5 eV for the 4G , 4P and 4D quadruplet group in the X-ray data. Next, the optical crystal field splitting can be used to predict a crude width for the X-ray quadruplet peak. The lowest lying microstate from amongst the 4G , 4P and 4D

multiplets is the $x^2-y^2(\uparrow) \rightarrow xy(\downarrow)$ state, the excitation energy for which is $10B+6C-\Delta_{CF}$, and the highest lying is the $xy(\uparrow) \rightarrow z^2(\downarrow)$ state, with excitation energy $18B+6C+\Delta_{CF}$, amounting to 2.07 and 5.13 eV respectively. Again, this is a close match for the span of approximately 2 – 5 eV in the X-ray data. So, whereas the resolution in the X-ray data not fine enough to resolve the three separate peaks found in the range 2 – 3 eV in optical absorption, the observed width of the X-ray quadruplet peak suggests a crystal field splitting close to that obtained directly from the absorption spectra.

Unfortunately, application of the UHF method to calculation of the excitations in MnO fails to yield energies close to those observed experimentally. Take, as an example, the $^4P z^2(\uparrow) \rightarrow xz(\downarrow)$ transition, to which the Kanamori Hamiltonian assigns an energy $12B+6C-\Delta_{CF}$, amounting to 2.26eV using the optical parameters. As in previous studies [54], the stability of the excited states was aided by performing all calculations for a Mn^{2+} ion located in the central plane of a slab of five ferromagnetically aligned (100) layers. The optimised UHF AF_2 lattice constant of 4.5217Å was used. A (2×2) surface supercell was used to further isolate the excited atoms in the xy -plane, leading to 40 atoms in each repeated cell. The co-ordinate system was aligned such that z is normal to the plane, while x and y lie within it. Thus, the local crystal field at the Mn site in the central plane is close to that in the bulk and of O_h symmetry. Now, a direct UHF calculation of the 4P excitation using this method, which relies upon the fact that the excited state is a variational minimum and can be converged toward, yields an energy of 3.60 eV, which is an overestimate by 1.34 eV of the experimental value. For the $^4S xy(\uparrow) \rightarrow xy(\downarrow)$ transition, the excitation energy is given by $10B+4C$, which equals 2.47 eV with optical parameters, whereas the UHF calculated value is 3.32 eV, overestimating the energy in this case by 0.85 eV. Finally, consider the $^4G x^2-y^2(\uparrow) \rightarrow xy(\downarrow)$ transition, which has a predicted energy $10B+6C-\Delta_{CF}$, summing to 2.08 eV with the optical parameters. The UHF method obtains a value of 3.48 eV, which is again an overestimate by 1.4 eV. The greatest contribution to the overestimate comes from the fact that the UHF method cannot account for the spin pairing correlation energy. So, in the case of the Mn^{2+} ion, for which all crystal field excitations involve the creation of at least one spin pair, the energy of the

final state is overestimated and the excitation energies are consequently much higher than experiment. Some estimates put the correlation energy at ~ 2 eV per spin pair, but the overestimates here are smaller than that. Of course, the 4S final state does not involve any spin pairing of electrons in the same d-orbital, and thus the overestimate here is smaller, at $\sim 60\%$ of the 4P and 4G values.

The effect of introducing LYP correlation in the $F_0 = 1.0$ method, at the optimised AF_2 lattice constant of 4.4190\AA is to lower all three excitation energies to 2.99, 2.86 and 2.86 eV for the 4P , 4S and 4G final states respectively. The calculated energies now overestimate the experimental values by 0.73, 0.40 and 0.78 eV respectively, which are all great improvements upon the UHF values. The improvement continues for the $F_0 = 0.9$ method, at an optimised AF_2 lattice constant of 4.4273\AA , where excitation energies of 2.84, 2.76 and 2.72 eV are found, representing overestimates of 0.59, 0.30 and 0.64 eV respectively. Due to the time consuming nature of the computations, only one further set of excitations could be calculated for a low weight of exact exchange. At $F_0 = 0.4$, the 4P , 4S and 4G excitations are stable and have energies of 2.17, 2.23 and 2.05 eV respectively, where the values represent underestimates of experiment by 0.09, 0.24 and 0.03 eV respectively. The fact that the difference from experiment crosses from over- to underestimation as F_0 decreases indicates that the hybrid scheme should be capable of a quantitative agreement with experiment for a value of F_0 close to 0.4. For the purposes of comparison, the values for the Racah B and C parameters and crystal field splitting are 0.059, 0.683 and 1.207 eV respectively in the UHF scheme, 0.066, 0.552 and 1.107 eV respectively at $F_0 = 1.0$, 0.064, 0.532 and 1.107 eV respectively at $F_0 = 0.9$ and 0.059, 0.410 and 1.000 eV respectively at $F_0 = 0.4$. The optical parameters are 0.09, 0.39 and 1.17 eV respectively, and so it is obvious that, at $F_0 = 0.4$ the C parameter is reproduced correctly, but the B parameter and crystal field splitting have moved further from experiment.

The excitations for the isolated Mn^{2+} ion were also calculated, to allow the effect of the extended lattice to be gauged. The values derived from the optical parameters were

obtained by removal of crystal field terms in the earlier expressions, leading to energies of 3.43, 2.47 and 3.24 eV respectively for transitions with 4P , 4S and 4G final states. UHF calculations yield 4.73, 3.47 and 4.49 eV, representing overestimates of experiment by 1.30, 1.00 and 1.25 eV respectively. The energy for the alternate $^4G_{xy(\uparrow)} \rightarrow x^2-y^2(\downarrow)$ transition was also computed and found to be equal to the $x^2-y^2(\uparrow) \rightarrow xy(\downarrow)$ value, as would be expected in the absence of a crystal field. The size of the overestimate of the 4P transition is virtually unchanged by lack of a crystal environment, whereas the 4S and $4G$ excitations increase and decrease by ~ 0.15 eV respectively. The UHF Racah parameters for the isolated ion are 0.123 and 0.509 eV for B and C respectively, where B has evidently increased and C decreased with respect to the lattice values.

As a final note, studies of the $d \rightarrow d$ excitations in NiO, VO and $Sr_2CuO_2Cl_2$ form part of the later work in this thesis. Since spin-allowed transitions are generally the lowest energy excitations in these materials, the latter work concentrates on them, save in VO, where a transition involving a change in spin is considered. It should be stressed that, save for the case of this one transition in VO, all other excitations in the three materials are expected to be free of the problems encountered in MnO, for no change in the number of spin pairs in any given d-manifold is involved.

(ix) The Pressure Induced B1 to B8 Transition in MnO

The high pressure phase diagram of MnO remains unclear, despite recent studies using modern techniques. The history of experimental observations in this material is presented prior to a discussion of theoretical approaches to determining the high pressure structures. Clendenen and Drickamer, in 1966 conducted an X-ray diffraction study of the effects of static compression on the lattice constants of a set of TM oxides and sulfides [38]. A Hugoniot curve was obtained for manganosite (MnO), and a transition to a tetrahedral, or possibly lower symmetry structure was found at 120 kbar (12 GPa). No evidence of this transition at low pressure is found in later studies. The diffraction techniques of the time were unable to resolve the small peak splittings that accompany the magnetostrictive

distortion, and so the structure was treated as being strictly cubic. A fit of the observed pressure-volume data to the Murnaghan equation of state (EOS) yielded $V_0 = 21.971 \text{ \AA}^3$, $K_0 = 144 \text{ GPa}$ and $K_0' = 3.3$. Measurements of electrical conductivity under shock compression by Syono *et al* indicated that MnO remained insulating at pressures up to 50 GPa [56]. Static experiments by Bloch *et al* in 1980 showed that the critical temperature, T_N , increases with pressure at a rate of 2.7 K GPa^{-1} up to the experimental limit of 3.3 GPa [57]. Piston-cylinder measurements of the thermal expansion conducted in 1987 by Tamura obtained a rate of increase of T_N with pressure of 3.5 K GPa^{-1} [58]. Assuming a continued linear trend in T_N to higher pressures, the extrapolated values for the pressure required to raise T_N to room temperature are 67 and 52 GPa respectively.

The static compression study by Jeanloz and Rudy in 1987 [39] was prompted by the ultrasonic measurements of Webb *et al* [59] in 1983, which indicated a progressive softening of the c_{44} elastic constant with increasing pressure. The trend in c_{44} was postulated by Webb and co-workers to be a precursor to a transformation to the B2 (CsCl type, shown in Figure 10 below) structure at approximately $40 \pm 20 \text{ GPa}$. The results of Jeanloz and Rudy show, however that no new phases emerge to a pressure of 60 GPa, although in this study the magnetostrictive distortion was once again neglected. The absence of a structural transformation led to an explanation of the c_{44} softening in terms of the magnetic contribution to the energy of the cell, which increasingly favours distortion as the pressure is increased, as discussed earlier in Section 2(vii) of this chapter. A third-order fit to the Birch EOS yielded $V_0 = 21.956 \text{ \AA}^3$, $K_0 = 162 \pm 17 \text{ GPa}$ and $K_0' = 4.8 \pm 0.1$. Webb *et al* in 1988 revised their estimate for the upper range of the B1 \rightarrow B2 transition to 90 GPa, based upon the ratio of c_{44} to the bulk modulus [40], and quoted a bulk modulus of $K_0 = 152.1 \pm 0.2 \text{ GPa}$.

A more recent shock compression study to 114 GPa was performed by Noguchi *et al* in 1996 [41]. The shock Hugoniot curve, after reduction to 293 K by way of the experimental Debye temperature and Grüneisen constant, indicates a structural transition at 90 GPa, with a volume change $\Delta V / V_T$ of approximately 8%. An EOS was obtained

which is in good agreement with the ultrasonic results of Webb *et al*, but is slightly more compressible than the static curve of Jeanloz and Rudy, with $K_0 = 151.6 \pm 0.2$ GPa and $K_0' = 3.6$. The volume change of $\sim 1\%$ associated with the magnetostrictive distortion was noted to be beyond the resolution achieved in the experiment. While the shock compression technique provides no structural information, this study concluded that the 90 GPa phase was of B2 type, since the combination of 90 GPa transition pressure and the radius of the Mn^{2+} radius lies on the extrapolated trend of B1 to B2 transition pressure to ionic radius established by the alkaline earth and TM monoxides. FeO, in contrast, lies well below the line, and indeed transforms to the B8 structure at 70 GPa.

In an attempt to clarify the high pressure phase diagram, Kondo *et al* in 1998 and 1999 conducted further static compression X-ray diffraction experiments to approximately 140 GPa [31,60]. A clear splitting of the cubic (220) line was observed for pressures above 35 GPa, indicating the onset of AF_2 order at room temperature and associated magnetostrictive distortion, as discussed earlier in Section 2(vii) of this chapter. This was verified by the observation that, under *in situ* laser heating of the sample to temperatures greater than T_N , the splitting disappears as the sample enters the paramagnetic state. The transition to the AF_2 state is shown to be second order by the continuous variation in d-spacings. The EOS obtained for the distorted B1 phase was found to be in better agreement with the earlier shock compression results of Noguchi *et al* than with the static results of Jeanloz and Rudy. The small discrepancy is explained by the strictly cubic symmetry assigned to the B1 phase at all pressures in the latter study. The fitted parameters of the third-order Birch-Murnaghan EOS were $V_0 = 21.956 \text{ \AA}^3$, $K_0 = 154 \pm 6$ GPa and $K_0' = 4.0 \pm 0.3$.

At 90 GPa, three definite, additional peaks indicate the presence of a new structural phase. A shoulder on the (102) distorted B1 peak is better resolved with increasing pressure. A volume change through the transition, $\Delta V / V_T$ of $\sim 1 - 2\%$ was found, in contrast to some 8% in the shock compression studies. Strong laser heating at the highest pressure attained (114 GPa) for this sample leaves the diffraction pattern unchanged, as

originating from a mixture of distorted B1, and the new 'intermediate' phase. Indexing of this new phase was attempted using two sets of data which comprised, firstly, all the observed lines and, secondly, only those lines deemed to originate from the new phase. In both cases the indexing failed, and it was concluded that a larger data set would be needed for effective analysis. It was tentatively suggested that the observed pattern might be produced by an orthorhombic structure. A metallic lustre of the intermediate phase was noted in optical observations by photomicrograph in the diamond anvil cell.

A second sample and separate instrument were used for a study to 137 GPa. At 126 GPa, new peaks emerge in the pattern and grow with increasing pressure. Indexing above this pressure yields a B8 structure, although one extra line at a d-spacing of 1.856\AA is present which Kondo *et al* attribute to the intermediate phase. One line which would be expected for the B8 structure was missing, although laser heating at 137 GPa produces a shoulder on one of the peaks around $d = 1.94\text{\AA}$ that the authors suggest lies in the correct range of angle. The B8 phase is only indexed over a pressure range of 11 GPa, and so no attempt to fit an EOS is made.

An infrared (IR) spectroscopy study of the pressure induced metallisation of semiconductors was conducted recently by Kobayashi [61]. Earlier Raman scattering measurements by the same worker and others [50] had demonstrated an abrupt downward shift in the 2TO phonon line at 30 GPa, which is attributed to the onset of AF_2 order. At 90 GPa, the Raman signal was observed to disappear over a large spectral range, which it is believed indicates an insulator-to-metal transition. The IR reflectance results show a steep rise at 90 GPa, although large variations in local pressure in the diamond anvil cell blurred the exact onset of the transition. Kobayashi links the metallisation in MnO to the magnetic collapse predicted to occur at 105 GPa from a knowledge both of the form of the Sugano-Tanabe diagram and the pressure dependence of the crystal field splitting and Racah B parameter from earlier optical absorption experiments.

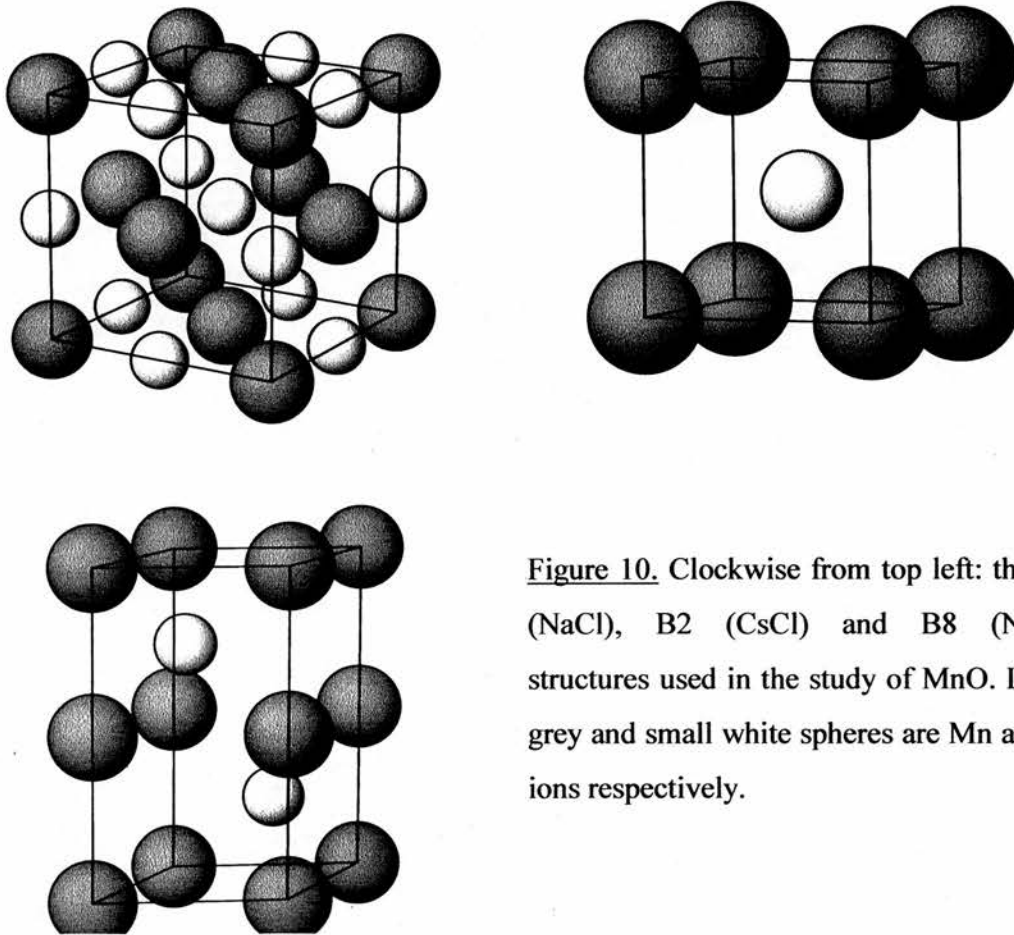


Figure 10. Clockwise from top left: the B1 (NaCl), B2 (CsCl) and B8 (NiAs) structures used in the study of MnO. Large grey and small white spheres are Mn and O ions respectively.

Prior theoretical work on the high pressure phase diagram of MnO is much more limited. Cohen *et al* in 1997 conducted a study of the magnetic properties at very high pressures of FeO, MnO, CoO, NiO and FeSiO₃ using both linear muffin-tin orbitals within the atomic sphere approximation and the linearised augmented plane wave method within the GGA [62]. A first-order high spin (HS) to low spin (LS) transition was predicted for MnO at 149 GPa with a fractional volume change across the transition $\Delta V / V_T$ of $\sim 5\%$, although a later publication by the same authors placed the transition at approximately 90 GPa [63]. Interestingly, the same workers find that the GGA predicts a HS to LS transition in FeO at 105 GPa, while LDA+U calculations place it at 320 GPa. The conflict was resolved by an X-ray emission spectroscopy study of FeO under pressure conducted by Badro *et al* [64]. In this experiment, the Fe $K\beta_{1,3}$ emission line is used, and the height of

the low energy satellite peak $K\beta'$ is monitored as pressure is varied. The $K\beta'$ line arises from the $3p$ core-hole $\rightarrow 3d$ exchange process, and any decrease in the moment on Fe would be signalled by a corresponding decrease in the height of this peak. The result of this study was that no evidence of a magnetic collapse is found to 143 GPa, in conflict with the GGA result of Cohen *et al.* The usefulness of the method is made clear by an identical study in FeS, which finds a magnetic collapse at 6.9 GPa, in good agreement with the transition from orthorhombic to monoclinic structure found by X-ray diffraction [65]. It seems clear, therefore, that LDA or GGA predictions of the onset pressures of HS to LS transitions should be treated with some scepticism.

Fang *et al* in 1998 [66] and 1999 [67] studied the phase stability of MnO and FeO under high pressure using the plane wave pseudopotential method within the GGA. The B1, B2 and B8 crystal structures, and the AF, FM and LS magnetic states are considered. The B1 AF_2 state is found to be insulating, whereas all the other magnetic and structural phases considered were metallic. At the equilibrium lattice constant, the Mn spin moment is found to be $4.5 \mu_B$. In the low pressure regime, the magnetostrictive compression of the cubic cell along the [111] direction is found. However, the distortion is too large, for a reduction in the c/a ratio of ~ 0.37 is found, whereas the experimental reduction is ~ 0.12 . The authors link this overestimate in size of the distortion to the large coupling constants found in GGA calculations, which matches with the results reported in Section 2(vii) of this chapter. Fang *et al* find that a low spin, metallic, rhombohedrally distorted B1 (LS rB1) structure becomes stable beyond 80 GPa. While local energy minima are found in both compressed and stretched modes of distortion, the stretched mode is favoured for all pressures. The authors link this structure to the phase transition found by Kondo *et al* at 90 GPa. There is strong experimental evidence for the presence of the B8 structure at pressures in excess of 100 GPa, but here Fang *et al* find a B1 \rightarrow B8 transition at a pressure of ~ 60 GPa, where the final state is metallic and antiferromagnetic. It should be noted that it is the normal B8 geometry that is favoured, i.e. Mn occupies the positions that Ni would in the prototypical NiAs structure, whereas in FeO, Fe occupies the As positions. It is clear that the transition pressure is much too low, but the authors

argue that the GGA cannot properly account for the correlations in the low pressure B1 phase, and that the real energy volume curve for B1 would therefore be lower than calculated. LDA+U calculations by the same workers do show a stabilisation of the AF₂ B1 phase relative to the LS rB1 and B8 phases.

Mackrodt *et al* in 1998 studied the properties of equilibrium and high pressure MnO within the UHF scheme, incorporating *a posteriori* correlation corrections via the PW-91 functional [68]. The B1, B2, B3 (zincblende-type), B4 (wurtzite-type) and B8 crystal structures were considered in this work, and all structural degrees of freedom were optimised at each volume. The conclusion of this study is that, from amongst those considered, the insulating B2 phase is the only candidate at high pressure. The B1 → B2 transition was found to occur at ~ 160 GPa from an extrapolation of the enthalpy – pressure curves. The application of *a posteriori* correlation correction reduces the transition pressure to ~ 149 GPa, but of course, the effect of correlation is not included within the SCF process. The paper contains a suggestion that the character of the valence band edge may change from O(p) to Mn(3d) at high pressure.

Now that a comprehensive overview of the current state of knowledge in MnO has been provided, the need for a hybrid study is clear. Pure GGA DFT can produce an insulating state within the B1 AF₂ structure, but the calculated transition to B8 is of the order of 66 GPa lower than experiment. In the associated material FeO, a HS to LS transition is predicted which is, at the very least ~ 40 GPa too low on the evidence of XES measurements. It was decided to determine whether the transition pressures emerging from pure DFT are constant with change in weight of exact exchange in the Becke-LYP scheme. The B1 AF₂, B2 AF₂, B8 AF, B1 LS $t_{2g}^3(\alpha)e_g^2(\beta)$ and B1 LS t_{2g}^5 crystal and electronic structures were considered. It was felt that the former 4-shell basis for O was not adequate for the description of a large range of atomic environments, and so one further optimised d-type polarisation shell with exponent 0.42 bohr⁻² was added. Convergence tests were carried out in the UHF method for a variety of structures at an

identical molecular volume of 21.7864\AA^3 , which is in the intermediate pressure regime for B1. Table 9 below presents the results of the convergence tests.

F_0	Structures	ΔE (Ha)
UHF	B1 AF ₂ ↔ B1 FM without O(d)	0.814×10^{-3}
	B1 AF ₂ ↔ B1 FM with O(d)	0.840×10^{-3}
	B1 AF ₂ ↔ B2 AF ₂ without O(d)	0.110383
	B1 AF ₂ ↔ B2 AF ₂ with O(d)	0.110675
	B1 AF ₂ ↔ B2 FM without O(d)	0.114451
	B1 AF ₂ ↔ B2 FM with O(d)	0.114775
0.0	B1 AF ₂ ↔ B1 FM without O(d)	13.264×10^{-3}
	B1 AF ₂ ↔ B1 FM with O(d)	13.134×10^{-3}
	B1 AF ₂ ↔ B2 AF ₂ without O(d)	0.071909
	B1 AF ₂ ↔ B2 AF ₂ with O(d)	0.072507

Table 9. The absolute total energy difference, ΔE (Ha) between different crystal and magnetic structures in the UHF and $F_0 = 0.0$ methods both with and without O(d) polarisation function.

After introduction of the polarisation function, the energy difference in Table 9 between the two magnetic states of the B1 cell varies by 0.036×10^{-3} Ha, or $\sim 3\%$. Between B1 AF₂ and B2 AF₂, the fractional energy change is much smaller at 0.3%, a value which is comparable to the fractional difference between B1 AF₂ and B2 FM. This would seem sensible, for the energy difference between different magnetic states is expected to be much smaller than that between structural phases. At $F_0 = 0.0$, the B2 FM structure is neglected, and the two remaining fractional changes are $\sim 1\%$ of the value computed without the O(d) shell. Energies are already well converged, but, to ensure high accuracy, the O(d) polarisation shell was retained in all subsequent calculations. A fuller treatment of the basis set would demand that the valence shells in O and Mn be optimised in the presence of the O(d) shell, but this has not been done here.

Convergence of the total energy with respect to density in reciprocal space sampling was also tested. The number of points along each axis of the reciprocal space grid is determined by the Monkhorst-Pack (MP) shrinking factor as discussed in Chapter 1, and the total energy of the B1 cell is monitored as the density of the \mathbf{k} -space mesh is increased. In the UHF method at the equilibrium molecular volume, an increase in MP shrinking factor from 8 to 10 made no difference to the total energy of the FM state to within 10^{-6} Ha. For the $F_0 = 0.0$ method at a molecular volume of $\sim 14.2 \text{ \AA}^3$ (or, at a pressure of ~ 130 GPa) the B1 AF_2 state is conducting and thus constitutes a particularly stringent test for \mathbf{k} -point sampling. An MP shrinking factor of 12 was found to converge the total energy to better than $0.1 \text{ mHa atom}^{-1}$. At $F_0 = 0.2$, the conducting B1 FM state was used at a molecular volume of $\sim 16.9 \text{ \AA}^3$. An MP shrinking factor of 8 was sufficient to converge the total energy to better than $0.1 \text{ mHa atom}^{-1}$.

The optimisation of the B8 c / a ratio for each cell volume at each weight of exact exchange is a large task, and so a more limited set of $F_0 = 0.0, 0.2, 0.4, 0.6, 0.8$ is chosen as this is deemed to cover the range quite well. The optimal ratio at each volume was determined by calculation of the total energy for twelve separate points of c / a , with six points lying below and five points above the UHF value. The resulting data was fitted by least squares fitting of a third order polynomial. Twelve volume points were considered at each value of F_0 , and the resulting energy volume data fitted to the Murnaghan EOS. Figure 11 below shows the variation in optimised c / a ratio with volume for all the Hamiltonians considered.

It is clear that the c / a ratio increases with pressure, with a gradient that decreases as F_0 is increased. The trend in the pure DFT curve is most dramatic, with an abrupt increase in c / a at the lowest volume for which the SCF process was convergent. The smoothness of the curves testifies to the adequacy of the numerical conditions used, and it is evident that as the weight of exact exchange increases, the curves approach a limiting form.

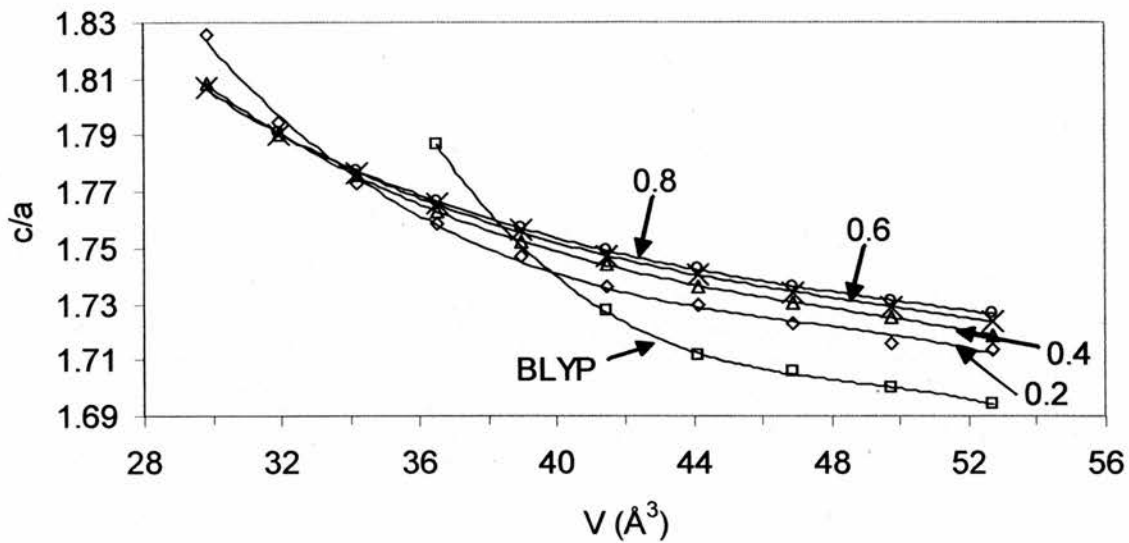


Figure 11. The variation in c/a ratio with volume, V (\AA^3) for the BLYP ($F_0 = 0.0$), $F_0 = 0.2, 0.4, 0.6$ and 0.8 Hamiltonians in the Becke-LYP scheme.

Now, from the energy-volume data for each phase the enthalpy, $H = E + PV$ can be calculated. In the athermal limit of the calculations, the enthalpy is equal to the free energy $G = H - TS$. The stable phase can then be predicted for any pressure as that which possesses the lowest free energy. Figure 12 below shows the relative enthalpy calculated for the labelled and B1 AF_2 phases as a function of pressure across the range of Hamiltonians.

(a) The High Pressure Phases at $F_0 = 0.0$ (pure BLYP DFT)

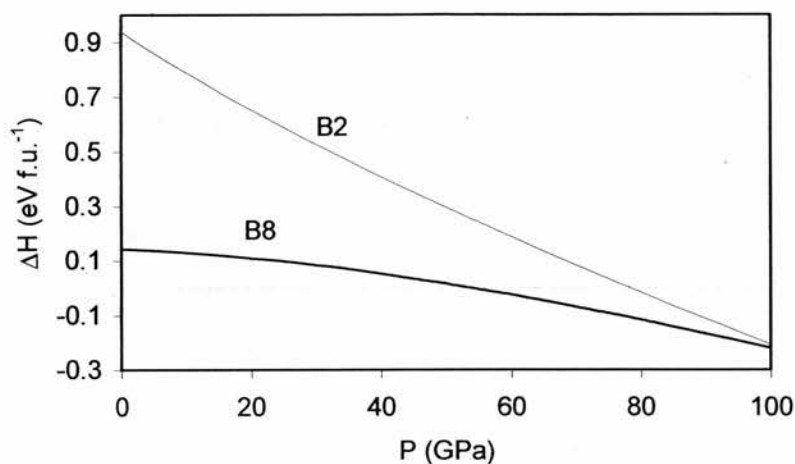


Figure 12(a). The variation in enthalpy differences relative to B1 AF₂ with pressure at $F_0 = 0.0$

For the $F_0 = 0.0$ Hamiltonian, the B1 LS $t_{2g}^3(\alpha)e_g^2(\beta)$ and B1 LS t_{2g}^5 states were not convergent in the SCF process. The B1 \rightarrow B8 and B1 \rightarrow B2 transitions at 54 and 78 GPa respectively match well with the values of 60 and 80 GPa reported by Fang *et al* [67] from their plane wave pseudopotential study. Table 10 below reports the EOS parameters of the various phases in the $F_0 = 0.0$ Hamiltonian. A comparison of the B1 bulk modulus with the value of 160.6 GPa quoted in Section 2(iv) reveals that the addition of the O(d) polarisation shell has softened the phase by ~ 6 GPa, which brings it into better agreement with the experimental range of 144 – 162 GPa. The lattice constant is reduced from 4.4742 Å without the O(d) shell to 4.4715 Å with it present, which represents a small fractional change of less than 0.1 %. The B2 and B8 phases have equilibrium molecular volumes which are ~ 2.5 Å³ and ~ 0.2 Å³ smaller than B1. It is the lower equilibrium energy of the B8 state, in combination with a low bulk modulus that leads to it being adopted as the next stable structure after B1 AF₂. The maximum pressures attained in all phases are low for pure DFT due to convergence problems in the compressed structures.

	ΔE_0	K_0	K_0'	V_0	P_{MAX}
B1 AF ₂	0	155.0	3.5928	22.351816	75
B2 AF	0.9387	175.3	3.6029	19.810475	65
B8 AF	0.1438	143.4	2.8873	22.179314	40

Table 10. The equilibrium energy per molecule relative to the B1 AF₂ state, ΔE_0 (eV f.u.⁻¹), bulk modulus, K_0 (GPa), pressure derivative of bulk modulus, K_0' , equilibrium volume per molecule, V_0 (Å³), and maximum pressure attained in simulation, P_{MAX} (GPa) for the listed phases of MnO at $F_0 = 0.0$ in the Becke-LYP scheme.

(b) The High Pressure Phases at $F_0 = 0.2$

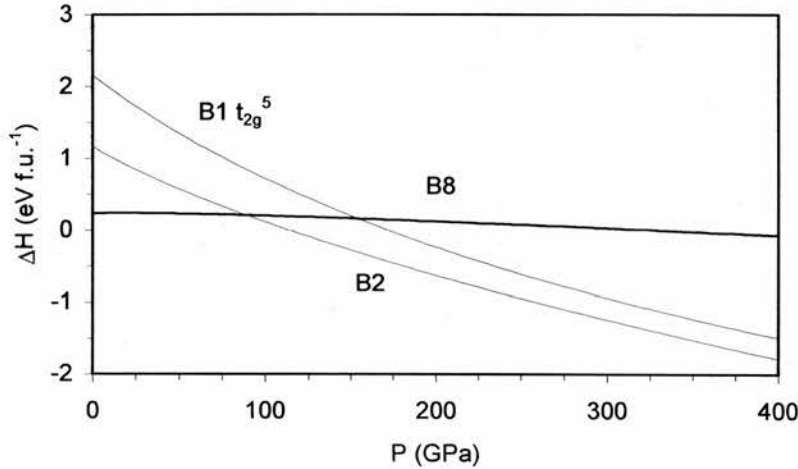


Figure 12(b). Enthalpy differences relative to B1 AF₂ against pressure at $F_0 = 0.2$

Only the B1 LS $t_{2g}^3(\alpha)e_g^2(\beta)$ state is unstable in this Hamiltonian, collapsing to the lower energy t_{2g}^5 state after the locking of eigenvalues is released. The picture in the present Hamiltonian, containing 20 % exact exchange, is quite different to that in the pure DFT case above. The B8 structure is shifted to higher equilibrium volume than B1, and upward in energy, so that the B2 phase remains the only candidate for stability at high pressure. The B1 \rightarrow B2, B1 \rightarrow B1 LS t_{2g}^5 and B1 \rightarrow B8 transition pressures are 114, 170 and 330 GPa respectively. Thus, for even this low content of exact exchange, the B8 transition pressure already exceeds the 126 GPa found in the experimental study by Kondo *et al.* Of

course, this transition pressure must be regarded as highly speculative, since, in the B8 phase, the last stable calculated point under compression lies much lower at 145 GPa. All that can be meaningfully said here is that the B1 \rightarrow B8 transition pressure for $F_0 = 0.2$ is not lower than ~ 150 GPa. The B2 transition pressure has also risen from the pure DFT value, albeit by a much more modest value of ~ 40 GPa. It should be noted that the presence of the O(d) polarisation shell has, once again, softened the B1 phase by ~ 3 GPa in comparison with the results of Section 2(iv).

The dramatic reduction in the equilibrium volume of the LS state is in qualitative agreement with the experimental ionic radii [69] presented in Chapter 1. The radius of the HS and LS Mn^{2+} ions are tabulated as being 97 and 81 pm respectively, and the O^{2-} ion as 126 pm. It would be expected, therefore, that the lattice constants of the HS and LS states would be 4.46 and 4.14 Å respectively. The lattice constants of the HS and LS states in the $F_0 = 0.2$ Hamiltonians are 4.4732 and 4.2653 Å respectively. The lattice in the LS state is too large relative to the value calculated from the radii, but the effect is qualitatively correct. The contraction in the Mn – O distance arises from the vacation of the Mn e_g orbitals, which are directed toward the nearest neighbour oxygen atoms. The lack of charge in the bonding directions permits the neighbouring oxygen atoms to approach the metal by a short way. It is of interest to note that the energy at equilibrium of the LS state is higher than the energies of all crystal structures in which the HS ground state of the Mn^{2+} ion is maintained. This seems at first sight surprising, but the on-site Coulomb interactions on the transition metal ions are very strong and would easily account for energy differences of this magnitude.

	ΔE_0	K_0	K_0'	V_0	P_{MAX}
B1 AF ₂	0	169.7	3.4442	22.377242	290
B2 AF	1.1631	185.7	3.5599	20.095529	160
B8 AF	0.2329	163.4	3.3848	22.444320	145
LS B1 t_{2g}^5 AF	2.1574	167.8	4.2374	19.399996	130

Table 11. As for Table 10, but at $F_0 = 0.2$ in the Becke-LYP scheme.

(c) The High Pressure Phases at $F_0 = 0.4$

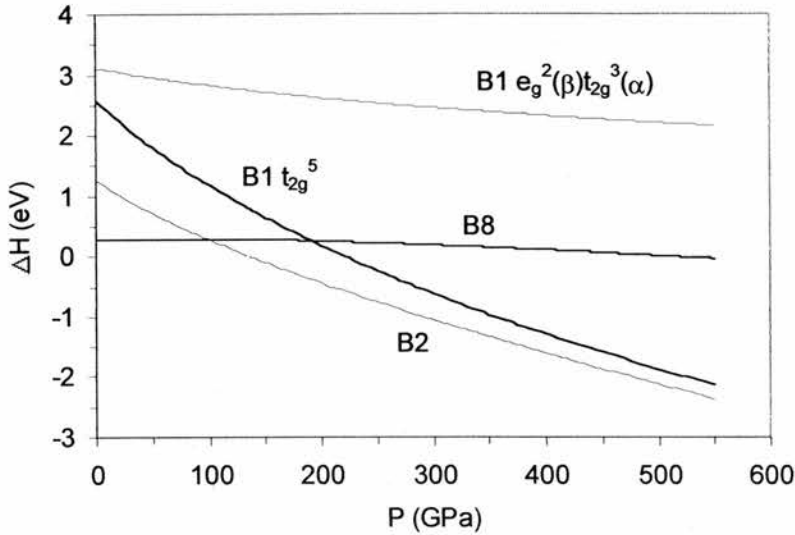


Figure 12(c). Enthalpy differences relative to B1 AF_2 against pressure at $F_0 = 0.4$

At $F_0 = 0.4$, the B1 LS $t_{2g}^3(\alpha)e_g^2(\beta)$ state becomes convergent. The picture revealed by Figure 12(c) is similar to that at $F_0 = 0.2$, save that the B1 \rightarrow B2, B1 \rightarrow B1 LS t_{2g}^5 and B1 \rightarrow B8 transition pressures have further increased to 136, 220 and 515 GPa respectively. In particular, given the maximum pressures reached as quoted in Table 12, the B8 transition must be regarded as extremely speculative, and, as for the case of $F_0 = 0.2$, all that can be meaningfully concluded is that the B8 transition in the $F_0 = 0.4$ method lies much higher than the 126 GPa found in experiment. The equilibrium volume of the B8 phase has increased relative to the B1 value in going from $F_0 = 0.2$ to the present. Again, the O(d) polarisation shell has lowered the bulk modulus of the B1 phase by ~ 6 GPa. The HS and LS t_{2g}^5 B1 lattice constants of 4.4634 and 4.2670 Å are essentially no closer to the values predicted from the ionic radii than at 20% exact exchange.

The EOS parameters for the LS $t_{2g}^3(\alpha)e_g^2(\beta)$ phase are interesting, for it would be anticipated that they will be similar to those for the B1 AF_2 phase, for the e_g orbitals remain occupied and the bonding interactions should be comparable. This expectation is borne out, as K_0 , K_0' and V_0 are all similar in the two states. The energy at equilibrium,

though, of the LS $t_{2g}^3(\alpha)e_g^2(\beta)$ phase is higher even than that of t_{2g}^5 , by an amount ~ 0.5 eV. An adequate explanation of this is provided by a Kanamori analysis of the two doublet states t_{2g}^5 and $t_{2g}^3(\alpha)e_g^2(\beta)$, which yields energies of $15B + 10C - 2\Delta_{CF}$ and $12B + 6C$ respectively. Now, the crystal field parameters derived from the optical absorption spectra in Section 2(viii) suggests that the $t_{2g}^3(\alpha)e_g^2(\beta)$ state should be higher than the t_{2g}^5 state by an amount $2\Delta_{CF} - (3B + 4C)$, or 0.51 eV which is very close to the calculated difference. Since the energies of two states with an equal number of spin pairs are being compared, the problems caused by a lack of pair correlation as discussed in Section 2(viii) do not arise here and the energy difference should be meaningful.

	ΔE_0	K_0	K_0'	V_0	P_{MAX}
B1 AF ₂	0	172.3	3.6228	22.229694	165
B2 AF	1.2718	192.0	3.6572	20.048422	120
B8 AF	0.2708	171.3	3.4771	22.336696	210
LS B1 t_{2g}^5 AF	2.5757	170.2	4.1705	19.421845	135
LS B1 $t_{2g}^3(\alpha)e_g^2(\beta)$ AF	3.1100	166.9	3.7670	21.724718	—

Table 12. As for Table 10, but at $F_0 = 0.4$ in the Becke-LYP scheme.

(d) The High Pressure Phases at $F_0 = 0.6$

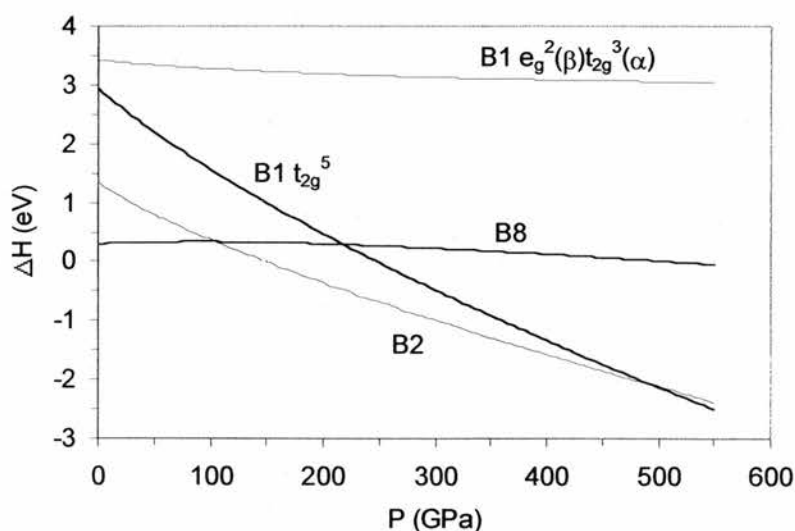


Figure 12(d). Enthalpy differences relative to B1 AF₂ against pressure at $F_0 = 0.6$

The situation at $F_0 = 0.6$ is very close to that described previously for $F_0 = 0.4$. The $B1 \rightarrow B2$ and $B1 \rightarrow B1$ LS t_{2g}^5 transition pressures have further increased to 147 and 247 GPa respectively, but the $B1 \rightarrow B8$ transition pressure has remained the same as that found in $F_0 = 0.4$ at 515 GPa. The values of ΔE_0 and K_0 for all states has increased, the quality of agreement between the LS t_{2g}^5 lattice constant and the value calculated from the ionic radii remains unchanged, and the $t_{2g}^3(\alpha)e_g^2(\beta)$ phase is still ~ 0.5 eV higher than the t_{2g}^5 phase in agreement with the Kanamori analysis. There is the possibility of a $B2 \rightarrow$ LS $B1$ t_{2g}^5 transition at a pressure at ~ 480 GPa, but this is an extrapolated behaviour and, again, must be considered extremely speculative.

	ΔE_0	K_0	K_0'	V_0	P_{MAX}
B1 AF ₂	0	177.5	3.7388	22.013898	120
B2 AF	1.3374	197.4	3.7219	19.908224	120
B8 AF	0.2965	177.3	3.5382	22.152575	210
LS B1 t_{2g}^5 AF	2.9356	172.3	3.9337	19.399840	85
LS B1 $t_{2g}^3(\alpha)e_g^2(\beta)$ AF	3.4259	178.6	3.8352	21.685647	—

Table 13. As for Table 10, but at $F_0 = 0.6$ in the Becke-LYP scheme

(e) The High Pressure Phases at $F_0 = 0.8$

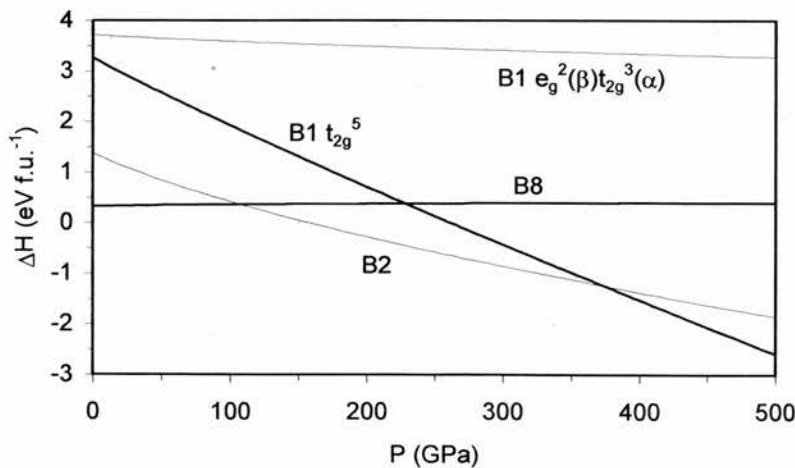


Figure 12(e). Enthalpy differences relative to B1 AF₂ against pressure at $F_0 = 0.8$

Again, the picture at $F_0 = 0.8$ is very similar to that at 60% exact exchange. The B1 \rightarrow B2 and B1 \rightarrow B1 LS t_{2g}^5 transition pressures have increased to 158 and 262 GPa respectively, while no transition to the B8 structure is predicted up to a maximum extrapolated pressure of 550 GPa. ΔE_0 and K_0 for all states has also increased relative to $F_0 = 0.6$, the quality of agreement between the LS t_{2g}^5 lattice constant and the value calculated from the ionic radii is degraded slightly, and the $t_{2g}^3(\alpha)e_g^2(\beta)$ phase is still ~ 0.45 eV higher than the t_{2g}^5 phase, which is still in reasonable agreement with the Kanamori analysis.

	ΔE_0	K_0	K_0'	V_0	P_{MAX}
B1 AF ₂	0	183.8	3.7788	21.782457	115
B2 AF	1.3802	203.6	3.8808	19.701969	80
B8 AF	0.3190	180.6	3.7684	21.909969	110
LS B1 t_{2g}^5 AF	3.2675	177.5	3.2596	19.414018	55
LS B1 $t_{2g}^3(\alpha)e_g^2(\beta)$ AF	3.7195	185.1	3.7980	21.514553	—

Table 14. As for Table 10, but at $F_0 = 0.8$ in the Becke-LYP scheme.

(f) Summary of High Pressure Simulations

The results above make clear that the observed transitions in MnO are a sensitive discriminator of performance of hybrid functionals. The B1 to B8 transition, found experimentally at a pressure of 126 GPa can be reproduced in the Becke-LYP scheme only by a content of exact exchange somewhere in the range 0 – 20 %. The transition from B1 to an unknown phase at 90 GPa is matched by hybrid calculations only at values of F_0 of 0.0 and 0.2, where the B1 \rightarrow B2 transition occurs at 78 and 114 GPa, which bracket the 90 GPa experimental value well. It must be assumed, though, that the X-ray diffraction study would have been able to index a straightforward B2 structure were it to occur. The energy difference in the Kanamori Hamiltonian between the B1 LS $t_{2g}^3(\alpha)e_g^2(\beta)$ and LS t_{2g}^5 states is well accounted for by hybrid Hamiltonians at all contents of exact exchange for which both LS states are stable. The reduction in lattice constant in the B1 LS t_{2g}^5 state is qualitatively explained by the experimental LS ionic

radii. The identity of the experimental phase at 90 GPa is not made any clearer by the current work, and a much more comprehensive study would need to be conducted.

(x) Conclusions

The work presented in this chapter constitutes a thorough study of the effect of varying content of exact exchange in density functionals upon the basic properties of MnO and NiO. Later, in Chapters 3 and 4, thorough studies of the effect of exact exchange upon the crystal field excitations and electronic defects respectively in NiO are presented. In view of the length of this chapter, it is appropriate to end with a summary of the principle conclusions.

(i) For the electronic structure of NiO in the PW91-PW91 scheme, a comparison of calculated magnetic moments for the AF₂ alignment with experimental values supports weights of exact exchange in a broad range $F_0 = 0.1 - 0.9$. The measured strong adsorption edge, at ~ 4 eV, if equated with calculated eigenvalue gaps, favours a weight in the range $F_0 = 0.1 - 0.2$. The experimental Fermi energy supports F_0 in the range $0.2 - 0.3$, where $F_0 = 0.2$ already leads to E_F in excellent agreement with experiment. The crossover from CT to MH insulating character occurs in the range $F_0 = 0.2 - 0.3$.

In the Becke-LYP scheme, the experimental spin moment supports a choice of F_0 in the broad range $0.1 - 1.0$, the experimental Fermi energy supports F_0 in the range $0.2 - 0.3$ and the experimental strong absorption supports $F_0 = 0.1 - 0.2$, and so all ranges are close to those found in the PW91 scheme. The transition to MH behaviour occurs in the region $F_0 = 0.1 - 0.2$. The VBE states are oxygen, mixed and metal derived for UHF, $F_0 = 0.2$ and pure DFT respectively, while the CBE states are oxygen, metal and metal derived respectively. Only in the pure DFT scheme, therefore, is the character of the insulating state clear.

(ii) For the electronic structure of MnO in the Becke-LYP scheme, the experimental spin moment supports a value of F_0 in a range 0.0 – 0.4, which is smaller than that found in NiO, and the experimental band gap supports a choice of F_0 in the range 0.1 – 0.2. In DOS plots, the VBE states are oxygen, mixed and metal derived for UHF, $F_0 = 0.2$ and pure DFT respectively, while the CBE states are oxygen, metal and metal derived respectively for the same choice of scheme. So, only at the pure DFT level is the character of the insulating state entirely clear. The oxygen derived nature of the CBE in UHF DOS plots does not agree with previous direct calculations of the electron addition state, which find a delocalised Mn character.

(iii) For NiO in the Becke-LYP scheme, the experimental lattice constant is reproduced by a value of F_0 in the range 0.9 – 1.0. No computed value for the bulk modulus of the AF_2 alignment falls within the range of experimental results, although both the pure DFT and UHF values are close to the upper extreme of that range.

(iv) In MnO, the experimental low temperature lattice constant is best matched by a choice of F_0 in the range 0.6 – 0.7 in the Becke-LYP scheme, while those arising within the Becke-no-LYP scheme are all higher than the experimental value. For the bulk modulus, only the $F_0 = 0.0$ value for K_0 in the Becke-LYP scheme falls within the experimental range, and is close to the uppermost extreme. The values arising from the uncorrelated functional match experiment in a broad range $0.1 \leq F_0 \leq 0.9$. A difficult situation arises in which the lattice constant and bulk modulus are better described by correlated and uncorrelated functionals respectively.

(v) A comparison of calculated magnetic coupling constants with experiment for NiO in the Becke-LYP scheme finds that values of $F_0 \geq 0.5$

lead to direct coupling constants in the experimental range, while a much narrower range of $0.2 \leq F_0 \leq 0.3$ leads to J_{se} and T_N in agreement with experiment. Thus, no common value of F_0 accurate for both types of coupling can be defined.

(vi) In MnO, for the Becke-LYP method, choices of F_0 in the range 0.1 – 0.2 and 0.5 – 0.6 reproduce the average experimental direct and superexchange coupling constants respectively, while agreement with the experimental critical temperature requires F_0 in the range 0.6 – 0.7. The uncorrelated Becke-no-LYP method yields agreement with experiment for F_0 in the ranges 0.0 – 0.1, 0.1 – 0.2 and 0.1 – 0.2 respectively. For the Bloch constant (which relates variation in J_{se} to variation in cell volume) F_0 in the Becke-LYP scheme in the range 0.1 – 0.2 brackets the proposed experimental value, while in the Becke-no-LYP scheme, the $F_0 = 0.0$ limit provides a value close to that observed. Alternatively, X-ray diffraction experiments have provided a direct measure of the pressure gradient of T_N , which is matched in the Becke-LYP scheme by F_0 in the range 0.1 to 0.2, and in the uncorrelated method by F_0 in the range 0.0 to 0.1.

(vii) For the magnetostrictive distortion in MnO in the Becke-LYP scheme, a weight of exact exchange in the range $0.1 \leq F_0 \leq 0.2$ yields a size of distortion angle in agreement with low temperature neutron scattering data. The weight of exact exchange matches that required to reproduce experimental values of J_d . At the UHF level, the distortion is predicted to be volume conserving.

(viii) The calculated energies for the 4P , 4G and 4S crystal field excitations in MnO are too high at the UHF level due to neglect of the pair correlation energy. At $F_0 = 1.0$ and 0.9 the excitations are still overestimated, while at $F_0 = 0.4$ they are underestimated. It appears that the optimal value for F_0 for

the $d \rightarrow d$ transitions in MnO is just greater than 0.4. The Racah B parameter is underestimated for all Hamiltonians, while the Racah C and crystal field parameters can apparently be systematically improved in regard to their agreement with experimental values by variation of F_0 .

(ix) The pressure at which the experimentally observed B1 to B8 structural transition occurs can be reproduced by a choice of F_0 in the narrow range 0.0 – 0.2. Higher contents of exact exchange grossly overestimate the critical pressure. The experimentally observed phase transition at 90 GPa cannot be satisfactorily explained by any hybrid Hamiltonian. The difference in energy between the two low spin states in the Kanamori Hamiltonian is in agreements with that emerging from first principles calculations.

3. References

- [1] S. Hüfner, *Adv. Phys.* **43**, 183 (1994)
- [2] B. H. Brandow, *Adv. Phys.* **26**, 651 (1977)
- [3] R. J. Powell and W. E. Spicer, *Phys. Rev. B* **2**, 2182 (1970)
- [4] K. Terakura, T. Oguchi, A. R. Williams and J. Kluber, *Phys. Rev. B* **30**, 4734 (1984)
- [5] T. C. Leung, C. T. Chan and B. N. Harmon, *Phys. Rev. B* **44**, 2923 (1991)
- [6] J. Zaanen, G. A. Sawatzky and J. W. Allen, *Phys. Rev. Lett.* **55**, 418 (1984)
- [7] W. C. Mackrodt, N. M. Harrison, V. R. Saunders, N. L. Allan and M. D. Towler, *Chem. Phys. Lett.* **250**, 66 (1996)
- [8] W. C. Mackrodt, *Ber Bunsenges. Phys. Chem.* **101**, 169 (1997)
- [9] P. Kuiper, G. Kruizinga, J. Ghijsen and G. A. Sawatzky, *Phys. Rev. Lett.* **62**, 221 (1989)
- [10] S. Hüfner, P. Steiner, I. Sander, F. Reinert, H. Schmitt, M. Neumann and S. Witzel, *Solid State Comm.* **80**, 869 (1991)

- [11] J. van Elp, B. G. Searle, G. A. Sawatzky and M. Sacchi, *Solid State Comm* **80**, 67 (1991)
- [12] J. van Elp, H. Eskes, P. Kuiper and G. A. Sawatzky, *Phys. Rev. B* **45**, 1612 (1992)
- [13] M. D. Towler, N. L. Allan, N. M. Harrison, V. R. Saunders, W. C. Mackrodt and E. Aprà, *Phys. Rev. B* **50**, 5041 (1994)
- [14] Z. Szotek, W. M. Temmerman and H. Winter, *Phys. Rev. B* **47**, 4029 (1993)
- [15] V. I. Anisimiv, J. Zaanen and O. K. Andersen, *Phys. Rev. B* **44**, 943 (1991)
- [16] S. Massidda, A. Continenza, M. Posternak and A. Baldereschi, *Phys. Rev. B* **55**, 13494 (1997)
- [17] T. Bredow and A. R. Gerson, *Phys. Rev. B* **61**, 5194 (2000)
- [18] I. de P. R. Moreira, F. Illas and R. L. Martin, *Phys. Rev. B* **65**, 155102 (2002)
- [19] J. van Elp, R. H. Potze, H. Eskes, R. Berger and G. A. Sawatzky, *Phys. Rev. B* **44**, 1530 (1991)
- [20] A. Svane and O. Gunnarsson, *Phys. Rev. Lett* **65**, 1148 (1990)
- [21] Z. Fang, I. V. Solovyev, H. Sawada and K. Terakura, *Phys. Rev. B* **59**, 762 (1999)
- [22] J. E. Pask, D. J. Singh, I. I. Mazin, C. S. Hellberg, and J. Kortus, *Phys. Rev. B* **64**, 024403-1 (2001)
- [23] W. C. Mackrodt and E.-A. Williamson, *J. Phys.: Condens. Matter* **9**, 6591 (1997)
- [24] L. C. Bartel and B. Morosin, *Phys. Rev. B* **3**, 1039 (1971)
- [25] B. E. F. Fender, A. J. Jacobson and F. A. Wedgewood, *J. Chem. Phys.* **48**, 990 (1968)
- [26] H. A. Alperin, *J. Phys. Soc. Jpn. Suppl. B* **17**, 12 (1962)
- [27] A. K. Cheetham and D. A. O. Hope, *Phys. Rev. B* **27**, 6964 (1983)
- [28] M. R. Notis, R. M. Spriggs and W. C. Hahn, *J. Appl. Phys.* **44**, 4165 (1973)
- [29] P. D. V. DuPleiss, S. J. Van Tonder, and L. Alberts, *J. Phys. C* **4**, 1983 (1971)
- [30] G. Witte, P. Senet and J. P. Toennies, *Phys. Rev. B* **58**, 13264 (1998)
- [31] T. Kondo, T. Yagi, Y. Syono, Y. Noguchi, T. Atou, T. Kikegawa and O. Shimomura, *J. App. Phys.* **87**, 4153 (2000)
- [32] P. A. Cox, *Transition Metal Oxides*, Clarendon Press, Oxford, 1995
- [33] J. Muscat, A. Wander and N. M. Harrison, *Chem. Phys. Lett.* **342**, 397 (2001)

- [34] F. D. Murnaghan, Proc. Natl. Acad. Sci. **30**, 244 (1944)
- [35] M. R. Notis, R. M. Spriggs and W. C. Hahn, J. Appl. Phys. **44**, 4165 (1973)
- [36] P. D. V. DuPleiss, S. J. Van Tonder, and L. Alberts, J. Phys. C **4**, 1983 (1971)
- [37] W. A. Harrison, *Electronic Structure and the Properties of Solids*, Dover, New York, 1989
- [38] R. L. Clendenen and H. G. Drickamer, J. Chem. Phys. **44**, 4223 (1966)
- [39] R. Jeanloz and A. Rudy, J. Geophys. Res. **92**, 11433 (1987)
- [40] S. L. Webb, I. Jackson and J. D. FitzGerald, Phy. Earth Planet. Inter. **52**, 117 (1988)
- [41] Y. Noguchi, K. Kusaba, K. Fukuoka and Y. Syono, Geophys. Res. Lett. **23**, 1469 (1996)
- [42] M. T. Hutchings and E. J. Samuelsen, Phys. Rev. B **6**, 3447 (1972)
- [43] R. Shanker and R. A. Singh, Phys. Rev. B **7**, 5000 (1973)
- [44] N. W. Ashcroft, N. D. Mermin, *Solid State Physics*, Harcourt Brace College, Fort Worth, 1976
- [45] M. E. Lines and E. D. Jones, Phys. Rev. **139**, A1313 (1965)
- [46] M. Kohgi, Y. Ishikawa and Y. Endoh, Solid State Commun. **11**, 391 (1972)
- [47] G. Pepy, J. Phys. Chem. Solids **35**, 433 (1974)
- [48] V. A. Sidorov, App. Phys. Lett. **72**, 2174 (1998)
- [49] H. Shaked, J. Faber Jr and R. L. Hitterman, Phys. Rev. B **38**, 11901 (1988)
- [50] Y. Mita, Y. Sakai, D. Izaki, M. Kobayashi, S. Endo and S. Mochizuki, Phys. Stat. Sol. (b) **223**, 247 (2001)
- [51] M. Kobayashi, T. Nakai, S. Mochizuki and N. Takayama, J. Phys. Chem. Solids **56**, 341 (1995)
- [52] S. M. Butorin, J.-H. Guo, M. Magnuson, P. Kuiper and J. Nordgren, Phys. Rev. B **54**, 4405 (1996)
- [53] S.-P. Jeng and V. E. Henrich, Solid State Commun. **82**, 879 (1992)
- [54] S. Sugano, Y. Tanabe and H. Kamimura, *Multiplets of Transition-Metal Ions in Crystals*, Academic Press, New York 1970
- [55] W. C. Mackrodt and C. Noguera, Surf. Sci. **457**, L386 (2000)

- [56] Y. Syono, T. Goto, J. Nakai and Y. Nakagawa, Proc. 4th International Conf. on High Pressure, *Special Issue Rev. Phys. Chem. Jpn*, 466 (1975)
- [57] D. Bloch, C. Vettier and P. Burlet, *Phys. Lett A* **75**, 301 (1980)
- [58] S. Tamura, *High Temp.- High Press.* **19**, 657 (1987)
- [59] S. L. Webb, I. Jackson and C. A. McCammon, *EOS Trans. AGU* **64**, 847 (1983)
- [60] T. Kondo, T. Yagi, Y. Syono, T. Kikegawa and O. Shimomura, *Rev. High Pressure Sci. Technol.* **7**, 148 (1998)
- [61] M. Kobayashi, *Phys. Stat. Sol (b)* **223**, 55 (2001)
- [62] R. E. Cohen, I. I. Mazin and D. G. Isaak, *Science* **275**, 654 (1997)
- [63] Private communication with Artem R. Oganov, University College London, April 2001
- [64] J. Badro, V. Struzhkin, J. Shu, R. Hemley, H. Mao, C. Kao, J. Rueff and G. Shen, *Phys. Rev. Lett.* **83**, 4101 (1999)
- [65] J. Rueff, C. Kao, V. Struzhkin, J. Badro, J. Shu, R. Hemley and H. Mao, *Phys. Rev. Lett.* **82**, 3284 (1999)
- [66] Z. Fang, K. Terakura, H. Sawada, T. Miyazaki and I. Solovyev, *Phys. Rev. Lett.* **81**, 1027 (1998)
- [67] Z. Fang, I. Solovyev, H. Sawada and K. Terakura, *Phys. Rev. B* **59**, 762 (1999)
- [68] W. C. Mackrodt, E.-A. Williamson, D. Williams and N. L. Allan, *Phil. Mag. B* **77**, 1063 (1998)
- [69] N. W. Alcock, *Bonding and Structure*, Ellis Horwood, 1990

Chapter 3

A Hybrid Hamiltonian Study of the Crystal Field Excitations in Bulk NiO

1. Introduction

As discussed in Chapter 1, at low energies, there are two different types of excitation in NiO of relevance to the present work. The first, and most widely studied, is the strong absorption in the range 3.0 – 4.5 eV [1], associated with cation to anion charge transfer [2-4]. The $d \rightarrow d$ excitations, which form the basis for the work of the current Chapter, occur below the CT threshold both within the bulk and at the surface of the crystal [3,5-12]. The latter are the lowest energy electronic excitations discovered thus far in NiO. They are of particular interest from a theoretical point of view, since the CT nature of the fundamental energy gap in NiO precludes any explanation of the $d \rightarrow d$ excitations in terms of the ground state distribution of one-electron energy levels. This conflict is yet another manifestation of the highly correlated nature of the electronic structure of NiO [13].

Two quite different approaches to the calculation of $d \rightarrow d$ excitation energies have been explored to circumvent this dilemma. The first, as outlined in section 1(ii) of Chapter 1, is based upon *ab initio* multi-reference CEPA [14] and CASSCF/CASPT2 [15,16] calculations of $(\text{NiO}_6)^{10-}$ clusters embedded in either a small array of optimised point charges or a larger array of formal ionic charges. Such calculations include a substantial proportion of the electron correlation, but neglect contributions from the extended lattice other than the electrostatic potential. The second is based on direct, periodic UHF calculations of the excited state [17-19], which neglect the electron correlation, but include all the effects of the extended lattice. Both sets of calculations give quantitative accounts of the three bulk and four (100) surface excitations in comparison with the full range of experimental spectra [3,5-12], with differences overall less than 0.4 eV and less

than 0.3 eV in the case of the direct calculations [17,19]. The study of excitations in the presence of electronic and lattice defects and different lattice spin alignments within the cluster approach requires large active spaces and is problematic. Such low symmetry arrangements are, however, easily accommodated within direct calculations based on periodic supercells, and thus it is this method which is used here.

Three important issues are addressed in the current study:

- (I) Can hybrid Hamiltonians be used to recover some of the correlation contribution to the excitation energy? For excitations from the high spin d^8 ground state, all one-electron excitations are of the type $d_\alpha^2 \rightarrow d_\beta^1$ and all two-electron excitations of the type $d_\alpha^2 d_\beta^2 \rightarrow d_\gamma^1 d_\delta^1$, where α, β, γ and δ each represent one of the five inequivalent d-states. Thus the leading order correlation contributions to the excitation energies are the differences in correlation energy between d_α^2 and d_β^2 for the one-electron excitation and between $d_\alpha^2 d_\beta^2$ and $d_\gamma^2 d_\delta^2$ for the two-electron excitations, namely the difference in the pair correlation energies of initial and final states. All reasonable estimates cannot see this amount to more than a few tenths of an eV, and this has indeed been found to be the case for both the bulk and (001) surface of NiO, for which (uncorrelated) UHF calculations are in agreement with the observed spectra to this order of accuracy [19]. It is of interest, therefore, to see whether hybrid calculations can improve on this, particularly in view of the apparent agreement between B3LYP and experimental band gaps of varying provenance [20]. Hybrid calculations have been examined previously in relation to the ground state properties of several systems [20-22], but not, to the best of the author's knowledge, for excitation energies.
- (II) To what extent are $d \rightarrow d$ excitation energies influenced by the spin alignment of the lattice and the interatomic spacing? Of course, both the predicted

magnetic coupling energies and lattice constant depend on the proportion of exact exchange in the hybrid Hamiltonian.

- (III) Finally, Racah and crystal-field parameters for the bulk lattice are obtained by mapping the ground and excited state energies onto the Kanamori Hamiltonian [23], as discussed in Chapter 1.

2. Theoretical and Computational Methods

Hybrid Hamiltonians

Hybrid Hamiltonians of the form discussed in Chapter 1 have been applied here in the range $0 \leq F_0 \leq 1$. Here, the same Becke-LYP combination is used, mixing the gradient-corrected LSDA exchange functional ($f_{\text{LSDA}}^x + 0.9\Delta f_{\text{B88}}^x$) with Fock exchange in the ratio $(1-F_0):F_0$ in an analogy of Becke's original three parameter formulation (which is obtained by setting $F_0=0.2$), and incorporating a correlation functional mixing Lee-Yang-Parr [24] and Vosko-Wilk-Nusair [25] contributions thus, $0.81f_{\text{LYP}}^c + 0.19f_{\text{VWN}}^c$.

Crystal Field and Magnetic Hamiltonians

The Kanamori crystal field Hamiltonian, \hat{H}_{CF} as discussed in Chapter 1 is applied here as a basis for mapping the energies of the $d \rightarrow d$ excitations. For the Ni^{2+} ion the energies of the crystal field states are,

$$\begin{aligned} E_{\text{ground}} &= E_{\text{CF}}^0 + 28A - 50B + 21C, \\ E_{xy \rightarrow z^2} &= E_{\text{CF}}^0 + 28A - 38B + 21C + \Delta_{\text{CF}}, \\ E_{xy \rightarrow x^2 - y^2} &= E_{\text{CF}}^0 + 28A - 50B + 21C + \Delta_{\text{CF}}, \\ E_{xz, yz \rightarrow z^2, x^2 - y^2} &= E_{\text{CF}}^0 + 28A - 47B + 21C + 2\Delta_{\text{CF}}, \end{aligned}$$

from which excitation energies are given simply as direct energy differences. It is of interest to note that the Racah A parameter is involved only in expressions for the energy to transfer an electron between metal sites, and the C parameter only in spin-forbidden excitations. Thus the energies of the excitations studied here contain only contributions from Δ_{CF} and B.

The expressions for the state energies and resulting excitation energies take no account of the spin alignment of the lattice. The AF₂ spin alignment in NiO consists of ferromagnetic {111} sheets of Ni²⁺ spins aligned antiferromagnetically in the <111> direction, and results from next-nearest-neighbour superexchange coupling, which depends on the $[t_{2g}(\uparrow)]^3[t_{2g}(\downarrow)]^3[e_g(\uparrow)]^2$ orbital occupancy of the ground state of the Ni²⁺ ion. It is clear, therefore, that changes in orbital occupancy resulting from d → d excitation change the stability of the AF₂ alignment leading to magnetic corrections to the excitation energy. The Ising Hamiltonian as presented in Chapter 1 can be used here to estimate the size of such corrections. Ground state values for J_d and J_{se} are extracted from the energies per molecule of the FM, AF₁ and AF₂ spin alignments, and the corrections are then estimated from these values.

It is straightforward to deduce that the superexchange contributions to the energies of the FM and AF₂ alignments change by -2J_{se}, and 2J_{se} respectively for excitations of the type $d_{t_{2g}} \rightarrow d_{z^2}$, which lead to double occupancy of the z² orbital, and by -4J_{se} and 4J_{se} for excitations of the type $d_{t_{2g}} \rightarrow d_{x^2-y^2}$, which lead to double occupancy of the x²-y² orbital. On the other hand, the unpaired t_{2g} spins resulting from d→d excitation cannot interact with the fully spin paired t_{2g} states on nearest neighbour metal sites. Thus, making the assumption that the e_g states on nn metal sites have negligible overlap, the direct exchange interaction does not contribute to the energies of crystal field excitations. Combining the Kanamori crystal-field and Ising spin Hamiltonians in this way leads to excitation energies in the AF₂ alignment which can be written as,

$$\begin{aligned}\Delta E_{xy \rightarrow z^2} &= 12B + \Delta_{CF} + 2J_{se}, \\ \Delta E_{xy \rightarrow x^2 - y^2} &= \Delta_{CF} + 4J_{se}, \\ \Delta E_{xz, yz \rightarrow z^2, x^2 - y^2} &= 3B + 2\Delta_{CF} + 6J_{se},\end{aligned}$$

and in the FM alignment as,

$$\begin{aligned}\Delta E_{xy \rightarrow z^2} &= 12B + \Delta_{CF} - 2J_{se}, \\ \Delta E_{xy \rightarrow x^2 - y^2} &= \Delta_{CF} - 4J_{se}, \\ \Delta E_{xz, yz \rightarrow z^2, x^2 - y^2} &= 3B + 2\Delta_{CF} - 6J_{se}.\end{aligned}$$

Computational Conditions

The hybrid DFT module of the CRYSTAL98 code [26] was used in this study, and, once again, open shell systems were treated by the Pople-Nesbet spin-unrestricted (UHF) procedure [27]. The nickel shells (functions) were of the type 1s(8) 2sp(6) 3sp(4) 4sp(1) 5sp(1) 3d(4) 4d(1) and oxygen of the type 1s(8)2sp(4)3sp(1)4sp(1). The basis set is identical to that used in Chapter 2. The auxiliary basis set for the fitting of the exchange-correlation potential consisted of, for Ni, 13 s-type functions with exponents in the range 0.1 – 4000.0, three p-type function with exponents in the range 0.3 – 0.9, one f-type function with exponent 0.8 and three g-type functions with exponents in the range 0.45 – 3.3, and for O, 14 s-type functions with exponents in the range 0.07 – 4000.0, and one p-type, one d-type and one f-type function, each with exponent 0.5. As before, a Monkhorst-Pack shrinking factor of 8 and truncation thresholds of 10^{-7} , 10^{-7} , 10^{-7} , 10^{-7} and 10^{-14} for the Coulomb and exchange series ensured convergence of the total UHF energies ≤ 0.1 meV, while SCF convergence thresholds were set to 10^{-7} a.u. for both eigenvalues and total energies. These tolerances are similar to those used for a wide range of previous calculations [17-19, 28-30]. Calculations were performed for the ferromagnetic (FM) and type-II (AF₂) spin alignments, in which the double primitive cell consists of ferromagnetic (111) planes of alternating spin in the [111] direction, where the Miller indices and crystal directions are for the conventional crystallographic cell. Excitation energies were obtained as the difference between the variationally minimised total energies of the ground and

excited states in 8-molecular supercells. Converged excited state solutions were obtained by shifting the Fock matrix eigenvalues corresponding to the desired unoccupied states upward in energy by 2 Ha for the first SCF cycle only. In cases of difficult convergence, the CRYSTAL98 code was modified to apply eigenvalue shifts throughout the SCF routine to completion, with the resulting constrained density matrix then being used to initialise a run omitting constraints from which the excited state total energy is taken.

3. Results

As reported previously in Chapter 2 of this work and elsewhere [28-30], at the UHF level of approximation and for the entire range of F_0 within the Becke-LYP hybrid scheme, the ground state of NiO is predicted to be largely ionic (q in the range 1.6—1.9 e for PW91 hybrids) and insulating, with a high spin $[t_{2g}(\uparrow)]^3[t_{2g}(\downarrow)]^3[e_g(\uparrow)]^2$ electron configuration and an AF₂ spin alignment of unpaired spins ($[e_g(\uparrow)]^2$) within the lattice. As noted again in Chapter 2, for proportions of exact exchange in excess of approximately 20% the filled-to-unfilled gap is of CT character, with a transition to MH behaviour at and below this value. This description of the electronic structure remains essentially the same in the FM spin alignment, except at the DFT limit where the spin-up and spin-down gaps are retained but the *net* filled-to-unfilled gap vanishes. As noted elsewhere [17-19], it is the strongly ionic nature of NiO and narrow d-band widths that lead to d→d excitations which are most appropriately viewed as strongly localised Frenkel excitons. All excitation energies lie well below the band gap

The spin-allowed, on-site d→d excitations in bulk NiO comprise two one-electron excitations, $t_{2g}^6 e_g^2 \rightarrow t_{2g}^5 e_g^3$, of ${}^3A_{2g} \rightarrow {}^3T_{2g}$ and ${}^3A_{2g} \rightarrow {}^3T_{1g}$ symmetry and a two-electron excitation, $t_{2g}^6 e_g^2 \rightarrow t_{2g}^4 e_g^4$, of ${}^3A_{2g} \rightarrow {}^3T_{1g}$ symmetry. In terms of the local orbitals used to construct the Bloch functions, the one-electron ${}^3T_{2g}$ and ${}^3T_{1g}$ excitations comprise the multiplet states $(d_{xy} \rightarrow d_{x^2-y^2}, d_{xz} \rightarrow d_{z^2}, d_{yz} \rightarrow d_{z^2})$ and $(d_{xy} \rightarrow d_{z^2}, d_{xz} \rightarrow d_{x^2-y^2}, d_{yz} \rightarrow d_{x^2-y^2})$ respectively, and the two-electron ${}^3T_{1g}$ excitation

comprises the single component, $d_{xz}/d_{yz} \rightarrow d_{z^2}/d_{x^2-y^2}$. As in previous studies [17-19], the calculations are for single determinant wavefunctions, with the one-electron excitations represented by the single components, $d_{xy} \rightarrow d_{x^2-y^2}$ and $d_{xy} \rightarrow d_{z^2}$. Formally, this is equivalent to taking one microstate as representative of the multiplet. While this is undoubtedly a crude approximation, it is justified by the fact that no multiplet splitting has been observed, and the variation in the reported energies is greater than the line widths of the individual reported absorptions. Tables 2 - 4 list the calculated energies of the one-electron $d_{xy} \rightarrow d_{x^2-y^2}$ and $d_{xy} \rightarrow d_{z^2}$ and two-electron $d_{xz}d_{yz} \rightarrow d_{z^2}d_{x^2-y^2}$ excitations as a function of F_0 for the AF₂ and FM spin alignments at the optimised lattice constants given in Table 1 and for the FM alignment at a fixed lattice constant of 4.2 Å. Also given are the energies obtained from optical [5,6] and EEL spectra [7-12].

$F_0(\%)$	a_0 (AF ₂)	a_0 (FM)
UHF	4.2589	4.2629
100	4.1658	4.1710
90	4.1732	4.1787
80	4.1804	4.1865
70	4.1871	4.1935
60	4.1942	4.2009
50	4.2015	4.2103
40	4.2072	4.2192
30	4.2120	4.2274
20	4.2158	4.2350
Expt.	4.1684 [28]	

Table 1. Calculated lattice constant, a_0 (Å), in the AF₂ spin alignment as a function of F_0

F ₀ (%)	AF ₂	FM	
	At a ₀ (AF ₂)	At a ₀ (FM)	At a ₀ = 4.2Å
UHF	0.773	0.744	0.813
100	0.891	0.848	0.817
90	0.895	0.853	0.822
80	0.900	0.849	0.840
70	0.902	0.848	0.846
60	0.914	0.857	0.857
50	0.959	0.862	0.867
40	0.952	0.862	0.897
30	0.983	0.878	0.899
20	—	0.902	0.944
Expt.	1.05 [7], 1.08 [6], 1.10 [8], 1.13 [5], 1.16 [3], 1.1 [9]		

Table 2. Calculated $xy \rightarrow x^2-y^2$ excitation energy (eV) as a function of F₀

F ₀ (%)	AF ₂	FM	
	At a ₀ (AF ₂)	At a ₀ (FM)	At a ₀ = 4.2Å
UHF	2.575	2.546	2.610
100	2.649	2.608	2.578
90	2.614	2.573	2.547
80	2.579	2.531	2.520
70	2.538	2.488	2.484
60	2.495	2.447	2.447
50	2.451	2.390	2.401
40	2.254	2.335	2.357
30	—	2.271	2.267
20	—	2.179	2.208
Expt	2.75[3], 2.8 [9], ~3 [7]		

Table 3. Calculated $xy \rightarrow z^2$ excitation energy (eV) as a function of F₀

F ₀ (%)	AF ₂	FM	
	At a ₀ (AF ₂)	At a ₀ (FM)	At a ₀ = 4.2Å
UHF	1.992	1.933	2.070
100	2.202	2.119	2.057
90	2.208	2.122	2.065
80	2.217	2.115	2.092
70	2.231	2.118	2.103
60	2.246	2.126	2.126
50	2.306	2.128	2.148
40	2.307	2.126	2.216
30	—	2.179	2.210
20	—	2.193	2.296
Expt	1.79[7], 1.86[6], 1.87[8], 1.95[5]		

Table 4. Calculated $xz, yz \rightarrow x^2-y^2, z^2$ excitation energy (eV) as a function of F₀

The results presented in Tables 2-4 for the Becke-LYP hybrid scheme indicate that 20% exact exchange appears to be the stability limit for all three excited states in both spin alignments, although this limit has not been pursued exhaustively. In such difficult cases, the maintenance of eigenvalue shifts to SCF completion results in sensible states, but unfortunately, these all collapse back to the ground state in subsequent runs with the shifts removed. It is clear that direct calculations based on the one-electron potentials considered here reproduce quantitatively the three most significant features of the d→d excitations in NiO. These are (i) the range in energy, which varies from ~ 1 eV to ~ 3eV, (ii) the order of the excitations, notably that the two-electron excitation, $d_{xz}d_{yz} \rightarrow d_{z^2}d_{x^2-y^2}$, is lower in energy than the one-electron excitation, $d_{xy} \rightarrow d_{z^2}$ and (iii) the large difference in energy of ~ 1.5 eV between the two one-electron excitations. It is also clear that the calculated excitation energies are sensitive to the proportion of exact exchange, to the spin alignment and to the lattice constant.

In a more detailed examination of the results, Table 2 shows that for calculations at the optimised lattice constants, the energy of the $d_{xy} \rightarrow d_{x^2-y^2}$ excitation increases from 0.89 eV (AF₂) and 0.85 eV (FM) at F₀ = 100% exact exchange to 0.98 eV (AF₂) and 0.88 eV (FM) at 20% exact exchange, compared with experimental values in the range 1.05–

1.16eV [3,5-9]. Thus, there is an evident improvement of 8% (AF₂) and 3% (FM) as the proportion of exact exchange is decreased from 100% to the stability limit of 20%. It is also evident that, in agreement with the prediction of the Ising Hamiltonian, the AF₂ excitation energy is higher than the FM, with the former closer to the experimental values. Calculated energies at a fixed lattice constant of 4.2 Å increase similarly as F₀ is decreased, with differences of ~ 3% from the values at the optimised constants in the FM alignment.

Table 3 shows that the improvement in the energy of the $d_{xy} \rightarrow d_{x^2-y^2}$ excitation as F₀ is decreased does not apply to the high energy $d_{xy} \rightarrow d_{z^2}$ excitation which decreases from 2.65 eV (AF₂) and 2.61 eV (FM) at the limit of 100% exact exchange to 2.25 eV at 40% and 2.18 eV at 20% exact exchange for the AF₂ and FM alignments respectively, compared with experimental values in the range ~ 2.75 – 3 eV [3,7,9]. For this excitation, there is instead a deterioration of 14% (AF₂) and 15% (FM) as the proportion of exact exchange is reduced to the stability limits of the two spin alignments. However, for all F₀ except 40% there is agreement with the order predicted from the Ising Hamiltonian, with the AF₂ energy higher than the FM, and closer to the experiment values, while differences in energy corresponding to fixed and optimised lattice constants for the FM alignment are similar to those noted above for $d_{xy} \rightarrow d_{x^2-y^2}$.

The calculated energies of the two-electron excitation, $d_{xz}/d_{yz} \rightarrow d_{z^2}/d_{x^2-y^2}$, are given in Table 4, where, at the optimised lattice constants, there is an increase in energy from 2.20 eV (AF₂) and 2.12 eV (FM) at F₀ = 100% to 2.31 eV at 40% exact and 2.29 eV at 20% exact exchange for the AF₂ and FM alignment respectively. These compare with experimental values in the range 1.79 – 1.95 eV [5-8]. As in the case of the $d_{xy} \rightarrow d_{z^2}$ excitation there is a deterioration of 4% (AF₂) and 3% (FM) in the calculated energy as F₀ is decreased from 100% exact exchange to the stability limits of the two alignments. However, there is an important differences between the calculated one- and two-electron excitation energies, namely that the former are underestimated whereas the

latter is overestimated in comparison with the experimental values. The order of the AF₂ and FM energies agrees with the prediction of the Ising model, with the AF₂ energy lying higher than the FM. In this case, though, this results in the FM energies lying closer to experimental values than AF₂. The sensitivity to the lattice constant is similar to the one-electron excitations.

Taken together, the results presented in Tables 2-4 for all three excitations suggest that energies based on 100% exact exchange, with and without (UHF) correlation, are closest to experiment and that density functional theory is unable to account for the small but subtle correlation corrections involved in d→d excitations, at least not in NiO. The small differences in energy between the d_{xy} → d_{x²-y²} excitation (which equals Δ_{CF}, after correction for magnetic effects) in the FM state at a = 4.2 Å and a_{opt} can be accounted for by the elementary crystal field theory, which gives an expression for the splitting energy of the form,

$$\Delta_{CF} = \frac{5Zq}{3a^5} \langle r^4 \rangle,$$

where Zq is the net charge on the oxygen ion (typically -2e), a is the Ni–O distance and $\langle r^4 \rangle$ denotes the expectation value. Now, for this excitation, a plot of $\log [E^{mc}(a_0) / E^{mc}(4.2)]$ against $\log [4.2 / a_0]$ for each value of F₀ is shown in Figure 1 below, where E^{mc} is the excitation energy corrected for magnetic effects. A fit to the data should yield a straight line with a gradient of five and intercept of zero if the crystal field theory is correct and if the factor Zq⟨r⁴⟩ is constant over the small change in Ni–O distance involved. It is, of course expected that this factor will vary for differing F₀. The data points are quite scattered, but a fitted line with gradient 5.488±0.437 and intercept 6.024×10⁻⁵±1.266×10⁻³ is obtained, and it may thus be concluded that the simple electrostatic model gives an adequate account of the sensitivity of the excitation to the lattice constant in the FM state.

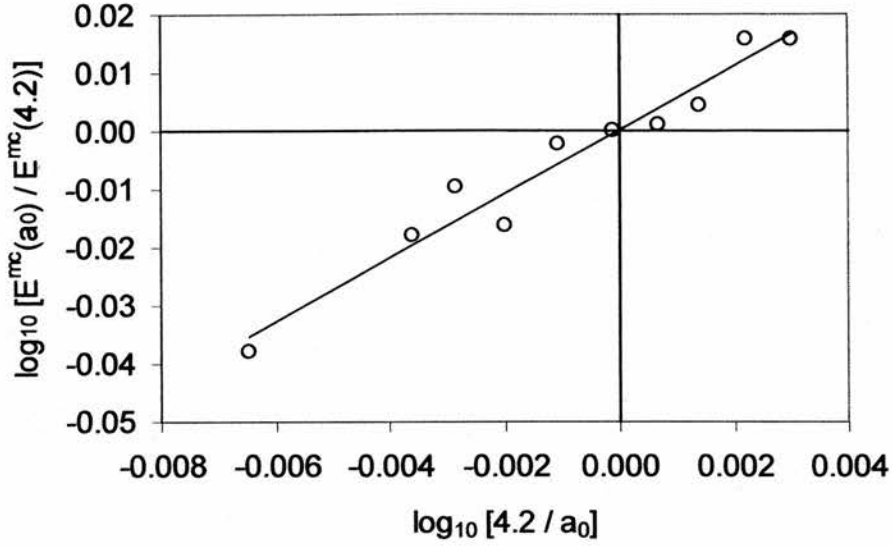


Figure 1. A plot of $\log_{10}[E^{mc}(a_0)/E^{mc}(4.2)]$ against $\log_{10}[4.2/a_0]$ for the ${}^3T_{2g}$ $d_{xy} \rightarrow d_{x^2-y^2}$ excitation at each value of F_0 . The straight line shows a linear fit.

Turning now to an analysis of the calculated excitation energies in terms of the combined Kanamori-Ising model, it is clear from the expressions given earlier in this chapter that values of B , Δ_{CF} and J_{se} can be obtained from the calculated excitation energies as a function of F_0 . However, a slightly different approach is used here which permits an examination of the validity and consistency of the model Hamiltonians in use. Firstly, values of J_{se} (and J_d) are derived from a mapping of the total ground state energies of the FM, AF_1 and AF_2 spin alignments onto the Ising Hamiltonian. Table 5 below lists these values (in K) along with the fluctuation corrected mean-field Néel temperature, T_N^{mf} , used here to gauge agreement with experiment. As earlier in Chapter 2, taking account of the fluctuation correction factor, the critical temperature is related to the superexchange coupling constant, J_{se} , by,

$$T_N^{mf} = \frac{9}{4} J_{se},$$

where J_{se} is in Kelvin. As noted previously [22], functionals containing ~20% proportion of exact exchange appear to yield the closest fit of calculated magnetic properties to experiment.

F_0	J_d	J_{se}	T_N^{mf}
UHF	8.601	39.556	89.00
100	9.366	56.918	128.07
90	9.912	63.298	142.42
80	10.736	70.674	159.02
70	11.691	80.339	180.76
60	13.881	95.065	213.90
50	15.879	114.719	258.12
40	18.804	141.972	319.44
30	22.668	186.187	418.92
20	28.542	248.948	560.13
10	36.392	353.586	795.57
DFT	85.175	670.744	1509.17
Expt	$<+16.2^{(1)}$	$+229.8$ $+197.28^{(1)}$	525

Table 5. Values of the magnetic coupling constants, J_d (K) and J_{se} (K) and the fluctuation corrected mean-field transition temperature, T_N^{mf} (K), obtained from the ground state total energies of the FM, AF₁ and AF₂ spin alignments in the Becke-LYP hybrid scheme.

The crystal-field parameter, Δ_{CF} , is now obtained from,

$$\Delta_{CF} = \Delta E_{xy \rightarrow x^2 - y^2} \pm 4J_{se},$$

and the Racah B parameter from,

$$B = \frac{1}{12} [\Delta E_{xy \rightarrow z^2} - \Delta_{CF} \pm 2J_{se}],$$

for the FM (+) and AF (-) alignments respectively. These values of J_{se} , Δ_{CF} and B can now be used to predict the energy of the two-electron excitation energy, $\Delta E_{xz, yz \rightarrow z^2, x^2 - y^2}$. In this way, the consistency of the model may be tested. Values of B,

Δ_{CF} and $\Delta E_{xz,yz \rightarrow z^2, x^2-y^2}$ obtained in this fashion are collected in Table 6 below, where the latter are compared with the directly calculated two-electron energies.

The crystal field splittings, Δ_{CF} , of 0.76 eV (UHF) and (0.87 - 0.92) eV for the hybrid calculations in the AF₂ alignment from Table 6 compare with values of 0.7 eV obtained from a combination of x-ray photoemission spectroscopy, bremsstrahlung isochromat spectroscopy and model-Hamiltonian cluster calculations [31] and a much lower value of 0.33 eV deduced previously from the UHF ground state DOS [28]. Only for values of F_0 less than 70% do the AF₂ and FM splittings begin to differ noticeably, with the FM values higher than AF₂ at 30% and 40% exact exchange. A comparison of optimised lattice constants does not account for this difference, since the FM lattice is more expanded than the AF₂ for all F_0 . In Figure 2 below, the variation in Δ_{CF} with F_0 is shown for fixed and optimised FM lattice constants, and it is noted that the splitting increases with decreasing exact exchange content for both cases. Lattice relaxation has had the effect of limiting the range of splitting energies that is established by change in F_0 alone in the fixed lattice. As discussed in Chapter 2, the ionicity of NiO falls as F_0 decreases, from $q = 1.860e$ within the PW91 hybrid scheme at 100% to $1.600e$ at 10%. In the simple crystal field model, it would be expected that this decrease in ionicity would lead to a decrease in the splitting energy. Instead, the opposite behaviour is found. This can be attributed to the effect of the increasing covalency in the Ni–O bond as F_0 is reduced. The crystal field theory lacks the metal–ligand overlap terms necessary to reproduce this increase in Δ_{CF} , but the more realistic ligand field theory should be able to account for it. Unfortunately, no simple expression linking the splitting energy to a parameter measuring covalency is known, but it is nevertheless clear that low content of exact exchange leads to a decreased localisation of charge at atomic sites and enhanced overlap.

Calculated Racah B parameters taken from Table 6 of 0.15 eV (UHF) and (0.15 – 0.11) eV for the hybrid method compare with a value of 0.13 eV deduced from the same combination of spectroscopic data and model calculations reported in Ref. [28]. The B parameter seems insensitive to the state of magnetic order for all F_0 above 40%, and, as

shown in Figure 2, is found to fall with decreasing F_0 . As for the crystal field splitting, it is the gradual increase in covalency that underlies this effect. The physical picture is of increasingly diffuse neighbouring oxygen orbitals penetrating the Ni site and partially screening the intra-atomic Coulomb interactions.

Finally, the differences between the Kanamori (fitted) and calculated excitation energies, $\Delta E_{xz,yz \rightarrow z^2, x^2-y^2}$, presented in Table 6 are found to be less than 0.08 eV for the full range of hybrid calculations and 0.005 eV at the UHF level of approximation. The close match of directly calculated and fitted results attests to the accuracy of the combined Kanamori-Ising Hamiltonian in describing the essential features of the crystal-field energetics in NiO.

F_0 (%)	Δ_{CF}			B		$\Delta E_{xz,yz \rightarrow z^2, x^2-y^2}$ (Kanamori)		$\Delta E_{xz,yz \rightarrow z^2, x^2-y^2}$ (calculated)	
	FM _{4.2}	FM	AF ₂	FM	AF ₂	FM	AF ₂	FM	AF ₂
UHF	0.827	0.757	0.760	0.150	0.150	1.938	1.997	1.933	1.992
100	0.837	0.868	0.871	0.147	0.147	2.136	2.220	2.119	2.202
90	0.844	0.874	0.873	0.143	0.143	2.135	2.220	2.122	2.208
80	0.864	0.874	0.876	0.140	0.140	2.119	2.220	2.115	2.217
70	0.874	0.875	0.875	0.137	0.136	2.105	2.214	2.118	2.231
60	0.890	0.890	0.882	0.133	0.132	2.112	2.224	2.126	2.246
50	0.907	0.902	0.920	0.127	0.124	2.106	2.292	2.128	2.306
40	0.946	0.911	0.903	0.123	0.109	2.093	2.229	2.126	2.307
30	0.963	0.942	0.919	0.116	—	2.104	—	2.179	—
20	1.030	0.987	—	0.107	—	2.123	—	2.193	—

Table 6. Values of the crystal-field splitting, Δ_{CF} (eV), and Racah B (eV) parameters and predicted, $\Delta E_{xz,yz \rightarrow z^2, x^2-y^2}$ (Kanamori) (eV), and directly calculated, $\Delta E_{xz,yz \rightarrow z^2, x^2-y^2}$ (calculated) (eV) two-electron excitation energies for the FM and AF₂ spin alignments at $a = 4.2\text{\AA}$ (for FM only) and the optimised lattice constants, $a_0(\text{opt})$.

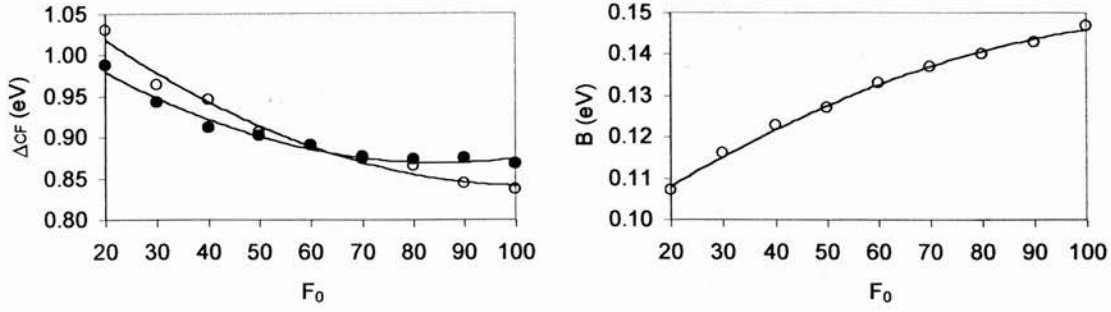


Figure 2. The FM crystal field splitting, Δ_{CF} (eV) both for the optimised lattice (●) and for a fixed lattice constant of 4.2Å (○), and the FM Racah B parameter (eV) for the optimised lattice as a function of proportion of exact exchange, F_0 (%).

However, as Table 7 below indicates, a much more demanding challenge is to predict the differences between the FM and AF₂ excitation energies by use of J_{se} determined within the ground state. The combined Kanamori-Ising model predicts differences of $8J_{se}$, $4J_{se}$ and $12J_{se}$ for the $xy \rightarrow x^2-y^2$, $xy \rightarrow z^2$ and $xz, yz \rightarrow z^2, x^2-y^2$ excitations respectively, and while the lowest energy excitation appears to be accounted for satisfactorily, the agreement for the higher energy excitations is somewhat wayward. The most likely reason for the discrepancy is a breakdown in the assumption inherent to the magnetic Hamiltonian, namely that the electronic structure of all states onto which it is mapped are identical, with differences in energy arising solely from the magnetic interactions. While this seems to hold for the low energy excitation, in the case of $xy \rightarrow z^2$ and $xz, yz \rightarrow z^2, x^2-y^2$, the ground and excited states may differ sufficiently that the effect is more apparent.

The direct approach to excitation energies as differences between ground and excited state total energies enables a straightforward decomposition of the total excitation energy into separate contributions. Recall that the calculated excitation energies of $\sim 1 - 3$ eV result from differences between much larger total energies of the order -3.5×10^5 eV, so that it is anticipated that the magnitudes of the separate contributions will be far in excess of the total excitation energy. Furthermore, the close, although not exact, adherence of the SCF energies to the Virial theorem might lead to the expectation that there are cancellations between the various large components.

F ₀ (%)	xy→x ² -y ²		xy→z ²		xz,yz→z ² ,x ² -y ²	
	Δ _{AF₂-FM}	8J _{se}	Δ _{AF₂-FM}	4J _{se}	Δ _{AF₂-FM}	12J _{se}
UHF	29.5	27.3	28.4	13.6	58.4	40.9
100	42.4	39.3	40.6	19.6	82.8	58.9
90	42.4	43.7	41.1	21.8	86.4	65.5
80	50.9	48.7	48.1	24.4	102.5	73.1
70	54.9	55.4	50.0	27.7	112.6	83.1
60	57.0	65.6	48.0	32.8	120.2	98.3
50	97.3	79.1	60.9	39.6	177.8	118.7
40	89.5	97.9	-80.8	49.0	180.5	146.9

Table 7. Comparisons of the calculated, Δ_{AF_2-FM} (meV), and theoretical, nJ_{se} (meV), AF₂-FM differences in excitation energy at the optimised lattice constants, a_0 (opt).

Table 8 below shows this decomposition of excitation energies calculated at the UHF level of approximation and those based on 50% exact exchange. The expectations for the breakdown are generally borne out. Thus for the $d_{xy} \rightarrow d_{x^2-y^2}$ excitation, for example, the UHF AF₂ kinetic energy (T) and electron-electron Coulomb (J) contributions of ~ 4 eV and ~ 5 eV respectively are nearly cancelled by the electron-nuclear (E-N) contribution of about -7.5 eV compared with the total excitation energy of ~ 0.8 eV. However, Table 8 does reveal some unexpectedly large differences in the component energies, notably between the three excitations. Thus the UHF FM value of E-N for the two-electron excitation, $d_{xz}/d_{yz} \rightarrow d_{z^2}/d_{x^2-y^2}$ at 1.93 eV is fifty times that for $d_{xy} \rightarrow d_{z^2}$ with an energy of 2.55 eV. There are also comparatively large differences between the decomposition of energy for the FM and AF₂ spin alignments, bearing in mind that the total energies are generally within 0.1 eV, and between UHF and 50% exact exchange T, J and E-N contributions in Table 8, given that the differences in the exchange energy are only a few tenths of an eV. The kinetic contribution, T, shows the most consistent trend, where the value of T for AF₂ is always greater than that for FM, and the UHF value is always greater than that for 50% exact exchange. In the $xy \rightarrow x^2-y^2$ and $xz,yz \rightarrow z^2,x^2-y^2$ excitations, the E-N and J contributions decrease with decreasing F₀,

but the opposite is true for the $xy \rightarrow z^2$ excitation. The exchange contributions are seen to be the most uniform, varying from +0.58 eV to -1.08 eV, but there is no trend evident for this contribution either with change of magnetic order or F_0 . The correlation contributions, C_{DFT} , all appear to be an order of magnitude too small, and make a negligible contribution to the excitation energies.

Exc.	F_0	Mag	E_{Total}	T	E-N	J	K_{exact}	K_{DFT}	K_{total}	C_{DFT}
$xy \rightarrow x^2-y^2$	UHF	AF ₂	0.773	4.141	-7.575	4.810	-0.604	—	-0.604	—
		FM	0.744	3.814	-7.140	4.595	-0.525	—	-0.525	—
	50%	AF ₂	0.959	4.868	-5.221	1.929	-0.403	-0.230	-0.633	0.016
		FM	0.862	4.191	-5.024	2.178	-0.289	-0.202	-0.491	0.008
$xy \rightarrow z^2$	UHF	AF ₂	2.575	1.687	-0.664	1.048	0.504	—	0.504	—
		FM	2.546	1.373	-0.242	0.839	0.576	—	0.576	—
	50%	AF ₂	2.427	3.348	-3.487	2.399	0.148	0.041	0.189	-0.022
		FM	2.390	2.479	-2.856	2.421	0.291	0.086	0.378	-0.032
$xz,yz \rightarrow x^2-y^2,z^2$	UHF	AF ₂	1.991	7.654	-13.099	8.379	-0.943	—	-0.943	—
		FM	1.933	7.005	-12.239	7.953	-0.787	—	-0.787	—
	50%	AF ₂	2.306	9.328	-8.606	2.653	-0.703	-0.377	-1.080	0.011
		FM	2.128	7.970	-8.282	3.219	-0.469	-0.304	-0.774	-0.005

Table 8. Decomposition of total excitation energies, E_{Total} (eV), into the kinetic energy, T, electron-nuclear, E-N, electron-electron Coulomb, J, exchange, K, and correlation, C_{DFT} , contributions

4. Discussion

To restate the aims of this study, crystal field excitations are a fundamental property of the rocksalt TMOs, and their measurement and calculation are important aspects of the physics of these systems. In the case of NiO both one- and two-electron spin allowed excitations [3,5-12] have been observed below the strong CT absorption edge [1,4]. Excitations from high spin d^8 (and d^9) ground state states are particularly interesting from a theoretical point of view, for all one-electron excitations are of the type $d_{\alpha}^2 d_{\beta}^1 \rightarrow d_{\alpha}^1 d_{\beta}^2$

and all two-electron excitations of the type $d_{\alpha}^2 d_{\beta}^2 d_{\gamma}^1 d_{\delta}^1 \rightarrow d_{\alpha}^1 d_{\beta}^1 d_{\gamma}^2 d_{\delta}^2$, where α , β , γ and δ label separate 3d states. Thus the leading order correlation contributions to the excitation energies are the differences in correlation energy between d_{α}^2 and d_{β}^2 for the one-electron excitation and between $d_{\alpha}^2 d_{\beta}^2$ and $d_{\gamma}^2 d_{\delta}^2$ for the two-electron excitations, and these cannot amount to more than a few tenths of an eV. CEPA [14] and CASSCF/CASPT2 [15,16] cluster calculations have confirmed this, and it has also been found to be the case for periodic lattice calculations of both the bulk and (001) surface of NiO [17-19]. Here, excitation energies generated by the uncorrelated UHF Hamiltonian match observed spectra to within this accuracy [17-19]. Thus one of the motivations of this study was to see whether hybrid calculations can improve on the performance of the UHF method, particularly in view of the putative agreement between the B3LYP energy gap and experimental band gaps of varying provenance [20].

While direct calculations clearly provide a useful, versatile and accurate approach to d→d excitation energies, it is instructive to see why such an approach is required. The 3d electrons in NiO are strongly correlated [13] and an important manifestation of this is that the position in energy of the d-states is directly dependent upon their occupation. It is clear, therefore, that since d→d excitations by their very nature change the occupation of the d-states, there must be an accompanying reordering of the states, which may or may not lead to a strong renormalisation of the energy. Following Brandow [32-34], and as shown previously for the ground state [28], it is straightforward to show that the Kanamori Hamiltonian leads to 3d-manifold energy levels for the ground and three d→d excited states of NiO of the form

Ground State

$$E[e_g(\uparrow)^2] = 7U' - 4J + \Delta_{CF}$$

$$E[t_{2g}(\uparrow)^3] = U + 6U' - 4J$$

$$E[t_{2g}(\downarrow)^3] = U + 6U' - 2J$$

$$E[e_g(\downarrow)^0] = U + 7U' - 3J + \Delta_{CF}$$

$$\underline{d_{xy} \rightarrow d_{x^2-y^2}}$$

$$E[xz(\uparrow)^1] = U + 6U' - 4J$$

$$E[xz(\downarrow)^1] = U + 6U' - 2J$$

$$E[yz(\uparrow)^1] = U + 6U' - 4J$$

$$E[yz(\downarrow)^1] = U + 6U' - 2J$$

$$E[xy(\uparrow)^1] = 7U' - 4J$$

$$E[x^2-y^2(\downarrow)^1] = U + 6U' - 2J + \Delta_{CF}$$

$$E[z^2(\uparrow)^1] = 7U' - 4J + \Delta_{CF}$$

$$E[xy(\downarrow)^0] = U + 7U' - 3J$$

$$E[x^2-y^2(\uparrow)^1] = U + 6U' - 4J + \Delta_{CF}$$

$$E[z^2(\downarrow)^0] = U + 7U' - 3J + \Delta_{CF}$$

$$\underline{d_{xy} \rightarrow d_{z^2}}$$

$$E[xz(\uparrow)^1] = U + 6U' - 4J$$

$$E[xz(\downarrow)^1] = U + 6U' - 2J$$

$$E[yz(\uparrow)^1] = U + 6U' - 4J$$

$$E[yz(\downarrow)^1] = U + 6U' - 2J$$

$$E[xy(\uparrow)^1] = 7U' - 4J$$

$$E[z^2(\downarrow)^1] = U + 6U' - 2J + \Delta_{CF}$$

$$E[z^2(\uparrow)^1] = U + 6U' - 4J + \Delta_{CF}$$

$$E[xy(\downarrow)^0] = U + 7U' - 3J$$

$$E[x^2-y^2(\uparrow)^1] = 7U' - 4J + \Delta_{CF}$$

$$E[x^2-y^2(\downarrow)^0] = U + 7U' - 3J + \Delta_{CF}$$

$$\underline{d_{xz}d_{yz} \rightarrow d_{z^2}d_{x^2-y^2}}$$

$$E[xz(\uparrow)^1] = 7U' - 4J$$

$$E[xy(\downarrow)^1] = U + 6U' - 2J$$

$$E[yz(\uparrow)^1] = 7U' - 4J$$

$$E[z^2(\downarrow)^1] = U + 6U' - 2J + \Delta_{CF}$$

$$E[xy(\uparrow)^1] = U + 6U' - 4J$$

$$E[x^2-y^2(\downarrow)^1] = U + 6U' - 2J + \Delta_{CF}$$

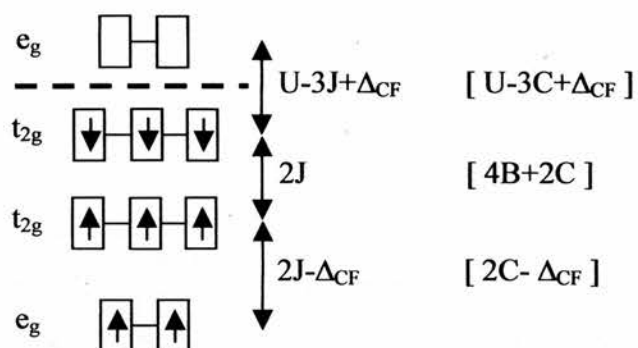
$$E[z^2(\uparrow)^1] = U + 6U' - 4J + \Delta_{CF}$$

$$E[xz(\downarrow)^0] = U + 7U' - 3J$$

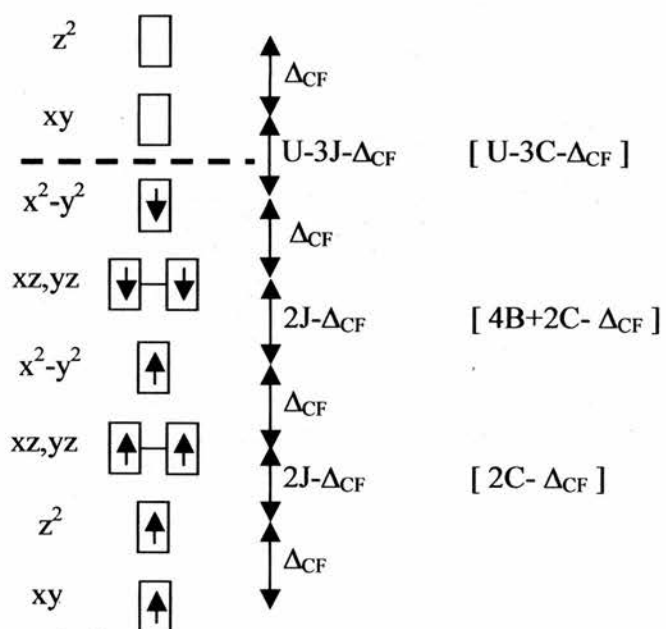
$$E[x^2-y^2(\uparrow)^1] = U + 6U' - 4J + \Delta_{CF}$$

$$E[yz(\downarrow)^0] = U + 7U' - 3J$$

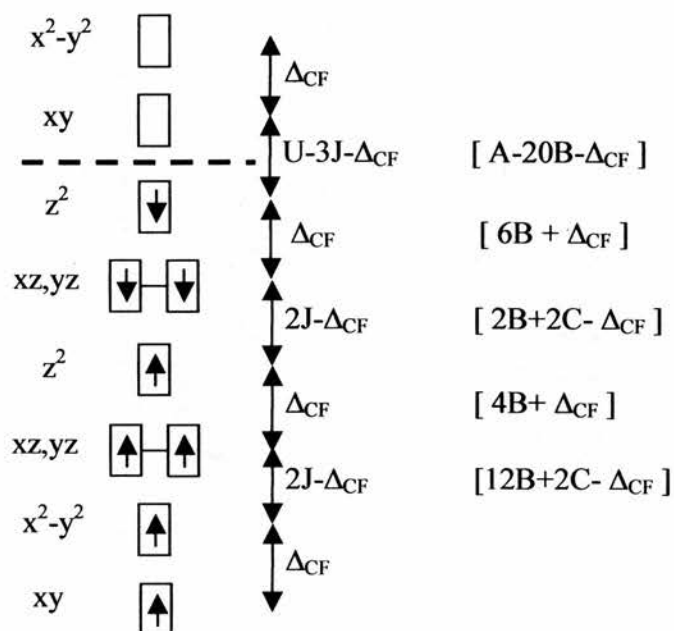
where it should be noted that the orbital averaged interband Coulomb, $U'=A-B+C$, and exchange, $J=(5/2)B+C$ interactions have been employed. This leads to the following order of the d-states, which are not drawn to scale.



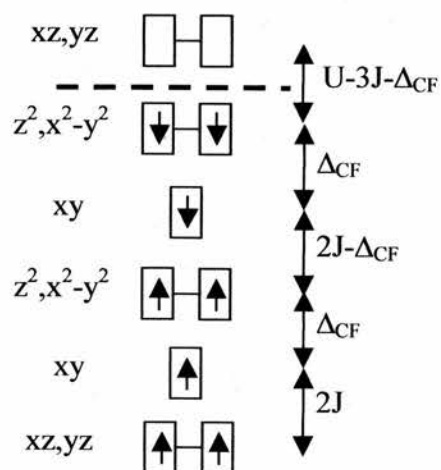
(a) Ground state, values in square brackets for orbital dependent U' and J .



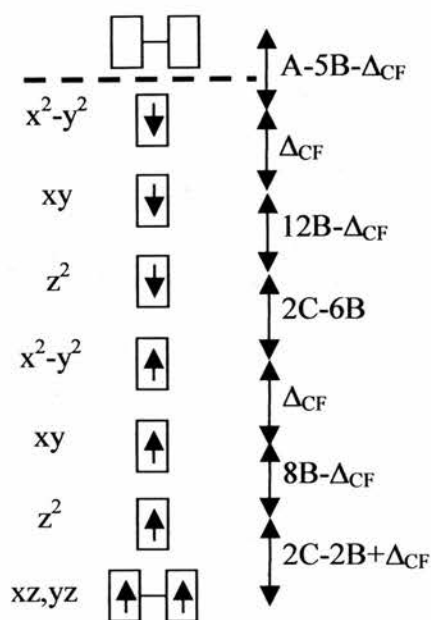
(b) $xy \rightarrow x^2-y^2$, values in square brackets for orbital dependent U' and J .



(c) $xy \rightarrow z^2$, values in square brackets for orbital dependent U' and J .



(d) $xz,yz \rightarrow z^2,x^2-y^2$, values for orbital averaged U' and J .



(e) $xz, yz \rightarrow z^2, x^2-y^2$, values for orbital dependent U' and J .

From this it is immediately evident that there is significant orbital reordering in the three excited states. This renders any type of rigid-band prediction of the spin-allowed $d \rightarrow d$ excitations from the ground state eigenvalues impossible. It is also clear that the much more complex analysis using orbital dependent Coulomb and exchange interactions is worthwhile, for it can make an appreciable difference to the predicted spectra. For example, in the ground state, the $e_g(\alpha)-t_{2g}(\alpha)$ gap would be overestimated by an energy of $2(J-C)$, amounting to $5B$ or 0.75eV in energy at the UHF level if the averaged interactions were used. The use of orbital dependent interactions alters some energy spacings, but the order of states remains unchanged, save in the spectrum of the two-particle excitation where the degeneracy of the e_g states is quite dramatically lifted by $8B$ and $12B$ for α and β spin respectively.

The UHF AF_2 DOS presented in Figure 3 below indicate that these theoretical predictions are supported by the calculated spectra, which show distributions of d -states which are similar to those derived from the Kanamori Hamiltonian. In addition to an explicit demonstration of the reordering of the d -states, Figure 3 indicates that $d \rightarrow d$ excitations also involve a strong renormalisation of the energies, for the rigid band estimates of these

energies are more than an order of magnitude greater than the directly calculated values and also greatly in excess of the band gap.

Estimates of the gaps between the centres of gravity (centroids) of the various bands in the ground and excited DOS of Figure 3 were made, so that the predicted energy splittings of the Kanamori Hamiltonian as presented above may be tested. For the AF_2 ground state, the $t_{2g}(\alpha) - t_{2g}(\beta)$ gap was estimated at $\sim 1.9\text{eV}$ from the DOS, compared with a predicted value of $4B+2C$. Taking $B = 0.15\text{ eV}$ for UHF AF_2 , an estimate of $\sim 0.65\text{eV}$ can be made for the Racah C parameter. Some support for this value is provided by the knowledge that the experimental free ion and theoretical UHF lattice values of the C parameter for the V^{2+} ion are essentially identical at 0.406 eV , as discussed in Chapter 5. Assuming the same scaling in Ni^{2+} , it would be expected that the UHF lattice value for C would be close to the experimental free ion value of 0.601 eV , lending some credibility to the crude value of 0.65 eV derived from the DOS above. It is also of interest to note that, for the V^{2+} ion, the ratio of the experimental free ion B parameter (0.094 eV) to the UHF lattice value (0.112 eV) at 0.84 is almost identical to the same ratio at 0.85 in Ni^{2+} with B parameters of 0.127 eV and 0.150 eV respectively. This would seem to establish that the scaling performed to arrive at a UHF lattice C parameter should be of some utility and accuracy. Now, the centroid of the $e_g(\alpha)$ band is found to lie $\sim 1.8\text{eV}$ below the centroid of the $t_{2g}(\alpha)$ band, as compared with a predicted splitting of $2C-\Delta_{CF}$, which can be estimated at $\sim 0.5\text{ eV}$ with C as derived earlier. It seems, therefore, that the e_g band has been shifted downward in energy by some 1.3 eV from its predicted position within the Brandow analysis, a stabilisation due presumably to the σ -bonding interaction with neighbouring ligand orbitals. It remains to be seen whether this shift is present in the excited states.

In the DOS of Figure 3 for the $AF_2\ xy \rightarrow x^2-y^2$ state, the general pattern of states established above is reproduced, although the e_g bands seem once again lowered with respect to their anticipated positions. The $z^2(\alpha)$ band is found to lie $\sim 0.5\text{ eV}$ below $xy(\alpha)$, whereas in the Brandow analysis it is positioned Δ_{CF} higher than the $xy(\alpha)$ state. This downward shift of $\sim 1.3\text{ eV}$ matches that discussed above for the ground state, and a

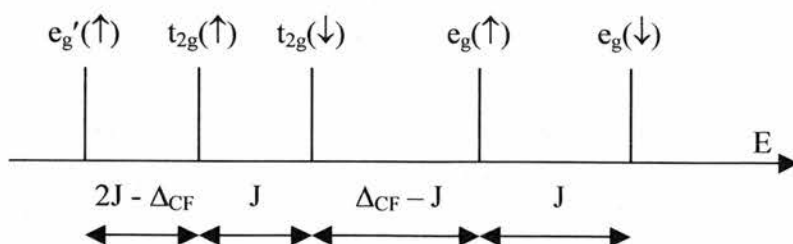
similar shift is evident in the $x^2-y^2(\alpha) - xz,yz(\alpha)$ and $x^2-y^2(\beta) - xz,yz(\beta)$ gaps. Other energy gaps seem to be accurately reproduced by the parameters derived in the ground state. For example, the $z^2(\alpha) - x^2-y^2(\alpha)$ gap of ~ 1.2 eV compares with a predicted value of $2C$, which amounts to ~ 1.3 eV. The $x^2-y^2(\alpha) - x^2-y^2(\beta)$ gap of ~ 2 eV compares with a predicted value of $4B+2C$, amounting to ~ 1.9 eV.

For the AF_2 $xy \rightarrow z^2$ state in Figure 3, the $x^2-y^2(\alpha)$ band lies below the $xy(\alpha)$ band by ~ 0.4 eV, whereas the prediction is that it should be positioned Δ_{CF} above. This apparent downward shift of ~ 1.2 eV again matches the 1.3 eV shift derived in the ground state. The $xz,yz(\alpha) - z^2(\alpha)$ gap is close to zero, which compares with a predicted interval of $4B+\Delta_{CF}$ or ~ 1.4 eV. Since this is close in size to the downward e_g shift, the bands appear as nearly superposed. The $xy(\alpha) - xz,yz(\alpha)$ gap is ~ 3.2 eV, which compares well with a predicted value of $12B+2C$, or ~ 3.1 eV, as does the $z^2(\alpha) - z^2(\beta)$ gap, measured at ~ 2.5 eV with a predicted value of $8B+2C$ or ~ 2.5 eV. The position of the $xz,yz(\beta)$ band seems to present a problem, in that its estimated centroid is higher than that of the $z^2(\beta)$ band by a few tenths of an eV, but the predicted gap is $6B+\Delta_{CF}$, which in combination with the e_g shift would be expected to leave the $z^2(\beta)$ band some 0.4eV higher than $xz,yz(\beta)$. The latter band is wider and more complex than the same in the previous two plots, and so estimation of the centroid is more difficult.

The ground state derived parameters are also predictive in determining the energy intervals of the two-particle $xz,yz \rightarrow z^2, x^2-y^2$ excitation. Here in Figure 3, the $xz,yz(\alpha) - z^2(\alpha)$ gap is of ~ 0.5 eV width, and compares well with a predicted value of $2C-2B+\Delta_{CF}$, or ~ 1.8 eV, providing the e_g stabilisation of 1.3 eV is applied. The $x^2-y^2(\alpha)$ band is found to lie ~ 0.6 eV below $xy(\alpha)$, whereas the prediction is that it will lie Δ_{CF} above. Again, the e_g shift of 1.3 eV brings them into agreement. The $xz,yz(\alpha) - xy(\alpha)$ gap is ~ 2.1 eV, with a predicted value of $6B+2C$ or ~ 2.2 eV, the $z^2(\alpha) - x^2-y^2(\alpha)$ gap is ~ 1.3 eV, with a prediction of $8B$, or ~ 1.2 eV and the $z^2(\alpha) - z^2(\beta)$ gap is ~ 1.7 eV, with a predicted value of $2B+2C$, or ~ 1.6 eV.

The UHF FM DOS plots for the ground and excited states are shown in Figure 4 below, the C parameter and e_g stabilisation will be obtained by the same analysis performed above for AF_2 . For the ground state, the $t_{2g}(\alpha) - t_{2g}(\beta)$ gap is of width ~ 2 eV, which establishes the FM value of the Racah C parameter at ~ 0.7 eV, close enough to the AF_2 value to be considered identical given the crudeness of the measurement. Now, the $e_g(\alpha)$ band is found to lie ~ 2 eV lower than the $t_{2g}(\alpha)$ band, with a predicted interval, $2C - \Delta_{CF} \sim 0.6$ eV in width. The downward e_g shift in the FM lattice is therefore ~ 1.4 eV, and is very close to the AF_2 value. The order in energy of the bands, established in AF_2 for the three excited states, is repeated here for the FM alignment. It can be concluded that the Brandow analysis of eigenvalues of the Kanamori Hamiltonian is a quick and accurate guide to the calculated spectrum of crystal field excitations, with the caveat that orbital dependent Coulomb and exchange interactions must be used.

The reordering of energy levels with changing occupation, and the consequences that follow from it, have repercussions for other excitations. While the CT nature of the gap in NiO would seem to preclude any attempts to rationalise the $d \rightarrow d$ excitations in terms of the ground state eigenvalues, quite apart from the problem of orbital reordering and the resulting renormalisation of the energies, it is widely accepted that the strong absorption at ~ 4 eV can be interpreted in terms of the filled-to-unfilled gap, specifically with the charge transfer, $O(p^6)Ni(d^8) \rightarrow O(p^5)Ni(d^9)$. However, since this involves a change in d-orbital occupation, a similar reordering of states might be expected. Writing the d^9 configuration as $d^9[(t_{2g})^6(e_g)^2(e_g')^1]$, a similar analysis to that given above shows that for $2J > \Delta_{CF} > J$, the orbital order is



This, again, is quite different to the ground state order, which calls into question the validity of interpreting the strong CT absorption in terms of the ground state filled-to-unfilled gap. Thus, once again, it would appear that the highly correlated nature of the d-states in NiO, precludes the straightforward interpretation of an excitation process in terms of the ground state eigenvalues.

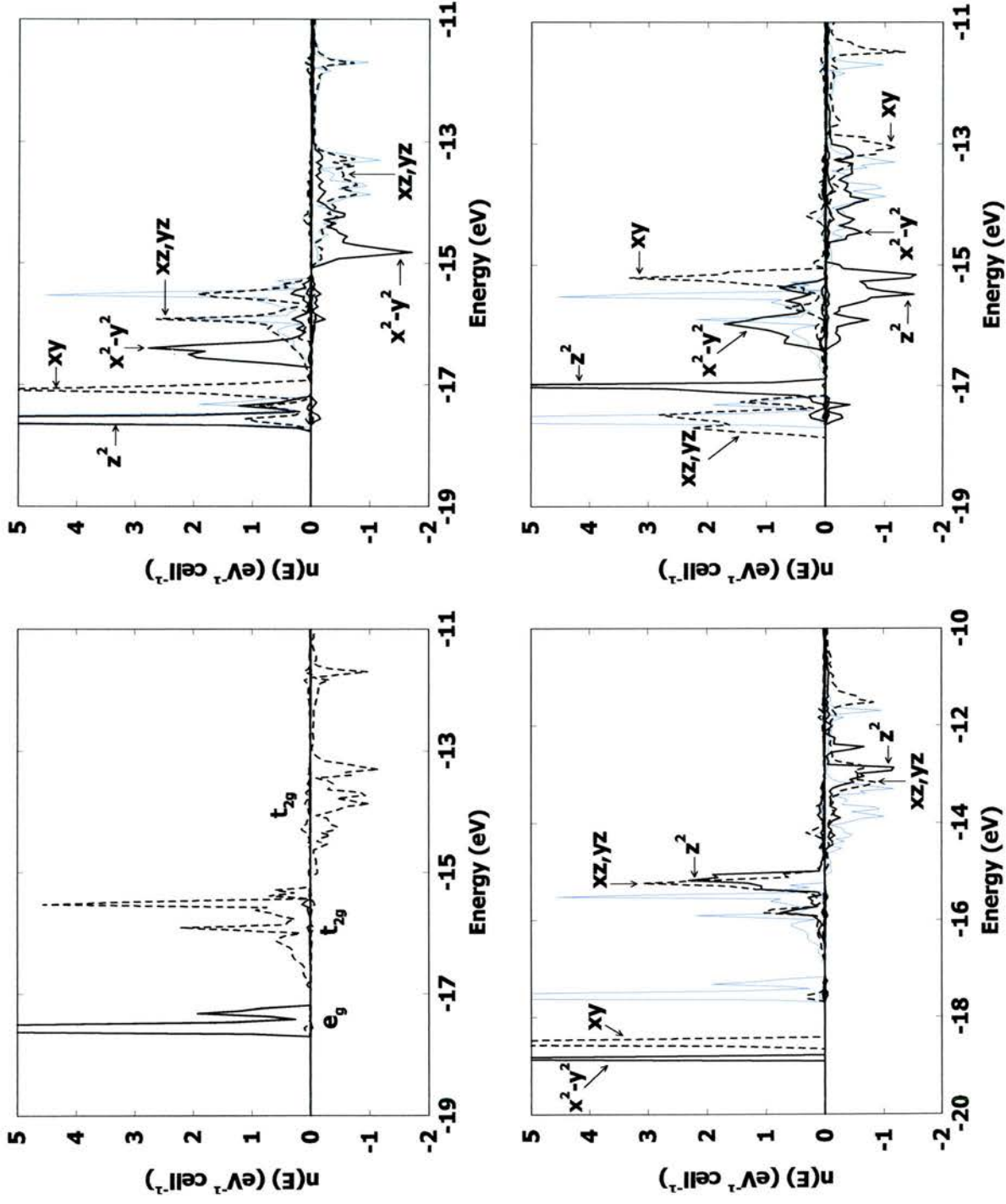


Figure 3. Orbital projected UHF AF₂ DOS for, clockwise from top left: ground state, $xy \rightarrow x^2-y^2$, $xy \rightarrow z^2$ and $xz,yz \rightarrow z^2, x^2-y^2$. Blue lines are ground state DOS. Solid line denotes e_g -type, dashed line denotes t_{2g} -type.

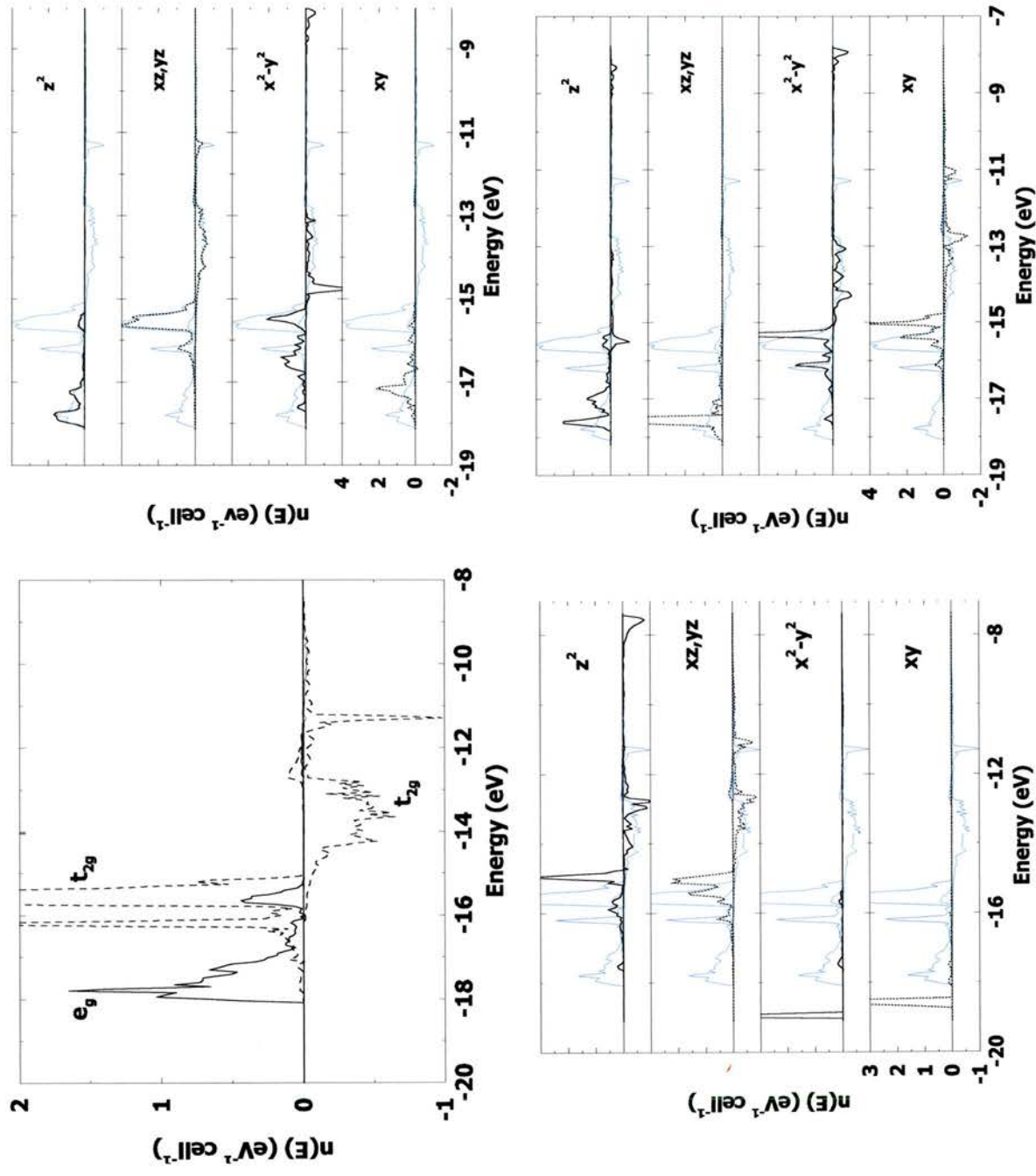


Figure 4. Orbital projected UHF FM DOS for, clockwise from top left: ground state, $xy \rightarrow x^2-y^2$, $xy \rightarrow z^2$ and $xz,yz \rightarrow z^2, x^2-y^2$. Blue lines are ground state DOS. Solid line denotes e_g -type, dashed line denotes t_{2g} -type.

5. Conclusions

The principal conclusion of this study is that, as suggested previously [17-19], direct calculations provide a useful approach to the calculation of crystal-field excitations in NiO and other strongly correlated TMOs [35]. Further important conclusions are that:

- (i) within the Becke-LYP scheme, at least, calculations at the limit of exact exchange lead to the most satisfactory overall agreement with the experimental spectra
- (ii) for the localised basis set used in this study the stability limit of the excited states is between 30% - 40% exact exchange for the AF₂ spin alignment and ~ 20% for the FM alignment
- (iii) a mapping of the crystal-field Hamiltonian suggested by Kanamori onto the directly calculated ground and excited state total energies leads to values of the crystal-field, Δ_{CF} , and the Racah B parameters which are close to those obtained previously from spectroscopic and theoretical studies
- (iv) the close agreement between the two-electron excitation energy obtained from the Kanamori Hamiltonian and that calculated directly attests to its validity
- (v) magnetic coupling constants obtained from a mapping of an Ising spin Hamiltonian onto ground state energies do not provide a quantitative guide to differences in energy between the AF₂ and FM spin alignments in the excited states

6. References

- [1] R. J. Powell and W. E. Spicer, Phys. Rev. B **2**, 2182 (1970)
- [2] P. Kuiper, G. Kruizinga, J. Ghijsen, G. A. Sawatzky and H. Verweij, Phys. Rev. Lett, **2**, 221 (1989)
- [3] S. Hüfner, P. Steiner, F. Reinert, H. Schmitt, and P. Sandl, Z. Phys. B **88**, 247 (1992)
- [4] A. Shukla, J-P. Rueff, J. Badro, G. Vanko, A. Mattila, F. M. F. de Groot and F. Sette, Phys. Rev. B **67**, 081101(R) (2003)

- [5] R. Newman and R. M. Chrenko, *Phys. Rev.* **114**, 1507 (1959)
- [6] V. Propach, D. Reinen, H. Drenkhahn and H. Müller Buschbaum, *Z. Naturforsch.* **33b**, 619 (1978)
- [7] P. A. Cox and A. A. Williams, *Surf. Sci.* **152**, 791 (1985)
- [8] A. Freitag, V. Staemmler, D. Cappus, C. A. Ventrice, K. Al Shamery, H. Kuhlenbeck and H.-J. Freund, *Chem. Phys. Lett.* **210**, 10 (1993)
- [9] B. Fromme, M. Schmitt, E. Kisker, A. Gorschlüter and H. Merz, *Phys. Rev. B* **50**, 1874 (1994)
- [10] B. Fromme, M. Möller, Th. Anschütz, C. Bethke and E. Kisker, *Phys. Rev. Lett.* **77**, 1548 (1996)
- [11] C. Xu, W. S. Oh, Q. Guo, and D. W. Goodman, *J. Vac. Sci. Technol A* **14**, 1395 (1996)
- [12] Q. Guo, C. Xu and D. W. Goodman, *Langmuir* **14**, 1371 (1998)
- [13] S. Hüfner, *Adv. Phys* **43**, 183 (1994)
- [14] A. Freitag, V. Staemmler, D. Cappus, C. A. Ventrice, K. Al Shamery, H. Kuhlenbeck and H.-J. Freund, *Chem. Phys. Lett.* **210**, 10 (1993)
- [15] C. de Graaf, R. Broer and W. C. Nieuwpoort, *Chem. Phys.* **208**, 35 (1996)
- [16] M. Geleijns, C. de Graaf, R. Broer and W. C. Nieuwpoort, *Surf. Sci.* **421**, 106 (1999)
- [17] W. C. Mackrodt, C. Noguera and N. L. Allan, *Faraday Discussions* **114**, 105 (1999)
- [18] C. Noguera and W. C. Mackrodt, *J. Physics: Condensed Matter* **12**, 2163 (2000)
- [19] W. C. Mackrodt and C. Noguera, *Surf. Sci.* **457**, L386 (2000)
- [20] J. Muscat, A. Wander and N. M. Harrison, *Chem. Phys. Lett.* **342**, 397 (2001)
- [21] T. Bredow and A. R. Gerson, *Phys. Rev. B* **61**, 5194 (2000)
- [22] I. de P. R. Moreira, F. Illas and R. L. Martin, *Phys. Rev. B* **65**, 155102 (2002)
- [23] J. Kanamori, *J. Phys. Chem. Solids* **10**, 87 (1959)
- [24] C. Lee, W. Yang and R. G. Parr, *Phys. Rev. B* **37**, 785 (1988)
- [25] S. H. Vosko, L. Wilk and M. Nusair, *Can. J. Phys.* **58**, 1200 (1980)

- [26] V. R. Saunders, R. Dovesi, C. Roetti, M. Causà, N. M. Harrison, R. Orlando and C. M. Zicovich-Wilson, *CRYSTAL 98, User's Manual* (Università di Torino, Torino, 1998)
- [27] J. A. Pople and R. K. Nesbet, *J. Chem. Phys.* **22**, 571 (1954)
- [28] M. D. Towler, N. L. Allan, N. M. Harrison, V. R. Saunders, W. C. Mackrodt and E. Aprá, *Phys. Rev. B* **50**, 5041 (1994)
- [29] M. D. Towler, N. L. Allan, N. M. Harrison, V. R. Saunders and W. C. Mackrodt, *J. Phys. C.: Condensed Matter* **7**, 6231 (1995)
- [30] W. C. Mackrodt, N. M. Harrison, V. R. Saunders, N. L. Allan and M. D. Towler, *Chem. Phys. Lett.* **250**, 66 (1996)
- [31] J. van Elp, H. Eskes, P. Kuiper and G. A. Sawatzky, *Phys. Rev. B* **45**, 1612 (1992)
- [32] B. Brandow, *Adv. Phys.* **24**, 651 (1977)
- [33] B. Brandow, in *Narrow-Band Phenomena – Influence of electrons with both bands and localised character*, edited J. C. Fuggle, G. A. Sawatzky and J. W. Allen (Plenum, New York, 1988)
- [34] B. Brandow, *J. Alloys Compounds* **181**, 377 (1992)
- [35] W. C. Mackrodt and H. J. Gotsis, *Phys. Rev. B* **62**, 10728 (2000)

Chapter 4

A Hybrid Hamiltonian Study of Hole States in Pure and Li-Doped NiO

1. Introduction

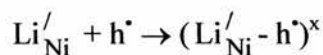
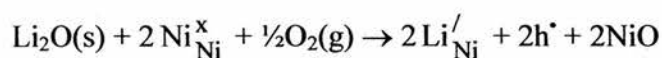
Little needs to be added here to the summary presented in Chapter 1 of the current experimental and theoretical knowledge of the electronic structure of NiO. However, it is worth re-emphasising that the oxygen K-edge spectra of Li-doped NiO ($\text{Li}_x\text{Ni}_{1-x}\text{O}$) in the range $0 \leq x \leq 0.5$ reveal $d^8\bar{L}$ holes in NiO, with empty O(p) states lying ~ 4 eV below the conduction band edge [1]. Importantly, these data also confirmed the insulating nature of the first ionised state within the specified range of stoichiometry. Subsequent spectroscopic studies have confirmed these observations, notably in respect of the lower energy of the $d^8\bar{L}$ state in $\text{Li}_x\text{Ni}_{1-x}\text{O}$ relative to d^7 [2-4]. All first principles calculations of NiO which include an orbital dependent potential by any appropriate means conclude that the ground electronic state is essentially CT insulating. A caution is appropriate here, for the calculated ground state electronic structure clearly provides important clues as to the nature of the ionised state, but the relaxation of the valence states that accompanies the removal of an electron cannot be accounted for in a quantitative way from the ground state.

The most straightforward approach which allows such changes to be included self-consistently is to calculate the electronic structure of the ionised state directly, that is to say, by direct variational minimisation of the total energy. Such calculations have been reported both for the bound hole in $\text{Li}_x\text{Ni}_{1-x}\text{O}$ (for stoichiometry $x = 0.25$ and 0.125) [5] and the free hole in NiO [6], but only at the UHF level of approximation. While these calculations have confirmed that both bound and free holes are essentially of $d^8\bar{L}$ character and that the overall states are insulating, UHF calculations neglect important aspects of electron correlation, which may have a significant effect on details of the hole state. These include the localisation energy, the differences between the (hole) charges and spin densities, the local magnetism and the higher energy states of the

hole. To gauge how these and other aspects of hole states might vary with the explicit, self-consistent inclusion of electron correlation, a hybrid scheme is applied to the single-particle description of the electronic structures of the Li-bound and free hole in NiO.

2. Defect states of $\text{Li}_x\text{Ni}_{1-x}\text{O}$

At ambient temperature and pressure, solid solutions of the type $\text{Li}_x\text{Ni}_{1-x}\text{O}$ are formed by the defect reactions



in Kröger-Vink notation [7], where $\text{Li}_{\text{Ni}}^{\prime}$ corresponds to an isolated Li substituent at a Ni site, h^{\bullet} to a free hole and $(\text{Li}_{\text{Ni}}^{\prime} - \text{h}^{\bullet})^{\times}$ to a bound hole nearest neighbour (nn) to $\text{Li}_{\text{Ni}}^{\prime}$. In this notation the superscripts /, •, and x correspond to net site charges of -1, +1 and 0 respectively, relative to the non-defective lattice. For present purposes, higher aggregates such as dipolar complexes formed from $(\text{Li}_{\text{Ni}}^{\prime} - \text{h}^{\bullet})^{\times}$ are neglected, so that the defect model for $\text{Li}_x\text{Ni}_{1-x}\text{O}$ consists of an NiO host lattice containing varying concentrations of $\text{Li}_{\text{Ni}}^{\prime}$, h^{\bullet} and $(\text{Li}_{\text{Ni}}^{\prime} - \text{h}^{\bullet})^{\times}$ defects, the associated electronic structures of which are the subject of this study. Lattice relaxation has been neglected throughout, largely because previous calculations [5,6] have suggested that the associated energies are small (a few tenths of an eV), and changes to the charge and spin distributions resulting from relaxation were found to be negligible.

Physically, doping NiO with Li^+ impurities creates an extrinsic semiconductor, in which the Li^+ sites deposit states in the band gap. Thermal excitation of electrons from the valence band to the vacancy states can occur, and it is possible that the resulting holes in the valence band could act as free carriers, if barriers to mobility including the holes' own polarisation field (the polaronic character) can be overcome. Hole states are also expected to be present in undoped NiO, as charge compensation for the small concentration of intrinsic Ni vacancies.

3. Hybrid Scheme and Computational Conditions

In this work, a hybrid based upon the Perdew-Wang [8-10] exchange and correlation functionals is used. As in Chapter 2, this is termed the PW91-PW91 scheme, with F_0 in the usual range 0 – 1. The Becke-LYP hybrid was used later to allow comparison of the results between different schemes. The hybrid module of the CRYSTAL98 code was used throughout, with a basis set for Ni of the type, 1s(8), 2sp(6), 3sp(4), 4sp(1), 5sp(1), 3d(4), 4d(1), and for O of the type 1s(8), 2sp(6), 3sp(4), 4sp(1). The basis set used is identical to that employed in the study of NiO in Chapter 2. The auxiliary basis used for fitting the exchange-correlation potential consisted of 14 s-functions with exponents in the range 0.1 – 6000.0, and one d- and one g-function, each with an exponent 0.5, and 3 f-functions with exponents in the range 0.5 – 6.0 for Ni and 14 s-functions with exponents in the range 0.07 – 4000.0, and one p-, one d- and one f-function, each with an exponent of 0.5 for O. A Monkhorst-Pack shrinking factor of 8 and truncation thresholds of 10^{-7} , 10^{-7} , 10^{-7} , 10^{-7} and 10^{-14} for the Coulomb and exchange series ensured convergence of the total UHF energies to ≤ 0.1 meV per molecule, while SCF convergence thresholds were set to 10^{-6} a.u. for both eigenvalues and total energies.

As on previous occasions [5,6], a supercell approach to the electronic structure associated with the point defects $\text{Li}_{\text{Ni}}^{\prime}$, h^{\bullet} and $(\text{Li}_{\text{Ni}}^{\prime} - \text{h}^{\bullet})^x$ is adopted, wherein multiple unit cells containing individual defects at concentrations of 1/2, 1/4 and 1/8 are used to construct the periodic lattice. Defect concentrations of 1/4 and 1/8 are well within the range of the oxygen K-edge and other spectroscopic data [1-4], while quadratic regressions based on these three concentrations allows rough estimates of the infinite dilution limit to be made. Two-, 4- and 8-fold unit cells with the ferromagnetic (FM) spin alignment and 8-fold cells with the antiferromagnetic (AF₂) alignment have been considered. Strictly speaking, the magnetic energy should be referenced to the paramagnetic state, but for convenience, the magnetic energy of an n-fold cell is defined as $n^{-1}[E(\text{FM}) - E(\text{AF}_2)]$, where this definition is applied both to the (non-defective) host lattice and to ionised states. Calculations have been carried out both at the full symmetry of the n-fold unit cell and in broken symmetry [5,6]. The latter does not involve any change in the physical structure of the lattice, but is simply a formal reduction in symmetry, which permits a localisation of the charge and net spin if this leads to a lowering of the total energy. The hole localisation

energy is defined simply as the difference in energy between the localised and delocalised states. For the charged defects, Li'_{Ni} and h^* , convergence of the Coulomb series demands that the lattice be immersed in a uniform charge compensating background [5,6]. Mulliken population analyses [11] of the crystalline orbitals were used to extract the net atomic charges, magnetic moments and individual orbital occupations as in previous studies.

4. Results

(i) Non-Defective NiO

The results for the NiO perfect lattice at the optimised lattice constants, in the PW91-PW91 scheme were presented in Chapter 2. Here, as earlier, a fixed lattice constant of 4.2 Å is used, which is close to the measured low temperature value of 4.1684 Å [12]. To summarise the results already obtained for the AF_2 state, in going from $F_0 = 1.0$ to 0.3 the Fermi energy, E_F , varies from -9.52eV to -5.02eV , the local spin moment from $1.92\mu_B$ to $1.76\mu_B$, the filled-to-unfilled energy gap from 14.2eV to 6.4eV and the weight of O(p) states at e_F from 92% to 71%. A transition from CT to MH insulating character was found between 30% and 20% exact exchange, and the system remains insulating in the AF_2 alignment at the DFT limit. In the FM alignment, there is no CT to MH insulator transition between 30% and 20% exact exchange. The magnetic energy, as defined above, varies quite considerably as a function of the proportion of exact exchange, ranging from 19.7 meV/Ni at the UHF limit to 277.7 meV/Ni for zero exact exchange. The closeness of calculated properties in the AF_2 and FM lattices permits the use of the computationally less expensive FM alignment in the following defect calculations.

Broadly speaking then, what might reasonably be deduced from the ground state electronic structure as to the nature of the first ionised, or hole state? Clearly the majority weight of oxygen states at the Fermi level from the UHF limit ($\sim 90\%$) down to 30% exact exchange ($\sim 70\%$) suggests holes of largely $d^8\bar{L}$ character. Mulliken charges and local moments suggest strong localisation in the limit of exact exchange, with decreasing localisation as the proportion of exact exchange is reduced. The increase in stability of the AF_2 state with decreasing exact exchange

also suggests strong retention of the spin alignment for lower values of the hybridisation parameter.

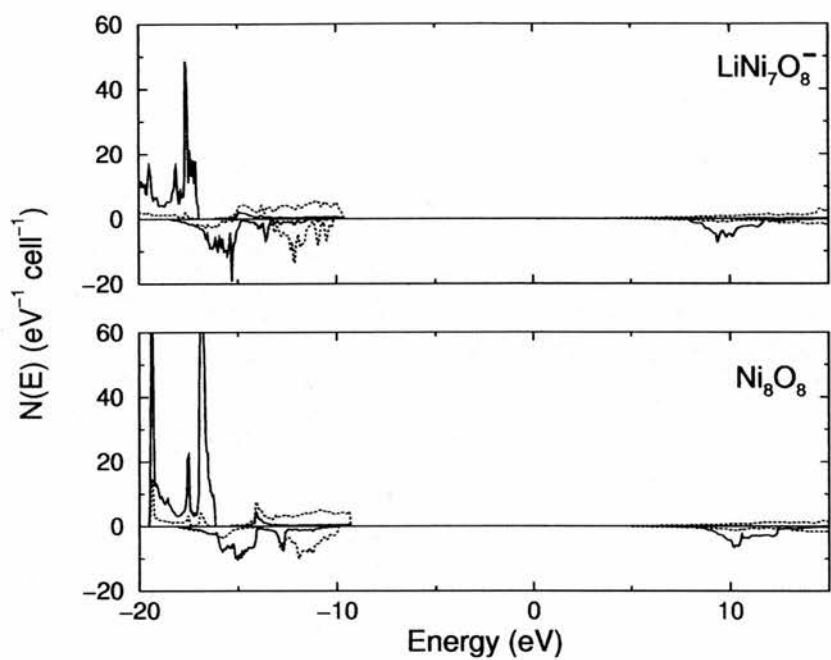
(ii) The Electronic Structure of $\text{Li}_{\text{Ni}}^{\prime}$

Calculations of the electronic structure of the uncompensated impurity defect, $\text{Li}_{\text{Ni}}^{\prime}$, were based on FM 8-fold unit cells containing a single Li^+ substituent at a cation site, which, for convenience, is referred to as $\text{LiNi}_7\text{O}_8^-$. The principal objective here was to examine the extent to which the electronic structure of the host lattice is perturbed by the presence of an uncompensated Li^+ impurity. As in the case of the non-defective host lattice, the electronic structure of $\text{LiNi}_7\text{O}_8^-$ is obtained by direct variational minimisation of the total energy of the 8-fold cell to self-consistency. Table 1 below presents the results.

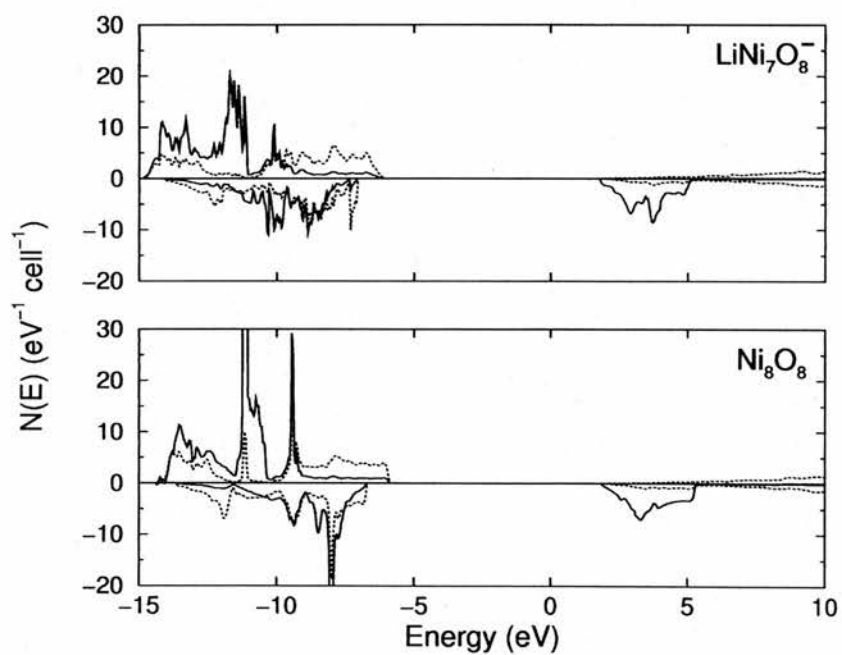
F_0	$E_F(\text{eV})$		$q_M(e)$		$n_s(\mu_B)$		$n_{e_F}^O(\%)$		$E_g(\text{eV})$	
	Li	Pure	Li	pure	Li	pure	Li	pure	Li	pure
UHF	-7.9	-7.7	1.86	1.87	1.92	1.93	86	86	14.2	14.2
1.0	-9.5	-9.3	1.86	1.88	1.92	1.92	85	87	13.9	14.0
0.9	-8.9	-8.6	1.85	1.87	1.91	1.92	85	85	12.7	12.7
0.8	-8.2	-7.9	1.84	1.86	1.90	1.92	83	85	11.5	11.5
0.7	-7.5	-7.2	1.83	1.85	1.88	1.89	83	82	10.3	10.3
0.6	-6.8	-6.5	1.81	1.83	1.87	1.88	80	80	9.2	9.0
0.5	-6.1	-5.8	1.79	1.81	1.84	1.86	78	77	8.0	8.0
0.4	-5.5	-5.6	1.76	1.78	1.81	1.83	75	74	6.9	6.8
0.3	-4.8	-5.0	1.73	1.75	1.78	1.79	70	70	5.7	5.5
0.2	-4.1	-4.4	1.69	1.71	1.73	1.75	65	64	4.5	4.4
0.1	-2.9	-3.0	1.64	1.65	1.66	1.68	55	57	3.2	3.2
0.0	-2.7	-	1.53	1.59	1.00	1.61	34	44	0.4	-

Table 1. Comparison of the Fermi energy, E_F , Mulliken charge of nn oxygen ions, q_M , local spin moments at nnn Ni sites, n_s , weight of oxygen states at the Fermi level, $n_{e_F}^O$, and energy gap, E_g for pure and Li-doped FM NiO ($\text{LiNi}_7\text{O}_8^-$) as a function of the hybridisation parameter, F_0 .

Figure 1 (a) and (b) below compares the valence and lower conduction band densities of states for both $F_0 = 1.0$ and $F_0 = 0.5$ respectively.



(a)



(b)

Figure 1. The valence and lower conduction band densities of states for the FM $\text{LiNi}_7\text{O}_8^-$ and FM Ni_8O_8 structures in the (a) 100% and (b) 50% hybrid schemes. Solid lines: Ni, dotted lines: O.

In both Table 1 and Figure 1, it is clear that, other than in the region of the DFT limit, the differences in the charge and spin distributions and single-particle energies are marginal. Furthermore, the effective charge of Li'_{Ni} remains close to $-e$ for the full range of hybridisation examined. This suggests that Li'_{Ni} behaves like an electronically inert entity with only a minor effect on the electronic, magnetic and excitonic properties of the host NiO lattice. It is reasonable to conclude, therefore, that the differences in the spectroscopic features of NiO and $\text{Li}_x\text{Ni}_{1-x}\text{O}$ highlighted by Kuiper et al [1] and later studies [2-4] do not relate to uncompensated Li'_{Ni} but to the presence of free and bound holes.

(iii) The Free Hole in NiO

The properties of the free hole are deduced from the self-consistent electronic structures of 2-, 4- and 8-fold unit cells from which a single electron has been removed. The corresponding hole concentrations are 0.5 / NiO, 0.25 / NiO and 0.125 / NiO respectively. Recall that the lattice is immersed in a uniform charge-neutralising background, which removes the Coulomb singularity, but has no effect on either the electronic charge ($\uparrow+\downarrow$) and spin ($\uparrow-\downarrow$) distributions or the differences in total energy between different states of the system with the same net charge. The primary interests here are the distribution of the hole charge between the cation and anion sublattices, the extent to which it is localised at one or more atomic sites, the different magnetic states of the hole and, importantly, whether the hole state is insulating or conducting. The hole charge and spin moment at a particular site are defined as the differences between the Mulliken values for the non-defective host lattice and the singly-charged lattices.

The first state considered is the hole in the FM lattice, for which there are four possible states corresponding to delocalised (d) and localised (l) charge and spin density with the unpaired electron spin (indicated as \uparrow or \downarrow) either ferromagnetic, $(\uparrow\uparrow)_d$ and $(\uparrow\uparrow)_l$, or antiferromagnetic, $(\uparrow\downarrow)_d$ and $(\uparrow\downarrow)_l$, to the lattice spin (indicated as \uparrow). The results of these calculations are presented in Table 2 (a-c). At the limit of 100% exact exchange, both with ($F_0 = 1.0$) and without (UHF) correlation, direct calculations for the three sizes of supercell indicate that, as reported

previously [6], in excess of 90% of the hole charge and spin are located on the anion sublattice, in accord with the CT character of the neutral ground state. For all three hole densities, the $(\uparrow\downarrow)$ spin configuration is more stable than $(\uparrow\uparrow)$. Calculations in broken symmetry lead to insulating states with substantial localisation of the hole charge on a single oxygen site, whereas calculations in the full symmetry of the respective supercells lead to conducting states of higher energy, in which the hole charge is delocalised over the anion lattice. Thus, at the UHF limit, the first ionised state of NiO is predicted to be essentially $d^8\bar{L}$ with a non-zero energy gap and the majority of the hole charge and spin localised at a single oxygen site. The four states, $(\uparrow\uparrow)_d$, $(\uparrow\uparrow)_l$, $(\uparrow\downarrow)_d$ and $(\uparrow\downarrow)_l$, have energies in the order, $E[(\uparrow\downarrow)_l] < E[(\uparrow\uparrow)_l] < E[(\uparrow\downarrow)_d] < E[(\uparrow\uparrow)_d]$. Now, as F_0 is reduced, two changes become evident in the electronic structure of the first ionised state.

- (i) The stability of the localised state, $(\uparrow\downarrow)_l$, increases relative to $(\uparrow\uparrow)_l$. The difference in energy between the two is the lowest lying excitation of the hole. This indicates a gradual increase in the effective antiferromagnetic coupling constant between the unpaired oxygen spin and the six surrounding metal spins.
- (ii) The localised hole charge and spin gradually reduce, and there is a decrease in the localisation energy down to $F_0 \sim 0.4$, at which point there is a transition of both $(\uparrow\downarrow)_l$ and $(\uparrow\uparrow)_l$ to conducting states. At this transition the differences in energy between $(\uparrow\downarrow)_l$ and $(\uparrow\uparrow)_l$ and $(\uparrow\downarrow)_d$ and $(\uparrow\uparrow)_d$ all fall to < 0.1 eV and the asymmetries in the charge and spin distributions associated with $(\uparrow\downarrow)_l$ and $(\uparrow\uparrow)_l$ disappear.

Since there is no evidence that $\text{Li}_x\text{Ni}_{1-x}\text{O}$ is conducting in the range, $0 \leq x \leq 0.5$, FM alignments at F_0 lower than 0.4 are not considered in this study. Full details of the energies of the $(\uparrow\uparrow)_l$, $(\uparrow\downarrow)_d$ and $(\uparrow\uparrow)_d$ states of 8-unit FM supercells relative to $(\uparrow\downarrow)_l$ as a function of F_0 are contained in Table 2(a) below, while Table 2(b) contains the local charge and spin of 2-, 4-, 8- and ∞ -unit FM $(\uparrow\downarrow)_l$ supercells, again as a function of F_0 . The extrapolated values for the infinite supercells, i.e. the isolated free hole, were obtained from quadratic regressions of the 2-, 4-, 8-unit supercell charges and spin moments as a function of n^{-1} . Finally, Table 2(c) presents a comparison of

localised hole charges and unpaired oxygen spin moments for 8-unit $(\uparrow\downarrow)_L$ and $(\uparrow\uparrow)_L$ FM supercells.

(a)				(c)				
F_0	$(\uparrow\uparrow)_L$	$(\uparrow\downarrow)_D$	$(\uparrow\uparrow)_D$	F_0	q_h		n_s	
					$(\uparrow\downarrow)_L$	$(\uparrow\uparrow)_L$	$(\uparrow\downarrow)_L$	$(\uparrow\uparrow)_L$
UHF	0.47	2.28	3.70	UHF	0.77	0.80	0.85	0.98
1.0	0.51	2.17	3.59	1.0	0.76	0.79	0.84	0.97
0.9	0.56	1.74	3.08	0.9	0.73	0.76	0.81	0.96
0.8	0.61	1.33	2.59	0.8	0.68	0.73	0.77	0.94
0.7	0.67	0.94	2.13	0.7	0.63	0.67	0.71	0.90
0.6	0.72	0.59	0.83	0.6	0.55	0.59	0.62	0.83
0.5	0.78	0.25	0.26	0.5	0.45	0.47	0.49	0.71
0.4	0.09	0.04	—	0.4	0.11 ^c	0.09	0.04 ^c	0.07

(b)								
F_0	2FM		4FM		8FM		∞ FM	
	q_h	n_s	q_h	n_s	q_h	n_s	q_h	n_s
UHF	0.85	0.88	0.81	0.87	0.77	0.85	0.71	0.82
1.0	0.84	0.87	0.80	0.86	0.76	0.84	0.70	0.80
0.9	0.82	0.85	0.78	0.84	0.73	0.81	0.65	0.76
0.8	0.80	0.82	0.75	0.81	0.68	0.77	0.59	0.70
0.7	0.76	0.78	0.71	0.77	0.63	0.71	0.51	0.61
0.6	0.72	0.73	0.65	0.71	0.55	0.62	0.40	0.48
0.5	0.66	0.67	0.58	0.62	0.45	0.49	0.27	0.30
0.4	0.47	0.39	0.20 ^c	0.09 ^c	0.11 ^c	0.04 ^c	0.05	0.06

Table 2. (a) Energies (eV) of 8-unit FM $(\uparrow\uparrow)_L$, $(\uparrow\downarrow)_D$ and $(\uparrow\uparrow)_D$ cells relative to $(\uparrow\downarrow)_L$ as a function of F_0 , (b) Comparison of localised hole charges, $q_h(e)$, and spin moments, $n_s(\mu_B)$, of 2-, 4-, 8- and ∞ -unit FM $(\uparrow\downarrow)_L$ cells as a function of F_0 , (c) Comparison of localised hole charges, $q_h(e)$, and unpaired oxygen spin moments, $n_s(\mu_B)$, of 8-unit FM $(\uparrow\downarrow)_L$ and $(\uparrow\uparrow)_L$ alignments as a function of F_0 . ^c indicates conducting state.

To investigate the influence of the antiferromagnetic spin alignment of the host lattice, similar direct calculations have been carried out for 8-unit AF_2 cells, for which there is only one alignment of the unpaired spin. Once again, calculations in full and broken symmetry yield delocalised and localised hole states respectively. Table 3 compares local hole charges, spin moments, magnetic and localisation energies of AF_2 and $(\uparrow\downarrow)$ FM spin alignments as a function

of the proportion of exact exchange. Also included is the variation of the magnetic energy of the host lattice, and the magnetic energy difference in the presence of the hole $E[(\uparrow\downarrow)_1 \text{ FM}] - E[\text{localised AF}_2]$.

F ₀	q _h		n _s		E _{mag}		E _{loc}		ΔE _{loc}
	AF ₂	FM	AF ₂	FM	host	h _L	AF ₂	FM	
UHF	0.78	0.77	0.91	0.85	19.7	-92.9	2.32	2.28	0.04
1.0	0.78	0.76	0.90	0.84	22.2	-106.7	2.20	2.17	0.03
0.9	0.76	0.72	0.88	0.81	25.3	-107.7	1.81	1.74	0.07
0.8	0.72	0.68	0.86	0.77	29.2	-109.7	1.43	1.33	0.10
0.7	0.67	0.63	0.81	0.71	34.0	-109.7	1.05	0.94	0.11
0.6	0.60	0.55	0.74	0.62	40.1	-95.1	0.68	0.59	0.09
0.5	0.50	0.45	0.63	0.49	50.6	-104.3	0.41	0.25	0.16
0.4	0.36	0.11 ^c	0.48	0.04 ^c	69.2	-75.0	0.23	0.04 ^c	0.19

Table 3. Comparison of 8-unit AF₂ and FM ($\uparrow\downarrow$)₁ localised hole charges, q_h(e), spin moments, n_s(μ_B) and localisation energies, E_{loc}(eV) and ΔE_{loc} (eV), and the magnetic energies, E_{mag}(meV), of the host lattice and localised FM ($\uparrow\downarrow$) and AF₂ holes. ^c indicates conducting state.

From this it is clear that while the AF₂ alignment stabilises the localised state to the extent that it remains insulating down to 20% exact exchange with a filled-to-unfilled gap of ~ 0.7 eV at 40%, the hole charge and spin distributions are largely independent of the alignment of the lattice moments, as are the atomic charges and cation moments of the non-defective lattice. The delocalisation energy is also largely independent of the spin alignment, as might have been predicted, since it is approximately three orders of magnitude larger than the magnetic energy of the non-defective host lattice. However, what Table 3 shows quite clearly is that the ($\uparrow\downarrow$)₁ hole in the FM spin alignment is more stable than the localised AF₂ hole alignment by ~ 100 meV from the UHF limit down to 50% exact exchange. In other words, flipping three of the Ni spins nn to the unpaired oxygen electron leads to a substantial lowering of the energy. Again, this might have been expected from the relative stability of the FM ($\uparrow\downarrow$)₁ and ($\uparrow\uparrow$)₁ states, for half their differences in energy, given in Table 2(a), is appreciably greater than the magnetic energy of the host lattice. Thus the calculations predict that the first ionised state in AF₂ NiO is essentially d⁸L̄ with strong spatial and spin polaron character. Furthermore, the large values for the

delocalisation and magnetic energies given in Table 3 suggest that both the spatial and spin polaronic character will persist into the paramagnetic phase.

(iv) The Li-Bound Hole in NiO: The Electronic Structure of $(\text{Li}'_{\text{Ni}} - \text{h})^x$

The study presented here of the bound hole involves the single system, $\text{Li}_{0.125}\text{Ni}_{0.875}\text{O}$, which is modelled by the 8-unit supercell LiNi_7O_8 confined to the FM spin alignment. The primary interest here is in the difference between the electronic structures of the free and bound hole, here represented by Ni_8O_8^+ and LiNi_7O_8 , and the way the electronic structure varies with F_0 . Once again calculations have been performed in full and broken symmetry and in both alignments of the unpaired spin. They range from the UHF limit down to 40% exact exchange, in the vicinity of which the free hole, Ni_8O_8^+ , goes from an insulating to conducting state. Starting at the limit of exact exchange, direct minimisation of the total energy leads to states in which over 90% of the hole charge resides on the oxygen sublattice, in exactly the same order of stability found for the free hole. In other words, essentially the same $d^8\bar{L}$ electronic configuration is found for the free and bound hole.

F_0	q_h		n_s		$\Delta E_{\uparrow\uparrow - \uparrow\downarrow}(\text{L})$		$\Delta E_{\text{LD}}(\uparrow\downarrow)$		E_{bind}
	8FM	Li7FM	8FM	Li7FM	8FM	Li7FM	8FM	Li7FM	
UHF	0.77	0.81	0.85	0.90	0.47	0.15	2.28	3.10	0.59
1.0	0.76	0.81	0.84	0.89	0.51	0.19	2.17	2.97	0.57
0.9	0.73	0.79	0.81	0.89	0.56	0.21	1.74	2.43	0.60
0.8	0.68	0.75	0.77	0.84	0.61	0.23	1.33	1.88	0.64
0.7	0.63	0.70	0.71	0.79	0.67	0.27	0.94	1.36	0.67
0.6	0.55	0.63	0.62	0.70	0.72	0.31	0.59	0.85	0.71
0.5	0.45	0.46	0.49	0.52	0.78	0.35	0.25	0.41	0.81
0.4	0.11 ^c	0.26	0.04 ^c	0.17	0.09 ^c	0.49	0.04 ^c	0.11	0.81

Table 4(a). Comparison of localised hole charge, $q_h(e)$, spin moment, $n_s(\mu_B)$ and energy (eV) differences, $\Delta E_{\uparrow\downarrow - \uparrow\uparrow}(\text{L})$ and $\Delta E_{\text{LD}}(\uparrow\downarrow)$ for Ni_8O_8^+ (8FM) and LiNi_7O_8 (Li7FM) and the Li-hole binding energy, E_{bind} (eV) in LiNi_7O_8 . ^c indicates a conducting state.

Table 4(a) compares the local hole charges and spin moments, the differences in energy between the two spin alignments of the localised hole, $\Delta E_{\uparrow\uparrow - \uparrow\downarrow}(\text{L}) = E[(\uparrow\uparrow)_i] - E[(\uparrow\downarrow)_i]$, and the

localisation energies for the antiferromagnetic alignment, $\Delta E_{LD}(\uparrow\downarrow) = E[(\uparrow\downarrow)_d] - E[(\uparrow\downarrow)_l]$, of LiNi_7O_8 and Ni_8O_8^+ . Also given is the unrelaxed binding energy of the localised hole to Li_{Ni}^+ , E_{bind} , in LiNi_7O_8 . From this two general points emerge. The first is that the evolution of the electronic structure of the bound hole as the proportion of exact exchange is reduced follows a similar pattern to that of the free hole; the second is that, as expected, the presence of the charge compensating defect, Li_{Ni}^+ , with an effective charge close to $-e$, stabilises the localised hole. Thus the local charge and spin moment of the bound hole are found to be $\sim 5\%$ greater than the free hole and the localisation energy $\sim 30\%$ greater across the range of exact exchange considered. The estimates of E_{bind} , which are obtained directly from the energies of LiNi_7O_8 , $\text{LiNi}_7\text{O}_8^-$, Ni_8O_8^+ and the host lattice, range from 0.59 eV at the UHF limit to 0.81 eV at 40% exact exchange. A further indication of the stabilising effect of Li_{Ni}^+ is that for 40% exact exchange, the free hole state is predicted to be conducting whereas there is a filled-to-unfilled gap of ~ 0.4 eV for the bound hole. At all values of F_0 , the (local) charge, spin moment and localisation energy of the bound hole, $\Delta E_{LD}(\uparrow\downarrow)$, are greater than those for the free hole. Correspondingly, the spin alignment energy, $\Delta E_{\uparrow\downarrow - \uparrow\uparrow}(L)$, is less.

In both the original report of the oxygen K-edge absorption of $\text{Li}_x\text{Ni}_{1-x}\text{O}$ by Kuiper et al [1] and subsequent studies [2-4], one of the most noteworthy features of the spectra is the gap of ~ 4 eV between absorptions attributed to the $\text{O}(1s)^2 + d^8\bar{L} \rightarrow \text{O}(1s)^1 + d^8$ and $\text{O}(1s)^2 + d^8\bar{L} \rightarrow \text{O}(1s)^1 + d^9\bar{L}$ transitions, in which an $\text{O}(1s)$ electron is excited into a $\text{O}(2p)$ hole in the former and into the conduction band in the latter. This is close to the energy of the strong absorption edge of NiO [13], which is often identified with the calculated CT gap. It is well known that the energy gap calculated at high proportions of exact exchange is much greater than the experimental absorption edge. One reason for this is the strong reorganisation of the valence states that accompanies the CT excitation from the valence to the conduction band. While a similar reorganisation is likely to occur for the transitions involved in the oxygen K-edge spectra, if the renormalisation energies are similar, the gap between the calculated empty $\text{O}(2p)$ state associated with the hole and the conduction band edge would be expected to be close to 4 eV. Table 4(b) below contains the calculated gap between the top edge of the empty $\text{O}(2p)$ band and the

conduction band lower edge, or $d^8L - d^9$ gap, as it is sometimes referred to [1], for $Ni_8O_8^+$ and $LiNi_7O_8$ as a function of the proportion of exact exchange. As seen in Figure 2, which corresponds to 100% exact exchange, the gaps associated with the free and bound holes within

F_0	8FM	8AF ₂	Li7FM
UHF	4.0	4.4	4.0
1.0	3.8	4.1	3.5
0.9	4.0	4.4	4.0
0.8	4.3	4.8	4.2
0.7	4.5	5.1	4.5
0.6	4.7	5.3	4.8
0.5	4.7	5.6	5.1
0.4	5.4 ^c	4.6	4.8

Table 4(b). Comparison of the edge-to-edge $d^8L - d^9$ gap (eV) for 8FM($\uparrow\downarrow$)_L, Li7FM ($\uparrow\downarrow$)_L and 8AF₂ as a function of F_0 . ^c indicates a conducting state.

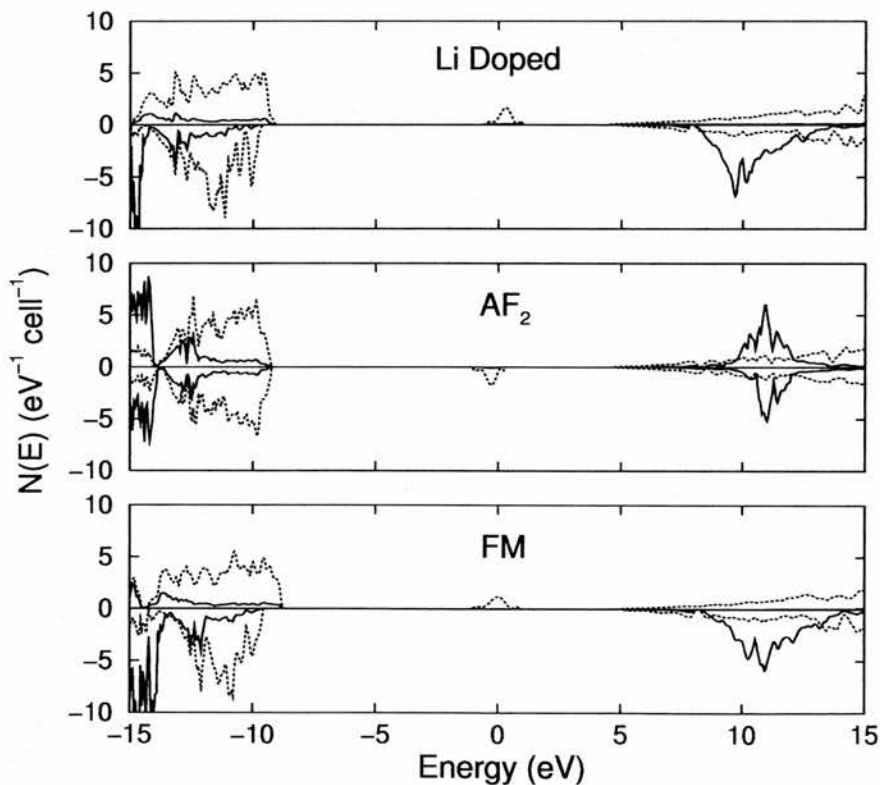


Figure 2. The valence, hole and conduction band densities of states for the bound hole in FM($\uparrow\downarrow$) $LiNi_7O_8$ and the free hole in FM($\uparrow\downarrow$) and AF₂ Ni_8O_8 . Solid line: Ni, dotted line: O.

the insulating regime are barely distinguishable, in accord with the observation of a single absorption peak, and for high proportions of exact exchange close to 4 eV.

5. Discussion

Elucidating the differences in the electronic and magnetic properties of closely related point defects is a difficult experimental task, which calculations should, in principle, facilitate. The present hybrid functional study has attempted to elucidate such differences for the hole-related defects in the paradigm system, $\text{Li}_x\text{Ni}_{1-x}\text{O}$ which, at high temperature at least, can be represented by Li'_{Ni} , h^\bullet and $(\text{Li}'_{\text{Ni}} - h^\bullet)^x$ point defects distributed upon a NiO host lattice. Starting with Li'_{Ni} , calculations within the full range of exact exchange from UHF to DFT suggest that it is inert electronically, with negligible perturbation of the electronic structure of the host lattice, despite its effective charge close to $-e$. It is reasonable to conclude, therefore, that other than as a potential site for hole capture, Li'_{Ni} plays no part in the electronic properties of $\text{Li}_x\text{Ni}_{1-x}\text{O}$.

The nature of the compensating hole, both free carrier, h^\bullet , and bound charge, $(\text{Li}'_{\text{Ni}} - h^\bullet)^x$, follows from the CT character of the host lattice and is essentially $d^8\bar{L}$ for the entire range of weights of exact exchange considered. At high F_0 , the charge and spin densities of the free hole are largely localised at a single oxygen site, with localisation energies in excess of 2 eV for both the AF₂ and FM spin alignments and filled-to-unfilled gaps in excess of 5 eV. For the hypothetical, though computationally convenient FM spin configuration, the antiferromagnetic alignment of the unpaired oxygen spin with respect to the FM lattice moments, $(\uparrow\downarrow)$, is favoured over the ferromagnetic alignment, $(\uparrow\uparrow)$. Evidently, the energy of the partial (spin) pairing between the unpaired oxygen spin and the six antiferromagnetically aligned nn Ni spins in $(\uparrow\downarrow)$ is greater than the direct exchange energy between the unpaired oxygen spin and the six ferromagnetically aligned nn Ni spins in $(\uparrow\uparrow)$. The partial spin pairing is clearly seen in Table 2(c) which shows that while the localised hole charges in $(\uparrow\downarrow)$ and $(\uparrow\uparrow)$ differ by less than 5%, the unpaired oxygen spin moments in $(\uparrow\downarrow)$ are less than those in $(\uparrow\uparrow)$ by up to 40% as a result of the overlap

with the neighbouring Ni spins. The differences in energy between these two spin configurations vary from ~ 80 meV / Ni to ~ 130 meV / Ni across the range of exact exchange considered, so that even in the absence of explicit calculations for the AF₂ hole state, the FM ($\uparrow\downarrow$) alignment would be expected to be lower in energy. Direct comparisons of the total energies given in Table 3(a) confirm this to be the case, leading to the prediction of spin polaron behaviour in which a localised unpaired oxygen spin in AF₂ NiO is surrounded by six antiferromagnetically aligned Ni spins. As F_0 is reduced, the charge and spin densities in both the FM and AF₂ alignments delocalise, with a corresponding decrease in both the localisation energy and filled-to-unfilled gap. In the case of both FM alignments this leads to metallic states between 50% and 40% exact exchange, whereas the AF₂ alignment remains insulating down to $F_0 = 0.2$, even though it remains higher in energy than FM ($\uparrow\downarrow$). The electronic structure of the bound hole, $(\text{Li}'_{\text{Ni}} - \text{h}^*)^x$, is found to be very similar to that of the free hole, allowing for the stabilising effect of Li'_{Ni} on h^* . The $\text{Li}'_{\text{Ni}} - \text{h}^*$ binding energy in an unrelaxed geometry is in the region of 0.7 eV, and for a given proportion of exact exchange, localised hole charges and spin moments are slightly greater for $(\text{Li}'_{\text{Ni}} - \text{h}^*)^x$ than for h^* . However, from a spectroscopic point of view, the $d^8\text{L} - d^9$ gaps are very close, leading to the prediction of a single gap in $\text{Li}_x\text{Ni}_{1-x}\text{O}$, in agreement with the reported oxygen K-edge and other spectra [1]. The stabilising effect of Li'_{Ni} is also manifest in the preservation of a filled-to-unfilled gap at 40% exact exchange where the free hole state is metallic. The principal conclusions of this study are summarised below.

- (i) Over a wide range of exact exchange, notably where both the free and bound carrier are insulating, the hole state is essentially $d^8\text{L}$, in agreement with spectroscopic studies [1-4], with substantial proportions of the hole charge and unpaired spin located at a single oxygen site.
- (ii) The electronic structure of the free hole is largely independent of the spin alignment of the lattice, but partial spin pairing of the unpaired electron with nearest neighbour, antiferromagnetically aligned Ni spins leads to strong spin polarisation of the surrounding lattice.

- (iii) Decreasing the proportion of exact exchange leads to a delocalisation of the charge and spin and corresponding decrease in the localisation energy, with a transition to a conducting state of the low energy FM ($\uparrow\downarrow$) alignment, and by implication the spin polaron, between 40% - 50%.
- (iv) The evolution of the electronic structure of the bound hole with F_0 follows a very similar pattern to that of the free carrier.

Finally, it would be wise to assess the effect of varying the content of exact exchange within another hybrid scheme. To this end, the free hole in the AF_2 spin alignment was studied within Becke-LYP scheme and compared with the earlier PW91 results. Table 5 presents the unpaired spin moment at the hole site, n_s , the localisation energy, E_{loc} , and the edge-to-edge $d^8\bar{L} - d^9$ gap for $AF_2 Ni_8O_8^+$ as a function of F_0 in the two schemes.

F_0	n_s		E_{loc}		$d^8\bar{L} - d^9$ gap	
	PW91	Becke - LYP	PW91	Becke - LYP	PW91	Becke - LYP
UHF	0.91	0.91	2.32	2.32	4.4	4.4
1.0	0.91	0.90	2.20	2.27	4.1	4.6
0.9	0.89	0.88	1.81	1.82	4.4	4.9
0.8	0.86	0.86	1.43	1.43	4.8	5.1
0.7	0.81	0.81	1.05	1.03	5.1	5.4
0.6	0.75	0.74	0.68	0.73	5.3	5.7
0.5	0.63	0.63	0.41	0.43	5.6	5.5
0.4	0.48	0.48	0.23	0.22	4.6	4.5
0.3	0.27	0.25	0.06	0.02	3.7	3.4
0.2	0.17	0.17	0.07	0.10	2.4	2.3

Table 5. Comparison of PW91 and Becke-LYP values of the unpaired spin moment, n_s (μ_B), localisation energy, E_{loc} (eV) and the edge-to-edge $d^8\bar{L} - d^9$ gap (eV) for $8AF_2$ cells as a function of F_0 .

From this it is clear that while there are small differences between the two methods, notably in the $d^8\bar{L} - d^9$ gap, overall the evolution of the electronic structure of the free hole state is very similar, so that the PW91 results seem to be generally applicable.

6. References

- [1] P. Kuiper, G. Kruizinga, J. Ghijsen and G. A. Sawatzky, *Phys. Rev. Lett.* **62**, 221 (1989)
- [2] S. Hüfner, P. Steiner, I. Sander, F. Reinert, H. Schmitt, M. Neumann and S. Witzel, *Solid State Comm.* **80**, 869 (1991)
- [3] J. van Elp, B. G. Searle, G. A. Sawatzky and M. Sacchi, *Solid State Comm.* **80**, 67 (1991)
- [4] J. van Elp, H. Eskes, P. Kuiper and G. A. Sawatzky, *Phys. Rev. B* **45**, 1612 (1992)
- [5] W. C. Mackrodt, N. M. Harrison, V. R. Saunders, N. L. Allan and M. D. Towler, *Chem. Phys. Lett.* **250**, 66 (1996)
- [6] W. C. Mackrodt, *Ber. Bunsenges. Phys. Chem.* **101**, 169 (1997)
- [7] F. Kröger, *The Chemistry of Imperfect Crystal*, North-Holland (Amsterdam) 1964
- [8] J. P. Perdew and Y. Wang, *Phys. Rev. B* **33**, 8800 (1986)
- [9] J. P. Perdew and Y. Wang, *Phys. Rev. B* **40**, 3399 (1989)
- [10] J. P. Perdew and Y. Wang, *Phys. Rev. B* **45**, 13244 (1992)
- [11] R. S. Mulliken, *J. Chem. Phys.* **23**, 1833 (1955); *ibid* **23**, 1841 (1955)
- [12] M. D. Towler, N. L. Allan, N. M. Harrison, V. R. Saunders, W. C. Mackrodt and E. Aprà, *Phys. Rev. B* **50**, 5041 (1994)
- [13] R. J. Powell and W. E. Spicer, *Phys. Rev. B* **2**, 2182 (1970)

Chapter 5

A Hybrid Hamiltonian Study of Vanadium Monoxide

1. Introduction

Amongst the transition metal oxides, those of the higher valence states of vanadium find diverse application as oxidation catalysts [1], lithium insertion electrodes [2], environmental sensors [3] and optical devices, and may even be formed into nanotubes [4]. Progress in application of these materials relies upon an understanding of their electronic and magnetic structures. The complexity and subtlety of the fundamental properties of the early TMOs continues to pose severe and particular difficulties for theory, but a sound description of the structurally simpler lower oxide, vanadium monoxide, VO_x , will contribute usefully to an understanding of the full V-O phase diagram. To date, however, such a basic description has proved to be elusive, although the reasons for this are clear. Tight control of the stoichiometry, x , is difficult to achieve, in addition to which, VO_x is undoubtedly close to a MH transition, while possessing a complex defect structure, over a wide composition range.

The structural and electrical characterisation of VO_x has an interesting history. Early work suggested that, at low temperature, VO_x breaks down into a mixture of a body centred tetragonal phase of composition V_3O and a V_3O_4 phase which is either body centred cubic or body centred tetragonal, with a c/a ratio close to unity [5]. Later work established that VO_x is structurally homogeneous in the $\text{Fm}\bar{3}\text{m}$ rocksalt lattice over a wide composition range, $0.8 < x < 1.3$ [6,7]. X-ray crystallography of phases with differing composition disclosed the presence of varying concentrations of vacancies on both cation and anion sublattices. Only for $x = 1.0$ are the concentrations of both metal and oxygen vacancies equal, amounting to approximately 15% of the available sites [8]. This is a very much larger concentration of intrinsic defects than that found in the oxides of later TMs. The lattice constant is found to increase across the homogeneity range, from approximately 4.03\AA at $x = 0.8$ to 4.13\AA at $x = 1.3$ at room temperature,

with values of 4.071Å [9] and 4.063Å [8] reported for the nominally stoichiometric phase, VO.

A metal to semi-conducting phase transition has been reported at a critical temperature $T_0 = 125^\circ\text{K}$ [10,11], although later authors [8,12] suggested that this transition in the earlier samples was due to the presence of V_2O_3 . A study of the magnetic properties of the system found antiferromagnetic behaviour for $x = 1.25$ and 1.147 with critical temperatures of 7.0 and 4.6°K respectively. Compositions with higher metal content display paramagnetic susceptibility, but no transitions associated with ordering of the atomic moments have been observed [9,12].

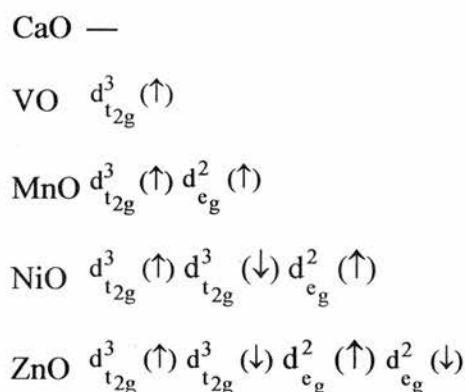
In terms of electrical characterisation, there is a large body of work which shows that VO_x displays metallic characteristics for $x < 1$ and semi-conductivity for $x > 1$. Activation energies for electronic conduction have been obtained which increase with x from 2×10^{-3} eV at $x = 1.0$ to approximately 50×10^{-3} eV at $x = 1.3$ [9,12–21], and variations in resistivity from 7×10^{-4} Ωcm to 1 Ωcm in the range $-0.2 < x < 0.2$ at room temperature. Such behaviour differs from that found in the structurally related compound TiO_x , which remains metallic throughout the stoichiometry range $0.75 < x < 1.3$, and undergoes a superconducting transition at low temperature. No superconductivity has been found in VO_x down to a temperature of 0.3°K. Measurements of the Seebeck coefficient, α , in VO_x show a change in sign at $x = 1$, indicating conduction by holes for higher metal content and by electrons for higher oxygen content. The coexistence of charge carriers of opposite electrical polarity in VO_x has been confirmed by magnetoresistance studies. [21,22]

Historically, band theoretical methods of varying sophistication have been applied to the ideal $\text{Fm}\bar{3}\text{m}$ VO lattice. Early non-self-consistent calculations based on an LCAO tight binding method, Slater's $\rho^{4/3}$ exchange potential [23] and a series of *ad hoc* crystal potentials yielded a metallic ground state, with the Fermi energy lying in the V(3d) band. A very broad d-band of width $\sim 7\text{eV}$ was also predicted on the basis of the neutral atom potential [24]. These calculations were performed at the experimental lattice constant of the defective lattice, and made no allowance for spin polarisation. Non-self-consistent APW calculations [25], again at the defective lattice constant, with

Slater exchange and *ad hoc* crystal potentials led to similar conclusions. A self-consistent APW study of the lighter transition metal monoxides based on X_α exchange predicted VO to be a d-band metal, with a band width of $\sim 7.5\text{eV}$, at the observed lattice constant [26]. Self-consistent ASA calculations employing the local spin exchange-correlation functional of von-Barth and Hedin [27] were conducted as a function of lattice constant [28], and once again indicated a d-band metal with an approximate band width of 8eV . More recently, a first principles spin-unrestricted Hartree-Fock (UHF) calculation based on localised atomic orbitals predicted VO to be a high spin antiferromagnetic MH insulator, with an optimised lattice constant of 4.460\AA [29].

Clearly there are fundamental differences between first principles DFT and UHF calculations as to the nature of the ground state of the fully stoichiometric, non-defective $Fm\bar{3}m$ VO lattice, with, perhaps, even more profound differences for the technologically important higher oxides. This is an unsatisfactory situation in view of the successes of both DFT and UHF methodologies in describing the ground states of a wide range of first-row transition metal oxides. Here, fresh studies of the ground state of VO are reported, which extend to the $d \rightarrow d$ excited states, in an attempt to shed light on some of these differences.

Initial insight into the ground state of fully stoichiometric, non-defective VO might be sought from a consideration of the d-band occupancies of the subgroup, CaO, VO, MnO, NiO and ZnO, of the $Fm\bar{3}m$ oxides. Assuming comparable ionicities and crystal field characteristics, the spin band occupancies can be written as,



Now CaO, MnO, NiO and (presumably) ZnO with 0, 2, 3 and 4 completely filled spin bands respectively are all insulating, from which it might reasonably be concluded that VO with one completely filled spin band, $d_{t_{2g}}^3 (\uparrow)$, would also be insulating. Furthermore, as argued in Chapter 1, it is expected that VO will display MH insulating characteristics within the ZSA classification [30]. It is known, both from studies of the elemental transition metals and the oxides, that the d-band gradually falls in energy relative to the O(2p) band and contracts spatially as it is filled, for the added electron cannot fully screen the increase in nuclear charge [28]. Therefore, CT behaviour at the right of the transition series should give way to MH behaviour at the left. Finally, it might also be expected that VO would exhibit antiferromagnetic spin alignment by comparison with the two magnetic members of the subgroup, MnO and NiO.

What is clearly needed is some form of theoretical evidence for either an insulating or conducting ground state in non-defective VO. Unfortunately, as discussed in Chapter 1, the LDA and GGA Hamiltonians cannot be relied upon to correctly describe the insulating ground state of the TMOs [31-36]. It is also well known that the HF method places metallic states at too high an energy. One strategy would be to introduce an orbital dependent potential into the LDA, either through self-interaction correction [37,38], or by imposition of an arbitrary U (LDA+U) [39-41]. Such methods do seem to correct the grosser deficiencies of the purely local functionals, opening gaps at the Fermi level and increasing atomic moments. Against these apparent limitations of DFT, at least within the LDA, it should be noted that a relatively recent study of the defective structures and energetics of TiO_x has demonstrated quantitative agreement between experimental and theoretical geometries and transition pressures [42]. It is apparent that, despite an inaccurate ground state, the LDA provides an acceptable account of the relative energetics of the structural phases.

Accordingly, to resolve some of these issues and to predict the magnetic characteristics of and elementary excitations in stoichiometric, non-defective VO, a hybrid density functional study of this system has been conducted along the lines reported recently for MgO [32], NiO [32,43] and CoO [32]. The focus of the current work is different from that of previous chapters. Reasonably clear and complete experimental data exists for

NiO and MnO, and the aim was then to compare the results of hybrid calculations against this data. In VO, by contrast, the aim is to use a known and tested hybrid method (the B3LYP potential) to make some prediction for the electronic structure of the non-defective structure, for clear experimental data is lacking.

2. Theoretical Methods

The hybrid methodology, as presented in Chapter 1 is followed in the present study. In the B3LYP Hamiltonian, the presence of only 20% of the exact exchange is not sufficient to cancel the Coulomb self-interaction, but the method has been shown to yield values for the gaps between the filled O(2p) and empty metal 3d states which are apparently in close agreement with experimental band gaps [44]. Optimised structural parameters are typically found to lie within a broad range of $\pm 2\%$ of the experimental values. The approach here was to vary F_0 in the range $0 \leq F_0 \leq 1$, yielding a series of hybrid Hamiltonians, including B3LYP ($F_0=0.2$). The specific values of F_0 used were 0.0, 0.1, 0.2, 0.4, 0.6, 0.8 and 1.0, which constitutes a sufficient number of points to permit an examination of the effect of varying amounts of exact exchange on the electronic and magnetic properties of VO. In addition, and for comparison, UHF calculations without correlation were also carried out.

Magnetic energies were mapped upon an Ising Hamiltonian as presented in Chapter 1 and used previously in Chapters 2 to 4 for NiO and MnO. Similarly, the ground and spin-allowed $d \rightarrow d$ excited states were mapped onto the Kanamori crystal field Hamiltonian, H_{CF} , as presented in Chapter 1. In VO, the energies of the states are given by

$$\begin{aligned}
 E_{\text{ground}} &= E_{CF}^0 + 3A - 15B \\
 E_{xy \rightarrow z^2} &= E_{CF}^0 + 3A - 3B + \Delta_{CF} \\
 E_{xy \rightarrow x^2 - y^2} &= E_{CF}^0 + 3A - 15B + \Delta_{CF} \\
 E_{xz, yz \rightarrow z^2, x^2 - y^2} &= E_{CF}^0 + 3A - 12B + 2\Delta_{CF}.
 \end{aligned}$$

The spin-forbidden $xy(\uparrow) \rightarrow xy(\downarrow)$ excitation can also be mapped onto H_{CF} , yielding

$$E_{xy(\uparrow) \rightarrow xy(\downarrow)} = E_{CF}^0 + 3A - 9B + 2C$$

As previously, the excitation energies derived from transitions between the above states can be equated directly to first principles total energy differences. Clearly, Δ_{CF} is obtained directly from $\Delta E_{xy \rightarrow x^2-y^2}$ while B can be derived from either of the two other Laporte forbidden, but spin-allowed transitions. In this way, the validity of mapping first principles calculations onto the Kanamori crystal field Hamiltonian can also be verified by comparing the first principles total energy difference for the spin-allowed two-electron excitation, $(xz,yz) \rightarrow (z^2, x^2-y^2)$, with that derived from Δ_{CF} and B obtained from the two spin-allowed one-electron excitations. This method of checking consistency was used conclusively for NiO in Chapter 3. Clearly, B can also be derived from $\Delta E_{xy,yz \rightarrow z^2, x^2-y^2}$, and this used to predict the energy for the $xy \rightarrow z^2$ excitation. The C parameter may be obtained only from the spin-forbidden excitation, $\Delta E_{xy(\uparrow) \rightarrow xy(\downarrow)}$. It should be noted that the problem of a change in number of d-electron pair correlations, as described for MnO in Chapter 2, arises here for the spin-forbidden transition, and so the value of the Racah C parameter is expected to show extreme sensitivity to change in F_0 .

Computational Conditions

The hybrid functional module of the CRYSTAL98 code [45] was used. The crystal orbitals were expanded in a set of 39 atomic orbitals, 25 for V and 14 for O. In the notation used previously [29,45], the V orbitals comprised 7 shells of the type 1s(8), 2sp(6), 3sp(4), 4sp(1), 5sp(1), 3d(4), 4d(1) and the O orbitals 4 shells of the type 1s(8), 2sp(6), 3sp(4), 4sp(1). The earlier UHF study of VO used a 6-shell basis for V [29]. The inclusion of a second d shell, 4d(1), and subsequent re-optimisation of all cation and anion valence exponents decreased the Mulliken charge by 0.14 e and led to energy differences between magnetic states that differed from previous values [29] by ≤ 10 meV per atom. However, since this compares with typical magnetic interactions within the first row transition metal oxides, the V(4d) shell and necessary valence re-optimisations were retained in all subsequent calculations. The number and angular

symmetry of the Gaussian functions used here are broadly similar to those employed recently by Moreira *et al* in their hybrid DFT study of NiO [43].

For the density functional fitting, the following auxiliary even-tempered bases of Gaussian-type functions were employed: 14 s-type functions with exponents in the range 0.07 – 4000.0, and one p-type, one d-type and one f-type function, each with exponent 0.5 were used for O, and 13 s-type functions with exponents in the range 0.1 – 4000.0, one p-type function with exponents in the range 0.3 – 0.9, one f-type function with exponent 0.8 and three g-type functions with exponents in the range 0.45 – 3.3 for V.

A Monkhorst-Pack shrinking factor of 8, which was used for cells of all sizes, and truncation thresholds of 10^{-7} , 10^{-7} , 10^{-7} , 10^{-7} and 10^{-14} for the Coulomb and exchange series [45] ensured convergence of the total UHF energies of three magnetic states to ≤ 0.1 meV, while SCF convergence thresholds were set to 10^{-7} a.u. for both eigenvalues and total energies. These tolerances are similar to those used for a wide range of previous calculations [32,43].

Of the four different types of magnetic order considered in this study, three are familiar from the earlier work on NiO and MnO in Chapter 2, namely the ferromagnetic (FM) and antiferromagnetic type-I and type-II (AF_1 and AF_2) alignments. A third AF alignment is considered; the type-III (AF_3) structure, in which the quadruple primitive cell consists of ferromagnetic (210) planes which alternate spin orientation successively in the direction normal to the planes. The Miller indices and crystal directions noted above are for the conventional crystallographic cell. The total energy and properties of the ferromagnetic (FM) state can, of course be calculated from the primitive cell, but in the present work, was always extracted from the double cell. This ensures that the restriction to FM order implicit in the primitive cell does not affect the energy of the state. As a test of the various numerical parameters used in this study, the energy of the FM state was calculated by the UHF method for the primitive, double and quadruple cells with the broken metal sublattice symmetries appropriate to the description of the various AF states. In each case, the total energy

per formula unit was found to be identical to within the convergence tolerance of the SCF procedure.

Mulliken population analyses of the crystalline orbitals were used to extract the net atomic charges, magnetic moments and individual orbital occupations as in previous studies.

3. Results and Discussion

(a) Bulk Lattice and Electronic Structure

For the entire range of hybrid Hamiltonians, the ground electronic states of the FM, AF₁ and AF₂ spin alignments were found to be insulating, with the exception of the FM alignment at $F_0 = 0.1$ and the pure DFT AF₁ alignment, which were found to be conducting. Lattice constants (a_0) were obtained from fourth order polynomials fitted to total energy-volume curves calculated within $\pm 10\%$ of the previous UHF value for the FM state (4.460 Å). The resulting a_0 for the full range of exchange-correlation potentials are given in the first three columns of Table 1 and shown graphically in Figure 1.

For the pure DFT description, convergence was problematic for all three magnetic structures, even with enhanced reciprocal space sampling and with Fermi function smearing of the Kohn-Sham orbital occupancies. At this limit of zero exact exchange only the AF₁ alignment produced an energy-volume curve which was sufficiently smooth to yield a_0 to an acceptable accuracy.

F_0	a_0			q_M			n_S		
	AF ₁	AF ₂	FM	AF ₁	AF ₂	FM	AF ₁	AF ₂	FM
UHF	4.4545	4.4539	4.4715	1.686	1.686	1.689	3.008	3.027	3.010
1.0	4.3511	4.3528	4.3767	1.647	1.647	1.647	2.967	2.983	2.988
0.8	4.3595	4.3615	4.3865	1.608	1.607	1.611	2.959	2.976	2.986
0.6	4.3692	4.3737	4.4049	1.562	1.560	1.566	2.945	2.965	2.984
0.4	4.3761	4.3815	4.4168	1.504	1.503	1.510	2.919	2.943	2.981
0.2	4.3813	4.3824	4.4311	1.433	1.431	1.442	2.860	2.891	2.978
0.1	4.3803	4.3898	4.4577 ^C	1.390	1.387	1.400	2.794	2.831	2.938
0.0	4.3601 ^C	—	—	1.320	—	—	2.446	—	—

F_0	ΔE_M	
	AF ₂ ⁽¹⁾	FM ⁽²⁾
UHF	10.1, 10.1	88.6, 86.9
1.0	15.8, 15.8	118.4, 115.9
0.8	18.4, 17.9	140.3, 135.3
0.6	21.4, 20.5	169.2, 161.3
0.4	26.1, 24.9	213.4, 201.4
0.2	31.1, 30.4	285.0, 269.3
0.1	35.8, 32.4	354.4, 324.2

^C conducting state.

(1) First entry = $[E(\text{AF}_2) - E(\text{AF}_1) \text{ at } a_0(\text{AF}_1)]$.

Second entry = $[E(\text{AF}_2) \text{ at } a_0(\text{AF}_2)] - [E(\text{AF}_1) \text{ at } a_0(\text{AF}_1)]$.

(2) FM, as for AF₂ above.

Table 1. Lattice constant $a_0(\text{\AA})$, total Mulliken charges $q_M(e)$, cation spin moment $n_S(\mu_B)$ and energy ΔE_M (meV/molecule) of the FM and AF₂ alignments relative to AF₁ as a function of F_0 .

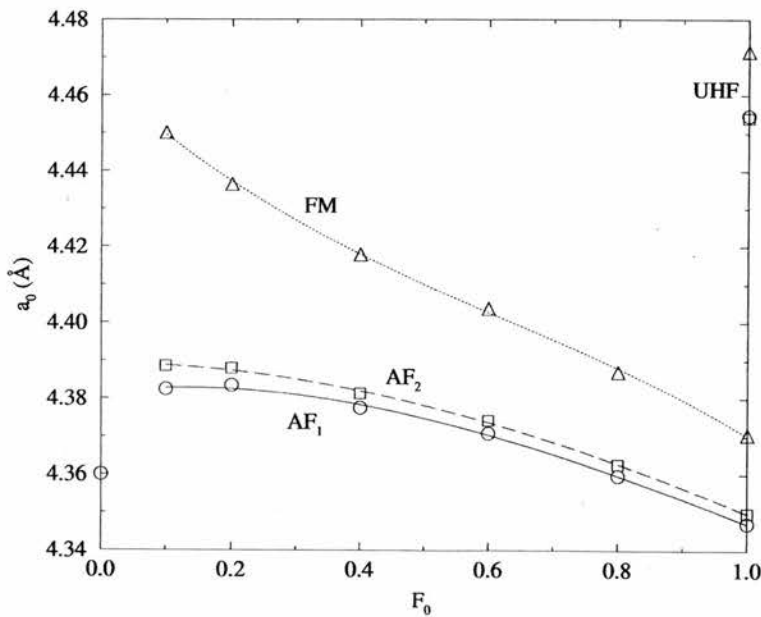


Figure 1. The AF₁ (O), AF₂ (□) and FM (△) optimised lattice constants, a_0 , as a function of F_0 .

As evident in Figure 1, the largest changes in a_0 result from the addition of correlation to exact exchange (UHF), at which point the lattice contracts by $\sim 2.4\%$ of the uncorrelated value with a slight increase in the differences between the three magnetic states. Thereafter, decreasing the amount of exact exchange leads to an increase in the AF₁ and AF₂ lattice constants to a maximum of $\sim 0.7\%$ above the correlated UHF values for $0.1 \leq F_0 \leq 0.2$. In contrast, the FM lattice constant shows no turning point at low F_0 and expands to a maximum of $\sim 1.9\%$ above the correlated UHF value. In the limit of zero exact exchange, the AF₁ lattice constant is seen to decrease sharply, the most likely cause of which is the onset of metallic behaviour. A possible explanation of this abrupt change is discussed later in this section in terms of the calculated density of states.

The equilibrium bulk modulus, K_0 , was obtained for each Hamiltonian by a least squares fitting of the AF₁ energy-volume data to the Murnaghan equation of state [46]. For this purpose, a restricted set of lattice constants within $\pm 2\%$ of the appropriate a_0 were used. The variation of K_0 with exchange-correlation functional is shown in Figure 2, where it is seen to range from ~ 175 GPa for $F_0 = 0.1$ to ~ 200 GPa for correlated UHF. The pure UHF value is ~ 170 GPa and pure DFT (metallic) 162 GPa. While there are no experimental data, the K_0 reported here might usefully be compared with values ranging from 120GPa for CaO [47] to 190GPa for NiO [48]. It should be noted that the Murnaghan and polynomial fits of the energy-volume data yield essentially identical optimised lattice parameters.

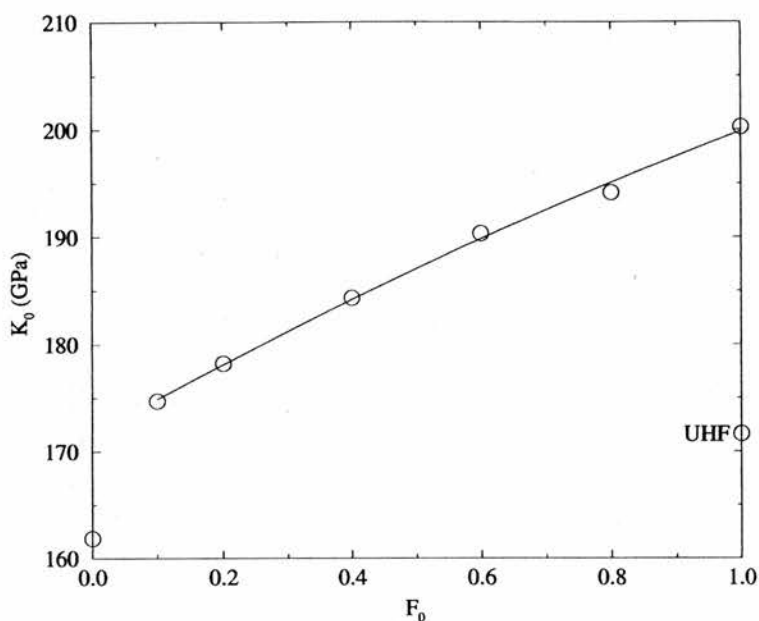


Figure 2. The bulk modulus, K_0 , of the AF_1 ground state as a function of F_0 .

Identical calculations for the low energy AF_2 spin alignment in MnO and NiO are reported in Chapter 2. They reveal very similar trends to those found for VO. Figure 6 for MnO in Chapter 2 shows that the addition of LYP correlation to exact exchange contracts the lattice by $\sim 2.3\%$, while decreasing the amount of exact exchange leads to an expansion of the lattice to a maximum of $\sim 1.3\%$ above the correlated UHF value at $F_0 = 0.1$. However, a noticeable difference from VO is that there is no abrupt decrease in volume at the DFT limit. Now, as previously discussed, the experimental low temperature lattice constant of MnO is best described by a value for F_0 in the Becke-LYP scheme in the range 0.6 – 0.7, and the lattice constant of NiO by F_0 in the range 0.9 – 1.0. Adopting a similar range of exchange-correlation potentials for the AF_1 alignment of VO leads to a predicted lattice constant in the region of 4.35 – 4.37 Å. In MnO, the bulk modulus increases from the pure DFT value of 161 GPa to 194 GPa for correlated UHF, with the pure UHF value ~ 30 GPa below this, as is the case for VO. These values compare with static and dynamic experimental bulk moduli in the range 144 – 162 GPa, which indicates that only the pure DFT value agrees with experiment. The pure DFT value for the bulk modulus of the AF_1 state in VO is ~ 162 GPa, which therefore constitutes the best estimate for the perfect lattice on the basis of the limited evidence from MnO

Turning now to the electronic structure, the Mulliken charges and cation spin moments for VO shown in Table 1 indicate a largely ionic system for $F_0 \geq 0.6$. Both the ionicity and local cation moment decrease as the proportion of exact exchange decreases. This implies that the gross electronic state of the crystal tends not toward singly charged ions, which would require an increase in the cation spin moment, but instead toward a metallic solution. As in MnO and NiO, the spin polarisation of the oxygen sublattice varies both with F_0 and magnetic order. Typical values for the net spin densities on the two oxygen atoms of the magnetic unit cell are (-0.007, 0.004) and (0.012, 0.012) for the AF₁ and FM alignments respectively at the limit of correlated exact exchange and (-0.010, 0.007) and (0.024, 0.024) for an F_0 value of 0.1. Spin polarisation of the anion is forbidden by symmetry in the AF₂ alignment. Such polarisation of the anion in the FM state has been noted in DFT studies of NiO [43] but has not been experimentally observed. The decreased ionicity of the FM state based on exact exchange derived from the present, enriched V basis set compared with that reported previously [29] can be attributed, in part, simply to the inclusion of a 4d polarisation function, and, in part, to the optimisation of the orbital exponent. To show this, an unoptimised V²⁺ bare ion 4d-shell was added to the 6-shell V basis of the previous study, leading to a decrease in the ionicity of the FM state by 0.05 e , without any change in the valence orbital exponents.

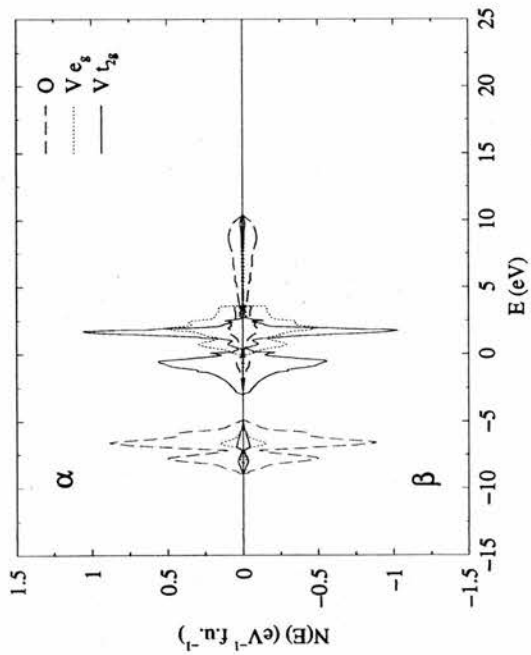
The energies of the AF₂ and FM alignments relative to AF₁ given in Table 1 show that AF₁ order is lowest in energy for the entire range of exchange-correlation functionals considered in this study. This is in keeping with the largely high-spin t_{2g}^3 d-orbital occupation and cation moments revealed by the Mulliken analyses. As discussed previously, the strength of the superexchange interaction in the rocksalt TMOs depends critically on the occupation of the e_g orbitals, for it is these that strongly overlap the 2p orbitals of the neighbouring anions. The superexchange dominated AF₂ ground state found in MnO and NiO would not therefore be expected as the ground state in this material. The dependence of a_0 on magnetic order is indicative of a strong isotropic spin-lattice interaction in VO, where a maximum variation of 0.026 Å, or 0.598 % is obtained between the AF₁ and FM states in VO. The comparable variation in MnO is 0.006 Å, or 0.136 % between the AF₂ and FM values, which is approximately one-quarter of that in VO. A strong anisotropic spin-lattice interaction

is also predicted for VO on the basis of an AF₁ ground state, with either compression or stretching of the conventional rocksalt cell along the [100] direction. Due to constraint of time, no calculations have been performed to test this prediction as yet.

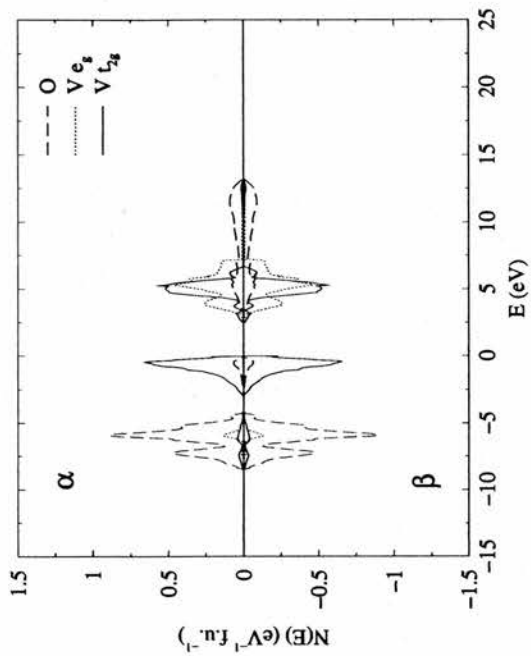
Figure 3 contains the atomic orbital projected densities of states (DOS) for the three magnetic states, for 20%, 60% and 100% exact exchange, all at the AF₁ lattice parameter. Also shown is the DOS for the metallic AF₁ state derived from the pure DFT potential. Details of the energy gaps and valence band widths extracted from these plots are given in Table 2. The filled to unfilled band gap for each of the magnetic states is found to vary linearly with F₀, as shown in Figure 4, with

$$\Delta E_g(\text{FM}) < \Delta E_g(\text{AF}_1) < \Delta E_g(\text{AF}_2).$$

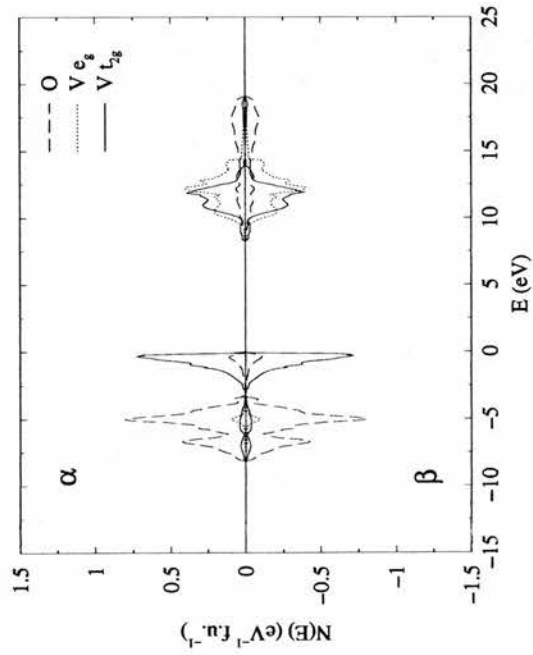
for the entire range of exchange-correlation potentials. They range from ~14 eV at the correlated UHF limit down to ~0.9 eV at the AF₁ stability limit of 10% exact exchange (In the interests of clarity the (wide) UHF gaps have been omitted from Figure 4). The trend in ΔE_g with change of F₀ for all magnetic states is very similar to that observed in MnO and NiO.



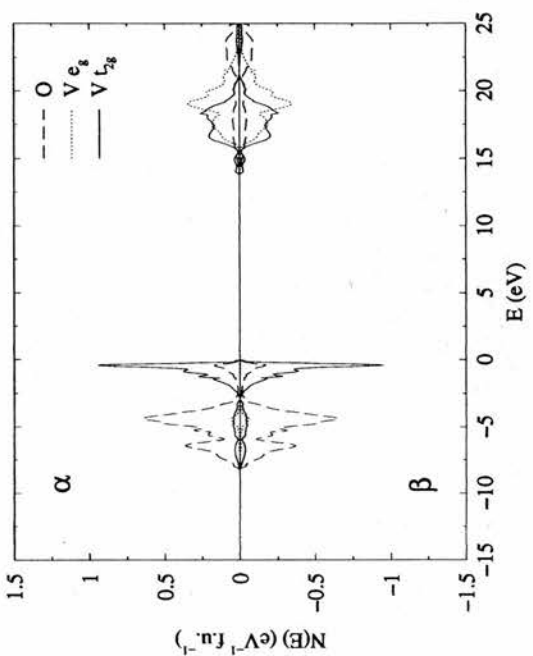
(a)



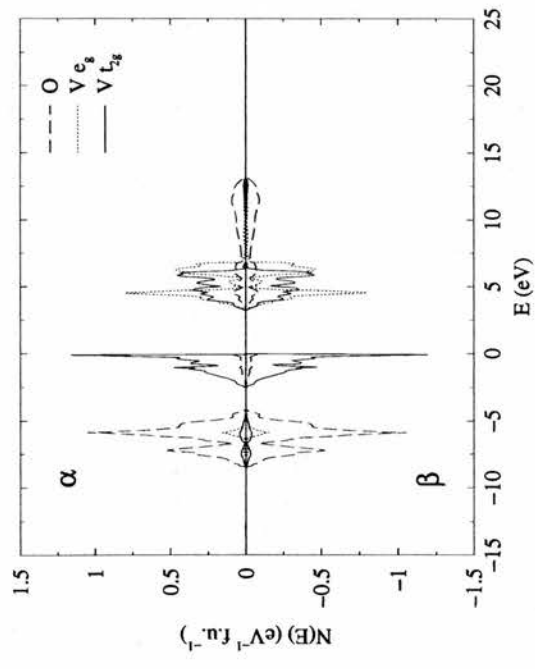
(b)



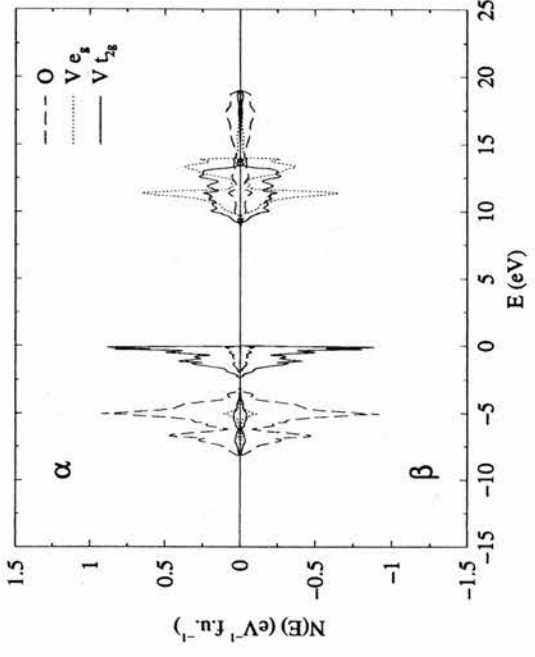
(c)



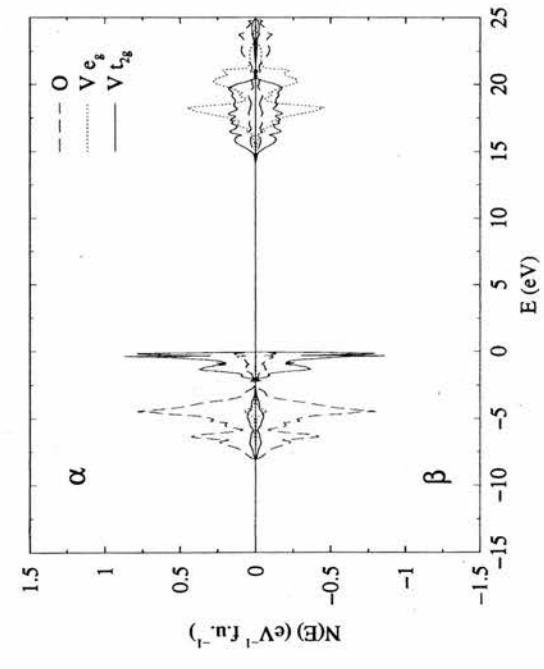
(d)



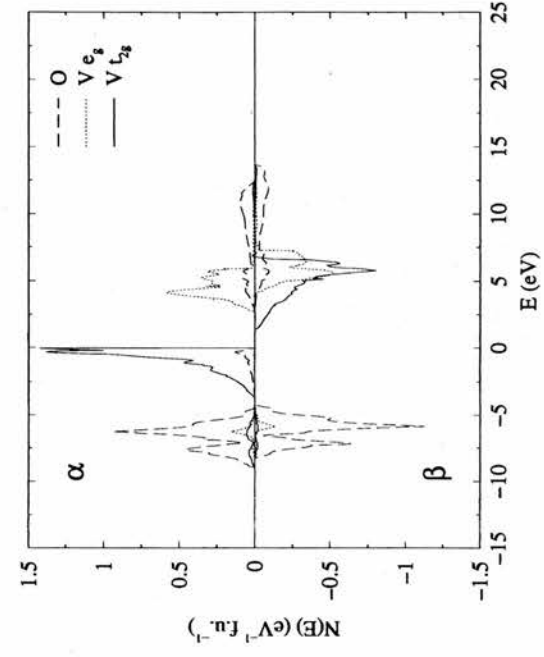
(e)



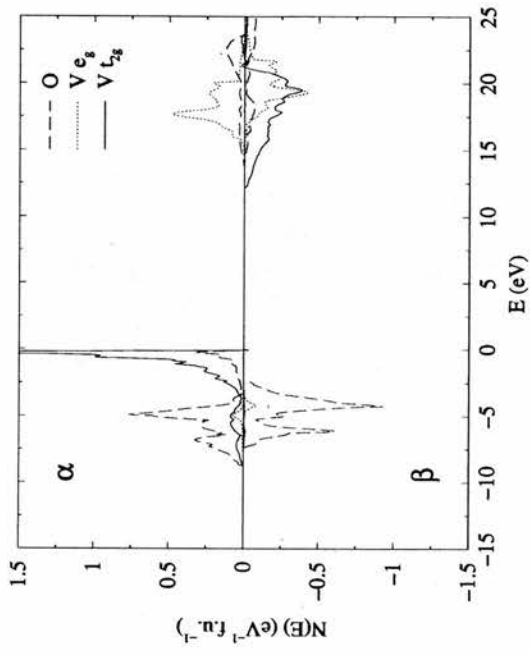
(f)



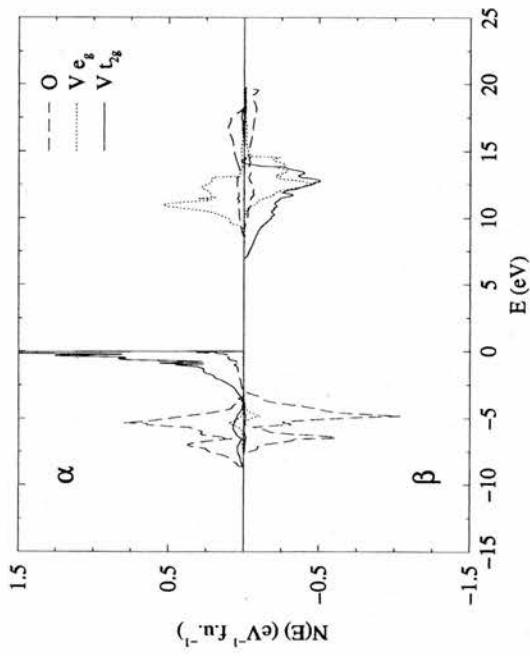
(g)



(h)



(i)



(j)

Figure 3(a-j). Orbital projected densities of states, $N(E)$ (eV^{-1} molecule $^{-1}$) against energy, E (eV); for the AF₁ state at (a) $F_0 = 0.0$, (b) $F_0 = 0.2$, (c) $F_0 = 0.6$, (d) $F_0 = 1.0$; for the AF₂ state at (e) $F_0 = 0.2$, (f) $F_0 = 0.6$, (g) $F_0 = 1.0$; for the FM state at (h) $F_0 = 0.2$, (i) $F_0 = 0.6$, (j) $F_0 = 1.0$.

F ₀	ΔE _g			AF ₁	AF ₂	FM
	AF ₁	AF ₂	FM	W _O , W _{t_{2g}}	W _O , W _{t_{2g}}	W _O , W _{t_{2g}}
UHF	13.955	14.039	13.153	7.297 [†]	7.114 [†]	7.899 [†]
1.0	13.805	14.142	12.141	8.269 [†]	5.537, 2.275	8.736 [†]
0.8	11.045	11.500	9.543	8.254 [†]	5.278, 2.335	8.696 [†]
0.6	8.242	8.896	6.935	5.053, 3.121	4.978, 2.340	8.638 [†]
0.4	5.416	6.196	4.203	4.681, 3.014	4.677, 2.424	8.737 [†]
0.2	2.445	3.239	1.358	4.343, 3.034	4.303, 2.521	4.731, 3.710
0.1	0.926	1.756	0.000	4.178, 3.087	4.104, 2.613	4.478, 3.748
0.0	0.000	—	—	4.046, 13.718 [‡]	—	—

Table 2. Filled to unfilled gap ΔE_g(eV) and filled O(2p) and V(t_{2g}) band widths, W_O(eV) and W_{t_{2g}}(eV) for the AF₁, AF₂ and FM alignments as a function of F₀. [†] Where the O(2p) and V(t_{2g}) bands overlap, the total valence band width is presented as a single entry. [‡] Where the filled V(t_{2g}) band and empty bands overlap, the O(2p) and net conduction band widths are both presented.

An extension of the lines of best fit in Figure 4 down to F₀ = 0.0 for the AF₂ and FM states suggests that the former may retain a small gap of perhaps (0.3 - 0.5) eV, whereas the latter will almost certainly be metallic. The DOS plots shown in Figure 3 indicate that for *all* insulating phases the filled to unfilled gaps are spanned by vanadium states, leading to an unambiguous classification of VO as a MH insulator. Furthermore, the character of the valence and conduction band edges is seen to be independent of magnetic order, so that pressure or temperature induced magnetic transitions would not be expected to result in any change of the insulating character of non-defective VO. An orbital projection of the V(3d) bands confirms that AF₁ symmetry splits the two-fold O_h degeneracy of the 3d-states in the FM and non-magnetic lattices into four non-degenerate sub-bands, leading to an overall d-level ordering and occupancy of the form

$$\underbrace{d_{xz}^1(\uparrow)/d_{yz}^1(\uparrow) < d_{xy}^1(\uparrow)}_{\text{filled}} < \underbrace{d_{xy}^0(\downarrow) < d_{xz}^0(\downarrow)/d_{yz}^0(\downarrow) < d_{z^2}^0(\uparrow) < d_{x^2-y^2}^0(\uparrow)}_{\text{empty}} \dots$$

(Again, in the interests of visual clarity, this set of more detailed projections is not shown on the DOS plots) As F_0 decreases from 0.6 to 0.1, a gap opens between the filled $V(t_{2g})$ and $O(2p)$ bands. The same bands broaden and narrow by $\sim 0.13\text{eV}$ and $\sim 0.88\text{eV}$ respectively across the same range. More importantly, despite an increase in the weight of the minority $V(e_g)$ states as the percentage of exact exchange is reduced, the lower edge of the conduction band in the AF_1 alignment remains predominantly of t_{2g} character for the entire range of single particle potentials considered.

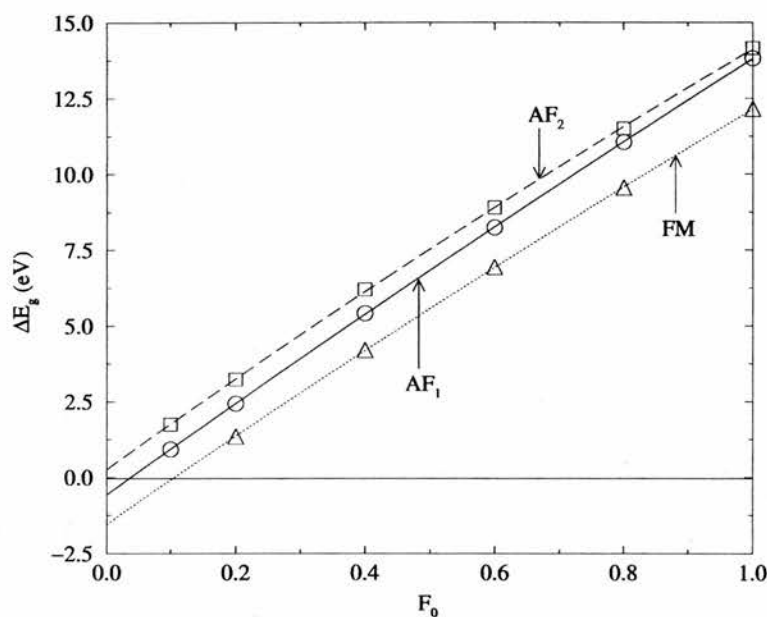


Figure 4. Filled to unfilled energy gap, ΔE_g (eV), for the AF_1 (O), AF_2 (\square) and FM (\triangle) states as a function of F_0 .

These observations raise some interesting issues. While all the low energy gap excitations are locally Laporte forbidden ($\Delta\ell = 0$), as they must be for a MH system, the lowest of these, $d_{xy}(\uparrow) \rightarrow d_{xy}(\downarrow)$, is also spin forbidden ($\Delta S \neq 0$). It is unlikely, therefore, that the latter could be identified with any measurable absorption edge. For the B3LYP potential, which has been observed to yield anion to cation transfer type gap widths in impressive agreement with data from a variety of sources [44], the edge to edge $d_{xy}(\uparrow) \rightarrow d_{xy}(\downarrow)$ ($\Delta S \neq 0$) gap in AF_1 VO is ~ 2.5 eV, the spin-allowed $d_{xy}(\uparrow) \rightarrow d_{z^2}(\uparrow)$ gap ~ 3.0 eV and the $V \rightarrow O$ CT gap ~ 3.5 eV, and it is the latter that might reasonably be expected to lead to a (strong) absorption edge. For interest, the electronic structure of non-defective VO within the B3LYP potential has been

calculated, but at the observed lattice constant for the stoichiometric, *defective* material, 4.063 Å [8]. These calculations indicate the continued stability of the AF₁ magnetic state, and the existence of a $d_{xy}(\uparrow) \rightarrow d_{xy}(\downarrow)$ gap of width 0.97 eV. While this is substantially lower than for the equilibrium structure, the system remains assuredly insulating. The calculations suggest, therefore, that the metallicity observed in samples of VO_x of varying stoichiometry should not be attributed to the properties of the underlying perfect lattice at the contracted cell dimensions, but is more likely a consequence of the presence of defects.

The description of the band structure is reflected in Mulliken analyses of the total wavefunction. At the UHF level of approximation, the overlap population between nearest neighbour V and O sites is -0.04 *e*, that between V(↑) and V(↓) sites is 0.006 *e* and there is virtually no overlap density between V sites with the same spin. The overlap population between O sites is -0.008 *e*, which is marginally antibonding, leading to an overall UHF description of the AF₁ spin alignment as essentially ionic. The introduction of correlation into the UHF potential leads to a general increase in bond populations, indicating a slight overall decrease in the degree of ionicity. Reducing the proportion of exact exchange results in further changes to the overlap populations in AF₁ VO, with an increase in bonding between all nearest neighbour V sites and a reduction in the antibonding character of both V-O and O-O interactions. Progression to the metallic state in the DFT limit leaves the latter two interactions virtually unchanged, whereas the populations associated with V(↑)-V(↓) and V(↑)-V(↑) nn pairing increase from 0.022 *e* and 0.002 *e* respectively at $F_0 = 0.1$ to 0.030 *e* and 0.016 *e*, with a lowering of the Fermi level within the *t*_{2g} manifold. Thus in the pure DFT description of VO it is likely that the metallic state arises from an increased overlap of nearest neighbour V(3d) orbitals.

Overall, the electronic structure of the AF₂ state revealed by the DOS and summarised in Table 2 is quite similar to that of the AF₁, with only minor changes resulting from the difference in symmetry. In contrast to the AF₁ alignment, no splitting of the V(*e_g*) and V(*t_{2g}*) states beyond that produced by the octahedral crystal field is observed, which is entirely consistent with the different symmetries of the two magnetic supercells. Decreasing the proportion of exact exchange leads to an increasing

separation of the valence O(2p) and V(t_{2g}) bands, as in the case of the AF₁ alignment. While the O(2p) band widths are similar, the V(t_{2g}) bands are narrower, indicating a more restricted overlap of orbitals than in the AF₁ alignment. The reason for this lies with the different number of nn cations with parallel and anti-parallel spins in the two alignments. In AF₁ symmetry, each cation interacts with four parallel and eight anti-parallel metal spins, whereas in AF₂ symmetry, the interactions are with six parallel and six anti-parallel spins. Overlap of the occupied d-states is thus more strongly inhibited by exchange in the latter magnetic structure, leading to a narrower d-band. This mechanism has no effect on the anion p-band, which is almost identical for both types of antiferromagnetism. The O(2p) band narrows by $\sim 1.4\text{eV}$ as F_0 varies from 1.0 to 0.1, whereas the V(t_{2g}) band broadens by $\sim 0.3\text{eV}$ across the same range. As in the AF₁ alignment, the conduction band edge is dominated by minority spin t_{2g} states with an increasing weighting of the e_g states as F_0 is decreased.

The DOS of the FM states, with summarising data in Table 2, are naturally quite different to those derived from antiferromagnetic order. The net spin polarisation carried by the lattice acts to suppress the energy of the majority spin orbitals relative to the corresponding minority spin orbitals, leading to broader bands. As shown in Figure 3, only majority spin V(t_{2g}) orbitals occupy the valence band edge, while the conduction band edge is formed from minority spin V(e_g) orbitals. As a result of the band broadening, a splitting of the O(2p) and V(t_{2g}) valence bands does not occur until the exact exchange falls below 20%.

(b) Magnetism and Phase Transitions

Direct and superexchange coupling energies extracted from the total energies of the FM, AF₁ and AF₂ spin alignments are given in Table 3. From the sign of J_d and J_{se} it is evident that both direct and superexchange interactions favour antiferromagnetic alignment of both nn and nnn vanadium spins. There is a four-fold increase in the magnitude of J_d and J_{se} over the range of single particle potentials considered and, as expected from arguments presented in Section 3(a) of this chapter, direct exchange is found to be more than five times stronger than superexchange. The results presented in Chapter 2 for the direct and superexchange coupling constants in NiO lie in the ranges

8.6 – 36.4 °K and 39.6 – 353.6 °K respectively, and for MnO in the ranges 1.6 – 13.1 °K and 6.3 – 25.9 °K respectively for $0.1 \leq F_0 \leq \text{UHF}$. So, it is clear that the direct coupling in VO is ~ 7 and ~ 36 times larger than in NiO and MnO respectively at the UHF level, and ~ 6 and ~ 17 times larger respectively for $F_0 = 0.1$. In contrast, the superexchange coupling in NiO is ~ 4 and ~ 8 times stronger than in VO within the UHF and $F_0 = 0.1$ schemes respectively, while the coupling in VO is stronger than that in MnO by a factor of ~ 2 at both UHF and $F_0 = 0.1$.

F_0	J_d	J_{se}	J_d / S^2 (°K)	J_{se} / S^2 (°K)	T_N AF ₁	T_N AF ₃
UHF	-11.08	+2.02	-57.14	+10.42	186.86	233.65
1.0	-14.80	+2.30	-76.33	+11.86	263.20	316.65
0.8	-17.54	+2.79	-90.47	+14.39	309.87	374.51
0.6	-21.15	+3.50	-109.09	+18.05	369.15	450.14
0.4	-26.67	+4.55	-137.56	+23.47	460.45	565.97
0.2	-35.62	+6.69	-183.72	+34.51	593.49	748.79
0.1	-44.31	+8.80	-228.54	+45.39	721.67	925.83

Table 3. The direct, J_d and superexchange, J_{se} , coupling constants expressed both as energies (meV) and as temperatures (°K, divided by factor $S^2 = 2.25$) and mean field transition temperatures, T_N (°K) for the AF₁ and AF₃ alignments at the optimised AF₁ lattice constants, all as a function of F_0 .

It is straightforward to show that the difference in energy between the AF₁ and AF₃ alignments in the Ising Hamiltonian, $[E(\text{AF}_1) - E(\text{AF}_3)]$, is $2J_{se}$. The mapping suggests that the AF₃ state should be more stable than the AF₁. For the value of J_{se} derived from UHF energies, for example, $[E(\text{AF}_1) - E(\text{AF}_3)]$ amounts to +4meV, whereas the direct total energy difference is -27.5meV. Thus for fully stoichiometric, non-defective VO the stability of the lowest energy spin alignments derived from a mapping of $E(\text{FM})$, $E(\text{AF}_1)$ and $E(\text{AF}_2)$ onto H_{Ising} is predicted to be in the order

$$\text{AF}_3 > \text{AF}_1 > \text{AF}_2 > \text{FM}$$

in contrast to the order of stability obtained *directly* from first principles calculations, which is

$$AF_1 > AF_2 > AF_3 > FM.$$

The root of the disparity lies in the assumption, which is implicit in all mappings of this sort, that the electronic structures and bonding in the four magnetic phases are essentially identical. Differences in energy between them are posited to arise solely from the direct and superexchange coupling of identical local moments in identical electronic environments, leading to identical coupling constants/energies. While this assumption seems to hold for the more ionic systems, MnO and NiO [49], it patently does not hold in the case of VO, as shown by the strong isotropic spin-lattice interaction discussed in Section 3(a) of this chapter. A similar breakdown of the Ising model was found in the study of the crystal field excitations in NiO presented in Chapter 3. Further evidence for the small, but important differences between the three antiferromagnetic phases is found in the integrated densities of valence states. The total p-band UHF oxygen populations (per formula unit) in the AF₁, AF₂ and AF₃ alignments are 5.97e, 5.92e and 5.44e respectively, and corresponding vanadium d-band populations 2.99e, 3.00e and 2.95e. Thus, the population of the O(2p) band in AF₃ alignment is ~ 0.5e less than in the two other AF phases and it is precisely this type of change in electronic structure between different spin states that is not represented by simple spin Hamiltonians.

The above remarks notwithstanding, J_d and J_{se} have been used to provide qualitative estimates of the Néel temperatures of the AF₁ and AF₃ phases. Elementary considerations indicate that within a mean field approximation for H_{Ising}, <σ> for these two phases is given by

$$\begin{aligned} \langle \sigma \rangle_{AF_1} &= \tanh \left[-\frac{2J_d + 3J_{se}}{k_B T} \right] \\ \langle \sigma \rangle_{AF_3} &= \tanh \left[-\frac{2J_d + J_{se}}{k_B T} \right] \end{aligned}$$

which as $\langle \sigma \rangle \rightarrow 0$ leads to

$$T_N[\text{AF}_1] = \frac{-2J_d - 3J_{se}}{k_B},$$

$$T_N[\text{AF}_3] = \frac{-2J_d - J_{se}}{k_B}.$$

The variation of T_N with F_0 is shown in Figure 5, where it should be noted that mean field theory is known to overestimate T_N by a factor $\sim 4/3$ through the neglect of fluctuations. The recent work on MnO and NiO, as presented in Chapter 1 and Ref. [50] has shown that direct and superexchange coupling constants close to the magnon derived values are obtained from hybrid functionals in the Becke-LYP scheme containing 20% to 50% exact exchange, which for VO would lead to a very approximate value for the AF_1 critical temperature in the range 300 – 450K.

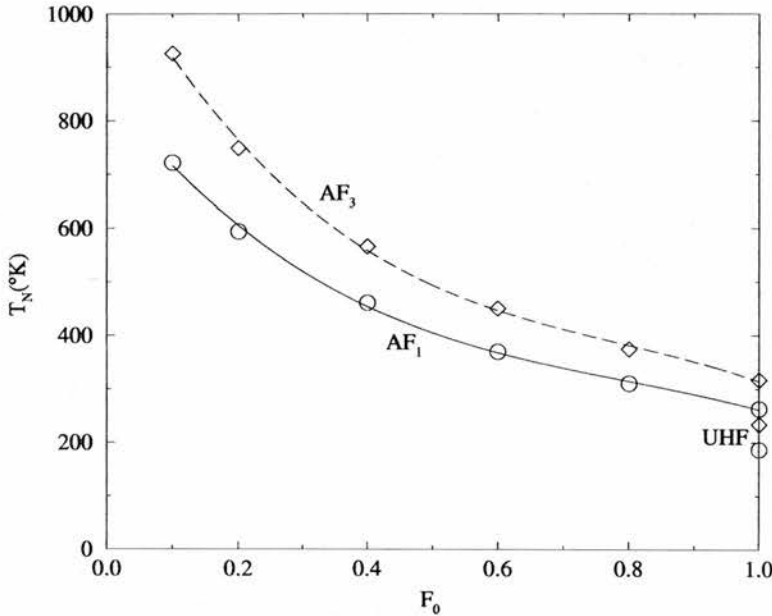


Figure 5. Mean field critical temperature for the AF_1 (O) and AF_3 (\diamond) magnetic states as a function of F_0 .

(c) Crystal Field Excitations

As discussed earlier in Chapters 1, 2 and 3, the existence of weak, orbitally forbidden ($\Delta\ell = 0$) excitations in the paradigm magnetic insulators NiO and MnO has been revealed by optical absorption and EELS studies. The absorptions are found to lie

within the bulk band gap, and have been attributed to $d \rightarrow d$ transitions on the basis of first-principles multi-reference cluster calculations [51-53]. Such excitations are best described as strongly localised Frenkel excitons [54]. In both previous studies and in Chapter 3 of this work, the $d \rightarrow d$ excited states in NiO were found to be stable both in the bulk and the reduced symmetries of the inner and outer layers of $\{100\}$ slabs, with differences in transition energy of $<0.05\text{eV}$ for identical O_h crystal field excitations in the two geometries [55]. The study of crystal field excitations in MnO reported in Chapter 2 used only the slab geometry, so the stability of excitations in the bulk is not clear for MnO. In the present work, stable excited states could not be obtained in the bulk, so that, as for MnO, all the calculations reported here refer to a V ion located upon the central plane of $\{100\}$ slabs consisting of three and five layers. As before [55], the slabs were constructed from (surface) 2×2 supercells in which the $d \rightarrow d$ excitation is confined to one vanadium atom per supercell of the central plane where the (local) crystal field is identical to the bulk and of O_h symmetry. The reference system used has the z^2 orbital perpendicular to the basal $\{100\}$ slab planes, with the (x^2-y^2) orbital pointing toward the neighbouring oxygen atoms.

Now the Kanamori Hamiltonian and the expressions for the crystal field state energies given in Section 2(c) hold for an isolated $3d^n$ ion only, so that they are appropriate for a free ion or an isolated impurity in a non-magnetic lattice. However, for ordered magnetic systems, the interaction with neighbouring spins must be included. In the case of VO, the magnetic states of which are dominated by the direct coupling of nn spins (J_d), the energies of the crystal field states in the FM alignment can be written as,

$$\begin{aligned}
 E_g &= E_{CF}^0 + 3A - 15B - 12J_d, \\
 E_{xy \rightarrow z^2} &= E_{CF}^0 + 3A - 3B + \Delta_{CF} - 8J_d, \\
 E_{xy \rightarrow x^2 - y^2} &= E_{CF}^0 + 3A - 15B + \Delta_{CF} - 8J_d, \\
 E_{xz, yz \rightarrow z^2, x^2 - y^2} &= E_{CF}^0 + 3A - 12B + 2\Delta_{CF} - J_d, \\
 E_{xy(\uparrow) \rightarrow xy(\downarrow)} &= E_{CF}^0 + 3A - 9B + 2C - 4J_d,
 \end{aligned}$$

leading to the following excitation energies,

$$\begin{aligned}
\Delta E_{xy \rightarrow z^2} &= 12B + \Delta_{CF} + 4J_d, \\
\Delta E_{xy \rightarrow x^2 - y^2} &= \Delta_{CF} + 4J_d, \\
\Delta E_{xz, yz \rightarrow z^2, x^2 - y^2} &= 3B + 2\Delta_{CF} + 8J_d, \\
\Delta E_{xy(\uparrow) \rightarrow xy(\downarrow)} &= 6B + 2C + 8J_d.
\end{aligned}$$

Likewise, in the AF₁ alignment, the crystal field energies can be written as,

$$\begin{aligned}
E_g &= E_{CF}^0 + 3A - 15B + 4J_d, \\
E_{xy \rightarrow z^2} &= E_{CF}^0 + 3A - 3B + \Delta_{CF} + 8J_d, \\
E_{xy \rightarrow x^2 - y^2} &= E_{CF}^0 + 3A - 15B + \Delta_{CF} + 8J_d, \\
E_{xz, yz \rightarrow z^2, x^2 - y^2} &= E_{CF}^0 + 3A - 12B + 2\Delta_{CF} - 4J_d, \\
E_{xy(\uparrow) \rightarrow xy(\downarrow)} &= E_{CF}^0 + 3A - 9B + 2C + 12J_d,
\end{aligned}$$

and the excitation energies as,

$$\begin{aligned}
\Delta E_{xy \rightarrow z^2} &= 12B + \Delta_{CF} + 4J_d, \\
\Delta E_{xy \rightarrow x^2 - y^2} &= \Delta_{CF} + 4J_d, \\
\Delta E_{xz, yz \rightarrow z^2, x^2 - y^2} &= 3B + 2\Delta_{CF} - 8J_d, \\
\Delta E_{xy(\uparrow) \rightarrow xy(\downarrow)} &= 6B + 2C + 8J_d.
\end{aligned}$$

From this, it is clear that within the approximation of including only J_d interactions, the energies of the three one-electron excitations are identical in the FM and AF₁ alignments, whereas there is a difference of magnitude $16|J_d|$ for the two-electron excitation. For this reason, the majority of calculations were performed in the computationally more convenient FM arrangement, although, as a check, the excitation energies in both spin alignments for $F_0 = 0.1$ and 0.3 have been calculated and compared. The optimised AF₁ lattice constants were used regardless of the magnetic alignment imposed.

The energies of the spin-allowed ($\Delta S = 0$) one-electron $xy \rightarrow z^2$ and $xy \rightarrow x^2 - y^2$, and two-electron $xz, yz \rightarrow z^2, x^2 - y^2$ trilayer excitations as a function of F_0 are given in Table 4 and those for the spin-forbidden $xy(\uparrow) \rightarrow xy(\downarrow)$ excitation in Table 5. In both cases, the $(\alpha + \beta)$ and $(\alpha - \beta)$ orbital occupancies of the excited state indicate that these excitations are highly local for the entire range of potentials. No stable excitations were found for $F_0 < 0.3$, so that the B3LYP potential ($F_0 = 0.2$) appears to be unable to support these elementary excitations in VO. The introduction of correlation into the UHF potential results increases the three spin-allowed excitation energies, and a decrease in the spin-forbidden energy, which is entirely reasonable, for only the latter involves spin-pairing. The effect is very similar, qualitatively to that observed in the excitations in MnO.

Tables 4 and 5 also support the inclusion of only the $nn J_d$ interactions in the crystal field energies, thus for the one-electron excitations, the differences between the FM and AF₁ energies vary from 0.008eV to 0.085eV, whereas the two-electron excitation, which in our approximation involves a difference of $16 | J_d |$, the differences between the two alignments vary from 0.25eV to 0.43eV. As a further check on the consistency of the calculations, the values of J_d given in Table 3, which are obtained solely from the ground electronic state, predict differences of 0.24eV and 0.48eV for the two-electron excitation. Thereafter, both the energies and occupancies of all four excitations were found to decrease with decreasing exact exchange. As a check on the influence of slab thickness, UHF calculations of the spin-allowed excitations were carried out for 5-layer slabs, resulting in decreases of 0.03eV and 0.08eV respectively for the $xy \rightarrow z^2$ and $xz, yz \rightarrow z^2, x^2 - y^2$ excitations, which are perpendicular to the slab, while the in-plane $xy \rightarrow x^2 - y^2$ energy does not change. Quite reasonably, perpendicular excitations are the more sensitive to slab thickness, though the relatively small differences between the 3- and 5-layer energies suggest that Tables 4 and 5 give a qualitatively correct indication of the weak absorptions in stoichiometric VO, especially in view of the relative insensitivity of the energies to the proportion of exact exchange.

F ₀	State	xy → z ²			xy → x ² -y ²			xz, yz → z ² , x ² -y ²		
		ΔE	α+β	α-β	ΔE	α+β	α-β	ΔE	α+β	α-β
UHF	FM	2.519	0.925	0.940	1.175	0.916	0.943	2.689	0.936, 0.936	0.934, 0.947
1.0	FM	2.638	0.921	0.939	1.300	0.911	0.939	2.932	0.931, 0.929	0.930, 0.942
	AF ₁	2.649	0.914	0.930	1.308	0.930	0.937	3.182	0.923, 0.924	0.923, 0.939
0.9	FM	2.602	0.916	0.934	1.294	0.907	0.936	2.920	0.927, 0.925	0.925, 0.940
0.8	FM	2.563	0.910	0.929	1.285	0.901	0.932	2.905	0.923, 0.921	0.921, 0.936
0.7	FM	2.522	0.902	0.924	1.278	0.896	0.929	2.888	0.916, 0.917	0.917, 0.932
0.6	FM	2.471	0.893	0.915	1.267	0.888	0.924	2.863	0.911, 0.911	0.910, 0.926
0.5	FM	2.416	0.877	0.900	1.251	0.878	0.918	2.837	0.902, 0.904	0.902, 0.921
0.4	FM	2.338	0.847	0.868	1.233	0.867	0.908	2.798	0.890, 0.895	0.887, 0.911
0.3	FM	2.194	0.761	0.770	1.200	0.849	0.896	2.734	0.867, 0.881	0.864, 0.898
	AF ₁	2.279	0.828	0.851	1.210	0.883	0.897	3.164	0.865, 0.872	0.868, 0.893

Table 4. Excitation energies, ΔE (eV) and excited orbital charge (α+β) and spin (α-β) occupation for the three spin-allowed, Laporte-forbidden transitions as a function of F₀.

In the case of NiO [56,57], La₂CuO₄ [58,59] and Sr₂CuO₂Cl₂ [60] and other first row TM chalcogenides where d→d excitations have been observed, an important consideration is their juxtaposition to the strong anion to cation CT absorption edge. For MH systems there is the added interest of comparing the energies of on-site and edge-to-edge (band) excitations of the same orbital types, from which energies of localisation of Frenkel excitons can be estimated. While such comparisons can be made for the full range of exchange-correlation potentials, the evidence presented in reference [48] suggests that comparisons for the B3LYP potential might be the most meaningful. In the absence of direct values, extrapolating the energies given in Tables 4 and 5 yields approximate B3LYP values of ~0.5 eV, ~2.1 eV and ~1.2 eV for the crystal field $xy(\uparrow)\rightarrow xy(\downarrow)$, $xy(\uparrow)\rightarrow z^2(\uparrow)$ and $xy(\uparrow)\rightarrow x^2-y^2(\uparrow)$ excitations respectively. These compare with edge-to-edge (band) values in the AF₁ alignment of ~ 2.5eV, ~ 3.2eV and ~ 3.1eV respectively, leading to Frenkel localisation energies of ~ 2.0 eV, ~ 1.1 eV and ~ 1.9 eV. Furthermore, all four crystal field excitations are predicted to lie below the strong V→O CT absorption.

F ₀	State	ΔE	α+β	α-β
UHF	FM	1.395	1.013	-0.976
1.0	FM	1.151	1.010	-0.964
	AF ₁	1.133	1.015	-0.971
0.9	FM	1.072	1.012	-0.964
0.8	FM	1.012	1.012	-0.959
0.7	FM	0.950	1.011	-0.952
0.6	FM	0.881	1.011	-0.943
0.5	FM	0.809	1.009	-0.930
0.4	FM	0.724	1.005	-0.911
0.3	FM	0.619	0.997	-0.882
	AF ₁	0.675	1.018	-0.905

Table 5. Excitation energy, ΔE (eV) and excited orbital charge and spin occupation for the spin- and Laporte-forbidden $xy(\uparrow)\rightarrow xy(\downarrow)$ transition as a function of F₀.

Values for B, C, Δ_{CF} , d-averaged J and the Tanabe-Sugano Γ parameter (C/B) [61] derived from the trilayer excitations and free V^{2+} ion are presented in Table 6. As the proportion of exact exchange is decreased the lattice values of B, C and J decrease, which once again reflects the increasing covalency of the bonding in VO as the limiting DFT description is approached. No real trend is apparent in Δ_{CF} with changing F_0 . For the free ion, both B and J decrease with F_0 , although there appears to be a very minor upturn in J as the stability limit for the crystal field excitations is reached.

The free ion B, C and Γ parameters for all Hamiltonians compare with values of 0.0936 eV, 0.4038 eV and 4.314 respectively reported by Tanabe and Sugano [61]. A comparison of the lattice and free ion parameters shows that the Racah C parameter is strongly reduced by the crystalline environment, notably as the proportion of exact exchange decreases, leading to reduced Hund exchange coupling. As previously discussed in Chapter 1, low spin states at unrealistic energies are a feature of pure DFT-GGA calculations in the late transition metal oxides, which predict magnetic collapse at modest hydrostatic pressures [62]. However, XES measurements in FeO [63] indicate that if such spin transitions do occur, they will be at significantly greater pressures than those derived from the GGA calculations. Data collected and presented by Tanabe and Sugano [61] suggest that the value of Γ for free ions, substitutional impurities and cations in the binary oxides is roughly constant and in the range 4.2 - 4.5 across the first row transition metals. Here, only the UHF values approach this range, and while the free ion values for low F_0 might be acceptably close, in the crystalline environment, Γ is reduced to pathologically low levels as the proportion of exact exchange is reduced.

F ₀	State	Lattice (Trilayer)						Free V ²⁺ Ion			
		B	C	Δ _{CF}	J	ΔE _{2P}	Γ	B	C	J	Γ
UHF	FM	0.1119	0.4059	1.220	0.6858	2.687 (-0.09%)	3.6264	0.1143	0.4536	0.7394	3.9685
1.0	FM	0.1115	0.3003	1.359	0.5790	2.934 (+0.07%)	2.6939	0.1152	0.3534	0.6414	3.0677
	AF ₁	0.1118	0.3895	1.367	0.6689	3.188 (+0.19%)	3.4853				
0.9	FM	0.1090	0.2721	1.357	0.5447	2.915 (-0.19%)	2.4965	0.1132	0.3369	0.6199	2.9761
0.8	FM	0.1064	0.2564	1.355	0.5225	2.890 (-0.52%)	2.4092	0.1113	0.3226	0.6009	2.8985
0.7	FM	0.1036	0.2415	1.356	0.5006	2.867 (-0.70%)	2.3310	0.1093	0.3131	0.5864	2.8646
0.6	FM	0.1004	0.2250	1.352	0.4759	2.835 (-1.00%)	2.2414	0.1073	0.3100	0.5783	2.8891
0.5	FM	0.0971	0.2078	1.345	0.4505	2.793 (-1.54%)	2.1401	0.1053	0.3132	0.5765	2.9744
0.4	FM	0.0921	0.1913	1.338	0.4216	2.742 (-2.03%)	2.0765	0.1033	0.3179	0.5762	3.0774
0.3	FM	0.0828	0.1819	1.321	0.3889	2.648 (-3.13%)	2.1965	0.1013	0.3248	0.5781	3.2063
	AF ₁	0.0891	0.1911	1.331	0.4139	3.170 (+0.19%)	2.1443				

Table 6. Racah B (eV) and C (eV) parameters, d-manifold averaged interband exchange constant, J (eV) and ratio $\Gamma = C / B$ for the V ion both free and within the lattice, as a function of F₀. Also shown are the crystal field splitting parameter, Δ_{CF} (eV) and the two-particle (xz,yz)→(z²,x²-y²) excitation energy, ΔE_{2P} (eV) and deviation from the directly calculated value (Table 4) predicted on the basis of the single-particle B and Δ_{CF} parameters

Also included in Table 6 is a comparison of $\Delta E_{xy,yz \rightarrow z^2, x^2-y^2}$ derived from the (mapped) crystal field parameters and those obtained directly from first principles calculations. The close agreement between the two supports the validity of mapping first principles energies onto the Kanamori crystal field Hamiltonian, notably at the UHF level of approximation. In the limit of exact exchange the percentage difference between the direct and indirect (mapped) excitation energies is 0.1% and even at the stability limit of the excited states, $F_0 = 0.3$, the difference is only 3%.

4. Summary and Conclusions

The principal conclusion of this first principles study of stoichiometric, non-defective VO is that the ground electronic state in the rocksalt ($Fm\bar{3}m$) structure is that of a d^3 high spin, antiferromagnetic, Mott-Hubbard insulator with an AF_1 spin alignment of the local cation moments. Furthermore, this description remains essentially unchanged for single particle Hamiltonians ranging from pure UHF, i.e. exact exchange, to exchange-correlation potentials containing down to 10% exact exchange. It is only for the pure DFT potential that the AF_1 phase is predicted to be metallic. Further important conclusions are that:

- (i) for the full range of insulating potentials there is strong spin-lattice interaction with differences in lattice constant of up to 1.6% between AF_1 and FM order
- (ii) the AF_1 lattice constant is predicted to lie in the range 4.35 – 4.37 Å, with a value of 4.37Å suggested by direct comparison with a similar range of calculations for the AF_2 alignment of MnO. These values are roughly 7% greater than the reported lattice constants for the stoichiometric, defective material [8,9]
- (iii) from a mapping of the total energies of the AF_1 , AF_2 and FM alignments onto an Ising spin Hamiltonian containing both direct and superexchange interactions the dominant magnetic interaction is revealed to be the direct coupling of antiferromagnetically aligned nearest neighbour cation spins which leads to the stability of the AF_1 phase. While the entire range of insulating potentials favours the AF_1 alignment, there is a four-fold increase in the direct coupling constant from -11.08 meV to -44.31 meV as the proportion of exact

exchange is reduced from the correlated UHF limit down to 10%. This in turn leads to an estimated critical disorder temperature in the range 300K – 450K

- (iv) the limitations of such a mapping are exposed by a consideration of the AF₃ structure which fitted coupling constants derived from FM, AF₁ and AF₂ total energies predict to be more stable than AF₁, in contrast to direct total energy calculations
- (v) from orbital projected densities of states the filled to unfilled gaps are found to depend strongly on the proportion of exact exchange and for the widely-examined B3LYP potential are ~2.5eV for the spin-forbidden $xy(\uparrow) \rightarrow xy(\downarrow)$ excitation, ~3.0 eV for $xy(\uparrow) \rightarrow z^2(\uparrow)$ and ~3.5eV for V→O charge transfer. The latter might reasonably be identified with a (strong) absorption edge
- (vi) that variationally stable, highly local crystal field excited states ranging in energy from ~0.6 eV to ~2.7 eV are predicted for exchange-correlation potentials down to 30 % exact exchange and that all these lie below the absorption edge. From comparisons with the corresponding band excitations estimates of ~1eV to ~2eV are obtained for the Frenkel localisation energy of the crystal field states
- (vii) that a mapping of the excited crystal field energies onto a Kanamori Hamiltonian leads to values for the (solid state) Racah B and C parameters, and d-orbital averaged exchange and crystal field energies. A comparison of fitted and directly-calculated energies for the spin-allowed two electron excitation $xz/yz \rightarrow z^2/x^2-y^2$ confirms the validity of such mapping

Finally, there is the problematic issue as to whether there is an ‘optimum’, or even ‘preferred’, hybridisation for VO, as discussed for NiO [32,43]. Clearly the lack of quantitative data for the fully stoichiometric, non-defective material leaves this unresolved at present. However, even for systems such as NiO and MnO, where the data are more plentiful, the values of F_0 that lead to the best agreement with experiment, as found in Chapter 2, appear to be both property and system dependent. For the currently reported range of exchange-correlation functionals, hybridisation in the mid-region, i.e. F_0 in the range 0.3 – 0.6 leads to the widest agreement with experiment, so that the final conclusion of this Chapter is that is that the ‘optimum’ choice for stoichiometric, non-defective VO lies within this range.

5. References

- [1] B. Weckuysen and D. E. Keller, *Cat. Today*, **78**, 25 (2003) (and references therein)
- [2] K. West, B. Zachaustriansen, M. J. J. Ostergard and T. Jacobsen, *J. Power Sources* **20**, 165 (1987)
- [3] J. Verkelis, Z. Bliznikas, K. Breive, V. Dikinis and R. Saramaitis, *Sensors and Actuators A – Physical* **68**, 338 (1998)
- [4] K. S. Pillai, F. Krumeich, H. J. Muhr, M. Niederberger, R. Nesper, *Solid State Ionics* **141**, 185 (2001)
- [5] W. Klemm and Z. Grimm, *Z. Anorg. Allgem. Chem.* **250**, 42 (1940)
- [6] N. Schönberg, *Acta Chem. Scand.* **8**, 221 (1954)
- [7] G. Andersson, *Acta Chem. Scand.* **8**, 1599 (1954)
- [8] R. E. Loehman, C. N. R. Rao and J. M. Honig, *J. Phys. Chem.* **73**, 1781 (1969)
- [9] M. D. Banus, T. B. Reed and A. J. Strauss, *Phys. Rev. B* **5**, 2775 (1972)
- [10] F. J. Morin, *Phys. Rev. Lett.* **3**, 34 (1959)
- [11] I. G. Austin, *Phil. Mag.* **7**, 961 (1962)
- [12] S. Kawano, K. Kosuge and S. Kachi, *J. Phys. Soc. Japan* **21**, 2744 (1966)
- [13] M. D. Banus and T. B. Reed in “The Chemistry of Extended Defects in Non-Metallic Solids”, L. Eyring and M. O’Keeffe eds. (North Holland, Amsterdam, 1970) pp. 488 ff.
- [14] P.V. Gel’d, S. I. Alyamovskii and I. I. Matveenکو, *Zhurn. Strukt. Khim.* **2**, 301 (1961)
- [15] C. M. Ariya, B. Y. Brach and V. A. Vladimirova, *Vestn. Leningrad Univ. Fiz. Khim.* **22**, 157 (1967)
- [16] H. Takei and S. Koide, *J. Phys. Soc. Japan* **24**, 1394 (1968)
- [17] S. Kawano, K. Kosuge and S. Kachi, *J. Phys. Soc. Japan* **27**, 1076 (1969)
- [18] J. M. Honig, W. E. Wahnsiedler, M. D. Banus and T. B. Reed, *J. Solid State Chem.* **2**, 74 (1970)
- [19] K. Suzuki and S. Takeuchi, *Ferrites*, Proc. Int. Conf. 1970, Y Hoshino ed. (University Park Press, Baltimore Md, 1971) p. 568 ff.

- [20] M. I. Aivazov, J. A. Domashnev, A. G. Sarkisyan and S. V. Gurov, *Izv. Akad. Nauk SSSR Neorg. Mater.* **8**, 1069 (1972)
- [21] W. E. Wahnsiedler and J. M. Honig, *J. Phys. Chem. Solids* **33**, 1836 (1972)
- [22] A. H. Wilson, "The Theory of Metals" (Cambridge University Press, 1954)
- [23] J. C. Slater, *Phys. Rev.* **81**, 385 (1951)
- [24] T. E. Norwood and J. L. Fry, *Phys. Rev. B* **2**, 472 (1970)
- [25] L. F. Mattheiss, *Phys. Rev. B* **5**, 290 and 306 (1972)
- [26] A. Neckel, P. Rastl, R. Eibler, P. Weinberger and K. Schwarz, *J. Phys. C* **9**, 579 (1976)
- [27] L. Hedin and B. I. Lundquist, *J. Phys. C* **4**, 2064 (1971)
- [28] O. K. Andersen, H. L. Skriver, H. Nohl and B. Johansson, *Pure Appl. Chem.* **52**, 93 (1979)
- [29] W.C. Mackrodt, N.M. Harrison, V.R. Saunders, N.L. Allan, M.D. Towler, E. Aprà and R. Dovesi, *Phil. Mag. A* **68**, 653 (1993)
- [30] J. Zaanen, G.A. Sawatzky and J.W. Allen, *Phys. Rev. Lett.* **55**, 418 (1985)
- [31] K. Terakura, T. Oguchi, A. R. Williams and J. Kübler, *Phys. Rev. B* **30**, 4734 (1984)
- [32] T. Bredow and A. R. Gerson, *Phys. Rev B* **61**, 5194 (2000)
- [33] Ph. Dufek, P. Blaha, V. Sliwko and K. Schwarz, *Phys. Rev. B* **49**, 10170 (1994)
- [34] Z.-X. Shen, R. S. List, D. S. Dessau, B. O. Wells, O. Jepsen, A. J. Arko, R. Bartlett, C. K. Shih, F. Parmigiani, J. C. Huang and P. A. P. Lindberg, *Phys. Rev B* **44**, 3604 (1991)
- [35] T. C. Leung, C. T. Chan and B. N. Harmon, *Phys. Rev. B* **44**, 2923 (1991)
- [36] W. E. Pickett, *Rev. Mod. Phys.* **61**, 433 (1989)
- [37] A. Svane and O. Gunnarsson, *Phys. Rev. Lett.* **65**, 1148 (1990)
- [38] Z. Szotek, W. M. Temmerman and H. Winter, *Phys. Rev. B* **47**, 4029 (1993)
- [39] V. I. Anisimov, J. Zaanen and O. K. Andersen, *Phys. Rev. B* **44**, 943 (1991)
- [40] V. I. Anisimov, I. V. Solovyev, M. A. Korotin, M. T. Czyzyk and G. A. Sawatzky, *Phys. Rev. B* **48**, 16929 (1993)
- [41] V.I. Anisimov, F. Aryasetiawan, and A.I. Liechtenstein. *J. Phys.: Condens. Matter.* **9**, 767 (1997)

- [42] C. Leung, M. Weinert, P. B. Allen and R. M. Wentzcovitch, *Phys. Rev. B* **54**, 7857 (1996)
- [43] I. P. R. Moreira, F. Illas and R. L. Martin, *Phys. Rev. B* **65**, 155102 (2002)
- [44] J. Muscat, A. Wander and N. M. Harrison, *Chem. Phys. Lett.* **342**, 397 (2001)
- [45] V. R. Saunders, R. Dovesi, C. Roetti, M. Causà, N. M. Harrison, R. Orlando and C. M. Zicovich-Wilson, *CRYSTAL98 User's Manual*, University of Torino, Torino, 1998
- [46] F. D. Murnaghan, *Proc. Natl. Acad. Sci.* **30**, 244 (1944)
- [47] P. R. Son and R. A. Bartels, *J. Phys. Chem. Solids* **33**, 819 (1972)
- [48] M. R. Notis, R. M. Spriggs and W. C. Hahn, *J. Appl. Phys.* **44**, 4165 (1973)
- [49] M. D. Towler, N. L. Allan, N. M. Harrison, V. R. Saunders, W. C. Mackrodt and E. Aprà, *Phys. Rev. B* **50**, 5041 (1994)
- [50] F. Corà, M. Alfredsson, G. Mallia, D. S. Middlemiss, W. C. Mackrodt, R. Dovesi and R. Orlando, to be published in *Structure and Bonding*, Springer-Verlag 2004.
- [51] A. Freitag, V. Staemmler, D. Cappus, C. A. Ventrice, K. Al Shamery, H. Kuhlenbeck, H.-J. Freund, *Chem. Phys. Lett.* **210**, 10 (1993)
- [52] C. de Graaf, H. Broer and W. C. Nieuwpoort, *Chem. Phys.* **208**, 35 (1996)
- [53] M. Geleijjins, C. de Graaf, H. Broer and W. C. Nieuwpoort, *Surf. Sci* **421**, 106 (1999)
- [54] C. Kittel, *Introduction to Solid State Physics 6th Edition*, Wiley and Sons New York, 1986
- [55] W. C. Mackrodt and C. Noguera, *Surf. Sci.* **457**, L386 (2000)
- [56] B. Fromme, M. Schmitt, E. Kisker, A. Gorschlüter and H. Merz, *Phys. Rev. B* **50**, 1874 (1994)
- [57] B. Fromme, M. Möller, Th. Anschütz, C. Bethke and E. Kisker, *Phys. Rev. Lett.* **77**, 1548 (1996)
- [58] R. Liu, D. Salamon, M. V. Klein, S. L. Cooper, W. C. Lee, S. W. Cheong and D. M. Ginsberg, *Phys. Rev. Lett.* **71**, 3709 (1993)
- [59] J. P. Falck, J. D. Perkins, A. Levy, M. A. Kastner, J. M. Graybeal and R. J. Birgeneau, *Phys. Rev. B* **49**, 6246 (1994)
- [60] P. Kuiper, J. H. Guo, C. Sàthe, L.-C. Duda, J. Nordgren, J. J. M. Poethuizen, F. M. F. de Groot and G. A. Sawatzky, *Phys. Rev. Lett.* **80**, 5204 (1998)

- [61] S. Sugano, Y. Tanabe and H. Kamimura, *Multiplets of Transition-Metal Ions in Crystals*, Academic Press, New York 1970
- [62] R. E. Cohen, I. I. Mazin and D. G. Isaak, *Science* 275, 654 (1997)
- [63] J. Badro, V. V. Struzhkin, J. Shu, R. J. Hemley, H. K. Mao, C. C. Kao, J-P. Rueff and G. Shen, *Phys. Rev. Lett.* 83, 4101 (1999)

Chapter 6

A Plane-Wave Pseudopotential Study of Defective Structures in Vanadium Monoxide

1. Introduction

The three monoxides TiO, VO and NbO all show the ability to accommodate large concentrations of anion and cation defects on underlying perfect rocksalt lattices. In NbO_{1.0} vacancies at 25% concentration on both sublattices are ordered up to the melt in a narrow homogeneity range [1], while in TiO_x two stable ordered defect structures are found, namely, the Ti₅O₅ structure with a 16% concentration of anion and cation vacancies [2] for temperatures below approximately 1300K and stoichiometry in the range $0.9 \leq x \leq 1.1$, and the TiO_{1.25} structure with 20% vacancies on the cation sublattice alone. In VO_x, curves of partial molar oxygen enthalpy against stoichiometry at 1323K [3] indicate that the strengths of the inter-vacancy interactions are weak, which would fit with the lack of observation of any ordered structure at lower temperatures. All three monoxides display semi-metallic or metallic conductivities [4-6] and it is credible that screening by conduction electrons could account for some weakening of the vacancy interactions, although why this would not affect the ordered phases of TiO and NbO remains unclear. Proceeding from this assumption, Giaconia and Tetot constructed a model for the randomly distributed defects in VO_x based upon the Ising lattice gas Hamiltonian with inter-vacancy interactions set to zero. It was found to account well for the observed partial molar oxygen free energy and enthalpy curves at 1300K [7].

Band theory calculations by Burdett and Highbanks [8] confirmed the stability of the Ti₅O₅-type structure in rocksalt oxides with d² metal orbital occupancy, and the NbO-type structure for d³ compounds. In NbO they concluded that the defect structure is stabilised by the appearance of filled states associated with anion vacancies in the gap between occupied oxygen and occupied metal bands. In their analysis, the square planar coordination of both Nb and O gives rise to a stabilisation of metal z² orbitals

which would normally be unoccupied in octahedral d^3 . The z^2 orbitals point toward and contribute significant electron density to the region of the neighbouring vacancy, resulting in overlap with eight nearest neighbour metal atoms and strong metal-metal bonding interaction. The oxygen p_z orbital is destabilised in the planar geometry, 4-fold coordinated oxygen normally favouring a tetrahedral environment, but Nb-O p_z π interactions can partially alleviate this providing that the occupation of Nb-O antibonding states can be avoided. Metal loss from the crystal then occurs so that the electron count leads to a Fermi energy lying just below the antibonding states, which occurs for the experimentally observed 25% vacancy concentration. Leung *et al* [9] in their LDA PW-PP calculations observe the formation of anion vacancy states below the Fermi energy in Ti_5O_5 and propose a similar stabilisation mechanism, although in this material only some of the metal atoms lie in square planar environments.

For $VO_{1.0}$, the X-ray and pycnometric densities are 6.5 and 5.6 g cm^{-3} respectively, indicating the presence of defects at $\sim 15\%$ concentration [10]. Lattice constants of 4.071\AA [11] and 4.063\AA [12] have been found at these vacancy concentrations.

1.1 The Plane-Wave Pseudopotential Method

The basic theory underlying the plane wave pseudopotential (PW-PP) method has been outlined in Chapter 1. This section will concentrate upon explaining why the PW-PP method is used in this study, in preference to the all-electron LCAO code. Ab-initio molecular dynamics simulations based upon density functional theory may now be routinely applied to systems containing some hundreds of atoms. The choice of plane-waves for the expansion of the single particle orbitals in these methods is a natural one; for it permits the use of economical fast Fourier transform algorithms, and, since plane-waves are independent of atomic position, direct access to the forces is achieved through the Hellman-Feynman theorem. The stress tensor acting upon the cell is also easily calculated, although a correction is usually applied here for the effect of a finite basis. In addition, plane-waves do not suffer from basis set superposition error and treat the representation of electron density at all points in the simulation cell equally. It is this ready availability of forces and stresses that is of great use in the current study, for two of the four structures under investigation have a

number of atomic and cell degrees of freedom which would be nigh impossible to optimise in an acceptable time with a localised basis set code.

The use of a plane-wave basis necessarily leads to the introduction of pseudopotentials for the interaction between valence electrons and atomic cores, for the representation of core penetrating valence states in a bare Coulomb potential would be prohibitively expensive. It is generally known that the use of conventional norm-conserving pseudopotentials is inadequate for the description of transition metal bearing structures, and so highly transferable ultra-soft pseudopotentials in the Vanderbilt formalism generated using the PBE functional are employed for vanadium and oxygen with valence 5 and 6 respectively. To take account of the interaction of vanadium valence electrons with the frozen semi-core $3s^2 3p^6$ states, non-linear core correction is applied. No core correction is used for oxygen, for there only the 1s states are frozen. As a validation of the pseudopotentials and computational conditions used in the plane-wave study, the results of CASTEP calculations for the FM alignment of a single unit cell of VO are compared with CRYSTAL98 all-electron results. Values of $a_0 = 4.360\text{\AA}$ for the lattice constant, $n_s = 2.44\mu_B$ for the unpaired vanadium spin and $q = 1.32e$ for the metal charge emerging in the AF₁ alignment at $F_0=0.0$ from the CRYSTAL98 code compare with $a_0 = 4.290\text{\AA}$, $n_s = 2.28\mu_B$ and $q = 0.72e$ for CASTEP calculations neglecting non-linear core correction and $a_0 = 4.367\text{\AA}$, $n_s = 2.30\mu_B$ and $q = 0.64e$ when the correction is applied. While lattice constants and unpaired spin densities appear to agree well between CRYSTAL98 and the core-corrected method, atomic charges obtained from the projection of the plane-wave wavefunction onto an arbitrary LCAO basis seem consistently lower than those obtained from CRYSTAL98. In a previous study of plane-wave population analysis techniques by Segall *et al* [13] the ionic transfer of NaCl and MgO were found to be 0.42 and 0.76e respectively. It would seem, therefore that underestimation of the ionic charge of oxides is common in the plane wave projection method, and this study adopts the strategy of analysing the relative differences in charge between different structures.

Convergence tests with respect to the plane wave kinetic energy cut-off were conducted for trial versions of each of the structures discussed below. Convergences of 1.6, 1.4, 1.4 and 1.5 meV atom⁻¹ were obtained between cut-off energies of 441eV

and 450eV for the non-defective VO and defective V_7O_7 , V_5O_5 and V_3O_3 structures respectively. Since it is known that differences in total energies converge more rapidly than absolute values, a cut-off of 450eV was deemed adequate. A Monkhorst-Pack shrinking factor of 12 was found to offer convergence to less than 1 meV atom⁻¹ in the primitive cell of the ferromagnetic $Fm\bar{3}m$ structure. The reciprocal space sampling for all other structures was performed upon meshes of a density as close to this as possible.

2. The 1 in 4 (NbO-Type) Ordered Defect Structure

As discussed in Section 1, for stoichiometric VO_x vacancies on the anion and cation sublattices are estimated to occur with ~16% concentration. The niobium oxide type defect structure (V_3O_3), shown in Figure 1 below, incorporates vacancies on both sublattices at 25% and thus exceeds the observed concentration for $VO_{1.0}$. The energetics and electronic structure of the lattice were nevertheless pursued for the insight they may offer into the lower defect concentrations. The ordered structure has space group $Pm\bar{3}m$ (international table number 221, origin 1) with 48 symmetry operators, and is equivalent to the conventional B1 crystallographic cell with the introduction of a metal vacancy at (0,0,0) and an oxygen vacancy at ($\frac{1}{2}, \frac{1}{2}, \frac{1}{2}$). In all subsequent calculations, a kinetic energy cut-off of 450eV, and an FFT grid of dimension (36,36,36) were employed. It was found that reciprocal space sampling with an isotropic Monkhorst-Pack shrinking factor of 8 was sufficient, leading to 20 k-points in the irreducible Brillouin zone (IBZ). SCF, total energy and RMS stress convergence tolerances were set at $2E-6$ eV atom⁻¹, $5E-6$ eV atom⁻¹ and 0.02 GPa respectively. The initial spin polarisation of the cell was held at $9\mu_B$ for the first 10 cycles of the 0GPa run, and allowed to relax thereafter. Stress tensors equivalent to hydrostatic pressures of -20, -10, 0, 10, 20 and 40 GPa were applied, and corresponding lattice constants, a_0 were obtained from geometry optimisations with finite basis set correction. Obviously, the lattice constant for a given pressure could also be obtained simply by interpolation between calculations at fixed atomic geometries, but the present method is used to allow comparison of the energies found in the NbO-type structure with those for more complex defect supercells in which finite basis correction of the stress is unavoidable.

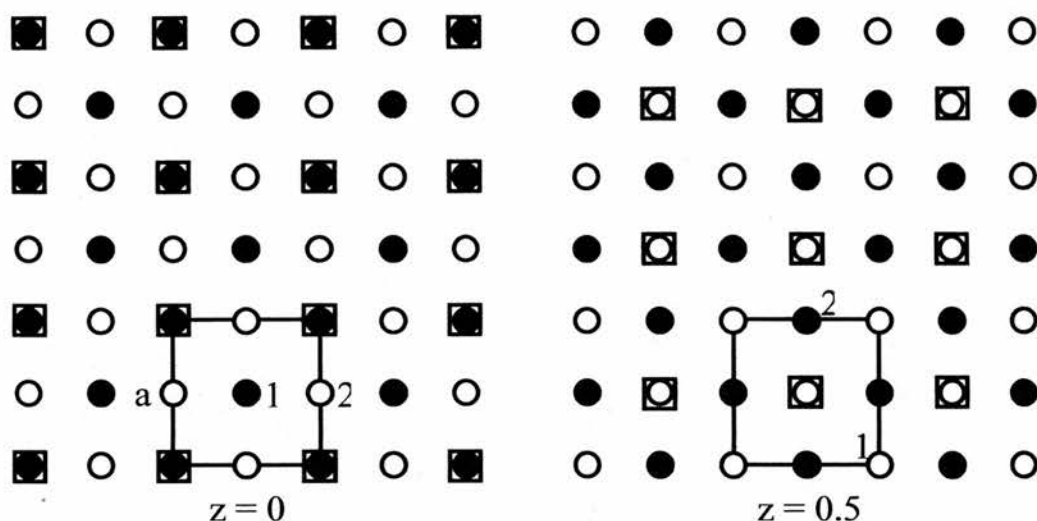


Figure 1. The $z = 0$ (left) and $z = 0.5$ (right) planes of the niobium oxide type defect structure. ● = vanadium, ○ = oxygen, □ = vacancy of appropriate type.

The optimised lattice constant and molecular volume for varying pressures are presented in Table 1 below. At equilibrium, the V_3O_3 structure has a molecular volume some 0.6059\AA^3 higher than the optimised perfect lattice, and a cell length some 0.057\AA lower than the value 4.063\AA observed in the random defect structure by Loehman *et al* [12]. The increase in molecular volume in V_3O_3 is of interest, for it suggests that the defects have a positive volume.

P	a_0	V	E
-10	4.0670	22.4234	-818.6996
0	4.0058	21.4263	-818.7450
10	3.9613	20.7202	-818.7085
20	3.9210	20.0948	-818.6507
40	3.8550	19.0969	-818.4676

Table 1. The lattice constant, a_0 (\AA), volume per molecule, V (\AA^3), and energy per molecule, E (eV) for the NbO-type defect structure at hydrostatic pressure P (GPa).

A Mulliken analysis is performed on the wavefunction as projected onto a set of atomic orbitals internal to the CASTEP code. It should be stressed that the localised

set of orbitals is in no way used in the SCF. An indication of the quality of the projection is provided by the spilling parameter, defined as the sum of the charge in the total plane-wave electronic density which is unaccounted for in the localised basis representation. A maximum spilling of 0.70% of the summed density is found at pressure -10GPa, which is entirely satisfactory. The results of the Mulliken analysis are presented in Table 2 below. Also included is the analysis of a run at the equilibrium volume in which the total spin of the cell was locked to $9\mu_B$ to convergence. This solution lies some 1.790 eV per molecule higher in energy than the ground magnetic state. At 0GPa, a reduction in ionic charge of $\sim 23\%$ is noted in going from the perfect lattice to V_3O_3 , with an increase in metal-oxygen bond population of $\sim 0.1e$. Most dramatically of all, a complete collapse of magnetism on the metal sites is predicted. The forced ferromagnetic run deposits all unpaired spin density on the metal atoms and shows an increase in ionic charge of $\sim 14\%$ over the unconstrained solution, while the metal-oxygen overlap remains essentially unchanged.

P	Oxygen					Vanadium					O
	s	p	d	q	n_s	s	p	d	q	n_s	
-10	1.84	4.66	0.00	-0.49	0.00	0.18	0.16	4.17	0.49	0.00	0.31
0	1.83	4.66	0.00	-0.49	0.00	0.17	0.13	4.22	0.49	0.00	0.31
0^\dagger	1.82	4.73	0.00	-0.56	0.00	0.14	0.22	4.08	0.56	3.00	0.30
10	1.82	4.66	0.00	-0.48	0.00	0.16	0.11	4.25	0.48	0.00	0.30
20	1.82	4.66	0.00	-0.48	0.00	0.15	0.09	4.28	0.48	0.00	0.30
40	1.81	4.65	0.00	-0.46	0.00	0.14	0.06	4.33	0.46	0.00	0.29

Table 2. The s, p and d-shell occupation (e), total ionic charge, q (e), unpaired spin population, n_s (μ_B) and nearest-neighbour vanadium-oxygen overlap population, O (e) for the NbO-type defect structure at hydrostatic pressure P (GPa). † Total spin of cell fixed to $9\mu_B$.

It is unclear whether the collapse of spin on the metal sites represents the ground state of the V_3O_3 structure, for the CASTEP code does not offer the ability to set the initial spin of individual atoms. The ferromagnetic solution is clearly much higher in energy, but the stabilities of antiferromagnetic alignments in this crystal structure are yet to be

determined in the plane-wave method. CASTEP calculations were attempted for broken metal symmetries with $9\mu_B$ and $3\mu_B$ total cell spin, but in both cases the converged electronic structure that emerged was the spin-collapsed ground state discussed earlier. For comparison, the energy per molecule of the perfect FM lattice at equilibrium is -817.8905eV . Previous work does however suggest that the ground magnetic state of perfect VO is the AF_1 alignment. Direct and superexchange coupling constants (including a factor $S_z^2=9/4$) of -43.21 and $+4.73\text{meV}$ were extracted from BLYP calculations for AF_1 , AF_2 and FM VO within CRYSTAL98 and may be used here to approximate the energy of the CASTEP GGA-PBE AF_1 state. Within the Ising model, the AF_1 alignment is lower in energy than the FM by an amount $8|J_d|$, yielding a correction of size 0.3457eV and an estimated CASTEP AF_1 energy of -818.2362eV . Of course, the application of this correction relies upon the hypothesis that coupling constants derived within GGAs of different functional form do not vary all that greatly. Recent work in the late TMOs, discussed in Chapters 1 and 2 has shown this to be true. The important point to note from the foregoing discussion is the stability of V_3O_3 over the perfect VO AF_1 lattice by $\sim 0.5\text{eV}$, and it is clear that no reasonable adjustment of the coupling constants could lower the energy of the perfect AF_1 lattice by this amount.

A comparison of the atom projected densities of states (PDOS) for the equilibrium ferromagnetic $Fm\bar{3}m$ cell (Figure 2) with that for the V_3O_3 structure (Figure 3) was carried out. The $Fm\bar{3}m$ PDOS shows that the Fermi energy falls at a point some 4eV from the lower edge of a broad band of metal-derived states of width $\sim 8\text{eV}$, while the upper edge of the oxygen-derived $2p$ states of band width $\sim 5\text{eV}$ starts some 5eV below the Fermi level and are thus separated from the metal states by a small gap $\sim 1\text{eV}$ in width. Metal-oxygen hybridisation is indicated by the significant $V3d$ contribution to the oxygen levels, and a smaller relative contribution of $O2p$ states to the metal bands. The PDOS clearly show ferromagnetic order, with a small ($\sim 0.5\text{eV}$) exchange splitting of the $O2p$ levels, and a much larger splitting of $\sim 2\text{eV}$ within the metal states, while the α and β $O2s$ states remain essentially degenerate. Taking the splitting into account, the metal bandwidth of both majority and minority spins is reduced to 6eV .

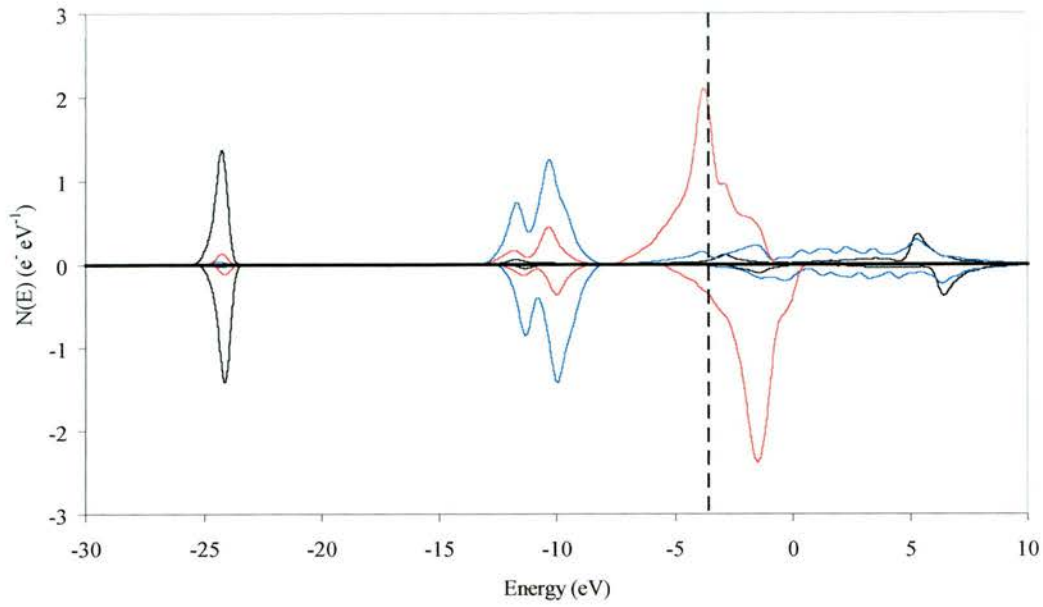


Figure 2. The atom-projected densities of states for FM VO. O(p) states are shown in blue, V(d) states in red, O(s) states in black. The Fermi energy is denoted by a vertical dashed line.

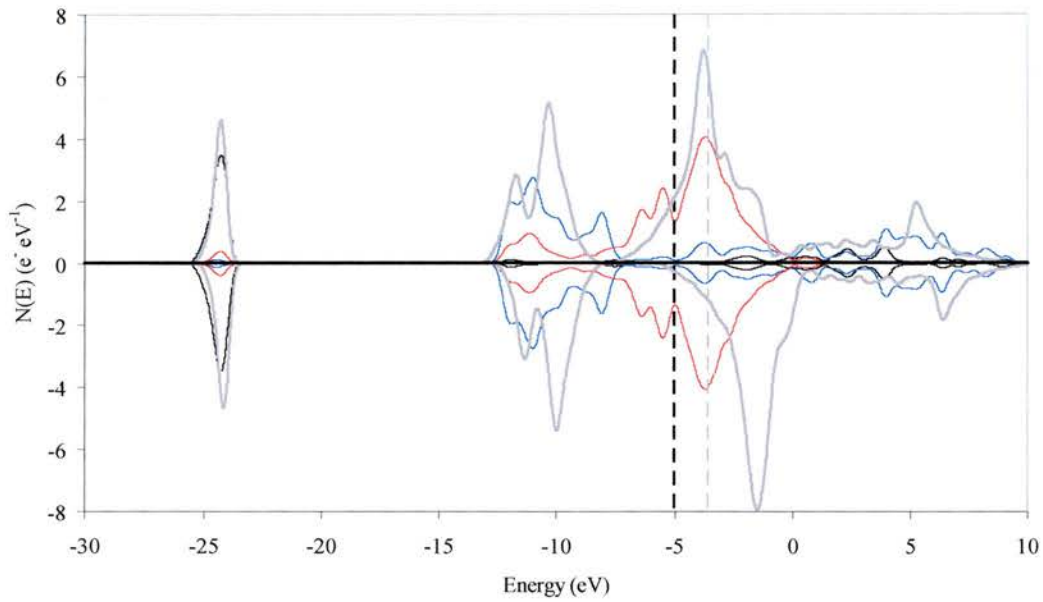


Figure 3. The atom-projected densities of states for the V_3O_3 structure. O(p) states are shown in blue, V(d) states in red, O(s) states in black and, for comparison, FM VO total DOS in thick grey. Fermi energies are denoted by vertical dashed black and grey lines for V_3O_3 and FM VO respectively.

In the equilibrium V_3O_3 structure the spin collapse on the metal sites means that there is no exchange splitting in the PDOS plots. The gap between the O2p and V3d

dominated bands in the perfect crystal is closed by split-off states, leading to an increase in widths of the O2p and V3d bands of $\sim 1\text{eV}$ and 7eV respectively. The dramatic increase in the metal band width is due to the joining of the band at the valence edge with the significant metal weight in the anion band, while the relative weight of oxygen states in the metal band decreases. The identity of the split-off states is unclear from the CASTEP PDOS. The O2s states remain unaffected by the introduction of vacancies, in contrast to the small upward shift noted by Burdett and Hughbanks. If the picture of the electronic structure in $d^3 \text{NbO}$ applies essentially unaltered to $d^3 \text{VO}$, then the split-off states from the oxygen band can be attributed to the destabilised p_z orbital, and those from the metal band to the stabilised z^2 orbital. The Fermi energies fall at -3.583eV for the equilibrium perfect lattice and at -5.041eV for the equilibrium V_3O_3 structure. The fall in Fermi energy further indicates the stabilising effect of the introduction of vacancies.

In order to further investigate the effect of vacancies on the electronic structure of VO, the properties of the V_3O_3 structure were computed using the CRYSTAL98 code within the B3LYP hybrid Hamiltonian. Here, the capabilities for projection of the DOS upon individual atomic orbitals was utilised, leading to the plot for the spin collapsed state shown in Figure 4 below.

The calculation was performed at a molecular volume of 21.0256\AA^3 , chosen deliberately to equal the primitive volume of the perfect AF_1 lattice within the B3LYP method. It is likely, with knowledge of the CASTEP results, that the equilibrium volume for the V_3O_3 structure is greater than this value. The basis set was of the same form as that used previously in studies of the perfect lattice, with the addition of an optimised O(d) polarisation function of exponent 0.35 bohr^{-2} . Unaltered anion and cation ghost basis sets were maintained at the positions of the vacancies. The results of the CRYSTAL98 calculations are collected in Table 3 below. Also considered is the V_3O_3 AF state, in which the symmetry of the cation and anion sublattices is broken, leading to inequivalence of atoms V_1 and V_2 , and O_1 and O_2 , and a reduction in the number of operators in the space group to 16. The net spins of V_1 and V_2 are initially set at β and α respectively.

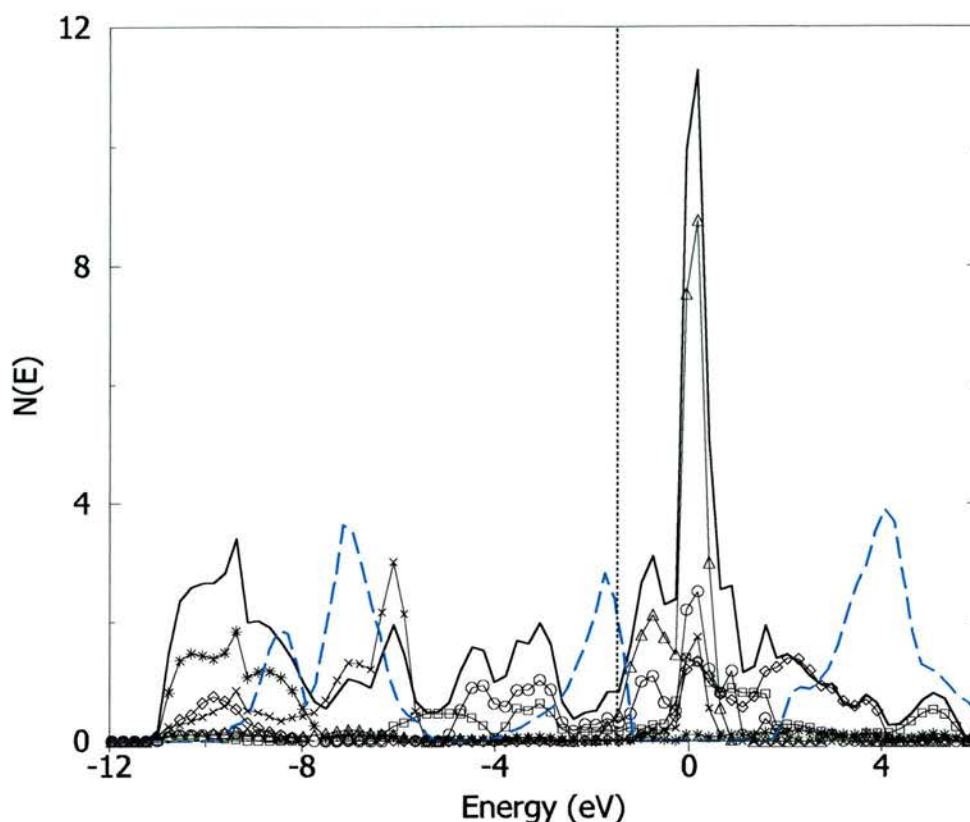


Figure 4. The atomic orbital projected densities of states for the spin-collapsed V_3O_3 structure emerging from the B3LYP hybrid method in the CRYSTAL98 code. Key: * $O(p_x/p_y)$, \times $O(p_z)$, \circ $V(xz/yz)$, \square $V(z^2)$, \triangle $V(xy)$, \diamond $V(x^2-y^2)$. Dashed line is $Fm\bar{3}m$ VO densities of states for comparison Dotted vertical line marks Fermi energy.

	TE		V_V	V_1	V_2	V_O	O_1	O_2
$AF_1 Fm\bar{3}m$	0	$\alpha+\beta$	—	21.550		—	9.450	
		$\alpha-\beta$	—	2.843		—	-0.021	
V_3O_3	+0.885	$\alpha+\beta$	-0.525	21.526		1.352	9.199	
		$\alpha-\beta$	-0.008		0.167	-0.020	-0.027	
$V_3O_3 AF$	+0.679	$\alpha+\beta$	-0.506	21.530	21.532	1.274	9.221	9.209
		$\alpha-\beta$	-0.002	-1.866	1.475	0.021	-0.066	0.007

Table 3. The total energy per molecule, TE (eV), relative to the AF_1 perfect lattice, and Mulliken charge, $\alpha+\beta$, and spin, $\alpha-\beta$ populations upon the vanadium and oxygen atoms and vacancies.

Considering first the V_3O_3 structure with full $Pm\bar{3}m$ symmetry, it is immediately clear from Figure 4 that the introduction of vacancies leads to a conducting state in accord with experiment, whereas in the perfect AF_1 lattice a band gap of width 2.445eV was obtained. At this molecular volume, and for the B3LYP Hamiltonian, the perfect AF_1 structure is found to be more stable than V_3O_3 . It is, however, the detail of the change in electronic structure upon introduction of the vacancies that is pursued here. The ionic charge on oxygen is reduced by $0.25e$ or 17% of the value in the perfect lattice, as compared to $0.15e$ or 23% within the GGA-PBE functional in CASTEP. Interestingly, the metal charge remains largely unchanged. In keeping with the CASTEP results, the spin moment on the metal atoms has all but vanished. The negative population on the metal vacancy is unphysical, and is indicative of negative V_V -neighbouring oxygen off-diagonal elements in \mathbf{DS} , the product of the density and overlap matrices. The Mulliken method partitions the charge contribution arising from basis functions on different atoms equally between the two atoms involved. It is expected that a population analysis in the Löwdin formalism, which uses the $\mathbf{S}^{1/2}\mathbf{DS}^{1/2}$ product, would remove the negative off-diagonal elements. To ascertain where the negative V_V population should properly reside, the calculation was repeated with the ghost basis at the V_V site removed. Comparison of the results with those including the V_V ghost basis shows that metal and V_O populations remain largely unchanged at $21.554e$ and $1.341e$ respectively, while oxygen populations were reduced by $0.2e$ from $9.199e$ to $8.999e$. As expected, oxygen atoms immediately neighbouring the metal vacancy take up the majority of the negative population. The total energy per formula unit relative to the AF_1 perfect lattice is $+0.909eV$, indicating that the removal of the V_V basis has a minimal effect on the energetics of the structure. A view along the V_V-O-V_V and V_O-V-V_O paths is presented in Figure 5 below. Total charges may be assigned as the sum of the charge on the vacancy and half of that on the six neighbouring atoms. It is found that this amounts to 1.280 holes or electrons for the V_V and V_O site respectively with the V_V ghost basis, and 1.353 holes or electrons without.

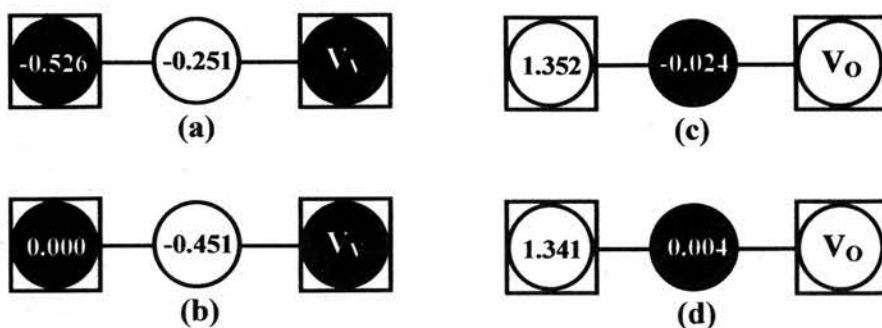


Figure 5. Electron populations of vacancies (\square) and changes in population of neighbouring atoms (\circ oxygen, \bullet metal) relative to perfect AF_1 lattice for (a) V_V site, cell includes V_V ghost basis, (b) V_V site omitting V_V ghost basis, (c) V_O site, cell includes V_V ghost basis and (d) V_O site omitting V_V ghost basis.

Cartesian axes for the projection in Figure 4 onto atomic orbitals were arranged for both metal and oxygen such that the z direction points toward the nearest neighbour vacancy, while x and y lie within the plane and point directly toward the neighbouring ligands. Along with metallic character, the densities of states reveal a splitting of orbital degeneracy in the oxygen band beyond that found in $Fm\bar{3}m$ AF_1 , with a small upward shift of p_z states, and large stabilisation of p_x and p_y states. The upper oxygen 2band edge, however, remains close to -5.5eV , as in the perfect lattice. The occupied metal orbitals are of mainly xz , yz and z^2 symmetry, with the lower vanadium band edge shifted downward in energy by $\sim 1.5\text{eV}$. The gap between the occupied oxygen and metal bands, which is $\sim 1.1\text{eV}$ in width in the perfect AF_1 lattice, is closed in the presence of vacancies. The majority of the x^2-y^2 and xy states lie above the Fermi energy, although the former orbital has a significant weight in the oxygen band, coincident in energy with the oxygen p_x and p_y states. The weight of such states indicates an increase in $V(x^2-y^2)\text{---}O(p_x/p_y)$ σ -type hybridisation at the reduced metal-oxygen bond length of the V_3O_3 structure. It can be concluded that the electronic structure of V_3O_3 revealed by the detailed projections is largely consistent with the shifts in energy proposed by Burdett and Hughbanks.

A further breakdown of the Mulliken charges into orbital contributions yields a $V(d)$ occupancy (z^2 , xz , yz , x^2-y^2 , xy) of the form (0.744, 0.936, 0.936, 0.500, 0.324), and an oxygen (s , p_x , p_y , p_z) occupancy of the form (3.852, 1.664, 1.664, 1.938), as

compared to (0.230, 1.010, 1.010, 0.229, 1.013) and (3.925, 1.828, 1.828, 1.827) respectively for the perfect AF₁ lattice. The V_O ghost basis occupancy is (0.812, 0.179, 0.179, 0.179), with the majority of the charge lying within the 4sp-shell. The unpaired spin arises only upon vanadium, and has orbital contributions of the form (0.016, 0.038, 0.038, 0.006, 0.067), as compared to (0.027, 0.911, 0.911, 0.021, 0.954) in the perfect lattice.

The V₃O₃ AF structure shows similar changes in ionicity, but here the total energy per molecule is 0.206eV lower than for unbroken symmetry, and a spin moment of 1.48—1.87 μ_B is retained. The V(d) occupancy for V₂ is (0.725, 0.940, 0.940, 0.504, 0.334), the oxygen occupancy for O₁ is (3.865, 1.660, 1.660, 1.959) and the V_O occupancy is (0.795, 0.160, 0.160, 0.157) (again, mainly in the 4sp shell). The unpaired spin on V₂ has contributions (-0.324, -0.685, -0.685, -0.019, -0.133).

A comparison of the B3LYP energy-volume curve for the defect structure to that for the perfect lattice is of some interest. As shown in Figure 6 below, the V₃O₃ structure lies at a much higher energy than the perfect lattice, and the equilibrium molecular volume is smaller at 20.1867Å³, as compared to 20.9656Å³ for the perfect lattice with the O(d) polarisation function. It is clear, therefore, that V₃O₃ may occur in the B3LYP phase diagram only as a potential high pressure structure. The results are quite different to those obtained within the GGA-PBE functional in CASTEP, wherein the V₃O₃ structure is predicted to be more stable than Fm $\bar{3}$ m VO. It was considered that the placing of an unaltered oxygen basis at the V_O site might be responsible for the high energy of V₃O₃, and so an optimisation of the relevant exponents was performed. Efforts were concentrated on the 4sp-shell at the V_O site, since all previous calculations indicated that only this part of the set held any significant charge. A change in the 4sp exponent, α , from 0.17 to 0.15 bohr⁻² yielded a minimal reduction in energy of 26meV per molecule, and a large increase in V_O occupancy from 1.352 to 1.563e. This highlights the dangers involved in treating the Mulliken populations as meaningful in an absolute sense. Interest should instead be focussed upon changes in population between calculations using the same basis. The optimal exponent seems to lie below 0.15 bohr⁻², but any further reduction in α leads to a divergent SCF sequence and numerical catastrophe. It is clear, though, that the high energy of V₃O₃ is not due to any inadequacy in the basis at the V_O site, and must

be considered a feature of the B3LYP Hamiltonian. Previous chapters have shown that Hamiltonians incorporating increasing amounts of Fock exchange display increasing localisation of charge. It is possible that the increase in localisation entailed in going from the PBE to the B3LYP functional may limit the penetration of metal states into neighbouring oxygen vacancies, and thus destabilise the V_3O_3 structure with respect to the perfect lattice.

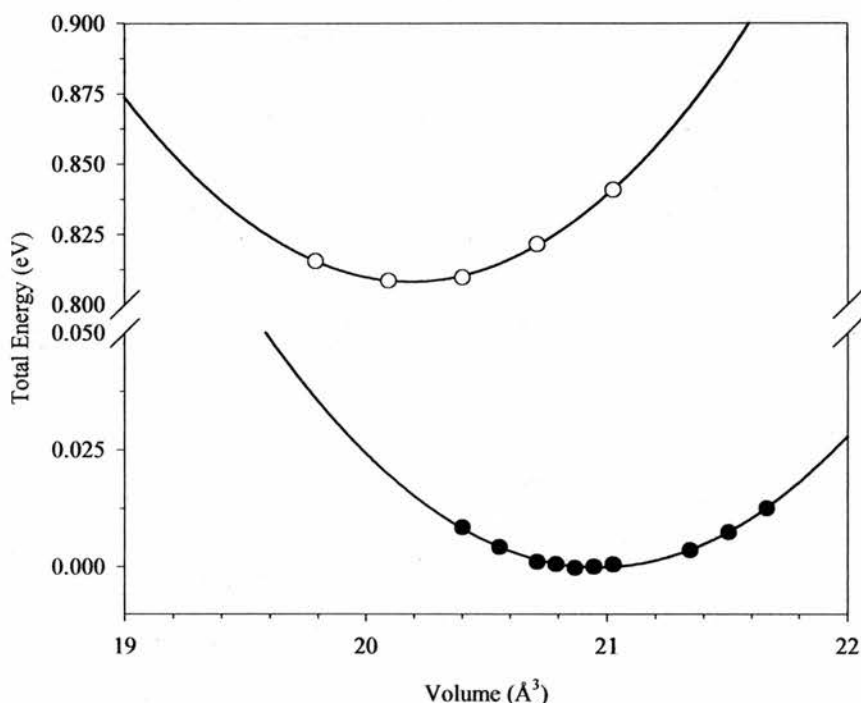


Figure 6. Plot of total energy against volume (both per molecule) for $Fm\bar{3}m AF_1 VO$ (●) and for the $Pm\bar{3}m V_3O_3$ structure (○). Note break in vertical axis.

3. The 1 in 8 Ordered Defect Structure

The V_7O_7 structure shown in Figure 7 below incorporates vanadium and oxygen vacancies at 12.5%, and is classified $P4/mmm$ (international table number 123, origin 1) with 16 symmetry operators in the group. Both a and c cell lengths and the positions of O and V atoms at sites 2 and 3 respectively are free to vary, while cell vectors \mathbf{a} , \mathbf{b} ($|\mathbf{b}| = a$) and \mathbf{c} are constrained to be mutually perpendicular. The ideal structure is realised for $a = \sqrt{2}c$ with oxygen type 1, O_1 , at positions $(0, \frac{1}{2}, \frac{1}{2})$ and $(\frac{1}{2}, 0, \frac{1}{2})$, O_2 at positions $(\pm\frac{1}{4}, \pm\frac{1}{4}, 0)$ and O_3 at $(0, 0, \frac{1}{2})$. Vanadium type 1, V_1 is at

position $(0, \frac{1}{2}, \frac{1}{2})$, V_2 at positions $(\frac{1}{2}, 0, 0)$ and $(0, \frac{1}{2}, 0)$ and V_3 at positions $(\pm\frac{1}{4}, \pm\frac{1}{4}, \frac{1}{2})$. Full optimisation of atomic and cell degrees of freedom was carried out under the imposition of stress tensors equivalent to hydrostatic pressures of -5, 0, 5, 10, 20 and 30 GPa. Computational conditions were identical to those employed for the NbO-type structure, with the exception of Monkhorst-Pack sampling on a (5,5,8) grid, leading to 24 special points in the IBZ, an FFT grid of dimension (36,36,25) and RMS atomic force and displacement tolerances of 0.01 eV\AA^{-1} and $5\text{E-}4\text{\AA}$ respectively.

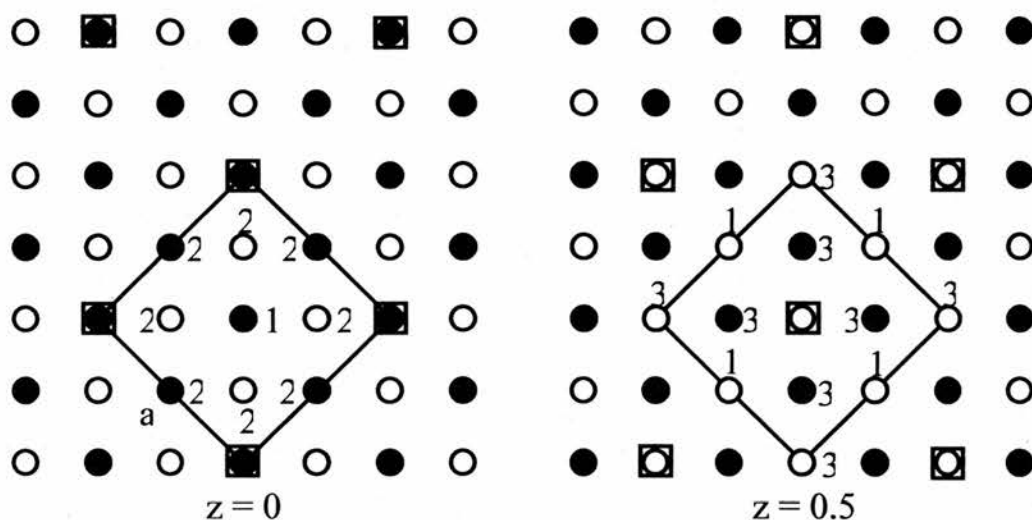


Figure 7. The $z = 0$ (left) and $z = 0.5$ (right) planes of the V_7O_7 defect structure. \bullet = vanadium, \circ = oxygen, \square = vacancy of appropriate type.

Within the $P4/mmm$ group, the displacement away from ideal positions permitted for atoms O_2 and V_3 lies along the line in the ab plane that links the atom with the nearest neighbour vacancy. The results of the geometry optimisations are presented in Table 4 below.

Under the influence of increasing hydrostatic pressure, the ratio of lattice constants decreases very slightly from the cubic value of $\sqrt{2}$. The free oxygen atom O_2 is displaced away from the nearest neighbour metal vacancy for negative and zero pressure, and displaced toward the vacancy for all positive pressures. The free metal atom V_3 is always displaced toward the neighbouring vacancy.

P	a	c	a/c	V	E	Atom	u,v	$\delta_{u,v} (\times 10^{-3})$
-5	6.0342	4.2799	1.4099	22.2624	-818.3868	O ₂	0.25714	-7.14
						V ₃	0.25275	+2.75
0	5.9287	4.2327	1.4007	21.2535	-818.4071	O ₂	0.25387	-3.87
						V ₃	0.25882	+8.82
5	5.8504	4.1887	1.3967	20.4807	-818.3974	O ₂	0.24901	+0.31
						V ₃	0.26173	+11.73
10	5.8043	4.1548	1.3970	19.9963	-818.3789	O ₂	0.24751	+2.49
						V ₃	0.26250	+12.5
20	5.7287	4.1014	1.3967	19.2282	-818.3076	O ₂	0.24405	+5.95
						V ₃	0.26388	+13.88
30	5.6662	4.0575	1.3965	18.6102	-818.2118	O ₂	0.24186	+8.14
						V ₃	0.26484	+14.84

Table 4. Optimised a and c lattice constants (\AA), ratio a/c, volume per molecule, V (\AA^3), energy per molecule, E (eV), fractional coordinates (u,v) of atoms O₂ and V₃ along **a** and **b** ($|\mathbf{b}| = a$) cell vectors and variation from ideal position, δ (in fractions of a, where $\delta > 0$ indicates movement toward nearest neighbour vacancy) for the V₇O₇ structure at hydrostatic pressure P (GPa).

The localisation of effective vacancy charges and the effect of polarisation both make it difficult to predict the nature of atomic relaxation around the vacancies. Curves of δ against P (not shown here) suggest that the magnitude of the displacement approaches a limiting value at high P. This can be rationalised as indicating that the atoms are approaching an optimal packing that is unchanged by further increase in pressure. The energy of V₇O₇ in equilibrium lies $\sim 0.2\text{eV}$ below the approximated value for perfect AF₁ VO, and so, while it is less stable than V₃O₃, the presence of concentrations of vacancies as dilute as 12.5% suffices to lower the energy of the lattice. Again, the molecular volume is greater in V₇O₇ than in the perfect lattice. The values of c and $a/\sqrt{2}$ might usefully be compared with the cubic lattice constant of 4.063\AA found in VO_{1.0} by Loehman *et al.* Here, at equilibrium, c is $\sim 0.17\text{\AA}$ and $a/\sqrt{2} \sim 0.13\text{\AA}$ greater than this value, as compared to the close match obtained in V₃O₃.

P	At.	s	p	d	q	n_s	At.	s	p	d	q	n_s
-5	O_1	1.82	4.80	0.00	-0.62	+0.02	V_1	0.12	0.17	4.17	0.54	+2.18
	O_2	1.84	4.75	0.00	-0.59	0.00	V_2	0.18	0.12	3.97	0.73	+2.52
	O_3	1.85	4.75	0.00	-0.60	+0.02	V_3	0.17	0.23	4.05	0.55	-2.14
0	O_1	1.82	4.79	0.00	-0.60	0.00	V_1	0.10	0.12	4.21	0.57	+1.78
	O_2	1.84	4.74	0.00	-0.58	0.00	V_2	0.17	0.09	4.01	0.73	+2.36
	O_3	1.85	4.74	0.00	-0.59	+0.02	V_3	0.16	0.20	4.12	0.52	-1.64
5	O_1	1.81	4.78	0.00	-0.59	0.00	V_1	0.10	0.09	4.27	0.54	+1.04
	O_2	1.83	4.73	0.00	-0.56	0.00	V_2	0.17	0.06	4.06	0.71	+2.14
	O_3	1.85	4.73	0.00	-0.59	+0.02	V_3	0.15	0.17	4.16	0.51	-1.30
10	O_1	1.81	4.78	0.00	-0.59	0.00	V_1	0.10	0.06	4.31	0.54	+0.56
	O_2	1.83	4.72	0.00	-0.55	0.00	V_2	0.16	0.04	4.09	0.70	+2.04
	O_3	1.85	4.73	0.00	-0.59	+0.02	V_3	0.15	0.16	4.19	0.51	-1.16
20	O_1	1.80	4.78	0.00	-0.58	0.00	V_1	0.10	0.03	4.35	0.52	+0.28
	O_2	1.83	4.71	0.00	-0.54	0.00	V_2	0.16	0.01	4.14	0.69	+1.86
	O_3	1.85	4.73	0.00	-0.58	+0.02	V_3	0.14	0.13	4.23	0.51	-0.98
30	O_1	1.80	4.77	0.00	-0.57	0.00	V_1	0.11	0.00	4.39	0.50	+0.16
	O_2	1.83	4.71	0.00	-0.54	0.00	V_2	0.15	-0.01	4.19	0.67	+1.74
	O_3	1.84	4.73	0.00	-0.58	+0.02	V_3	0.13	0.10	4.26	0.50	-0.86

Table 5. The s, p and d-shell occupation (e), total ionic charge, q (e) and unpaired spin population, n_s (μ_B) for all atoms comprising the V_7O_7 defect structure at hydrostatic pressure P (GPa).

Table 5 above contains the detail of the electronic structure of V_7O_7 at various applied stresses. The charges upon metal atoms at equilibrium are in the range $q = 0.52 - 0.73e$ for the square pyramidal and octahedral sites respectively. The average value lies at $0.59e$, some $0.1e$ higher than in V_3O_3 and remains largely unchanged by increase in pressure. The charges upon the oxygen atoms are in a smaller range $-0.58 - -0.60e$, corresponding to the square pyramidal and octahedral sites respectively. In contrast with the spin-collapse in V_3O_3 , unpaired spin is found on each of the three types of metal site. The spin alignments are such that an antiferromagnetic ground state is obtained, rendered imperfect by the presence of defects. In an indexing

appropriate for the $Fm\bar{3}m$ conventional cell, ferromagnetically aligned (100) planes are arranged such that their magnetisation reverses with progress along the [100] direction. Were it not for the presence of the vacancies, a supercell of the perfect lattice AF_1 arrangement would be realised. The V_7O_7 cell would be expected to bear a net spin moment given the spin alignments discussed above, but the magnitude of the moments on the individual metal atoms are arranged such that their sum is close to zero. For example, the value of $\int\{\rho_\alpha(\mathbf{r}) - \rho_\beta(\mathbf{r})\}d\mathbf{r}$ directly integrated upon the fast Fourier transform grid is $0.0033\mu_B$ in the equilibrium structure, rising to $0.1575\mu_B$ at 20GPa. For comparison, the sums of the moments arising from the Mulliken analyses are $-0.06\mu_B$ and $0.08\mu_B$ for 0GPa and 20GPa respectively. The sensitivity of the spin moment at the square-planar V_1 site to change in the V—O bond length is striking. For example, in the equilibrium structure, a large value of $1.78\mu_B$ is obtained at a V—O bond length ($a/\sqrt{8}$) of 2.0961\AA . However, the V_1 moment at 30GPa undergoes a dramatic collapse to $0.16\mu_B$ for a relatively small reduction in bond length to 2.0033\AA . The latter bond length is similar to the value of 2.0029\AA found in the V_3O_3 cell at equilibrium, where a complete collapse of the magnetic moment is predicted. So, the behaviour of vanadium in square-planar coordination seems similar in V_3O_3 and V_7O_7 . The spin moments borne by the octahedral V_2 and square-pyramidal V_3 sites seem much less affected by change in bond length, although the moment at the latter site does effectively halve with an increase in pressure from 0 to 30GPa.

The atomic orbital projected densities of states were calculated for the equilibrium structure, and are shown in Figure 8 below, along with the total DOS for perfect FM. Whereas in V_3O_3 , the upper edge of the O(2p) band lay $\sim 1\text{eV}$ higher in energy than in perfect FM, the V_7O_7 band edge is almost coincident with that of the defect-free material. The spin-up PDOS for the V(3d) states shows similar band edges in the defective and perfect material, although the maximal weight of states is pushed to higher energy in V_7O_7 . The O(2s) states are noticeably split in V_7O_7 into three separate peaks which correspond to the octahedral, square-pyramidal and square-planar environments of the O_1 , O_2 and O_3 sites respectively. The gap between occupied oxygen and metal bands now features a small band of O(2p) states of approximately 1.1eV width. The changes wrought in the DOS plots in progress from V_3O_3 to V_7O_7 are understandable in terms of the decreasing concentration of defects:

in the extreme case of a well isolated vacancy in a large supercell, the defect would be expected to contribute a narrow feature to the band gap with minimal change elsewhere. The Fermi energy for V_7O_7 falls at -4.4712eV , in comparison with -3.5825eV in FM VO and -5.0409eV in V_3O_3 .

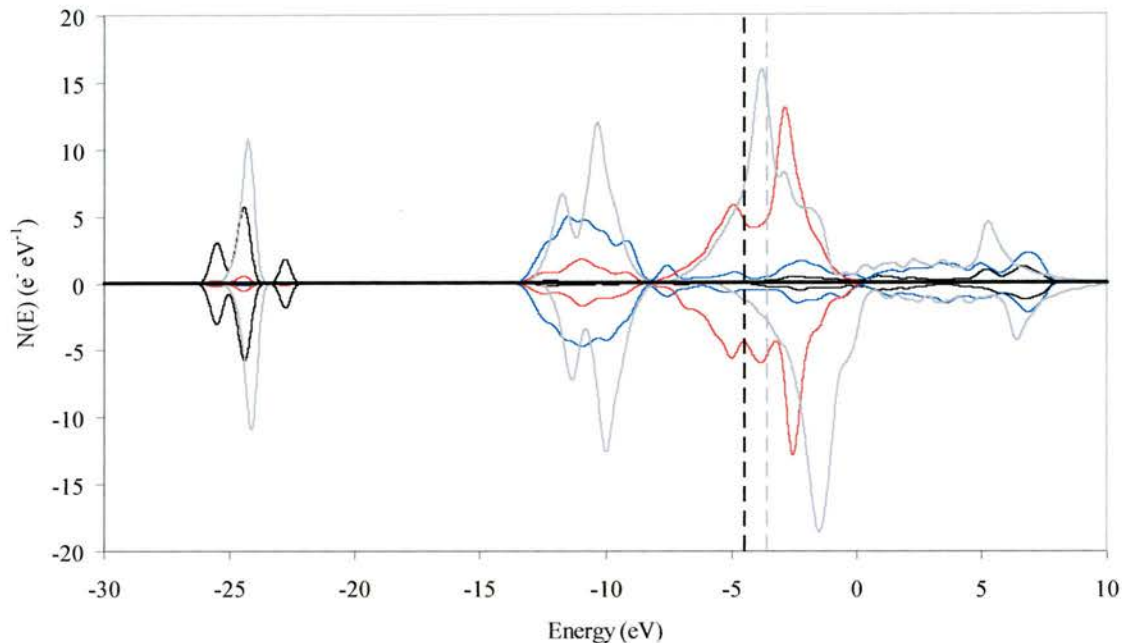


Figure 8. The atom-projected densities of states for the V_7O_7 structure. O(p) states are shown in blue, V(d) states in red, O(s) states in black and, for comparison, FM VO total DOS in thick grey. Fermi energies are denoted by vertical dashed black and grey lines for V_7O_7 and FM VO respectively.

4. The 1 in 6 (TiO-Type) Ordered Defect Structure

The monoclinic V_5O_5 structure, shown in the $V_{10}O_{10}$ conventional cell in Figure 9 below, incorporates vanadium and oxygen vacancies at 16.66%, and is classified as $A112/m$ (international table number 12, C-unique, cell-1 setting), with 8 and 4 symmetry operators in the conventional and primitive cells respectively. The “ideal” $V_{10}O_{10}$ structure (i.e. that in which, neglecting vacancies, the underlying face centred cubic arrangement is reproduced) is realised for lattice vectors

$$\mathbf{a} = \begin{pmatrix} a_c \\ -a_c \\ 0 \end{pmatrix}, \mathbf{b} = \begin{pmatrix} a_c \\ 2a_c \\ 0 \end{pmatrix} \text{ and } \mathbf{c} = \begin{pmatrix} 0 \\ 0 \\ a_c \end{pmatrix},$$

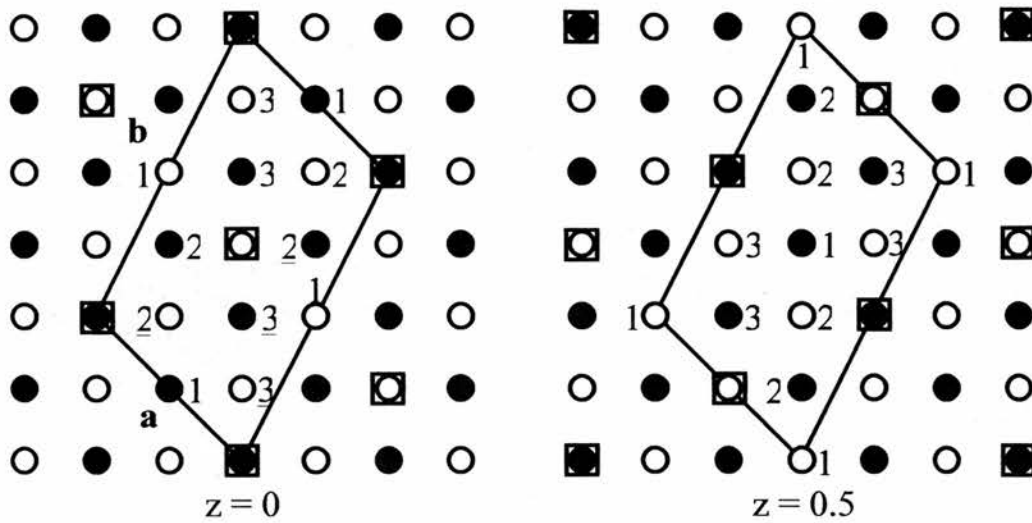


Figure 9. The $z = 0$ (left) and $z = 0.5$ (right) planes of the $V_{10}O_{10}$ defect structure. \bullet = vanadium, \circ = oxygen, \square = vacancy of appropriate type. Underlined labels indicate atoms for which displacements are reported in Table 7 below.

where a_c is the lattice constant of the conventional fcc cell. The magnitudes of the cell vectors are therefore $a = \sqrt{2}a_c$, $b = \sqrt{5}a_c$ and $c = a_c$, while angles are of size $\alpha = \beta = 90^\circ$ and $\gamma = 108.4349488^\circ$. The volume of the general $V_{10}O_{10}$ cell is given by $V = (abc)\cos(\gamma - 90)$. Within the idealised structure, metal and oxygen atoms of site types 1, 2 and 3 occupy positions in fractional coordinates as follows,

- 2 V_1 atoms in the 2(c) position $(\frac{1}{2}, 0, 0)$ $(\frac{1}{2}, \frac{1}{2}, \frac{1}{2})$,
- 2 O_1 atoms in the 2(b) position $(0, \frac{1}{2}, 0)$ $(0, 0, \frac{1}{2})$,
- 4 V_2 atoms in the 4(i) position $(0, 0, 0 : 0, \frac{1}{2}, \frac{1}{2}) + x, y, 0 : \bar{x}, \bar{y}, 0$,
with $x = \frac{1}{6}, y = \frac{1}{3}$,
- 4 V_3 atoms in the 4(i) position with $x = \frac{2}{3}, y = \frac{1}{3}$,
- 4 O_2 atoms in the 4(i) position with $x = \frac{1}{3}, y = \frac{1}{6}$,
- 4 O_3 atoms in the 4(i) position with $x = \frac{5}{6}, y = \frac{1}{6}$.

In general the structure will be non-ideal and then all of the a , b and c cell lengths, the angle γ and the (x,y) parameters of oxygen and metal atoms at sites O_2 , O_3 , V_2 and V_3 are free to vary, yielding 12 parameters that must be optimised for each volume of cell. In terms of the conventional lattice vectors, the ideal V_5O_5 primitive cell is defined by,

$$\mathbf{a}_p = \frac{1}{2}\mathbf{b} + \frac{1}{2}\mathbf{c}, \mathbf{b}_p = \frac{1}{2}\mathbf{b} - \frac{1}{2}\mathbf{c} \text{ and } \mathbf{c}_p = \mathbf{a}.$$

The magnitudes of the cell vectors are then $a_p = b_p = \sqrt{\frac{3}{2}}a_c$ and $c_p = \sqrt{2}a_c$, while cell angles are of size $\alpha = \beta = 106.7786549^\circ$ and $\gamma = 48.18968511^\circ$. The fractional coordinates of the atoms along the primitive vectors then become,

$$\begin{aligned} O_1 &= \left(\frac{1}{2}, \frac{1}{2}, 0\right), & V_1 &= \left(0, 0, \frac{1}{2}\right), \\ O_2 &= \left(\frac{1}{6}, \frac{1}{6}, \frac{5}{6}\right), \left(\frac{\bar{1}}{6}, \frac{\bar{1}}{6}, \frac{\bar{5}}{6}\right), & V_2 &= \left(\frac{1}{3}, \frac{1}{3}, \frac{1}{6}\right), \left(\frac{\bar{1}}{3}, \frac{\bar{1}}{3}, \frac{\bar{1}}{6}\right), \\ O_3 &= \left(\frac{1}{6}, \frac{1}{6}, \frac{1}{3}\right), \left(\frac{\bar{1}}{6}, \frac{\bar{1}}{6}, \frac{\bar{1}}{3}\right), & V_3 &= \left(\frac{1}{3}, \frac{1}{3}, \frac{2}{3}\right), \left(\frac{\bar{1}}{3}, \frac{\bar{1}}{3}, \frac{\bar{2}}{3}\right). \end{aligned}$$

As before, the positions of atoms O_2 , O_3 , V_2 and V_3 are free to vary. All of the following calculations were performed in the primitive cell, but the optimised geometries have been transformed back to the conventional cell for ease of visualisation. Full optimisation of atomic and cell degrees of freedom was carried out under the imposition of stress tensors equivalent to hydrostatic pressures of -5, 0, 5, 10, and 20GPa. Computational conditions were identical to those employed for the V_3O_3 and V_7O_7 structures, with the exception of Monkhorst-Pack sampling on a (9,9,6) grid, leading to 135 special points in the IBZ and an FFT grid of dimension (40,40,48). The initial guess for the the geometry of the equilibrium cell was the ideal lattice with $a_c = 4\text{\AA}$. All subsequent runs took as an initial guess the final structure of the closest run at lower magnitude of pressure. Tables 6 and 7 below report the results of the geometry optimisations.

P	a	b	c	γ	V	E
-5	5.9700	9.2558	4.1386	107.0456	21.8642	-818.6749
0	5.9043	9.1757	4.1092	107.2347	21.2627	-818.6866
5	5.8367	9.1278	4.0818	107.4464	20.7462	-818.6800
10	5.8058	9.0777	4.0468	107.9430	20.2916	-818.6672
20	5.6944	8.9070	4.0058	108.4844	19.2690	-818.5979

Table 6. Optimised a , b and c lattice constants (\AA), cell angle γ ($^\circ$), volume per molecule, V (\AA^3) and energy per molecule, E (eV) for the $V_{10}O_{10}$ structure at hydrostatic pressure P (GPa).

P	At.	$\delta_u (\times 10^{-2})$	$\delta_v (\times 10^{-2})$	$d(V_O)$	At.	$\delta_u (\times 10^{-2})$	$\delta_v (\times 10^{-2})$	$d(V_V)$
-5	V_2	-1.6963	-1.4482	1.998	O_2	+1.8137	+1.0963	2.255
	V_3	-0.9297	+3.3352	1.756	O_3	-1.3813	+1.6788	2.262
0	V_2	-1.7483	-1.4502	1.971	O_2	+1.4977	+0.9543	2.208
	V_3	-1.0907	+3.3902	1.730	O_3	-1.2763	+1.7008	2.241
5	V_2	-1.8080	-1.4770	1.944	O_2	+1.1450	+0.8021	2.161
	V_3	-1.2302	+3.3941	1.713	O_3	-1.1473	+1.7239	2.224
10	V_2	-2.1536	-1.6370	1.902	O_2	+0.7906	+0.5951	2.113
	V_3	-1.2452	+3.2953	1.716	O_3	-0.9845	+1.7498	2.214
20	V_2	-2.3510	-1.8337	1.839	O_2	-0.9441	-0.1618	1.961
	V_3	-1.8126	+2.5645	1.722	O_3	-0.5553	+1.5460	2.145

Table 7. Displacements, δ_u and δ_v , in fractions of a and b respectively of atoms V_2 , V_3 , O_2 and O_3 (underlined on Figure 9) from ideal positions, $V_2 \left(\frac{5}{6}, \frac{2}{3}, 0\right)$, $V_3 \left(\frac{2}{3}, \frac{1}{3}, 0\right)$, $O_2 \left(\frac{1}{3}, \frac{1}{6}, 0\right)$ and $O_3 \left(\frac{5}{6}, \frac{1}{6}, 0\right)$ and distances of atoms from nearest neighbour vacancies, d (\AA) in the $V_{10}O_{10}$ structure at hydrostatic pressure P (GPa).

As Figure 10 below shows, the variation in the a , b and c lattice parameters with hydrostatic pressure is smooth up to 10GPa. In the range 10–20GPa the data suggest that there may be a discontinuous change in structure involving sharp reductions in constants a and b and an increase in constant c . The data are too sparse to identify

whether this effect is real or merely an artefact of the limited set of pressures studied. Nevertheless, the variation in molecular volume with pressure is smooth across the whole range -5 to 20GPa. A plot of the cell angle γ against pressure (not shown here) also yields a smooth, increasing trend.

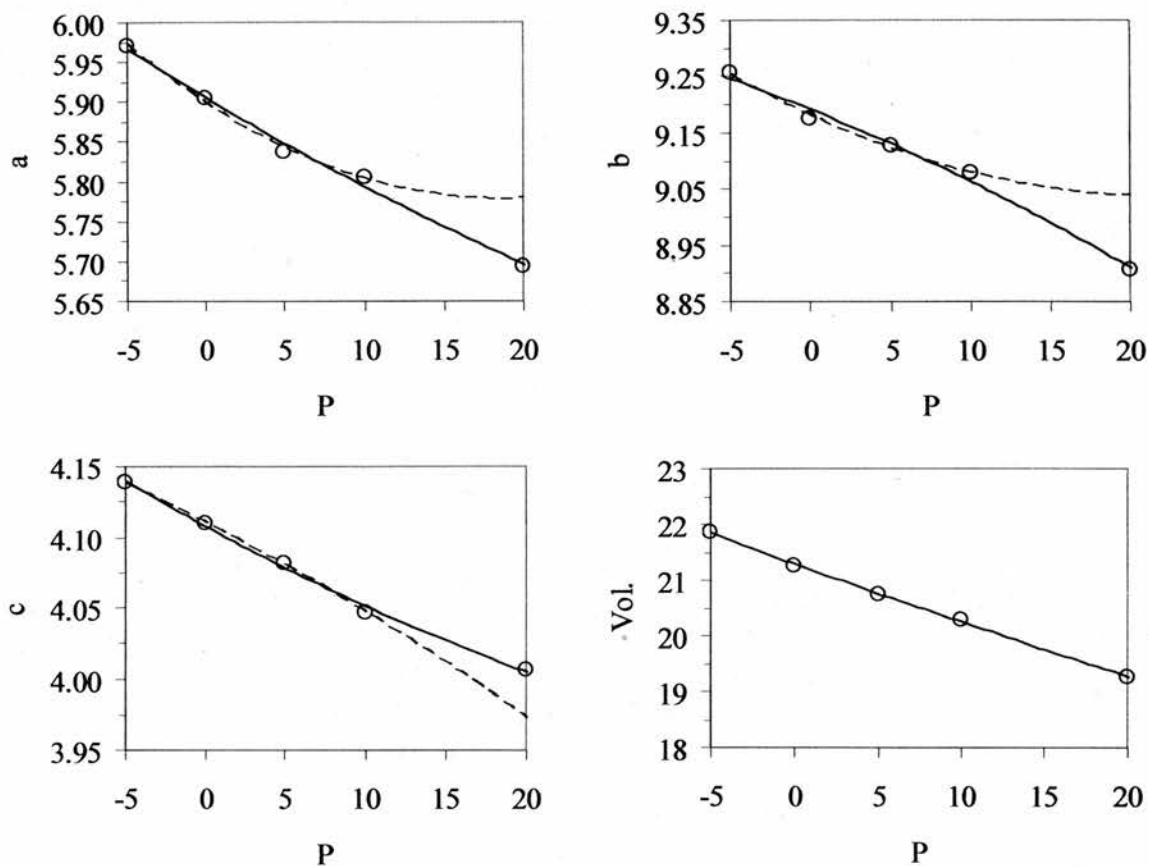


Figure 10. Plots of lattice constants a , b and c (\AA) and molecular volume (\AA^3) against pressure, P (GPa) for the $V_{10}O_{10}$ structure. Solid and dashed lines are quadratic fits to the whole data set and the set excluding the 20GPa point respectively.

In interpreting the pattern of atomic displacements reported in Table 7, it is useful to know what would be expected in the ideal material. The components of the displacements in ideal $V_{10}O_{10}$ for movement toward the nearest neighbour vacancies obey the following relationships,

$$V_2: \delta_u = 2\delta_v, \delta_u < 0,$$

$$V_3: \delta_u = -\delta_v, \delta_u < 0,$$

$$O_2: \delta_u = 2\delta_v, \delta_u < 0,$$

$$O_3: \delta_u = -\delta_v, \delta_u > 0.$$

In the relaxed structures it is evident that V_2 and V_3 are both displaced toward their nearest neighbour oxygen vacancies, although the ratios of $|\delta_v|$ to $|\delta_u|$ are much larger than the ideal values of $\frac{1}{2}$ and 1 respectively. This indicates a significant deviation in the displacement from motion along the line joining the ideal metal position to the vacancy. The components of the displacements of the free oxygen atoms O_2 and O_3 indicate relaxation away from their nearest neighbour metal vacancies, save at 20GPa where O_2 displays relaxation toward V_O . At low pressures the ratios of $|\delta_v|$ to $|\delta_u|$ are close to the ideal values, but the agreement degrades with increasing pressure. The change in mode of relaxation of O_2 at 20GPa supports the potential discontinuity in lattice constants at the same pressure discussed earlier. As an aid to visualisation, Figure 11 below shows the optimised structure of the $V_{10}O_{10}$ cell at equilibrium. Comparison of the energies per molecule obtained thus far shows that the V_5O_5 structure at equilibrium is more stable than the estimated AF_1 VO by $\sim 0.45\text{eV}$. The V_3O_3 structure, however, still lies some 0.15eV lower than V_5O_5 , and thus remains the predicted ground state for all the structures studied.

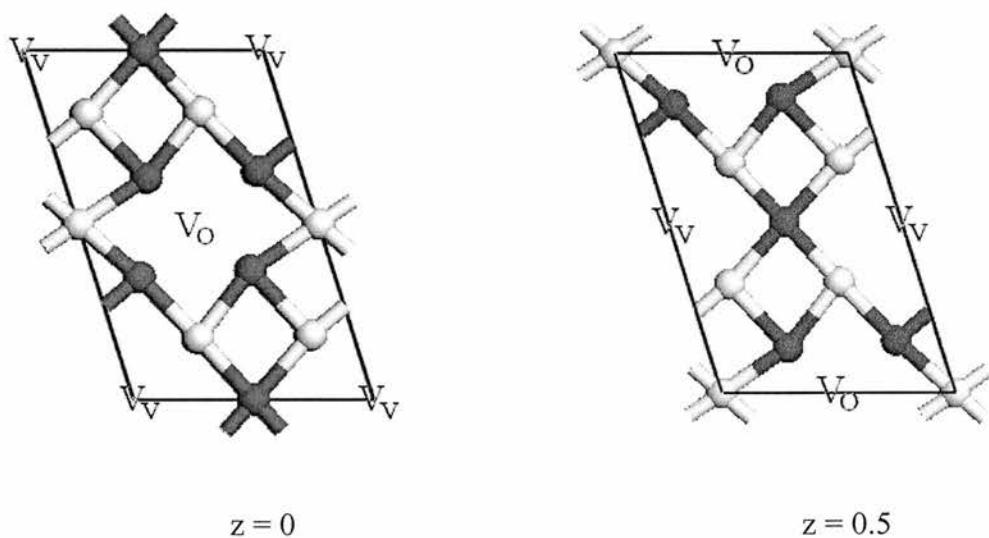


Figure 11. A representation of the atomic positions and the cell in the relaxed structure of equilibrium $V_{10}O_{10}$. Dark and light atoms are vanadium and oxygen respectively.

Table 8 below contains the Mulliken analyses of the electronic structure of V_5O_5 for various hydrostatic pressures. The charges on the metal atoms are in the range from $0.45e$ to $0.64e$ corresponding to the square planar and one of the square pyramidal sites respectively, with an average charge of $0.53e$, some $0.05e$ higher than in V_3O_3 . As in V_7O_7 , the oxygen charges show a much smaller range of values, from $0.55e$ to $0.58e$ for square planar and one of the square pyramidal sites respectively.

P	At.	s	p	d	q	n_s	At.	s	p	d	q	n_s
-5	O_1	1.84	4.72	0.00	-0.55	-0.04	V_1	0.19	0.16	4.19	0.46	+1.04
	O_2	1.84	4.74	0.00	-0.59	-0.02	V_2	0.18	0.22	4.04	0.56	+1.66
	O_3	1.84	4.74	0.00	-0.59	+0.02	V_3	0.14	0.14	4.07	0.65	-1.54
0	O_1	1.83	4.71	0.00	-0.55	-0.04	V_1	0.18	0.14	4.22	0.45	+0.90
	O_2	1.84	4.74	0.00	-0.58	-0.02	V_2	0.17	0.20	4.07	0.56	+1.54
	O_3	1.83	4.74	0.00	-0.57	0.00	V_3	0.14	0.12	4.10	0.64	-1.36
5	O_1	1.83	4.71	0.00	-0.54	-0.02	V_1	0.18	0.13	4.24	0.45	+0.80
	O_2	1.84	4.74	0.00	-0.58	0.00	V_2	0.16	0.18	4.09	0.56	+1.44
	O_3	1.83	4.74	0.00	-0.57	0.00	V_3	0.14	0.11	4.13	0.63	-1.22
10	O_1	1.83	4.70	0.00	-0.53	-0.04	V_1	0.18	0.11	4.25	0.46	-0.88
	O_2	1.83	4.74	0.00	-0.58	0.00	V_2	0.15	0.16	4.13	0.56	+1.36
	O_3	1.83	4.73	0.00	-0.53	0.00	V_3	0.13	0.10	4.16	0.61	-0.64
20	O_1	1.82	4.69	0.00	-0.51	-0.04	V_1	0.17	0.09	4.32	0.42	-0.78
	O_2	1.83	4.73	0.00	-0.56	0.00	V_2	0.14	0.11	4.17	0.58	+0.90
	O_3	1.83	4.72	0.00	-0.55	0.00	V_3	0.13	0.07	4.23	0.57	-0.16

Table 8. The s, p and d-shell occupation (e), total ionic charge, q (e) and unpaired spin population, n_s (μ_B) for all atoms comprising the $V_{10}O_{10}$ defect structure at hydrostatic pressure P (GPa).

The V_5O_5 structure lacks sites with octahedral coordination, so that comparison with the charges at this site in V_7O_7 or perfect VO is not possible. The ionic charge shows a slight decrease with increasing pressure, but the effect is not pronounced. Spin density is, in the main, confined to the metal sublattice. The moments at 0GPa for

sites V_2 and V_3 , which are square-pyramidal coordinated with nine and ten next-nearest neighbour (nnn) metal atoms respectively, are only slightly smaller than the corresponding moment in V_7O_7 , by amounts $0.10\mu_B$ and $0.28\mu_B$ respectively. The moment at equilibrium borne by the square-planar site V_1 is $0.88\mu_B$ smaller than that in V_7O_7 : a large reduction. The moment at this site, however, does not exhibit the same dramatic fall with increasing pressure as was found previously in V_7O_7 . The reason for the retention of moment in V_5O_5 is unclear, since the pattern of displacements sees the V_1-O_2 and V_1-O_3 bond lengths go from 2.067 \AA and 2.129 \AA respectively at 0 GPa to 2.025 \AA and 2.048 \AA respectively at 20 GPa . Changes of that order in the bond length in V_7O_7 saw the moment collapse from $1.78\mu_B$ to $0.28\mu_B$. Instead, in V_5O_5 , it is the moment at the 10 nnn V_3 site that collapses under pressure, going from $-1.36\mu_B$ at 0 GPa to $-0.16\mu_B$ at 20 GPa .

The alignment of the V_1 moment flips at 10 GPa due to the relative reductions in the size of the moments at all metal sites. To see why this should occur, consider the scalar products of the moments at sites 1 and 2, $S_1 \cdot S_2$, and at sites 1 and 3, $S_1 \cdot S_3$, where, in the Ising model, all moments being taken pairwise, each moment is constrained to lie either parallel or antiparallel to the other member of the pair. Now, including only direct exchange terms, and neglecting changes in the coupling constant due to atomic displacements, the contribution to the energy of the $V_{10}O_{10}$ cell of terms involving S_1 is $[-8 J_d S_1 \cdot S_2 - 12 J_d S_1 \cdot S_3]$. An assumption inherent to this model is that the size of any given moment depends only upon the local environment (i.e., upon the $V-O$ bond length) and is unaffected by its alignment. Table 9 below presents the factors multiplying J_d as figured for the values of the metal spin moments presented previously in Table 8.

The pure DFT CRYSTAL98 results in the BLYP Hamiltonian show that $J_d < 0$ (i.e. the direct coupling is antiferromagnetic), and thus this simple model correctly predicts the stability of magnetic states with $S_1 > 0$ for pressures of $-5, 0$ and 5 GPa , and $S_1 < 0$ for pressures of 10 and 20 GPa . The transition point must lie somewhere in the range $5 < P \leq 10 \text{ GPa}$, and occurs primarily due to the rapid collapse in magnetic moment on the 10 nnn V_3 site, for the term involving S_2 in Table 9 can be seen to vary very little in magnitude across the transition range, while that involving S_3 falls rapidly. For the

P	S_1	S_2	S_3	$-8 S_1 \cdot S_2$	$-12 S_1 \cdot S_3$	Total
-5	1.04	1.66	-1.54	-13.81	19.22	5.41
	-1.04	1.66	-1.54	13.81	-19.22	-5.41
0	0.9	1.54	-1.36	-11.09	14.69	3.60
	-0.9	1.54	-1.36	11.09	-14.69	-3.60
5	0.8	1.44	-1.22	-9.22	11.71	2.50
	-0.8	1.44	-1.22	9.22	-11.71	-2.50
10	0.88	1.36	-0.64	-9.57	6.76	-2.82
	-0.88	1.36	-0.64	9.57	-6.76	2.82
20	0.78	0.9	-0.16	-5.62	1.50	-4.12
	-0.78	0.9	-0.16	5.62	-1.50	4.12

Table 9. The spin moments S_1 , S_2 and S_3 (μ_B) on corresponding metal sites, and the components and summed total of factors (μ_B^2) multiplying J_d in the expression $[-8 J_d S_1 \cdot S_2 - 12 J_d S_1 \cdot S_3]$ for various hydrostatic pressures, P (GPa).

V_5O_5 primitive cell at 0GPa, the value of $\int \{\rho_\alpha(\mathbf{r}) - \rho_\beta(\mathbf{r})\} d\mathbf{r}$ integrated directly upon the FFT grid is $1.23\mu_B$, which compares very favourably with the calculated Mulliken value ($S_1+2S_2+2S_3$) of $1.26\mu_B$ and lends credibility to the use of Mulliken spin moments in the model above. It is clear that the moments in V_5O_5 are not arranged in orientation or magnitude such that the net spin of the cell is brought close to zero, as was found in V_7O_7 .

The atom projected densities of states for V_5O_5 at equilibrium are plotted in Figure 12 below, and there compared with the perfect FM total DOS. The top and bottom O(2p) edges are $\sim 0.7\text{eV}$ and $\sim 0.3\text{eV}$ higher respectively in V_5O_5 than in the majority spin projection of perfect FM. The top V(3d) edge, meanwhile, lies close to that in perfect FM, while the lower edge shows extension of metal states into the gap between the two topmost valence bands. The O(2s) band is little changed in shape from the perfect FM form, but the top edge is pushed $\sim 0.4\text{eV}$ higher in energy. The Fermi energy of V_5O_5 lies at -4.7086eV , as compared to the perfect FM value of -3.5825eV . As discussed above, the V_5O_5 cell bears a net spin moment, but a comparison of the band edges of majority and minority spins does not reveal a splitting. The spin polarisation instead arises from the relative weights of α and β states up to the Fermi energy.

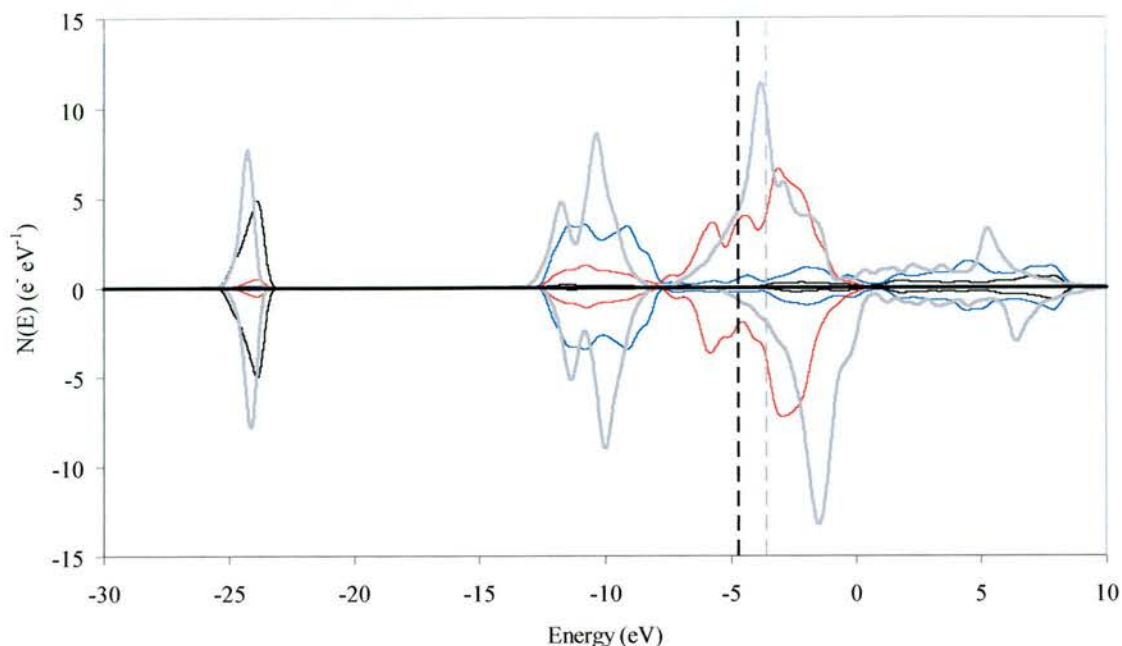


Figure 12. The atom-projected densities of states for the V_5O_5 structure. O(p) states are shown in blue, V(d) states in red, O(s) states in black and, for comparison, FM VO total DOS in thick grey. Fermi energies are denoted by vertical dashed black and grey lines for V_5O_5 and FM VO respectively.

5. Conclusions

The primary conclusion of this study is that, within the $VO_{1.0}$ stoichiometry, all defect structures simulated have a lower energy per molecule than the perfect rocksalt lattice, with the 1 in 4 V_3O_3 structure showing the greatest stability. The predicted ground states of V_3O_3 type in the present GGA-PBE study of VO, and V_5O_5 type in the LDA PW-PP study of TiO by Leung *et al* are both in agreement with the simple models proposed by Burdett and Hughbanks. Figure 13 below shows the energy-volume curves for all structures studied within $VO_{1.0}$.

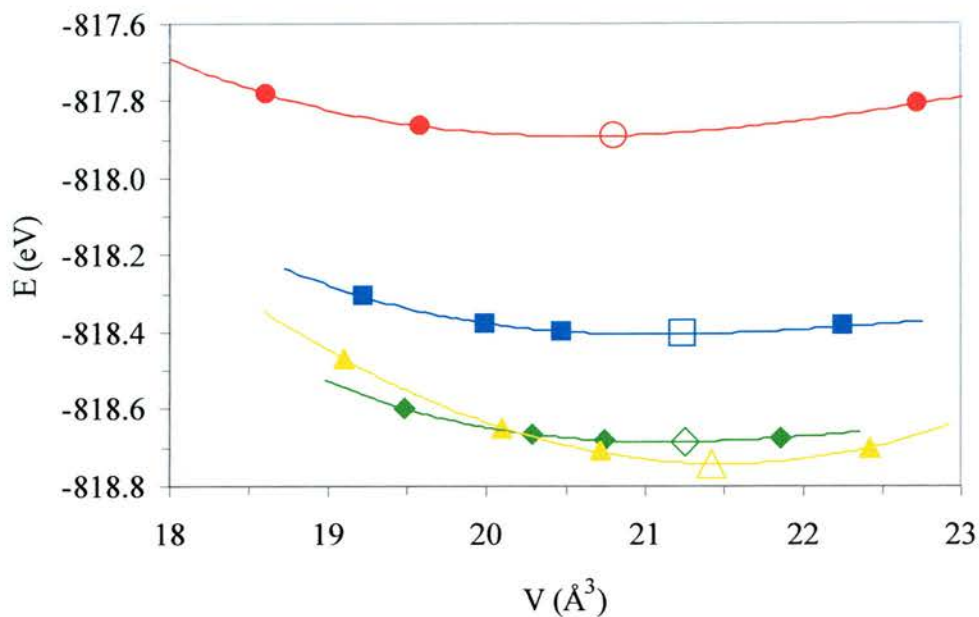


Figure 13. Plots of energy, E (eV), against volume, V (\AA^3) both per molecule for perfect rocksalt VO (estimated AF_1 energy) (\circ), V_7O_7 (\square), V_5O_5 (\diamond) and V_3O_3 (\triangle).

It is clear from the figure that vacancies at all concentrations contribute positively to the volume of the lattice. In the previous study of TiO, the molecular volume for the Ti_3O_3 structure was found to be $\sim 3\text{\AA}^3$ higher than for the perfect lattice. Here, in VO, the same comparison yields a difference of only $\sim 0.6\text{\AA}^3$. Additionally, the difference in energy between equilibrium Ti_5O_5 and Ti_3O_3 was found to be quite large at $\sim 0.2\text{eV}$, but here in VO amounts to only $\sim 0.06\text{eV}$. Of course, there is prior experimental and theoretical evidence that the vacancies in $VO_{1.0}$ do not form an ordered structure, due to inter-vacancy interactions of low strength. The calculations reported here, though, suggest that the defects in $VO_{1.0}$ will occur at a concentration close to 25%, relatively far from the 15% derived experimentally by comparison of X-ray and pycnometric densities. The calculated equilibrium lattice constant of V_3O_3 , 4.0058\AA falls within 1.4% of the value 4.063\AA observed in the random defect structure by Loehman *et al.* In equilibrium V_7O_7 , $(a/\sqrt{2}) = 4.1922\text{\AA}$ and $c = 4.2327\text{\AA}$ are respectively 3.2% and 4.2% from the experimental value, while in equilibrium V_5O_5 , $(a/\sqrt{2}) = 4.1750\text{\AA}$, $(b/\sqrt{5}) = 4.1035\text{\AA}$ and $c = 4.1092\text{\AA}$ fall within 2.8%, 1.0% and 1.1% respectively of experiment. It is clear that either V_3O_3 or V_5O_5 provide approximately cubic cell edges of the appropriate dimension, and it is difficult to say which of them more closely matches experiment.

6. References

- [1] K. Naito and T. Matsui, *Solid State Ionics* **12**, 125 (1984)
- [2] D. Watanabe, J. R. Castles, A. Jostsons and A. S. Malin, *Acta. Cryst.* **23**, 307 (1967)
- [3] R. Tetot and C. Picard, *J. Solid State Chem*, **66** 324 (1987)
- [4] J. A. Roberson and R. A. Rapp, *J. Phys. Chem. Solids* **30**, 119 (1969)
- [5] M. D. Banus and T. B. Reed in "The Chemistry of Extended Defects in Non-Metallic Solids" ed. By L. Eyring and M. O'Keefe, North-Holland, Amsterdam, 488 (1970)
- [6] C. N. R. Rao and G. V. Subba Rao, *Phys. Stat. Sol (a)* **1**, 597 (1970)
- [7] C. Giaconia and R. Tetot, *J. Phys. Chem. Solids* **58**, 1041 (1997)
- [8] J. K. Burdett and T. Hughbanks, *J. Am. Chem. Soc.* **106**, 3101 (1984)
- [9] C. Leung, M. Weinert, P. B. Allen and R. M. Wentzcovitch, *Phys. Rev. B* **54**, 7857 (1996)
- [10] P.V. Gel'd, S. I. Alyamovskii and I. I. Matveenکو, *Zhurn. Strukt. Khim.* **2**, 301 (1961)
- [11] M. D. Banus, T. B. Reed and A. J. Strauss, *Phys. Rev. B* **5**, 2775 (1972)
- [12] R. E. Loehman, C. N. R. Rao and J. M. Honig, *J. Phys. Chem.* **73**, 1781 (1969)
- [13] M. D. Segall, R. Shah, C. J. Pickard, and M. C. Payne, *Phys. Rev. B* **54**, 16317 (1996)

Chapter 7

A UHF Study of Crystal Field Excitations in Pure and Hole-Doped $\text{Sr}_2\text{CuO}_2\text{Cl}_2$

1. Introduction

Chapter 1 has already provided an overview of the crystal field excitations in the TMOs, the experimental results for the cuprate $\text{Sr}_2\text{CuO}_2\text{Cl}_2$ will be presented here. An early study of the optical spectra of $\text{Sr}_2\text{CuO}_2\text{Cl}_2$ was made by Perkins et al [1], in which it was surmised that the $d_{z^2} \rightarrow d_{x^2-y^2}$ excitation occurred at an energy ~ 0.5 eV, with possible implications for the mechanism of superconductivity in the doped system. Kuiper et al [2] reported the resonant x-ray Raman spectra, from which they assigned directly the $d_{xy} \rightarrow d_{x^2-y^2}$ and degenerate $d_{yz} \rightarrow d_{x^2-y^2}$ and $d_{xz} \rightarrow d_{x^2-y^2}$ transitions at 1.35 eV and 1.8 eV respectively and inferred a value of 1.5 eV for the $d_{z^2} \rightarrow d_{x^2-y^2}$ transition. Using theoretical arguments they showed the latter to be accompanied by a spin-flip which increased the energy by 0.2 eV, thereby denying its direct assignment from the x-ray Raman spectra. While the case made by the later authors [2] for the last of these assignments well above the previous value [1] appears to be both robust and convincing, independent support of this view, or otherwise, would be useful. Furthermore, while it is reasonable to assume that the $d \rightarrow d$ excitonic properties of pure $\text{Sr}_2\text{CuO}_2\text{Cl}_2$ remain essentially unchanged in the hole-doped (superconducting) system, this may not be precisely the case, so that the possible involvement of the $d_{z^2} \rightarrow d_{x^2-y^2}$ excitation in the superconducting mechanism may not be completely resolved. Accordingly, this chapter reports, for the first time, direct first principles calculations of the Cu $d \rightarrow d$ excitations in pure and hole-doped $\text{Sr}_2\text{CuO}_2\text{Cl}_2$, clarifying the position with regard to the energy of the $d_{z^2} \rightarrow d_{x^2-y^2}$ excited state in this model high T_c cuprate. As in previous chapters, the formal basis for the analysis of the excitations is contained within the Kanamori Hamiltonian, as discussed previously in Chapter 1.

One earlier study reported Cu $d \rightarrow d$ excitations in the range 1.26 eV – 2.20 eV for the quasi one-dimensional, spin- $\frac{1}{2}$ Heisenberg antiferromagnet, Sr_2CuO_3 [3] in which the local symmetry at the Cu site is D_{4h} , as it is in $\text{Sr}_2\text{CuO}_2\text{Cl}_2$. In this material, the $d_{z^2} \rightarrow d_{x^2-y^2}$ transition was predicted to lie at 2.20 eV, but, to the best of the author's knowledge, this has not been confirmed experimentally.

2. Theoretical Method

The theoretical basis and computational procedures used in the current study are documented in Chapter 1. As was the case for VO in Chapter 5, the aim here is not the same as that of previous chapters, for in the case of NiO and MnO, experimental properties were well established, and it was the ability of hybrid schemes to reproduce the experimental values that was under test. In $\text{Sr}_2\text{CuO}_2\text{Cl}_2$, by contrast, no clear conclusion has arisen from experiment as to the energies of the $d \rightarrow d$ excitations, and it is hoped to provide some theoretical input. To this end, the earlier strategy of varying the weight of exact exchange is surfeit to requirements, and instead the UHF method is used, for its performance in NiO is well documented [4,5]. All calculations refer to the experimental I4/mmm (International Table No. 139) structure of $\text{Sr}_2\text{CuO}_2\text{Cl}_2$ [6,7], with a ($\equiv b$) and c lattice constants of 3.972 Å and 15.613 Å respectively.

Figure 1 below shows the crystallographic cell, while Figure 2 depicts the antiferromagnetic supercell. The Sr, Cu and O basis sets used previously for Sr_2CuO_3 [3] are employed here, with the addition of an optimised {1s,2sp,3sp,4sp,3d} set for Cl. As for the study of holes in NiO in Chapter 4 and on previous occasions [3-5], the approach to local defects is based on the use of periodic supercells of varying size, from which the energies and properties of isolated defects can be extracted.

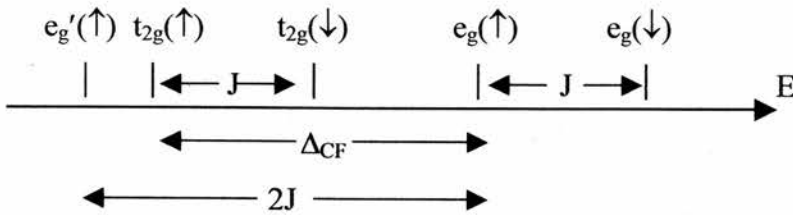
3. Results

UHF calculations predict the ground state of $\text{Sr}_2\text{CuO}_2\text{Cl}_2$ to be a highly ionic, d^9 antiferromagnetic (AF) insulator with an in-plane $d_{x^2-y^2}$ hole, i.e. oriented in the Cu-O bond directions. The hypothetical ferromagnetic (FM) spin arrangement, which is also insulating, in contrast to previous LMTO [8] and FLMTTO [9] calculations, is 26.5 meV/Cu higher in energy

	q_{Sr}	q_{Cu}	q_{O}	q_{Cl}	n_{xy}	$n_{xz/yz}$	n_{z^2}	$n_{x^2-y^2}$	n_s
Ground	2.03	1.83	1.92	1.03	2.00	2.00	1.99	1.01	0.92
$d_{xy} \rightarrow d_{x^2-y^2}$	2.03	1.89	1.93	1.03	1.02	2.00	2.00	2.03	0.98
$d_{z^2} \rightarrow d_{x^2-y^2}$	2.03	1.89	1.93	1.03	2.00	2.00	1.02	2.03	0.98
$d_{xz}/d_{yz} \rightarrow d_{x^2-y^2}$	2.03	1.90	1.93	1.03	2.00	1.02	2.01	2.03	0.99

Table 1. $\text{Sr}_2\text{CuO}_2\text{Cl}_2$ AF ground and excited state UHF atomic charges, q_α (e), d-orbital populations, n_α and Cu spin moments, n_s (μ_B)

Atom projected valence band densities of states, shown in the upper panel of Figure 3, confirm the strong ionicity in $\text{Sr}_2\text{CuO}_2\text{Cl}_2$ for these reveal overlapping O(p), Cl(p) bands spread over ~ 6.5 eV from the Fermi level, with the Cl(p) upper edge shifted by ~ 1 eV. The Cu(d) bands, which range from ~ -8 eV to ~ -12 eV, are each extremely narrow, in keeping with their highly atomic character. The conduction band edge is predominantly $d_{x^2-y^2}$, so that the band gap of ~ 15 eV is essentially of $p \rightarrow d$ CT character, in keeping with the position of the cuprates in the ZSA scheme. Once again, this contrasts with previous LMTO calculations [8,9] which find $\text{Sr}_2\text{CuO}_2\text{Cl}_2$ to be a MH system. The lower panel of Figure 3 shows the projected densities of states for the Cu d-levels where their juxtaposition indicates clear orbital polarisation linked to strong on-site Coulomb (U,U') and exchange (J) interactions. Now a Kanamori analysis of a d^9 [$(t_{2g})^6(e_g)^2(e_g')^1$] configuration in the more symmetric O_h crystal field (used here as an approximation to the true D_{4h} symmetry) indicates that the energies of the individual d-levels depend on the relative magnitudes of the crystal field splitting Δ_{CF} and the average on-site exchange energy, J. Specifically, for $2J > \Delta_{\text{CF}} > J$, the filled d-level spectrum is of the form



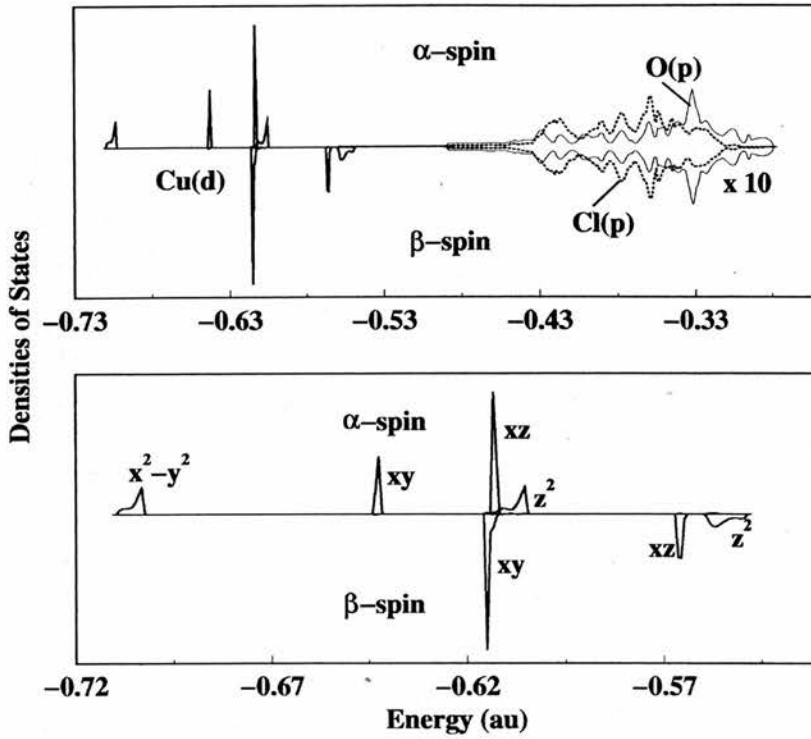


Figure 3. Upper panel: AF ground state Cu(d), O(p) and Cl(p) valence band densities of states of $\text{Sr}_2\text{CuO}_2\text{Cl}_2$. Lower panel: expanded Cu(d) densities of states.

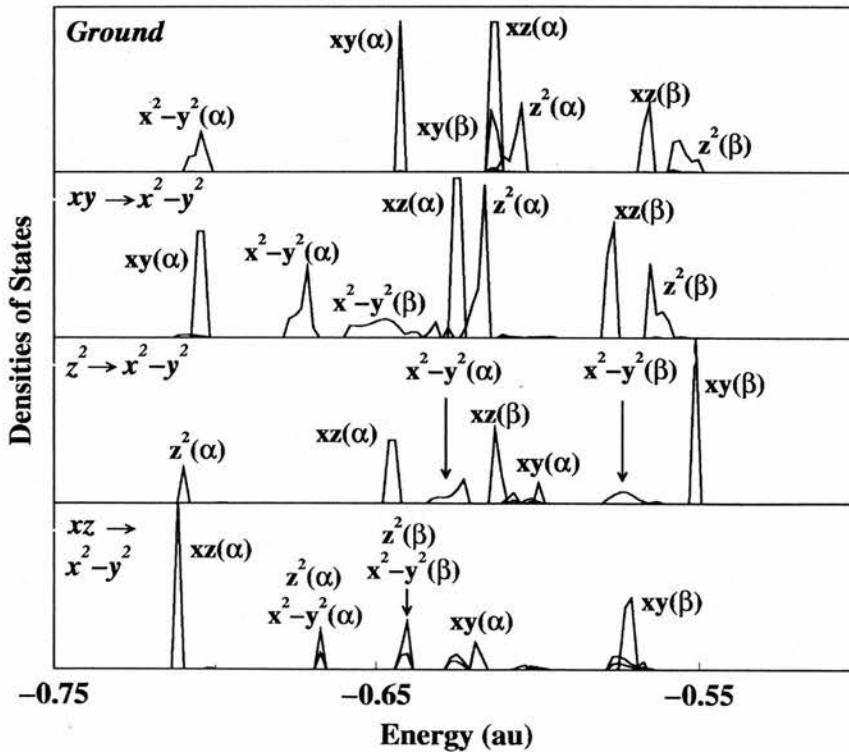


Figure 4. Comparison of AF ground and $d \rightarrow d$ excited state Cu(d) densities of states.

This is broadly similar to the calculated spectrum shown in Figure 3, with $e_g' \equiv d_{x^2-y^2}$ and $e_g \equiv d_{z^2}$, but modified by the reduced D_{4h} symmetry of Cu in $Sr_2CuO_2Cl_2$, so that the $e_g'(\uparrow) - e_g(\uparrow)$ separation is $(U - U')$ and the splitting of the doubly-occupied d_{xy} , d_{xz}/d_{yz} and d_{z^2} bands are 0.7 eV, 1.2 eV and 1.4 eV respectively and not all equal. One necessary caution here is that the Kanamori analysis has neglected the orbital dependencies of the Coulomb and exchange interactions. These were shown to be important in the analysis of the $d \rightarrow d$ excitations in NiO presented in Chapter 3. It is immediately clear that in the $d_{z^2} \rightarrow d_{x^2-y^2}$ excited state, for example, the e_g' and e_g levels are inverted, thus ruling out the possibility of any type of rigid-band prediction of the spin-allowed $d \rightarrow d$ excitations from the ground state eigenvalues. Such a naïve analysis would place the excited states in the order $d_{z^2} \rightarrow d_{x^2-y^2} < d_{xz}/d_{yz} \rightarrow d_{x^2-y^2} < d_{xy} \rightarrow d_{x^2-y^2}$, which is exactly the reverse of the observed order, with energies of ~ 25 eV, which is more than an order of magnitude greater than the experimental (and directly calculated) values. Furthermore, the $d \rightarrow d$ states would be predicted to be higher in energy than the charge-transfer states, which calculations by Tanaka and Kotani [10] have estimated to be in the region of 5 eV.

Similar calculations to those for the ground state find the three spin-allowed $d \rightarrow d$ excited states in the AF alignment to be variationally stable. As shown in Table 1, the ionicity of these states is practically identical to that of the ground state, with conservation of the total d population and local spin moment. Changes in the individual d -orbital populations, which are within 2% of ± 1 , are characteristic of highly local atomic transitions corresponding to fully localised Frenkel excitons. The energies of supercells containing multiple excited Cu atoms, including the fully excited Cu sublattice, indicate that the excitonic interactions between nearest neighbour sites are all less than 0.007 eV, which further confirms the highly local nature of these excitations. Direct total energy differences between the AF ground and excited states lead to UHF energies of 1.10 eV, 1.53 eV and 1.57 eV for the $d_{xy} \rightarrow d_{x^2-y^2}$, $d_{z^2} \rightarrow d_{x^2-y^2}$ and $d_{xz}/d_{yz} \rightarrow d_{x^2-y^2}$ excitations respectively, as presented in Table 2 below.

The reasonable assumptions can now be made that the leading correction to the $e_g \rightarrow e_g$ excitation energy is the difference between the $(d_{z^2})^2$ and $(d_{x^2-y^2})^2$ pair correlation energies, and that, similarly, the leading correction to the two $t_{2g} \rightarrow e_g$ excitation energies is the difference between $(d_{x^2-y^2})^2$ and $(d_{xy})^2$ and $(d_{xy})^2 / (d_{yz})^2$ pair correlation energies. Furthermore, it seems reasonable to propose that the corrections to the two $t_{2g} \rightarrow e_g$ excitations will be close in magnitude. Now, a comparison of the UHF calculated excitation energies with the experimental results of Kuiper *et al* [2] reveals that the UHF $d_{xy} \rightarrow d_{x^2-y^2}$ energy underestimates experiment by 0.25 eV, and that the degenerate UHF $d_{xz}/d_{yz} \rightarrow d_{x^2-y^2}$ excitation underestimates experiment by 0.23 eV. The argument presented above would therefore seem to be correct, in that the pair correlation corrections to the two $t_{2g} \rightarrow e_g$ excitations are essentially identical. Importantly, no such correction is necessary for the UHF $d_{z^2} \rightarrow d_{x^2-y^2}$ excitation (as evidenced by the similarity of UHF and Raman results), and thus the current calculations fully support the conclusion of Kuiper *et al* [2] that the energy of the $d_{z^2} \rightarrow d_{x^2-y^2}$ excited state is close to 1.5 eV and not in the mid-infrared at ~ 0.5 eV, as suggested previously by Perkins *et al* [1].

Excitation	Periodic UHF	Apparent Pair Correlation Correction	Correlated Cluster	'Uncorrelated' Cluster	Raman [2]
$d_{xy} \rightarrow d_{x^2-y^2}$	1.10	0.25	1.23	0.98	1.35
$d_{z^2} \rightarrow d_{x^2-y^2}$	1.53	-0.03	1.18	1.18	1.5
$d_{xz}/d_{yz} \rightarrow d_{x^2-y^2}$	1.57	0.23	1.50	1.25	1.8

Table 2. Comparison of the energies (eV) of the three spin-allowed $d \rightarrow d$ excited states in $\text{Sr}_2\text{CuO}_2\text{Cl}_2$ from first principles periodic and cluster calculations [11] with experiment [2].

Figure 4 shows the projected densities of Cu(d) states for the three excitations compared with the ground state, from which the origin of the strong renormalisation is evident. In addition to the largely uniform relaxation of the O(p) and Cl(p) states, there is extensive reorganisation of the Cu d-manifold driven by the changes in the on-site Coulomb and exchange interactions,

which UHF calculations treat exactly, and it is these adjustments, notably those of the local d-states, that lead to the substantial reductions in energy from the rigid band values. Figure 4 also shows that while the excited state d-level structures differ quite clearly from that of ground state, the effects of orbital occupancy and crystal field asymmetry are the same. For all three excited states the singly occupied band is lowest in energy and there is unequal spin-splitting of the four doubly occupied bands in each case.

It is instructive to compare the current results with the correlated cluster calculations reported by de Graaf and Broer [11] for the insight this offers into the influence of the extended surrounding lattice, even for such highly local excitations. Table 2 above presents the relevant data. These authors found energies of 1.23 eV, 1.18 eV and 1.50 eV for the $d_{xy} \rightarrow d_{x^2-y^2}$, $d_{z^2} \rightarrow d_{x^2-y^2}$ and $d_{xz} / d_{yz} \rightarrow d_{x^2-y^2}$ respectively, which are qualitatively incorrect with respect to the order of the excited states and too low by 0.12 eV - 0.3 eV, although they do support the view that the $d_{z^2} \rightarrow d_{x^2-y^2}$ excitation is not in the mid infra-red region. If, as a rough guide, the correlation corrections deduced above are subtracted from these values to give an estimate of the ‘uncorrelated’ energies, it can be seen that the clusters used by de Graaf and Broer [11] underestimate the effect of the extended lattice by an amount comparable to the correlation energy. This is interesting, for clusters of the size used by de Graaf and Broer enable the inclusion of a substantial fraction of the correlation energy. While the magnitude of this underestimate might be considered to be small, it can result in a qualitatively different picture of the low energy spectrum from that derived from periodic calculations. In the case of Sr_2CuO_3 , for example, for which the periodic UHF $d \rightarrow d$ excitation energies have been reported previously [3], the inclusion of the correlation corrections deduced here for $t_{2g} \rightarrow e_g$ transitions suggest that all the $d \rightarrow d$ excitations lie above the insulating gap of ~ 1.5 eV reported by Maiti et al [12], whereas cluster calculations [11] suggest that the $d_{xy} \rightarrow d_{x^2-y^2}$ excitation lies below the absorption edge, as indicated in

Table 3.

Excitation	Periodic UHF + Correction	Correlated Cluster [11]
$d_{xy} \rightarrow d_{x^2-y^2}$	1.51	1.08
$d_{yz} \rightarrow d_{x^2-y^2}$	2.12	1.53
$d_{xz} \rightarrow d_{x^2-y^2}$	2.18	1.67
$d_{z^2} \rightarrow d_{x^2-y^2}$	2.20	2.11

Table 3. Predicted energies (eV) of the spin-allowed $d \rightarrow d$ excited states in Sr_2CuO_3 from [3].

In their assignment of the $d_{z^2} \rightarrow d_{x^2-y^2}$ excitation, which is not observed directly in the x-ray Raman spectra, a crucial step in the argument invoked by Kuiper et al [2] is that the excitation is accompanied by a local spin flip which increases the energy by ~ 0.2 eV to a value close to that for $d_{xz} / d_{yz} \rightarrow d_{x^2-y^2}$, thereby denying its direct observation. To address the origin and magnitude of this spin-flip energy, the Ising model may be used, with the form

$$H_{\text{Spin}} = \frac{1}{2} J \sum_{ij}^{\text{nn}} \sigma_i \sigma_j,$$

where the summation runs over nearest neighbour (nn) Cu atoms, σ_i and σ_j are spin variables with values of ± 1 and J is the superexchange coupling between nn spins. The mean field disorder temperature is given by $2J/k_B$, which by simple scaling by 0.56 to allow for fluctuations [13], leads to a Néel temperature, T_N , of $\sim 1.12J/k_B$. Now Vaknin et al [7] have reported T_N for $\text{Sr}_2\text{CuO}_2\text{Cl}_2$ to lie in the range 251 K – 310 K, which leads to values of J from ~ 19 meV to ~ 24 meV coupling Cu $d_{x^2-y^2}$ spins in the AF ground state. The energy to flip a single spin in the AF alignment can be computed from H_{spin} as $8J$, leading to a spin-flip energy of ~ 0.15 eV to ~ 0.19 eV based on the values for J deduced from the Néel temperature. Given the approximations involved, it is believed that this estimate is supportive of the value proposed by Kuiper et al [2]. This suggests that the increase in energy of ~ 0.2 eV for the $d_{z^2} \rightarrow d_{x^2-y^2}$ excitation in the resonant x-ray Raman spectra of $\text{Sr}_2\text{CuO}_2\text{Cl}_2$ is due essentially to the flip of a $d_{x^2-y^2}$ spin in the AF ground state rather than a d_{z^2} spin in the excited state. UHF calculations support this interpretation, for while the directly calculated

ground state spin flip energy of 0.05 eV would appear to be too low by a factor of four, the energy to flip a d_{z^2} spin in the excited state is predicted to be ~ 0.002 eV, which is much lower still. However, Moreira et al [14] have shown that the Fock-35 hybrid yields accurate exchange constants in NiO, and it was proposed to try this method in $\text{Sr}_2\text{CuO}_2\text{Cl}_2$. Following their prescription, but keeping all other aspects identical to those for the UHF calculations, a value for J of 32.73 meV is found, leading to a ground state spin flip energy of 0.26 eV, which, again, is close to the value proposed by Kuiper et al [2].

The same supercell approach to that used previously in Chapter 4 for NiO and in Ref. [3] for Sr_2CuO_3 is used here for the study of hole-doped $\text{Sr}_2\text{CuO}_2\text{Cl}_2$. As before, variationally minimised states are sought for singly ionised supercells within a uniform charge-compensating background to remove the Coulomb singularity. Operating under identical computational conditions to those for the ground and $d \rightarrow d$ excited states, the lowest energy free hole state is found to be essentially of O(p) character (ie $\sim d^9\bar{L}$), in accord with the ground state densities of states. The lowest energy O(p) hole is π polarised, lying in the CuO_2 planes (denoted π_{\parallel}) and has $\sim 84\%$ of the charge density and $\sim 98\%$ of the spin density localised at a single site. Two excited O(p) hole states of π_{\perp} and σ polarisations have also been found, lying ~ 0.2 eV and ~ 0.9 eV respectively higher in energy. The charge and spin densities of the π_{\perp} state are very similar to those of the π_{\parallel} state but are more dispersed in the high energy σ state, though it is still essentially localised. Apart from the changes in the charge and spin densities at the hole site, all other atomic charges, d-orbital populations and local Cu spin moments remain within 2% of the (neutral) ground state values. As before, a naïve rigid-band prediction of the spin-allowed $d \rightarrow d$ excitations nearest neighbour to the hole site put these in the order $d_{z^2} \rightarrow d_{x^2-y^2} < d_{xz} / d_{yz} \rightarrow d_{x^2-y^2} < d_{xy} \rightarrow d_{x^2-y^2}$. Variationally stable Cl(p) and Cu(d) holes have been obtained, at energies 2.3 eV and 4.6 eV respectively above the O($p\pi_{\parallel}$) state. The influence of these holes, if any, on the $d \rightarrow d$ excited states have not been pursued due to their high energies.

Once again UHF calculations employing identical computational conditions find the three spin-allowed $d \rightarrow d$ excitations nearest neighbour to the O(p) hole to be variationally stable by minimisation of the total energy for all three polarizations of the hole in configurations in which the unpaired spin at the hole site is both ferromagnetic $\{p(\uparrow) - d(\uparrow)\}$ and antiferromagnetic $\{p(\uparrow) - d(\downarrow)\}$ to the excited Cu spin. The energies of these excited states

with the inclusion of the correlation correction of 0.25 eV for the two $t_{2g} \rightarrow e_g$ excited states are given in Table 4.

Excitation	$p(\uparrow) - d(\downarrow)$			$p(\uparrow) - d(\uparrow)$			Defect Free*
	π_{\parallel}	π_{\perp}	σ	π_{\parallel}	π_{\perp}	σ	
$d_{xy} \rightarrow d_{x^2-y^2}$	1.31	1.30	1.24	1.39	1.33	0.86	1.35
$d_{z^2} \rightarrow d_{x^2-y^2}$	1.31	1.39	1.44	1.36	1.41	0.76	1.53
$d_{xz}/d_{yz} \rightarrow d_{x^2-y^2}$	1.62	1.64	1.47	1.66	1.68	1.07	1.82

Table 4. Energies (eV) of the three spin-allowed $d \rightarrow d$ excited states nearest neighbour to π_{\parallel} , π_{\perp} and σ O(p) holes in AF $Sr_2CuO_2Cl_2$ compared with the defect free values

While the presence of an O(p) hole in all three polarizations and in both local spin alignments reduces the energies of the $d \rightarrow d$ states, for the two low energy O(p_{π}) holes the reduction is predicted to be in the region of 0.1 eV – 0.2 eV, with no evidence for the $d_{z^2} \rightarrow d_{x^2-y^2}$ state in the region of 0.5 eV. There is a marked reduction for the O(p_{σ}) hole, but the energy of this state, ~ 0.9 eV, might reasonably be taken to preclude any rôle it might play in the low temperature properties of $Sr_2CuO_2Cl_2$. An analysis of the atomic charges, d-orbital populations and densities of states reveals $d \rightarrow d$ states whose electronic distributions are changed little from those in the absence of a nearest neighbour hole, with very similar re-organisation of the t_{2g} and e_g levels.

Finally, to put the results into context, both from the point of view of the low energy excited states of $Sr_2CuO_2Cl_2$, and the more general methodological question as to the wider utility of direct excited state calculations, the energies of the nearest neighbour (nn) $p\pi_{\parallel} \rightarrow d_{x^2-y^2}$, $p\pi_{\perp} \rightarrow d_{x^2-y^2}$ and $p\sigma \rightarrow d_{x^2-y^2}$ CT states have been calculated, in which the unpaired oxygen spin is either parallel or antiparallel to the transferred electron spin. The method used in calculations of the CT states involves placing constraints upon the occupation of the atomic states involved through shifting of the relevant eigenvalues of the Fock matrix. This is not a normal feature of CRYSTAL98, and so the code was altered to fit the purpose. It should be noted that an interpretation of the UHF band gap at face value places these around 15 eV.

Once again, a Kanamori analysis is instructive, for, quite apart from any changes to the O(p) states at the hole site, the d^{10} configuration at the acceptor site now assumes the ideal, spin-independent splitting of the t_{2g} and e_g states by Δ_{CF} , quite unlike that for the d^9 ground state, so that any recourse to a rigid-band estimate is totally inappropriate. Under identical computational conditions to those for the ground and $d \rightarrow d$ states, direct UHF calculations find energies of (5.249, 5.274), (5.572, 5.598) and (5.545, 5.284) eV respectively for the ($\uparrow\uparrow, \uparrow\downarrow$) charge-transfer states, which compare with values of around 5 eV predicted by Tanaka and Kotani [10] based on a parameterised impurity Anderson model. A similar calculation for the nearest off-site $Cu(d_{z^2}) \rightarrow Cu(d_{x^2-y^2})$ charge transfer yields an energy of 9.4 eV. These energies calculated from direct total energy differences neglect the dipole-dipole interaction between supercells so that it is reasonable to assume that they are upper bounds to the UHF value of the isolated excitation. As in the case of the $d \rightarrow d$ excited states, the leading correction to the UHF energies are the difference between the $(p\pi_{\parallel})^2 / (p\pi_{\perp})^2$ and $(d_{x^2-y^2})^2$ pair correlation energies, but it is unlikely that these amount to more than a few tenths of an eV, at most. Allowing for the effect of band widths, as extracted from the densities of states, leads to an absorption edge in the region of 2 eV, which is close to that observed experimentally [15]. Mulliken analyses suggest that in these nn CT states $\sim 70\%$ of net electron charge density is localised at the acceptor (Cu) site and $\sim 76\%$ of net hole charge density at the nn (O) donor site with $\sim 88\%$ of the transfer net spin density localised at the two sites. Changes to the surrounding atomic charges and orbital populations amount to less than 2% of the ground state values, so that these nn CT states are also predicted to be Frenkel excitonic in nature. As expected, the extensive re-organisation of the valence levels at both the donor and acceptor sites, leads to substantial relaxations from the rigid band energies.

4. Conclusions

In conclusion, it has been shown that a direct SCF approach to the three spin-allowed $d \rightarrow d$ excited states in $Sr_2CuO_2Cl_2$ leads to energies in good agreement with the resonant X-ray Raman spectra of the $d_{xy} \rightarrow d_{x^2-y^2}$ and $d_{xz} \rightarrow d_{x^2-y^2}$ excitations observed by Kuiper et al [2] and in full support of their conclusion that the energy of the $d_{z^2} \rightarrow d_{x^2-y^2}$ state, which is not observed directly, is 1.5 eV rather than 0.5 eV which had been suggested previously [1].

The difference between the UHF and experimental $d_{xy} \rightarrow d_{x^2-y^2}$ energies, which can be ascribed largely to the difference between $(d_{x^2-y^2})^2$ and $(d_{xy})^2$ pair correlation, is 0.25 eV, a value which is very close to the corresponding difference in NiO [5] and might reasonably represent a useful estimate of the correlation correction to UHF $t_{2g} \rightarrow e_g$ energies more generally for other late first-row transition metal ions in an octahedral crystal field. Assuming this correction applies to the $d_{xz} \rightarrow d_{x^2-y^2}$ excitation and that the $(d_{z^2})^2$ and $(d_{x^2-y^2})^2$ pair correlation energies are similar so that there is essentially no correction to the UHF $d_{z^2} \rightarrow d_{x^2-y^2}$ excitation energy, leads to values of 1.35 eV, 1.53 eV and 1.83 eV for the $d_{xy} \rightarrow d_{x^2-y^2}$, $d_{z^2} \rightarrow d_{x^2-y^2}$ and $d_{xz} \rightarrow d_{x^2-y^2}$ states respectively, compared with values of 1.35 eV, 1.5 eV and 1.8 eV reported by Kuiper et al [2].

Crucial to the assignment of the $d_{z^2} \rightarrow d_{x^2-y^2}$ energy is the associated spin flip energy of ~ 0.2 eV, which has been shown to be entirely consistent with the Néel temperature and the magnetic coupling constant arising from the Fock-35 hybrid. A comparison with previous correlated cluster calculations, which predict an incorrect order of the $d \rightarrow d$ excited states, indicates that these do not capture fully the influence of the extended surrounding lattice. Identical calculations, but in the presence of a nearest neighbour $O(p\pi_{||})$ hole, find changes to the excited state energies of no more than 0.1 eV – 0.2 eV, thereby removing any lingering possibility that the $d_{z^2} \rightarrow d_{x^2-y^2}$ state might be involved in the mechanism of high- T_c behaviour.

With regard to two, more general points, first, the calculations highlight the extent to which even highly atomic excitations involve extensive re-organisation of open-shell levels in particular, leading to a substantial lowering of UHF rigid band energies. It follows from this that comparisons of the ground state eigenvalues with experimental spectra are an ill-founded guide as to the quality of the UHF ground state. Secondly, the chapter shows that inter-site transitions, such as CT excitations are also amenable to a direct SCF approach, leading to excitation energies that are comparable in accuracy to those for on-site transitions and in apparent agreement with previous estimates.

5. References

- [1] J. D. Perkins, J. M. Graybeal, M. A. Kasatner, R. J. Birgenau, J. P. Falck and M. Greven, *Phys. Rev. Lett.* **71**, 1621 (1993)
- [2] P. Kuiper, J-H. Guo, C. Sâthe, L.-C. Duda, J. Norgren, J. J. M. Pothuizen, F. M. F. de Groot and G. A. Sawatzky, *Phys. Rev. Lett.* **80**, 5204 (1998)
- [3] W. C. Mackrodt and H. J. Gotsis, *Phys. Rev. B* **62**, 10728 (2000)
- [4] C. Noguera and W. C. Mackrodt, *J. Phys C: Cond. Matter* **12**, 2163 (2000)
- [5] W. C. Mackrodt and C. Noguera, *Surf. Sci.* **457**, L386 (2000)
- [6] B. von Grande and Hk. Müller-Buscgbaum, *Z. Anorg. Allg. Chem.* **417**, 68 (1975)
- [7] D. Vaknin, S. K. Sinha, C. Stassis, L. L. Miller and D. C. Johnson, *Phys. Rev. B* **41**, 1926 (1990)
- [8] M. Korotin and V. I. Asanimov, *Materials Letters* **10**, 28 (1990)
- [9] D. L. Noviskov, A. J. Freeman and J. D. Jorgensen, *Phys. Rev. B* **51**, 6675 (1995)
- [10] S. Tanaka and A. Kotani, *J. Phys. Soc. Jpn.* **62**, 464 (1993)
- [11] C. de Graaf and R. Broer, *Phys. Rev. B* **62**, 702 (2000)
- [12] K. Maiti, D. D. Sarma, T. Mizokawa and A. Fujimori, *Phys. Rev. B* **59**, 1572 (1998)
- [13] N. W. Ashcroft and N. D. Mermin, *Solid State Physics*, Saunders College, Fort Worth 1976
- [14] I. de P. R. Moreira, F. Illas and R. L. Martin, *Phys. Rev. B* **65**, 115102 (2002)
- [15] H. S. Choi, Y. S. Lee, T. W. Noh, E. J. Choi, Y. Bang and Y. J. Kim, *Phys. Rev. B* **60**, 4646 (1999)

Chapter 8

Conclusion, Publications and Acknowledgements

1. A Universal Functional for the Transition Metal Oxides?

Chapters 1, 2, 3, and 4 of this work are those which directly address the question of whether there exists a single hybrid functional which yield values for most properties in good agreement with experiment. There is a large amount of data to retain here, and so a summary is provided in the Table below.

Material	Property	Hybrid Scheme	Range of F_0
NiO	Spin Moment	PW91-PW91	0.1 – 0.9
"	Energy Gap	"	0.1 – 0.2
"	Fermi Energy	"	0.2 – 0.3
"	CT Insulating	"	≥ 0.3
"	Spin Moment	Becke-LYP	0.1 – 1.0
"	Energy Gap	"	0.1 – 0.2
"	Fermi Energy	"	0.2 – 0.3
"	CT Insulating	"	≥ 0.2
MnO	Spin Moment	Becke-LYP	0.0 – 0.4
"	Energy Gap	"	0.1 – 0.2
NiO	Lattice Constant	"	0.9 – 1.0
"	Bulk Modulus	"	no agreement
MnO	Lattice Constant	"	0.6 – 0.7
"	"	Becke-no-LYP	no agreement
"	Bulk Modulus	Becke-LYP	0.0 – 0.1
"	"	Becke-no-LYP	0.1 – 0.9
NiO	Direct Coupling	Becke-LYP	≥ 0.5
"	Superexchange Coupling	"	0.2 – 0.3
MnO	Direct Coupling	"	0.1 – 0.2
"	Superexchange Coupling	"	0.5 – 0.6
"	Direct Coupling	Becke-no-LYP	0.0 – 0.1
"	Superexchange Coupling	"	0.1 – 0.2
"	Pressure Gradient of T_N	Becke-LYP	0.1 – 0.2
"	"	Becke-no-LYP	0.0 – 0.1
"	Magnetostriction	Becke-LYP	0.1 – 0.2
"	Crystal Field Excitations	"	0.4 – 0.5
"	B1 to B8 Transition	"	0.0 – 0.2
NiO	Crystal Field Excitations	"	1.0 - UHF
"	$d^8\bar{L}$ Hole State	"	≥ 0.4
≥ 0.5	$d^8\bar{L}$ Hole Insulating	"	≥ 0.4

- Grouping properties into crude ‘types’, it is clear that the lattice constants of MnO and NiO in the correlated scheme are best described by a high $F_0 > 0.5$, whereas the bulk modulus is better described by a broad range of F_0 in functionals lacking correlation. Thus, there is no clear consensus for the ‘structural’ types of property.
- The spin moments of MnO and NiO are best described by a small range of weights of $F_0 < 0.5$, and this applied also to energy gaps and Fermi energies. The requirement for a CT insulating ground state in NiO falls within this range, and thus, for the ‘electronic structure’ type of property, a choice of $F_0 < 0.5$ seems to be advised
- A consideration of direct magnetic coupling in MnO and NiO in the correlated scheme leads to ranges of F_0 that do not overlap, with similar occurring for the superexchange coupling. However, the ranges of best-fit F_0 do seem to be concentrated around the mid-range. The most consistent description of magnetism occurs in MnO with the uncorrelated method, where J_d , J_{sc} and the pressure gradient of T_N can all be described by F_0 in the range 0.0 – 0.2. The agreement between the range of F_0 in the correlated scheme for a best description of J_d and the size of the magnetostriction effect in MnO is gratifying. The conclusion must be, though, that there is no clear consensus for the ‘magnetic’ types of property.
- The crystal field excitations in NiO and MnO produce best-fit ranges of F_0 that are far from overlapping. This is due to the problem of pair correlation energy that arises in MnO. A fairer test would therefore use NiO and at least one other TMO in which the crystal field excitations can occur without change in metal spin. The fact that the crystal field excitations in $Sr_2CuO_2Cl_2$ are in good agreement with experiment at the UHF level, in combination with the high best fit range of F_0 for the excitations in NiO argues for $F_0 = 1.0$ – UHF for the “crystal field” types of property. Finally, the holes in NiO imposes a broad range of $F_0 \geq 0.4$

A careful consideration of the results presented above, in addition to those few entries in the literature makes it clear that the main conclusion of this thesis must be that there is no one universally applicable hybrid functional suitable for the TMOs. The case for developing a viable post-HF correlation technique applicable to the solid state is strengthened by this finding, for only then may reliable *ab initio* predictions of many of the properties of the TMOs be made, without appeal to precedents in the literature. Yet, hybrid functionals will continue to play an important role in solid state calculations. As Chapter 1 discussed, systematic improvement of many properties is possible where calculated values at the pure HF and DFT limits bracket the experimental range. The most obvious and dramatic example of this effect in the present work occurs for the magnetic properties of the late TMOs, where UHF and DFT approaches under- and overestimate respectively coupling constants (and, consequently, ordering temperatures) and the strength of the spin-lattice interaction. Band gaps and phonon spectra have been shown to display qualitatively similar, although quantitatively less extreme dependence on weight of exact exchange. The description of weak bonds, such as the interlayer interactions in the alkaline earth hydroxides and the properties of hydrogen bonded systems have been found to be dramatically improved by hybrid functionals. In addition, at a more practical level, functionals containing high weights of exact exchange have been shown to stabilise SCF cycles in TM bearing compounds, avoiding the problems associated with near-degenerate or degenerate d-orbital occupancies; an experience shared in the current study.

The clearest, and most important trend to emerge from the current work is the dependence of the degree of electronic localisation on the nature of the exchange in the functional. High weights of exact exchange always lead to increased ionicity, with corresponding systematic decrease of the lattice parameter (due to increased strength of the Madelung potential), and increase in bulk moduli and elastic constants. As demonstrated by the work in Chapters 3 and 4 on crystal field excitations and doping of NiO, this localisation effect is particularly important for electronic or lattice defects which break the translational symmetry of the crystal. In such cases, the lack of orbital dependence in DFT, even in broken symmetry, invariably results in delocalised, metallic solutions for directly calculated defects, and instability of excited states. Such an effect has also been noted in simpler compounds lacking TM

cations, such as MgO. One clear requirement here is a quantitative measure of the degree of localisation of such states, beyond simple Mulliken analyses. The use of localiser algorithms to arrive at a description of electronic structure in terms of Wannier functions may be a fruitful approach in the future.

As a further note, the work reported in this thesis has made apparent the real utility of phenomenological Hamiltonians for the interpretation of the results of more complex calculations. In particular, the Kanamori crystal field and Ising spin Hamiltonians have proven themselves of great value in the end analysis of many of the simulations conducted, irrespective, essentially, of the nature of the material under investigation. The effect of the weight of exact exchange upon magnetic coupling constants has already been discussed in this section, but clear universal trends are also apparent in the crystal field parameters of the TMOs. In spin allowed excitations, low weights of exact exchange always lead to underestimates of the B and C Racah parameters. This is a direct manifestation of the lack of orbital dependence in DFT already discussed, where microstates of similar multiplicity approach degeneracy. In spin forbidden excitations, it is clear from the outset that the UHF method cannot provide quantitatively correct energies, and here a lower weight of exact exchange is more appropriate. It is clear that there await many more applications for this sort of analysis in the field.

As a final note, and in summary, it is clear that the optimal weight of exact exchange for the study of any given problem is both system and property specific. Furthermore, it is clear that the B3LYP potential, of such proven universal utility in molecular theory is inadequate in the solid state. Generally, all that can be meaningfully said is that higher weights of exact exchange than 20% would seem to be required in solids, and that this is due to the added localising effect of the long-range electrostatic potential in periodic boundary conditions.

2. Publications Arising from This Work

1. "A Hybrid Density Functional Theory Study of Vanadium Monoxide" by W. C. Mackrodt, D. S. Middlemiss and T. G. Owens, *Physical Review B* **69**, 115100 (2004)
2. "A hybrid Hartree-Fock density functional study of $\text{Li}_x\text{Ni}_{1-x}\text{O}$ " by W. C. Mackrodt and D. S. Middlemiss, *Journal of Physics: Condensed Matter* **16**, S2811 (2004)
3. "The Performance of Hybrid Density Functionals in Solid State Chemistry" by F. Corà, M. Alfredsson, G. Mallia, D. S. Middlemiss, W. C. Mackrodt, R. Dovesi and R. Orlando, a review article in *Structure and Bonding*, Springer-Verlag, Berlin, at press (2004)
4. "First Principles Study of $d \rightarrow d$ Excitations in NiO" by D. S. Middlemiss and W. C. Mackrodt, *Molecular Physics*, at press (2004)

3. Acknowledgements

I would like to thank my supervisor, Dr. William C. Mackrodt for his enthusiasm, his patience and his kindness over the course of the Ph. D. It has been a great pleasure and a privilege working with him. I would also like to thank Stuart Purdie for useful discussions and a lot of help with the administration of the computers. I have been involved in fruitful collaboration with Dr. Furio Corà of the Royal Institution, London, and with Dr. Victor Saunders of CLRC Daresbury, for both of which I am most grateful. I have also helped to supervise Tom Owens during his Senior Honours year, and I thank him for his contribution to the work that we did together. Finally, I would like to extend my great gratitude to my family and friends, who have never flagged in their enthusiasm and support.